Dissertation

submitted to the

Combined Faculty of Mathematics, Engineering and Natural Sciences

of Heidelberg University, Germany

for the degree of

Doctor of Natural Sciences

Put forward by

M.Sc. Nicola Alain Ackermann

born in: Ottweiler

Oral examination: 23-10-2025

Coherent Elastic Antineutrino-Nucleus Scattering with CONUS+:

Precision Background Modeling and Signal Extraction

Referees: Prof. Dr. Dr. h.c. Manfred Lindner

JProf. Dr. Loredana Gastaldo

Abstract

Coherent elastic neutrino-nucleus scattering (CEνNS) is a Standard Model process which had long evaded observation at reactor energies due to the tiny recoil energies and challenging background conditions involved. The CONUS+ experiment is a dedicated CEνNS experiment operating four high-purity germanium detectors inside a massive composite shield located at the commercial nuclear power plant KKL in Leibstadt, Switzerland. The first physics run of the experiment (run 1), which lasted from November 2023 to August 2024 and collected 326.8 kg d of reactor on and 59.7 kg d of reactor off data, yielded the first measurement of CEνNS for reactor antineutrinos. This thesis first presents the full decomposition and modelling of the background spectra of the CONUS+ detectors in both reactor on and off data taking periods in run 1. The establishment of such a background model is a crucial step towards the full understanding of the measured data and allows the extraction of the CEνNS signal in a full likelihood analysis, also presented in this work. The findings of this thesis therefore directly enabled and provided the first successful measurement of the interaction at reactor site.

Monte Carlo simulations show that the dominant background sources of the experiment are cosmic rays (muons and neutrons), contributing approximately 70 - 80% of the background rate below 1 keV. At larger energies above the region of interest of the experiment, other sources like the influence of radon in the detector chamber and ^{210}Pb become more dominant. Reactor-correlated backgrounds are found to be subdominant. The differences in the measured reactor on and off spectra of the detectors were able to be explained by reduced cosmic ray fluxes in the room due to an increased overburden and changes in the radon concentration during the reactor off measurement. The full background model correctly describes the measured detector spectra in both reactor on and off measurements for all energy ranges. The analysis of the CONUS+ run 1 data, which uses these models along with all relevant detector properties and the predicted CEνNS spectrum, reveals a clear signal at energies below 350 eV, corresponding to (395 $\pm$ 106) neutrino events and excluding the background-only hypothesis at 3.7σ confidence level. The observed signal is consistent with the Standard Model prediction within 0.5σ.

Zusammenfassung

Kohärente elastische Neutrino-Kern-Streuung (CEvNS) ist ein Prozess des Standardmodells, der aufgrund der äußerst geringen Rückstoßenergien und herausfordernder Untergrundbedingungen lange Zeit bei Reaktorenergien nicht beobachtet werden konnte. Das CONUS+ Experiment ist ein dediziertes CEvNS-Experiment, das vier hochreine Germaniumdetektoren in einem massiven, mehrschichtigen Schild am kommerziellen Kernkraftwerk KKL in Leibstadt, Schweiz, betreibt. Die erste Messkampagne des Experiments (Run 1), die von November 2023 bis August 2024 dauerte, sammelte 326,8 kg·d Daten bei laufendem Reaktorbetrieb (Reaktor-an-Phase) sowie 59,7 kg·d außerhalb des Leistungsbetriebs (Reaktor-aus-Phase) und ermöglichte die erste Messung von CEvNS mit Reaktorantineutrinos. Diese Arbeit präsentiert zunächst die vollständige Entschlüsselung und Modellierung der Untergrundspektren der CONUS+-Detektoren während der beiden Messphasen in Run 1. Die Anfertigung eines solchen Untergrundmodells ist ein entscheidender Schritt zum vollständigen Verständnis der gemessenen Daten und ermöglicht die Extraktion des CEvNS-Signals in einer Likelihood-Analyse, die ebenfalls in dieser Arbeit vorgestellt wird. Die Ergebnisse dieser Arbeit ermöglichten somit direkt die erste erfolgreiche Messung dieser Wechselwirkung am Reaktorstandort.

Monte-Carlo-Simulationen zeigen, dass die dominanten Untergrundquellen des Experiments kosmische Strahlung (Myonen und Neutronen) sind, die etwa 90 % der Untergrundgrundrate unterhalb von 1 keV ausmachen. Bei höheren Energien außerhalb des interessierenden Bereichs des Experiments werden andere Quellen wie der Einfluss von Radon in der Detektorkammer und ^{210}Pb dominanter. Reaktor-korrelierte Untergrundereignisse erweisen sich hingegen als untergeordnet. Die Unterschiede zwischen den gemessenen Reaktor-an- und Reaktor-aus-Spektren der Detektoren konnten durch eine verringerte kosmische Strahlungsflussrate im Raum infolge einer größeren Abschirmung sowie durch Veränderungen der Radonkonzentration während der Reaktor-aus-Messung erklärt werden. Das vollständige Untergrundmodell beschreibt die gemessenen Detektorspektren in beiden Messphasen über alle Energiebereiche hinweg korrekt. Die Analyse der CONUS+ Run-1-Daten, die diese Modelle zusammen mit allen relevanten Detektoreigenschaften und dem vorhergesagten CEvNS-Spektrum verwendet, zeigt ein deutliches Signal bei Energien unterhalb von

350 eV, entsprechend (395 ± 106) Neutrinoereignissen, und schließt die Null-Hypothese mit einer Signifikanz von 3,7σ aus. Das beobachtete Signal stimmt innerhalb von 0,5σ mit der Vorhersage des Standardmodells überein.

Contents

Abstract **vii**

Zusammenfassung **ix**

Contents **xi**

List of Figures **xv**

List of Tables **xxix**

1 Introduction **1**

1.1 CEνNS in the Standard Model 3

1.2 Artificial neutrino sources 6

1.2.1 Accelerator neutrinos 6

1.2.2 Neutrinos from nuclear reactors 7

1.3 Potential of CEνNS 7

1.3.1 BSM physics 7

1.3.2 Measurement of nuclear form factor and nuclear structure of target isotopes 8

1.3.3 Supernova detection and modelling 9

1.3.4 CEνNS for dark matter experiments 9

1.3.5 Nuclear reactor monitoring 10

1.4 Experimental requirements 11

1.5 Technologies for CEνNS measurements 12

1.5.1 Bolometers and transition edge sensors 12

1.5.2 Scintillating crystals 13

1.5.3 Liquid noble detectors 13

1.5.4 Charged-coupled devices 14

1.5.5 High-purity germanium detectors 14

2 The CONUS+ experiment **17**
2.1 Experimental location 17
2.2 Timeline 18
2.2.1 From CONUS to CONUS+ 18
2.2.2 CONUS+ commissioning and first runs 21
2.3 Germanium detectors 21
2.3.1 Ge semiconductor principles 21
2.3.2 Nuclear quenching 23
2.3.3 Signal processing in the preamplifier 25
2.3.4 Data acquisition and energy reconstruction 27
2.3.5 Energy resolution of a germanium detector 28
2.3.6 The CONUS+ detectors 29
2.3.7 Detector upgrades 29
2.3.8 Detector performance 30
2.3.9 CONUS+ DAQ system 34
2.4 CONUS+ shield and backgrounds 36
2.4.1 Background sources for the CONUS+ experiment 36
2.4.2 Shield setup 46
2.5 Additional infrastructure and data pipeline 48

3 Background Model **51**
3.1 Motivation 51
3.2 Background characterisation of the CONUS+ location 52
3.2.1 Gamma rays 53
3.2.2 Cosmic muons 56
3.2.3 Neutrons 57
3.3 Monte Carlo framework and approach 62
3.4 Muon-induced background 65
3.4.1 Muon veto and application to simulations 67
3.4.2 Efficiency correction of the High E channels with muon simulations 72
3.5 Cosmic neutron background 75
3.5.1 Cosmic neutron flux in the CONUS+ room 75
3.5.2 Impact on background 79
3.6 Muon-induced neutrons in the overburden 80
3.7 Radon in the detector chamber 82
3.8 Cosmogenic activation 86
3.8.1 Germanium crystals 87

3.8.2 Contributions of copper . . . 97
3.9 ^{210}Pb in lead . . . 99
3.9.1 ^{210}Pb in the shield . . . 100
3.9.2 ^{210}Pb in the cryostat . . . 101
3.10 Additional contaminations inside the cryostat . . . 103
3.11 Leakage test background . . . 104
3.12 Reactor backgrounds . . . 106
3.12.1 Reactor neutrons . . . 107
3.12.2 Inert gases . . . 109
3.12.3 High energy γ radiation . . . 110
3.13 Model differences between reactor on and off measurement . . . 111
3.13.1 Impact of drywell lid . . . 111
3.13.2 Reduced radon contamination in off measurement . . . 112
3.13.3 Reactor-correlated background sources . . . 112
3.14 The full background model . . . 113

4 First CEνNS observation at a nuclear reactor 127
4.1 Definition of data sets . . . 127
4.1.1 Selection cuts and dead-time . . . 128
4.2 Background and performance stability . . . 132
4.3 Energy scale calibration . . . 134
4.4 Definition of thresholds and region of interest . . . 137
4.5 Signal expectation . . . 140
4.6 Likelihood function . . . 142
4.6.1 Maximum likelihood method . . . 142
4.6.2 Gaussian pull terms . . . 144
4.6.3 Likelihood function for CEνNS analysis . . . 145
4.6.4 Overview of fit parameters . . . 147
4.7 CEνNS result . . . 149
4.7.1 Single detector results . . . 149
4.7.2 Combined detector result . . . 152
4.7.3 Checks with different data sets . . . 158
4.7.4 Alternative quenching descriptions . . . 159
4.7.5 Comparison to other CEνNS measurements . . . 160

5 Next steps in the CONUS+ experiment 165
5.1 Detector upgrade . . . 165
5.2 Stability and detector performance . . . 167

5.2.1 Performance of new detectors 167
5.2.2 Run 2 data taking 169
5.2.3 Noise rate and stability 170
5.3 New data sets 171
5.3.1 Background level and stability 173
5.4 Sensitivity study 175

6 Conclusions **179**

Appendices **185**

A Supplementary figures for background model **187**

B Supplementary figures for CEνNS result **191**

List of Publications **195**

Bibliography **197**

Acknowledgements **207**

List of Figures

1.1 Running of the nuclear form factor for different momentum transfers for ^{40}Ar (left) and ^{48}Ti (right) from [1]. Blue dots show experimental measurements, the yellow dashed line shows the nuclear form factor based on the fourier transform of the nuclear charge density distribution, and the red dashed lines show a simplified prediction from a shell model of the nucleus. The green line and black line are improvements of this model made from different theoretical considerations. Here, FOP stands for fractional occupation probability of states in the nucleus, while BCS stands for the Bardeen Cooper Schriffer equations, which can be solved to find occupation probabilities for different nucleon levels within the nucleus. 4

1.2 Neutrino cross sections for energies below 50 MeV. The CEνNS cross section is two orders of magnitude bigger than that of inverse beta decay and four to five orders of magnitude bigger than that of elastic neutrino electron scattering. Plot taken from [2]. 5

1.3 Current and future limits on DM direct detection spin-independent cross section (σ_p^{SI}) as a function of DM mass (m_χ), and impact of solar and atmospheric neutrinos on these measurements. Taken from [3] 10

2.1 Schematic drawing of the KKL reactor building with the CONUS+ location, taken from [4] 18

2.2 Location of CONUS+ within room ZA28R027 [5]. The red dashed line indicates the separation wall between the CONUS+ area (left) and the rest of the room. Green dots indicate the positions used in the background characterisation performed before the move to KKL. The Blue line indicates the position of the reactor drywell head during reactor outage above room ZA28R027. 19

2.3 Spectra measured with the C2 detector in run 5 of the CONUS experiment. The ROI was defined as 210 eV to 1000 eV. Reactor on data is shown in black, while reactor off data is shown in blue and good agreement was in principal found between both spectra, indicating no clear sign of a measured CEνNS interaction. Additionally, three theoretical predictions for the CEνNS signature are shown. Red shows the standard prediction using the Lindhard model described in Section 2.3.2 as well as the two quenching descriptions from [6]. 20

2.4 Schematic of a point contact p-type Ge detector like the ones used in CONUS+ [2] 23

2.5 Ionization quenching factor as a function of the nuclear recoil energy [7]. The data points were obtained for four different neutron beam energies. Indicated error bars are uncorrelated uncertainties, correlated uncertainties are represented by the blue band. The data fits the Lindhard theory description with k = 0.162 ± 0.004 (stat + sys)(black curve) 25

2.6 Examples of pulses generated in the CONUS+ detectors from [8]. The shape of the pulse gives information about the location of the event within the germanium crystal: Bulk events (black) are standard events happening in the main active volume of the detectors, surface events (red) happen in the transition layer of the crystal and feature slower rise times, Multi-site events (green) are events in which multiple energy depositions happen in one event, leading to one or multiple steps in the rise of the pulse. 26

2.7 Detectors for the CONUS+ experiment 29

2.8 Pulser resolution of C2 before (blue) and after (red) the upgrade [8]. 32

2.9 Improvement of the trigger efficiencies of all detectors used in the CONUS+ experiment. Dashed lines show values measured in the commissioning phase at KKL, while the solid lines how the values for the CONUS experiment at KBR. As C5 was not used at KBR, the solid line presents values measured at MPIK before the upgrade. [8]. 33

2.10 Deviation from a purely linear scale for the C2, C3 and C5 detectors. The line shows the fit function NL(E) (fourth order polynomial) chosen to describe the energy dependence of the deviation. This fit function was implemented in the energy calibration of the final data sets. 35

2.11 Spectrum of primary cosmic rays in units of intensity multiplied by kinetic energy squared. Points show measurements of negative muons with E > 1 GeV from different experiments. Taken from [9] 37

2.12 Spectrum of secondary cosmic rays at different altitudes / atmospheric depths. Extracted from [10] 38

2.13 Spectrum of cosmic ray muons at sea level for $\theta = 0°$. $\diamond$ additionally shows $\theta = 75°$. Taken from [10] 39

2.14 Muon charge ratio measured in different experiments. Taken from [10] . . 40

2.15 Vertical integral intensity of muons for different depths of overburden, from [2]. Different models for the calculation of the intensity are compared and show good agreement. Furthermore, the vertical integrated intensity for cosmic ray neutrons is shown. 41

2.16 Typical spectrum of cosmic ray neutrons at sea level, measured in New York, USA from [11] 43

2.17 Picture of the eight bottles (10 L, 300 b) of radon-free air in the CONUS+ room. The bottles are stored in a rack and connected with pressure reducers to a system of tubes which guide the air inside the shield. A flowmeter (not pictured) is included to check the air flux. 44

2.18 Shield design of the CONUS+ experiment, consisting of layers of stainless steel (silver), polyethylene (red), borated polyethylene (white) and lead (black). Additionally, two layers of plastic scintillator (blue) with integrated PMTs act as a double muon veto system. In the centre, the four HPGe detectors are embedded, housed in ultra low background copper cryostats. The inner detector chamber is continuously flushed with radon-free air. 47

2.19 Background suppression capability of the shield setup used in the CONUS experiment in Brokdorf, measured for one HPGe detector (C1) [12]. ”Passive shield” refers to the shield setup without active muon veto. For the CONUS+ experiment one lead layer was replaced with an additional muon veto, thereby slightly decreasing the suppression of the passive shielding, while increasing the capability of the muon veto system. 49

2.20 Schematic of the slow control systems and overall infrastructure of the CONUS+ experiment. A local network connects the CONUS+ server to all data taking devices in the CONUS+ room (inside the containment area) through the Raspberry Pi, the two PCs and the NIM/VME crates. The server is connected to MPIK through a VPN. 50

3.1 Gamma ray spectrum below 2.7 MeV measured with the CONRAD detector inside of the CONUS+ room at KKL with identification of the isotopes producing the peaks from [5]. The spectrum is dominated by naturally occurring isotopes. The most prominent contribution is from the decay of ^{60}Co. The spectrum also features a single escape peak (SEP) from ^{208}Tl, where a the γ-ray induces pair production, the produced electron and positron annihilate and one of the resulting 511 keV photons escapes the detector. 53

3.2 Gamma ray spectrum above 3.5 MeV measured with the CONRAD detector inside of the CONUS+ room at KKL with identification of the isotopes producing the peaks from [5]. The spectrum is dominated by isotopes that are induced from neutron capture of the reactor neutrons on the surrounding materials. The spectrum also features single escape peaks (SEP), where the gamma rays from the decay induce e^+e^- pair production and subsequent annihilation in the Ge crystal and one of the annihilation gammas escapes the crystal. 54

3.3 Energy spectra of two representative wipe tests taken at the CONUS and CONUS+ locations at KBR and KKL respectively. They were evaluated with the BRUNO Ge spectrometer at MPIK. 55

3.4 Liquid scintillator used for the measurement of the muon flux in the CONUS+ room. The detector is enclosed in an aluminium housing and connected to a CAEN V1725 analog-to-digital converter for data acquisition. 57

3.5 Distribution of F_{40} variable versus total reconstructed energy of the event measured in the CONUS+ room in one day. The combination of the F_{40} variable and energy allows for the distinction between three different populations of events: natural radioactivity, muons, and neutrons. 58

3.6 Muon energy spectra measured in the CONUS+ room at KKL and at MPIK above ground. The spectra share the same shape with a scaling factor of 1.9, which is equivalent to an overburden of 7.3 m w.e.. MPIK and KKL are located at a very similar altitude of approximately 350 m above sea level. 59

3.7 Response functions of the different Bonner spheres used in the measurement. The diameter of the spheres in inches is given, The brown line is the response function of an 8 inch sphere with an additional Cu shell. 60

3.8 Neutron count rates in the individual Bonner spheres during reactor on as function of the sphere diameter. The rates are normalised to 1 GW h. 0 corresponds to the bare counter and 18” corresponds to the 8” modified sphere. 61

3.9 Energy distribution of neutrons in the CONUS+ room, acquired from the Bonner sphere measurement and normalised to the thermal power of the reactor. 62

3.10 Neutron count rates in the individual Bonner spheres during reactor off as function of the sphere diameter. 0 corresponds to the bare counter and 18” corresponds to the 8” modified sphere. 63

3.11 Differential vertical muon flux spectrum at an overburden of 7.4 m w.e. as in the CONUS+ room. 65

3.12 Simulated spectrum of the muon-induced background in the C5 detector without application of the muon veto. The left plot shows the background induced by negative muons, while the right plot shows positive muons. . . 66

3.13 Comparison of the total simulated muon background spectrum and data taken by the C5 detector in run 1 without the application of the muon veto from 0.4 to 30 keV. Very good agreement is found. At 10.3 keV the gamma line from the decay of $^{68/71}$Ge can be seen in the data. 67

3.14 Comparison of C5 run 1 data with and without the applied muon veto cut. . 68

3.15 Illustration of the origin of the muon veto tagging inefficiency. An incoming muon passes through the outer layers of the shield without passing through the outer muon veto layer. In the shield, it induces an electromagnetic shower, which propagates through the shield and induces events in the Ge detectors. 69

3.16 Simulated spectrum of muon-induced events from muons that do not cross a muon veto layer (red) and from muons that cross a muon veto layer (blue). At low energies below 15 keV, it can be seen that most of the events originate from muons that do not cross a plastic scintillator plate. These events are not triggered in the veto system and therefore induce an inefficiency at low energies. 70

3.17 Left: Polynomial fit to the ratio of the spectrum of muon-induced events with no tagged muon to the spectrum of muon-induced events with a tagged muon. Right: Resulting muon veto efficiency. For very low energies the efficiency drops to 96.5 % 71

3.18 Muon simulation result with the applied muon veto efficiency from Figure 3.17 compared to the data taken with the C5 detector in run 1. In the shown energy range the muon spectrum is flat at higher energies and rises exponentially towards low energies. This rise is due to the presence of neutrons that are induced by the muons in the high-Z materials of the CONUS+ shield. 72

3.19 Muon simulation result split into hadronic (left) and electromagnetic (right) component. The distinction is made by the type of particle directly responsible for the energy deposition in the detector. 73

3.20 Data taken during run 1 in the high energy channels of the four detectors with muon veto cut applied. Clear efficiency losses are visible starting above energies of approximately 100 keV. The efficiency loss is especially visible for the C5 and C3 detectors. 74

3.21 High E data measured in the C5 detector without muon veto cut compared to the result of the muon simulation presented in the previous sections. The data without muon veto cut should be completely dominated by muon-induced events and the simulations should therefore describe the data. . . . 75

3.22 Corrected high energy spectra of the three detectors used in the analysis of run 1. The spectra match the expected shape after the efficiency correction with the muon simulation results. The method introduces large uncertainties in the bins above 300 keV due to the limited statistics in the original data. Therefore, only the spectra up to 300 keV are used for analysis. 76

3.23 Neutron spectrum measured in Yorktown, NY, USA in [11]. The spectrum shows the characteristic thermal, evaporation and cascade peaks described in 2.4.1. 77

3.24 Model of the KKL reactor building built in Geant4. Only the structure above the CONUS+ room is simulated. The materials that are used are: Standard concrete (red), reinforced concrete (orange) and steel (blue). The CONUS+ experimental room is shown in green. 78

3.25 Flux of cosmic neutrons in the CONUS+ room from simulations of neutrons passing through the reactor building. 79

3.26 Neutron simulation result compared to the data taken in run 1 of the CONUS+ experiment with the C5 detector in the low energy channel up to 30 keV (top) and the high E channel (bottom). The neutrons feature an exponential rise towards very low energies and their spectrum flattens towards higher energies. 81

3.27 Spectrum of muons on the outside of the KKL reactor building. These muons are propagated through the model of the reactor building. 82

3.28 Muon-induced neutron flux in the CONUS+ room from simulation. The thermal and evaporation peak are present again, while a small cascade peak at 100 MeV is also visible. 83

3.29 Simulation result for muon-induced neutrons compared to the data taken in run 1 of the CONUS+ experiment with the C5 detector in the low energy channel up to 30 keV (top) and the high E channel (bottom). The impact of these neutrons is small compared to the contributions from prompt muons and cosmic neutrons, however a small contribution at very low energies (in the ROI for CEνNS) is visible. The impact at energies above 30 keV is negligible, as the background decreases strongly towards higher energies, as was the case for the cosmic neutrons 84

3.30 Example of Gaussian fit to the 352 keV ^{214}Pb line in C5 reactor on data . . 87

3.31 Simulation result for radon in the detector chamber compared to the data taken in run 1 of the CONUS+ experiment with the C5 detector in the low energy channel up to 30 keV (top) and the high E channel (bottom). The impact of radon is small in the low energy channel and the ROI but is considerable and one of the largest contributions in the high energy range. . . 88

3.32 Simulation result for the background contribution of ^{68}Ge and ^{68}Ge in the C5 detector in reactor on data of run 1. 90

3.33 Simulation result for the background contribution of ^{68}Ga in the C5 detector in reactor on data of run 1 91

3.34 Simulation result for the background contribution of ^{65}Zn in the C5 detector in reactor on data of run 1 92

3.35 Data taken in the C5 detector between 100 and 200 keV. No line at 143.5 keV is visible. The line at 140 keV comes from the decay of a metastable germanium state, ^{75m}Ge. 94

3.36 Background contributions from cosmogenically activated isotopes in the germanium crystals without visible lines. Their corresponding activities were calculated from Table 3.12 and Formula 3.8 assuming an exposure of 100 days. 95

3.37 Decay scheme of the three metastable states in germanium. 96

3.38 Simulation result for the background contribution of the metastable state ^{71m}Ge in the germanium crystal of the C5 detector in reactor on during run 1. 97

3.39 Explanation of the shape of the double-peak structure visible in the spectrum of ^{73m}Ge. Left: After the first event (the emission of the 53 keV γ) the second event (13.3 keV) happens in very close succession. The energy of the whole event is reconstructed at the maximal height of the recorded pulse, leading to a value between 53 and 66 keV. Right: The second pulse arrives later, after the first pulse has already sufficiently decayed. The highest point in the pulse is still the maximum of the first pulse, the reconstructed energy is therefore just the energy of the first γ. 98

3.40 Simulation result for the background contribution of the metastable state ^{73m}Ge in the germanium crystal of the C5 detector in reactor on during run 1. 99

3.41 Simulation result for the background contribution of the metastable state ^{75m}Ge in the germanium crystal of the C5 detector in reactor on during run 1. 100

3.42 Background contributions from cosmogenically activated isotopes in the copper parts of the setup. Their corresponding activities were calculated from Table 3.12 and Formula 3.8 assuming an exposure of 100 days. . . . 101

3.43 Decay chain of ^{210}Pb. 102

3.44 Simulation result for ^{210}Pb in the innermost shield layer. Left: Contribution from different sides to the total ^{210}Pb background from the shield. Right: Comparison of total to the spectrum of the C5 detector in reactor on measurement in run 1. 103

3.45 46.5 keV line from the decay of ^{210}Pb in the cryostat in the C1 detector in the CONUS experiment from [2]. 104

3.46 High energy data taken during run 1 of the CONUS+ experiment with the C5 detector. No line at 46.5 keV is visible, pointing to the absence of ^{210}Pb from the inside of the cryostat. 105

3.47 Simulation result of the ^{210}Pb contamination on the germanium diode of C5 with the calculated upper limit on the activity of 10 μBq. 106

3.48 Simulation result of a 5 μBq ^{60}Co contamination in close proximity to the germanium crystal of C2. The spectrum matches the missing background component in the C2 and C3 background model. 107

3.49 Simulation result of the reactor neutrons compared to the C5 spectrum during reactor on measurement. 108

3.50 Simulation result of ^{3}H, ^{85}Kr, and ^{135}Xe and their impact on the background of the C5 detector in reactor off measurement during run 1. 110

3.51 Evolution of the radon contamination in the detector chamber shown through the count rate in the 353 keV line in C2. The reactor off measurement was in May, where the radon contamination was considerably lower than for most of the on measurement. 112
3.52 Complete background model and separate components for the C5 detector in reactor on measurement. 114
3.53 Complete background model and separate components for the C5 detector in reactor off measurement. 115
3.54 Complete background model and separate components for the C2 detector in reactor on measurement. 116
3.55 Complete background model and separate components for the C2 detector in reactor off measurement. 117
3.56 Complete background model and separate components for the C3 detector in reactor on measurement. 118
3.57 Complete background model and separate components for the C3 detector in reactor off measurement. 119

4.1 C5 run 1 reactor on data from 120 to 800 eV. Below 150 eV a large increase in the count rate can be seen, this is the noise peak. The region above 150 eV is well described by the background model of the detectors as shown in Section 3.14. 128
4.2 Noise and environmental parameters for the four detectors of the CONUS+ experiment: C5 (upper right), C5 (upper left), C3 (lower left), and C4 (lower right). Periods with red shading for the C5, C2 and C3 detectors are excluded due to large variations in the noise integral. The reactor off period is marked between the blue lines. The C4 detector is completely excluded from the analysis due to consistently large variations in both its noise integral and noise peak FWHM. The figures (except for the C4 figure) are extracted from [13]. 130
4.3 Time-difference distribution of events in the C5 detector in run 1. The red dashed line indicates the TDD cut placed at 10^{-1}s. Below this value are microphonic and spurious events, while above it are poisson-distributed physical events. 132
4.4 Count rate in the 0.4 to 1 keV energy region for all detectors over the course of reactor on data taking of run 1. 134
4.5 Count rate in the 2 to 8 keV energy region for all detectors over the course of reactor on data taking of run 1. 135

4.6 Count rate in the 10.37 keV $^{68/71}$Ge line for all detectors over the course of reactor on data taking of run 1. 136

4.7 Stability of the two trigger efficiency parameters μ and σ during run 1 of the CONUS+ experiment. In total five measurements were performed. . . . 137

4.8 Stability of the muon veto rate during run 1 of the CONUS+ experiment. An average rate of 188 Hz is found. 138

4.9 Picture of the setup during the californium irradiation campaign of the CONUS experiment at the KBR power plant. The source is contained in the white plastic cylinder. The setup during the irradiation of CONUS+ is the same. . 139

4.10 Stability of the calibration coefficients a (top) and b (bottom) during run 1 of the CONUS+ experiment. 140

4.11 Illustration of threshold definition for the C3 detector. The threshold is defined as the point where the gaussian fit of the electronic noise (red) intersects with 10 % of the theoretically predicted CEνNS spectrum (green). C3 data is shown in black. The maximum deviation of the noise peak during the run is also considered (red dashed line). 141

4.12 Thermal power of the KKL power plant during large parts of run 1 of the CONUS+ experiment. The reactor runs almost consistently at full power with 3.6 GW. Short periods of power reduction are visible. 142

4.13 Anti-electronneutrino spectrum of the KKL power plant as seen by one of the CONUS+ detectors with an energy threshold of 160 eV. The red graph is the the antineutrino spectrum, while the blue histogram shows the fraction of CEνNS events in the detector induced by neutrinos with this energy. the fractions have their maximum at around 7 MeV, meaning that neutrinos with 7 - 7.5 MeV contribute about 20% of the total CEνNS interactions. The fraction falls towards lower energies due to the trigger efficiency of the detectors. 143

4.14 Expected CEνNS spectrum in the C5 detector in run 1 after an reactor on live time of 119 d. The red dashed lines shows the energy threshold of C5 at 170 eV. 144

4.15 Result of the likelihood fit of C5 data in run 1. The upper left plot shows the fit to reactor on data, and the upper right plot shows the fit for reactor off data. The lower plots show the respective residuals. Very good agreement between data and model is found in both fits. 150

4.16 Result of the likelihood fit of C2 data in run 1. The upper left plot shows the fit to reactor on data, and the upper right plot shows the fit for reactor off data. The lower plots show the respective residuals. Very good agreement between data and model is found in both fits. 152

4.17 Result of the likelihood fit of C3 data in run 1. The upper left plot shows the fit to reactor on data, and the upper right plot shows the fit for reactor off data. The lower plots show the respective residuals. Very good agreement between data and model is found in both fits. 154

4.18 Combined result of run 1 of the CONUS+ experiment. The plot shows bin-by-bin excess in the measured data compared to the background model normalised to 1 kg detector mass. The background model includes all relevant best fit parameters from the combined fit. Red-dashed lines show the energy thresholds of the three detectors: Above 180 eV, data of all thee detectors is included. The [170 eV, 180 eV] bin includes data from C3 and C5. The [160 eV, 170 eV] bin only includes C3 data. The signal prediction for a 1 kg Germanium detector with the characteristics of the CONUS+ detectors and an exposure of 119 days is shown in blue. Uncertainties on the data points are statistical uncertainties from the data and model. 156

4.19 Left: Excess of data compared to model for energies above 350 eV, in accordance to Figure 4.18. Right: Deviation of the data from zero in units of the data uncertainty. A gaussian is fitted through the distribution and the mean of the gaussian is found to be compatible with zero. Thus, no significant excess is found between 350 and 800 eV, where no signal is expected. 157

4.20 Distribution of likelihood values obtained from varying the background model of the detectors within the uncertainties of the main contributions (left) and varying the fit function used for the implementation of the non-linearity correction (right). The distribution is fitted with a Gaussian and a standard deviation of 40 (background model) and 47 (non-linearity) is found respectively. 158

4.21 Comparison of the CONUS+ excess as plotted in Figure 4.18 to signal predictions from alternative quenching descriptions from [6]. An additional data point at 200 eV is included and was extracted from Figure 4 in [14]. . . 159

4.22 Comparison of all CEνNS measurements listed in Table 4.14 to the predicted flux-averaged cross section from the Standard Model. The calculated cross sections and the framework for the creation of this plot were provided by Kate Scholberg of the COHERENT collaboration. The CONUS+ experiment measured a cross section of $(0.215 \pm 0.071) \cdot 10^{-40}$ cm^{-2}. For the π DAR source, two separate predictions are plotted: one considering a fully coherent interaction (FF=1, black line) and the more realistic case of a smaller form factor (green line) as is expected for this neutrino source. . . . 160

5.1 View of the CONUS+ detectors in the opened shield. Left: Old setup in run 1 with four 1 kg detectors. Right: New setup for run 2 with three new 2.4 kg detectors. 166

5.2 Projected count rate for the CONUS setup, the CONUS+ setup in run 1, and the CONUS+ setup in run 2 assuming four 2.4 kg detectors. Three possible thresholds are marked at 210 eV (CONUS), 150 eV (approximately CONUS+ run 1), and 120 eV. 167

5.3 Trigger efficiency measurement for the new C6 and C7 detectors at KKL alongside the trigger efficiency of the old C3 detector. 168

5.4 Evolution of the two trigger efficiency parameters for C3, C6 and C7 during run 2. Both values vary only slightly in the order of $\sim$2 eV. 169

5.5 Evolution of the calibration coefficients a and b for C3, C6 and C7 during run 2. 171

5.6 Noise and environmental parameters for the three detectors currently operating in run 2 of the CONUS+ experiment: C3 (upper left), C6 (upper right), and C7 (lower middle). 172

5.7 Evolution of count rate in the 10.4 keV $^{68/71}$Ge line in all three detectors over the course of run 2. 173

5.8 Evolution of integrated count rate between 400 and 1000 eV in all three detectors over the course of run 2. 174

5.9 Evolution of integrated count rate between 2 and 8 keV in all three detectors over the course of run 2. 175

5.10 Toy Monte Carlo for 365 days of reactor on measurement time, assuming the same background level as for the C5 detector in run 1 (indicated by ”Bkg 1.0”). 176

5.11 Predicted statistical sensitivity of the CONUS+ setup for three different energy thresholds at different exposures. 176

5.12 Predicted statistical sensitivity of the CONUS+ setup for the three listed scenarios. 177

A.1 Simulation of the radon component in the C2 detector. 187
A.2 Simulation of the radon component in the C3 detector. 188
A.3 Simulation of cosmogenically activated isotopes in the germanium crystals of C2 (left) and C3 (right). 188
A.4 Simulation of metastable germanium isotopes in the crystals of C2 (left) and C3 (right). 188
A.5 Simulation of inert gases in the detector chamber for the C2 detector in reactor on 189
A.6 Simulation of inert gases in the detector chamber for the C3 detector in reactor on 189
A.7 Complete background model for the C2 (top), C3 (middle), and C5 (bottom) detectors during reactor on measurement. Excellent agreement is found for both detectors in all energy regions. 190

B.1 Combined fit result for the sum of all detector background models to the full reactor on run 1 data set, with all relevant fit parameters included. The fit clearly shows an excess at energies below 400 eV, which is the CEνNS signal. 192
B.2 Combined fit result for the sum of all detector background models to the full reactor off run 1 data set, with all relevant fit parameters included. 193

List of Tables

2.1 Pulser resolution of each CONUS+ detector measured by Mirion (ΔE_{Mirion}) and in the full experimental setup at KKL (ΔE_{KKL}). These values are compared to the pulser resolution before the detector upgrade in the CONUS setup at the KBR power plant (ΔE_{KBR}) [8]. The C5 detector was mainly a prototype detector during the CONUS experiment and not used in KBR, explaining its very high resolution before the upgrade. 31

2.2 Resolution of the ^{241}Am peak for each CONUS+ detector measured by Mirion (ΔE_{Mirion}) and at MPIK (ΔE_{MPIK}). For this measurement the source was placed on top of the cryostat of the detectors [8]. 31

2.3 Trigger efficiency values for the C4 detector before and after the detector upgrade. 32

2.4 Calibration coefficients a and b for the low energy channels of all four detectors in run 1 of the CONUS+ experiment. a describes a constant offset of the energy calibration function (in keV), while b describes the slope of the function (see Equation 2.7). 34

2.5 Most relevant cosmogenically induced isotopes in copper for CONUS+ and their impact on the CONUS+ spectrum. x denotes the presence of X-rays or β-decay for the isotope. "Above range" indicates the presence of γ-lines above the sensitive energy range of the CONUS+ measurement [12]. 45

2.6 Most relevant cosmogenically induced isotopes in germanium for CONUS+ and their impact on the CONUS+ spectrum. x denotes the presence of X-rays or β-decay for the isotope. "Above range" indicates the presence of γ-lines above the range of the CONUS+ measurement [12]. 46

3.1 Neutron fluxes in different energy regions. Thermal neutrons are by far the dominating part of the spectrum. 60

3.2 Background reduction in the C5 detector with the muon veto cut in different energy regions. Count rates are given without error, since they are only used to get a first approximation of the muon veto cut efficiency 68

3.3 Contribution to the background count rates in the three detectors from muons in the energy region from 400 to 1000 eV. The slightly different count rates for the muon contribution originate from different dead layer thicknesses between the detectors. The difference in the percentages of the total background in each detector arise from the presence of different other background sources depending on the detector. 73
3.4 Contribution to the background count rates in the three detectors from neutrons in the energy region from 400 to 1000 eV. 80
3.5 Contribution to the background count rates in the three detectors from muon-induced neutrons in the energy region from 400 to 1000 eV. 83
3.6 γ-ray lines from radon decay chain in the CONUS+ high energy channels. Information on the energy and relative intensities are taken from [15] . . . 85
3.7 Count rates of the radon induced lines in the high energy channels of the three detectors used in the run 1 analysis. The values for the count rates in the 352 keV line (marked with *) are not completely reliable, since at these high energies the efficiency correction with the muon simulation fails due to the low number of statistics in the original data, as explained in Section 3.4.2. The uncertainties given for the count rates only considers the poissonian uncertainty from the extracted value. For the case of the 352 keV line, this uncertainty is too small and an additional term from the efficiency correction should also be included for a more complete picture. 86
3.8 Contribution to the background count rates in the three detectors from radon in the detector chamber in the energy region from 400 to 1000 eV. 86
3.9 Count rates of the 10.37 keV line from K shell transitions of ^{68}Ge and ^{71}Ge in the CONUS+ detectors in reactor on data in run 1 90
3.10 Count rates of the 9.69 keV line from the K shell transition of ^{68}Ga in the CONUS+ detectors in reactor on data in run 1 91
3.11 Count rates of the 8.96 keV line from the K shell transition of ^{68}Ga in the CONUS+ detectors in reactor on data in run 1 92
3.12 Production rates of different cosmogenically induced isotopes with no visible lines in the CONUS+ spectrum in germanium. Values in the table are taken from [12] 93
3.13 Production rates of different cosmogenically induced isotopes with no visible lines in the CONUS+ spectrum in copper. Values in the table are taken from [12] 98
3.14 Missing count rates in the background model of the C2 and C3 detectors for different energy ranges. 103

3.15 Deconstruction of the background model of the C5 detector in reactor on in different energy regions with comparison to data. Values for the lowest energy region are not listed for reactor on data, since in this energy region the expected CEνNS signal is expected. In this way, no biases are introduced ahead of the analysis in the following chapter. 120
3.16 Deconstruction of the background model of the C5 detector in reactor off in different energy regions with comparison to data. 121
3.17 Deconstruction of the background model of the C2 detector in reactor on in different energy regions with comparison to data. Values for the lowest energy region are not listed for reactor on data, since in this energy region the expected CEνNS signal is expected. In this way, no biases are introduced ahead of the analysis in the following chapter. 122
3.18 Deconstruction of the background model of the C2 detector in reactor off in different energy regions with comparison to data. 123
3.19 Deconstruction of the background model of the C3 detector in reactor on in different energy regions with comparison to data. Values for the lowest energy region are not listed for reactor on data, since in this energy region the expected CEνNS signal is expected. In this way, no biases are introduced ahead of the analysis in the following chapter. 124
3.20 Deconstruction of the background model of the C3 detector in reactor off in different energy regions with comparison to data. 125

4.1 Total collected exposure of the three detectors used in the CEνNS analysis in both reactor on and off periods. 129
4.2 Rejection efficiencies of selection cuts for all detectors in run 1. The cuts are applied consecutively, meaning the muon veto cut is performed first and the efficiency of the TRP cut refers to the remaning data after the muon veto cut etc. 133
4.3 Best fit values for the two parameters of the trigger efficiency function for all detectors in the CEνNS analysis. 134
4.4 Calibration coefficients a and b for run 1 of the CONUS+ experiment, prior to the californium irradiation in August of 2024 for the low E channels. . . 135
4.5 Calibration coefficients a and b for run 1 of the CONUS+ experiment after the californium irradiation in August of 2024 for the low E channels. 136
4.6 Energy thresholds for all four detectors in run 1 of the CONUS+ experiment. For C4, no threshold is listed, since the detector was not used in the final analysis due to issues with its stability. 139

4.7 Expected total number of CEνNS events during run 1 of CONUS+ for each detector. 142

4.8 Overview of parameters of the likelihood function in the CEνNS analysis of CONUS+. Each detector has 10 independent parameters and the signal strength s is shared for all detectors. The combined fit of all detectors therefore has 31 free parameters. The neutrino flux is a separate parameter for all three detectors, due to possible influences of different baseline lengths. . 149

4.9 Best fit parameters for the single detector fit of C5. Pull value refers to the previously measured values for each parameter which are used in the Gaussian pull terms of the likelihood function. 151

4.10 Best fit parameters for the single detector fit of C2. Pull value refers to the previously measured values for each parameter which are used in the Gaussian pull terms of the likelihood function. 153

4.11 Best fit parameters for the single detector fit of C3. Pull value refers to the previously measured values for each parameter which are used in the Gaussian pull terms of the likelihood function. 155

4.12 Overview of the measured CEνNS counts in the single detector fits of run 1 of the CONUS+ experiment and comparison to the SM prediction 155

4.13 Best fit parameters for the combined fit of all detectors. Pull value refers to the previously measured values for each parameter which are used in the Gaussian pull terms of the likelihood function. 162

4.14 Comparison of the CONUS+ run 1 result with other CEνNS measurements. 163

5.1 Best fit values for the two parameters of the trigger efficiency function for C6 and C7 in run 2 of the CONUS+ experiment. As explained in Section 4.2, μ gives the position of ϵ_{trig} = 0.5, and σ is the width of the efficiency increase, or in other words a measure for the sharpness of the increase. . . . 169

5.2 Result of latest pulser resolution measurement in run 2 for the C3, C6, and C7 detectors, performed on 26.6.25. ΔE_{Pulser} refers to the FWHM of the pulser signal in the spectra of each detector. 170

5.3 Calibration coefficients a and b for all four detectors in run 2 of the CONUS+ experiment. a describes a constant offset of the energy calibration function (in keV), while b describes the slope of the function (see Equation 2.7). . . 170

5.4 Total collected exposure of the three detectors in run 2 in both reactor on and off periods. 171

Chapter 1

Introduction

A neutrino is an electrically neutral elementary particle that only interacts weakly within the Standard Model. It was first postulated by Wolfgang Pauli in 1930 as a solution to the apparent violation of energy and spin conservation in the beta decay spectrum of the electron [16] and then first discovered by Reines and Cowan in 1956 [17]. Today, we know that there are three flavours of neutrinos, namely the electron-neutrino (ν_e), the muon-neutrino (ν_μ), and the tau-neutrino (ν_τ). The neutrino occupies a uniquely compelling position in particle physics due to its extremely small mass, lack of electric charge and only weak interactions with matter, making it a valuable candidate for tests of the Standard Model (SM) and a key probe of physics Beyond the Standard Model (BSM). An example of such BSM physics is the discovery of neutrino flavour oscillations by the Super Kamiokande experiment in 1998 [18], implying that neutrinos have mass. This necessitated a revision of the Standard Model, which predicts the neutrino to be massless, and opens a critical window into flavour physics, CP violation in the lepton sector, and the origin of mass. Another active area of research is the potential Majorana nature of the neutrino, which, if confirmed, would violate lepton number conservation and offer insights into the origin of the matter-antimatter asymmetry of our universe via leptogenesis. Additionally, many other candidates for BSM physics in the neutrino sector have been theorised, including but not limited to such concepts as possible additional neutrino flavours and proposed electromagnetic properties of neutrinos.

All of these features make the neutrino a central focus of both experimental and theoretical efforts to uncover new fundamental principles in particle physics. In order to test these properties and achieve a more complete understanding, direct neutrino measurements have to be performed, a task which is made difficult by the very small cross-sections for neutrino interactions in the Standard Model (only weak interactions). The Standard Model predicts six possible interactions of the neutrino with matter: inverse β/τ decay, elastic neutrino electron scattering, (quasi-) elastic neutrino nucleon scattering, nucleon excitation, resonance production, as well as deep inelastic scattering and jet production [19]. This work is specifically focused on one of these interactions, the so-called coherent elastic neutrino-nucleus scattering (CEνNS). For reasons which will be explained in Section 1.1, this interaction is at a unique position in the field of neutrino detection, since it offers cross-sections which can be several orders of magnitude bigger than for the other typical neutrino detection channels like inverse β decay, depending on the target material. Nevertheless, the use of CEνNS for neutrino detection features other challenges, mainly due to the very small recoil energies in the target material induced by an interaction, which necessitates the use of detector technologies with extremely low energy thresholds and very good resolutions. In fact, the first successful measurement of CEνNS was only performed in 2017, over 40 years after its prediction, by the COHERENT experiment, using neutrinos with energies between 20 and 50 MeV from a pion-decay-at-rest (πDAR) source and a CsI crystal as target material [20]. Since then, the COHERENT experiment has measured the interaction for two other target materials, argon and germanium [21, 22], both with the aforementioned πDAR source. However, for a few years after the initial discovery the picture was still incomplete and an observation of the interaction for neutrinos with energies below 10 MeV was still pending, which led to the development of many dedicated experiments worldwide. The usual location of choice for these experiments is in close proximity to a nuclear power plant, since the neutrinos, which are produced in large abundance in the β decays of fission products in the reactor core, produce antineutrinos with exactly the desired energies below 10 MeV. The very first successful measurement of the CEνNS interaction with these neutrinos, the topic of this work, was performed by the CONUS+ experiment, located at the KKL nuclear power plant in Leibstadt, Switzerland, in 2025 with data from the run 1 measurement campaign from November 2023 to August 2024 [13].

In this thesis, the full decomposition and development of a background model for the CONUS+ run 1 data will be presented. Here, as is common in the field of particle physics, the term ”background” refers to all data collected by the CONUS+ detectors not coming from the CEνNS interaction (the signal) and can consist of a vast number of different types of radiation originating inside or outside the detectors. In the context of this work, ”background” also does not refer to noise (electronic or microphonic), which is defined as events induced by random fluctuations in the detector’s readout signal, originating from electronics, the readout chain or vibrations, which mainly influences the energy range below the region of interest for the CEνNS search of the experiment. The complete understanding of the background and a precise model is crucial in finding the CEνNS signature in the data. The developed model will then be used to perform a full likelihood analysis of the CONUS+ run 1 data, which finally leads to the successful first measurement of coherent neutrino-nucleus scattering for reactor neutrinos and the result in [13].

The following chapter will describe the properties of the CEνNS interaction in terms of the Standard Model, as well as the experimental requirements for a dedicated CEνNS experiment that can be derived from its cross section.

1.1 CEνNS in the Standard Model

The CEνNS interaction was first predicted by D. Freedman in 1974 [23] and describes a flavour blind interaction, where the neutrino scatters elastically off an atomic nucleus with neutron number N and proton number Z via exchange of a Z boson.

$$\nu + (N, Z) \rightarrow \nu + (N, Z) \tag{1.1}$$

Here, the neutrino interacts coherently with the whole nucleus and not with its single constituents. The differential cross section of CEνNS in the Standard Model is given as

$$\frac{d\sigma}{dT} = \frac{G_f^2}{4\pi}(N - (1 - 4sin^2\theta_W)Z)^2 F^2(q^2) M \left(1 - \frac{MT}{2E_\nu^2}\right) \tag{1.2}$$

with the Fermi constant G_f, the Weinberg angle θ_W, the neutrino energy E_ν, the energy transfer T, the mass of the target nucleus M, and the nuclear form factor $F(q)$ in dependence on the transferred momentum q. The nuclear form factor is the Fourier transform of the spatial density distribution of the target nucleus and as such gives information about its structure. For low momentum transfer q, and therefore low neutrino energies, this form factor approaches $F(q) = 1$. This is typically the case for neutrino energies below 20 MeV for medium-sized nuclei such as Germanium (fully coherent regime). Furthermore, it can be observed that the dependence of the cross section on the number of protons Z in the target nucleus is small, since [24]

$$\begin{gathered} sin^2(\theta_W) = 0.23122(4) \\ \rightarrow 1 - 4sin^2\theta_W \approx 0. \end{gathered} \tag{1.3}$$

Integrating the differential cross section yields:

$$\sigma \sim N^2 E_\nu^2 \tag{1.4}$$

An experiment aiming at an observation of the CEνNS interaction should be set up in a way that maximises the total cross section in order to have a high probability of measuring a signal. From Formula 1.4, two possible ways to achieve this can be found. First, the use of target nuclei with high neutron numbers N is favoured. However, a CEνNS detector does not directly measure the full energy of the incoming neutrino. Instead, it measures the recoil energy (or part of the recoil energy) of the nucleus that was hit by the neutrino. Due to the much greater mass of the nucleus, this recoil energy is very small, and its maximum is

$$T_{max} = \frac{2E_\nu^2}{M}. \tag{1.5}$$

The maximum energy is inversely proportional to the mass of the nucleus. This creates a push-pull situation when choosing an ideal target material, since an isotope with a high neutron number increases the total cross section, but decreases the maximum recoil energy that can be transferred to a nucleus, therefore making a detection harder. As a result, the choice of isotopes with medium mass numbers as target materials, such as Germanium in the CONUS+ experiment, is ideal for CEνNS detection. Another way to increase the total cross section is to maximise the energy of the neutrinos, i.e. choosing a neutrino source with high energy neutrinos. However, the impact of the nuclear form factor and the coherency condition has to be considered. As mentioned above, the nuclear form factor approaches F = 1 for low neutrino energies and decreases for larger neutrino energies, as shown in Figure 1.1.

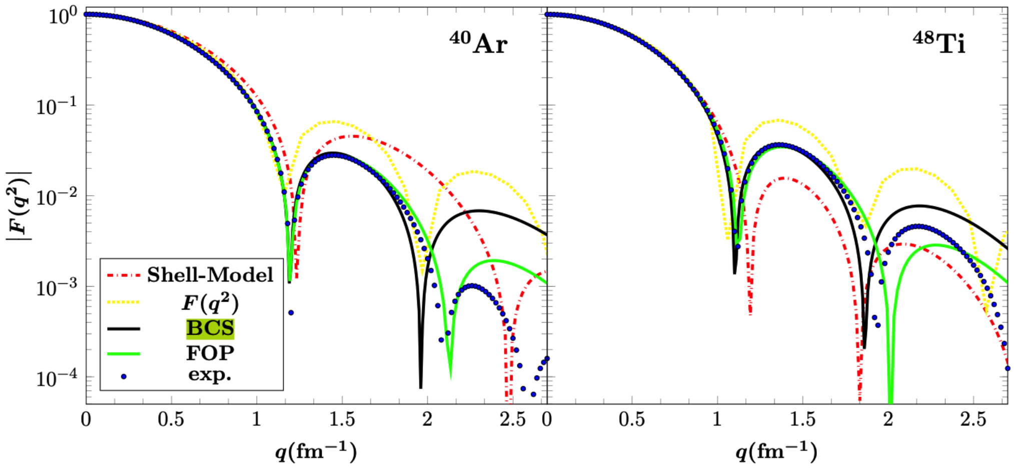

Figure 1.1. Running of the nuclear form factor for different momentum transfers for ^{40}Ar (left) and ^{48}Ti (right) from [1]. Blue dots show experimental measurements, the yellow dashed line shows the nuclear form factor based on the fourier transform of the nuclear charge density distribution, and the red dashed lines show a simplified prediction from a shell model of the nucleus. The green line and black line are improvements of this model made from different theoretical considerations. Here, FOP stands for fractional occupation probability of states in the nucleus, while BCS stands for the Bardeen Cooper Schriffer equations, which can be solved to find occupation probabilities for different nucleon levels within the nucleus.

An estimate of the corresponding neutrino energy below which full coherency is ensured can be made by comparing it to the inverse diameter of the target nucleus:

$$E_\nu \leq \frac{1}{d_{nuc}} \approx \frac{197}{2\sqrt[3]{A}}[MeV] \approx 20 \text{ MeV for } {}^{76}Ge \tag{1.6}$$

For ${}^{76}Ge$ nuclei the CEνNS interaction is fully coherent for neutrino energies below 20 MeV, while for larger energies the single constituents of the nucleus become visible to the neutrino. Section 1.2 will give an overview of possible neutrino sources and how they impact this coherency condition.

Due to the possible coherency of the CEνNS interaction (proportional to N^2), its cross section is large compared to other neutrino channels in the Standard Model, as shown in Figure 1.2. This unique feature allows for the building of small and compact neutrino experiments, such as the CONUS+ experiment with a size of approximately 2 m^3, and is in stark contrast to the very large size of other contemporary neutrino experiments such as the Super Kamiokande experiment (50,000 m^3 [25]) or the IceCube experiment ($\sim$ 1km^3 [26]).

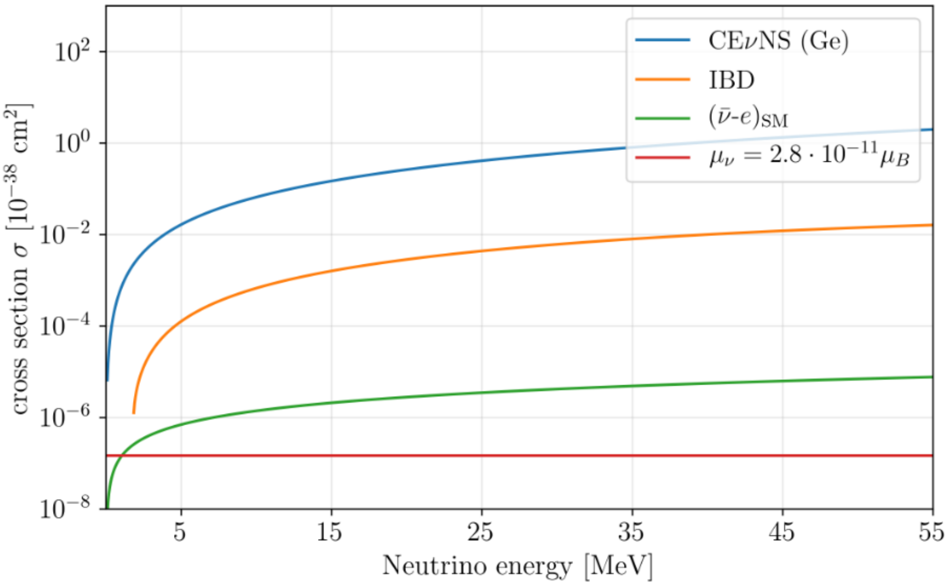

Figure 1.2. Neutrino cross sections for energies below 50 MeV. The CEνNS cross section is two orders of magnitude bigger than that of inverse beta decay and four to five orders of magnitude bigger than that of elastic neutrino electron scattering. Plot taken from [2].

1.2 Artificial neutrino sources

Neutrinos, the second most abundant type of particle in the universe after photons, are produced in large quantities in different kinds of astrophysical mechanisms. These include core-collapse supernovae, where they carry away 99% of the released energy, and also the proton-proton chain (and other fusion chains) inside stars like the Sun. Furthermore, they are produced in the decay chains of naturally occurring radioisotopes, such as ^{238}U and ^{232}Th in the crust and mantle of the Earth. Although all of these phenomena produce a large number of neutrinos in total, the flux of these neutrinos arriving at Earth's surface is too low for a successful CEνNS observation with a compact experiment like the CONUS+ experiment. Therefore, dedicated CEνNS experiments are usually located near artificial neutrino sources, namely accelerator sources or nuclear power plants. The choice of either of these options has consequences for the energy of the neutrinos and therefore for the coherency of the interaction that the experiment is aiming to measure.

1.2.1 Accelerator neutrinos

Particle accelerators supply neutrinos from pion-decay-at-rest (π-DAR) sources. These sources first direct a proton beam from the accelerator at a thick target, producing pions via hadronic interactions. These pions lose energy and come to rest inside the target, in which they decay into a muon and a neutrino.

$$\pi^+ \rightarrow \mu^+ + \nu_\mu \tag{1.7}$$

The muon neutrinos from this decay are monoenergetic with an energy of 29.8 MeV. Two more neutrinos are emitted in the further decay of the muon.

$$\mu^+ \rightarrow e^+ + \nu_e + \bar{\nu_\mu} \tag{1.8}$$

Thus, three different flavours of neutrinos are produced at π-DAR sources. Their experimentally relevant energy range lies between 20 and 50 MeV (depending on the detector threshold) and they are therefore in the partially coherent regime for medium-sized target nuclei, as discussed in Section 1.1. The advantages of π-DAR sources for a CEνNS observation, especially compared to a nuclear power plant, are the increased control of the experiment over the neutrino source and its surroundings. This allows for a very good understanding of the expected signal, good control of the background, and also the frequent taking of background-only data, due to the use of a pulsed beam. Furthermore, because of the higher neutrino energies, the required energy thresholds for the detectors used in an experiment are not as low, allowing in principle an easier observation. An example of a

CEνNS experiment located at an accelerator source is the COHERENT experiment mentioned in the introduction to this chapter.

1.2.2 Neutrinos from nuclear reactors

In nuclear reactors, neutrinos originate from the beta decay of neutron-rich fission products. First, a heavy nucleus, such as ^{235}U, undergoes fission after capturing a thermal neutron.

$$^{235}U + n \rightarrow \text{ Fission products} + \text{ Neutrons} + \text{ Energy} \tag{1.9}$$

The fission products can then perform beta decay, where a neutron in the nucleus decays into a proton, an electron, and a neutrino.

$$n \rightarrow p + e^{-} + \bar{\nu}_e \tag{1.10}$$

Thus, in a nuclear reactor only electron antineutrinos are produced. The energy of these neutrinos is below 10 MeV, allowing a fully coherent interaction with a nucleus in a CEνNS experiment. The final neutrino spectrum is dependent on the exact amounts of different fissile isotopes present in the reactor at different times, later referred to as fission fractions. Compared to a π-DAR source, a nuclear reactor poses some challenges for the operation of a low background experiment. These include an environment that is potentially contaminated with radioactive isotopes, as well as other background sources from the reactor itself. In addition, a commercial nuclear power plant is designed to run almost continuously, making a background-only measurement only possible in the brief periods of reactor maintenance that are usually performed for one month per year. Furthermore, the placement of a low-background experiment inside a nuclear reactor building puts constraints on the amount of shielding that the experimental setup can incorporate due to weight constraints, as well as often featuring less overburden compared to accelerator experiments.

1.3 Potential of CEνNS

The CEνNS interaction and detectors based on its measurement have a range of possible applications in both fundamental physics and practical technologies. The following section will give a broad overview of these potentials.

1.3.1 BSM physics

CEνNS experiments provide a powerful tool for validating the Standard Model and also probing into potential physics beyond the Standard Model (BSM). Examples of such BSM physics are possible electro-magnetic properties of the neutrino, like a millicharge and a corresponding magnetic moment, which have been proposed by various groups and are an active field of research (see [27] for an overview). The presence of such properties would change the SM CEνNS cross section in Formula 1.2 to additionally include an electro-magnetic term:

$$\frac{d\sigma}{dT} = (\frac{d\sigma}{dT})_{SM} + (\frac{d\sigma}{dT})_{EM} \tag{1.11}$$

and this would lead to changes in the expected rate of CEνNS counts, primarily at very low energies. Precision measurements could therefore find hints for such electromagnetic physics in the neutrino sector.

Further examples of BSM physics that could potentially be probed with CEνNS are neutrino non-standard interactions (NSIs). These are neutrino interactions with other standard model particles that are not permitted in the SM, such as four-fermion interactions of the following type:

$$\mathcal{L}_{NSI} \sim \epsilon_{\alpha\beta}(\bar{\nu}_\alpha \gamma^\mu P_L \nu_\beta)(f\gamma_\mu f), \tag{1.12}$$

where $\bar{\nu}_\alpha$ and ν_β are neutrinos, f is a fermion, P$_{L,R}$ is the left or right-handed projection operator and ϵ is a dimensionless parameter indicating the coupling strength of the proposed interaction. Such NSIs would again alter the CEνNS rate in an experiment and would be visible in a precision measurement.

Lastly, another popular model for BSM neutrino physics are hypothetical light mediators, either in the form of a scalar, vector or tensor mediator. These mediators would give rise to new types of interactions between neutrinos and SM particles and would therefore also lead to changes in the SM CEνNS cross section particularly an enhancement at very low energies due to their hypothetical low mass.

1.3.2 Measurement of nuclear form factor and nuclear structure of target isotopes

As shown in Formula 1.2, the CEνNS cross section is proportional to the nuclear form factor of the isotope on which the interaction is happening. As such, CEνNS experiments, particularly experiments that feature higher neutrino energies, where the form factor is expected to deviate from unity, can probe the structure of the target nucleus by performing careful analyses of the measured CEνNS spectrum. Such studies were already performed in the past for data recorded with the CsI setup of the COHERENT experiment, for example in [28], where the nuclear neutron radius was calculated.

1.3.3 Supernova detection and modelling

Another interesting application of CEνNS would be the study of astronomical neutrino sources such as supernovae. As explained above, neutrinos carry away approximately 99% of the energy of a supernova and CEνNS detectors would allow for the detection of a higher percentage of this neutrino flux due to the enlarged cross section at lower energies. Not only would CEνNS detectors be another viable alternative for the detection of these neutrinos and therefore the early detection of super novae, but their measurement also gives important insights into super nova modelling. Neutrinos, as opposed to photons, escape directly from the core of the explosion and therefore offer a direct window into the mechanisms in the stellar core, which would otherwise be unobservable. With this input, super nova simulation can be tested and verified, the equations of state (EoS) of nuclear matter governing the processes in the core can be better understood and other characteristics, like neutrino opacity and interactions in the developing explosion, can be observed.

In general, it must be noted, that the current generation of low mass CEνNS detectors is likely unable to measure the neutrino flux of a supernova. The last detected super nova on earth is SN1987A, a supernova recorded in 1987 and determined to have happened in the Large Megellanic cloud at a distance of 51.4 kpc from earth. Several neutrino experiments measured neutrinos coming from this supernova over a time span of 13 seconds and from studies of these measurements it can be estimated that the supernova released approximately 10^{58} neutrinos [29]. This value corresponds to a neutrino flux of circa 10^9 cm^{-2} s^{-1} on earth, which is around four orders of magnitude smaller than the neutrino flux in the CONUS+ experiment presented in this work. Thus, only a significantly larger experiment in the style of CONUS+ would be able to measure such an event in case it happened at a comparable distance. A supernova happening at a smaller distance to earth increases the chances of a successful measurement, as the flux on earth scales with $\frac{1}{r^2}$.

1.3.4 CEνNS for dark matter experiments

A correct understanding of CEνNS is crucial for dark matter experiments, where CEνNS and the so-called neutrino floor are the prominent background source for current and future sensitivities [30]. This is shown in Figure 1.3, taken from [3], with the sensitivities of current dark matter experiments like XENONnT [31] and PandaX [32].

The neutrinos which induce this background are produced either in the sun, mainly in the pp-chain, or in earths atmosphere through the decay of radioactive isotopes or interactions of cosmic rays (see Chapter 2.4.1). Recently, the aforementioned XENONnT and PandaX experiments, two experiments looking for weakly-interacting massive particles (WIMPs) as dark matter candidates, have measured CEνNS from solar ^{8}B neutrinos for the first time

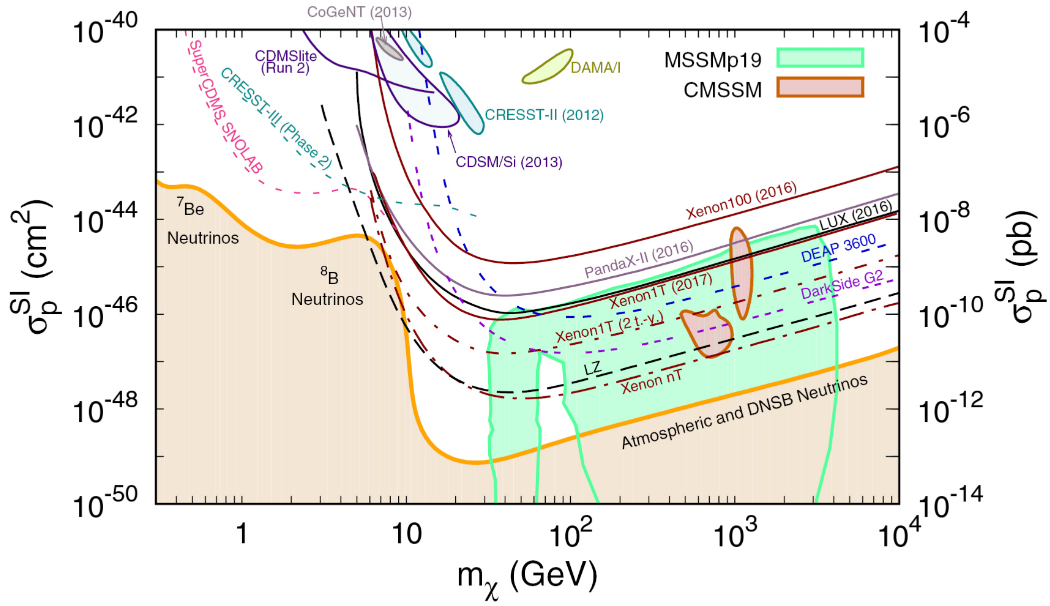

Figure 1.3. Current and future limits on DM direct detection spin-independent cross section (σ_p^{SI}) as a function of DM mass (m_χ), and impact of solar and atmospheric neutrinos on these measurements. Taken from [3]

.

[33, 34]. The ^{8}B-branch of the pp-chain in the sun is only responsible for a small part of its energy and neutrino output (about 0.02 %). However, the neutrinos that are produced in this way are among the highest energy solar neutrinos with an endpoint energy of their spectrum of 14 MeV. They are produced, when a ^{3}He and ^{4}He nucleus fuse, creating ^{7}Be:

$$^3He +^4 He \rightarrow^7 Be + \gamma \tag{1.13}$$

The resulting ^{7}Be nucleus can then capture a free proton resulting in the creation of ^{8}B, which then immediately decays into ^{8}Be, producing a neutrino:

$$\begin{aligned} {}^7\mathrm{Be} + p \rightarrow {}& {}^8\mathrm{B} + \gamma \\ {}^8\mathrm{B} \rightarrow {}& {}^8\mathrm{Be} + e^+ + \nu_e \end{aligned} \tag{1.14}$$

As is shown in Figure 1.3, these neutrinos form background events that are highly relevant for dark matter searches in the 1 to 10 GeV mass range and for smaller cross sections. For lower masses, primarily the solar neutrinos from the ^{7}Be-branch, a similar mechanism, are relevant, while for higher masses atmospheric neutrinos have more impact.

1.3.5 Nuclear reactor monitoring

CEνNS detectors could also potentially be used as a tool for nuclear reactor monitoring and safeguards. They provide a novel approach for reactor diagnostics through the reactors neutrino flux and due to the high cross section of CEνNS compared to other neutrino channels they can be built to be very small, as mentioned before. With such a system the operational status, the thermal power and even fuel composition changes of a nuclear reactor could potentially be monitored in the future. Typically the status of reactors is, among other tools, monitored with neutron measurements. The measurement of neutrinos as opposed to neutrons has two unique advantages: 1. Neutrinos are directly produced from the decay of fission products and can therefore give information on the fission fractions and the isotopes in the reactor. 2. Neutrinos are not moderated by materials in between the reactor and the measurement, which means that the monitoring system can be placed further from the reactor, making readout and operation simpler.

1.4 Experimental requirements

From the topics discussed in the previous sections, three main requirements for a successful CEνNS experiment can be derived.

1. **High signal strength**
   The first requirement is a high signal strength and a high neutrino flux at the experimental location. This is necessary, because of the cross section of the CEνNS interaction which, despite being large for neutrino standards, is still very small at approximately 10^{-16} barn for neutrinos with an energy of 10 MeV (see Figure 1.2). The neutrino flux can be increased by choosing a location that is close to the neutrino source. In the case of a nuclear reactor, this can involve choosing a location inside the reactor building or the control zone, as was done for the CONUS+ experiment. The exact location of the CONUS+ experiment and its impact on the neutrino flux will be discussed in Section 2.1.

2. **Low background**
   The low cross section and therefore rare nature of the CEνNS interaction require extremely low background conditions and proficient background mitigation techniques, since the sensitivity of the experiment scales with $\frac{1}{\sqrt{B}}$, with B being the background rate in the detectors. This involves the use of many different types of shielding, including passive and active components, as well as a selection of ultra radiopure materials in both the shielding and the detectors themselves, and high caution when dealing with possible contaminations. Additionally, locations with a sufficiently large overburden are favoured to ensure effective shielding from cosmic rays. The CONUS+ shield and background mitigation techniques will be detailed in Section 2.4.

3. **Very low energy threshold**
   Lastly, a very low energy threshold for the detectors is required. This ensures that the detectors can measure physical signals down to the very low energies where the CEνNS interaction is expected to be the strongest. Considering, for example, neutrinos with energies of 10 MeV and 1 MeV and a Germanium detector, Formula 1.5 gives a maximum recoil energy of approximately 3 keV$_{nr}$ and 0.03 keV$_{nr}$ respectively. Moreover, the nuclear quenching effect has to be considered. Due to this effect, which will be discussed in more detail in Section 2.3.2, only a certain part of the recoil energy of the Germanium nucleus that was hit by the neutrino is converted into ionization of the surrounding crystal lattice, while the rest goes into heat and phonons. Depending on the detection technique used, only the ionization energy is available for measurement, as is the case for the Germanium detectors in the CONUS+ experiment. Considering a quenching factor of 0.16, this results in only 480 eV$_{ee}$ and 4.8 eV$_{ee}$ available for the measurement of 10 MeV and 1 MeV neutrinos. These examples demonstrate the need for extremely low energy thresholds, especially in reactor CEνNS experiments where initial neutrino energies are below 10 MeV, as explained in Section 1.2.2. The energy thresholds which are achieved in the four detectors of the CONUS+ experiment depend on the detection efficiency of the detectors and the level of electronic noise events in the measured spectra. These aspects will be discussed in Sections 2.3.8 and 4.1.1 and the thresholds will be defined in Section 4.4.

1.5 Technologies for CEνNS measurements

The search for and study of the CEνNS interaction is a worldwide research effort in the field of neutrino physics with many dedicated experiments. These experiments employ a wide range of different experimental techniques in order to measure the signal. The following section will give a broad overview of these techniques as well as some of the experiments using them and their most recent results.

1.5.1 Bolometers and transition edge sensors

Cryogenic detectors are one of the most sensitive technologies for CEνNS searches due to their extremely low energy thresholds. A cryogenic bolometer works by measuring energy depositions from CEνNS as tiny temperature rises (in the order of μK) in a crystal kept at millikelvin temperatures with an extremely sensitive thermometer. The change in temperature can be measured in several different ways, one of them being the use of a transition-edge sensor (TES) [35]. In these types of experiments, a superconducting target material is operated exactly at the transition point between its superconducting and its normal phase. An energy deposition from a CEνNS interaction then leads to a small increase in its temperature, leading to a sharp increase in the resistance of the material, which is read out with Superconducting Quantum Interference Device (SQUID) [36] with ultra-high sensitivity. Examples of experiments using such technologies are the RICOCHET experiment [37], an upcoming CEνNS experiment at the ILL reactor in Grenoble, France, which aims to use an array of 30 g Ge and Si crystals operated as TESs, and the NUCLEUS experiment [38], another CEνNS experiment located at the CHOOZ power plant in France, which will use $CaWO_3$ and Al_2O_3 crystals.

1.5.2 Scintillating crystals

Another prominent technology for CEνNS searches and measurements is the use of scintillating crystals. Here, the energy deposition of a CEνNS interaction in the crystal leads to the recoil of an atom in the crystal lattice, which then ionises surrounding atoms. Once the excited electrons recombine with an atom, scintillation light is produced that can be readout with photo-multiplier tubes (PMTs). An example of an experiment using such a technology is the COHERENT experiment already mentioned in Section 1.1. The collaboration used a scintillating 14.6 CsI crystal, doped with Na and located at Spallation Neutron Source (SNS) at the Oak Ridge National Laboratory, in order to achieve the first measurement of CEνNS in 2017 [20]. At the time, the process was observed at a 6.7 σ confidence level. Another experiment, currently in its R&D phase, that is investigating scintillation detectors as a possibility for CEνNS searches is the MINER experiment which will be located in very close proximity to a 1 MW reactor at Texas A&M university, USA [39].

1.5.3 Liquid noble detectors

Liquid noble gas detectors, primarily using liquid argon (LAr) and liquid xenon (LXe), are another detector technology used in different CEνNS experiments worldwide. In these experiments, similarly to the scintillating crystals in the previous section, recoils from CEνNS induce scintillation from excited molecular states in the noble liquid. This light can then again be readout with PMTs. An advantage of this technology are its excellent pulse shape discrimination capabilities, allowing the distinction between electronic and nuclear recoils based on the amount of light produced at the start of an event compared to that produced over the whole event (explained in more detail in 3.2.2) [40]. The previously mentioned COHERENT collaboration used such a liquid argon detector to achieve the first measurement of CEνNS on argon in 2020 at a significance of over 3 σ [40]. Another example of such an experiment is the upcoming RED-100 experiment in Kalinin, Russia [41]. The experiment aims at using a liquid xenon dual-phase time projection chamber (TPC) to detect CEνNS. This technology works by combining two measurements in one experiment. The first is the previously described scintillation light of liquid xenon, which is picked up with PMTs lining the sides and bottom of the liquid xenon vessel (S1 signal). Additionally, the TPC features a thin layer of gaseous xenon on top of the liquid phase (”dual phase”). As a CEνNS interaction (or any other interaction) happens in the liquid xenon, the recoiled xenon molecule ionises the surrounding xenon and electrons are released. Due to an applied electric field, these electron drift upwards into the gaseous xenon, where they are accelerated and produce secondary scintillation light (S2 signal). The use of both signals allows for excellent positional reconstruction of the original interaction and also features the possibility of PSD mentioned before. The technology is typically also used in dark matter WIMP searches like the XENONnT and PandaX experiments mentioned in Section 1.3.4, two experiments that measured CEνNS from solar ^{8}B neutrinos in 2024.

1.5.4 Charged-coupled devices

A charged-coupled device (CCD) is a type of silicon-base detector used to sense light or ionising radiation, which was originally developed for imaging in cameras or telescopes. In such a detector, a CEνNS interaction on a silicon atom again induced ionisation of the surrounding lattice and the free electrons drift through the material under a small electric field [42]. They are then collected and stored as charge in a pixel array and the charges in each pixel are shifted out row by row and measured at the edge of the chip. The total collected energy is equivalent to the total energy of the event while the information on which pixel was active gives excellent spatial resolution. CCDs have very low energy thresholds (down to $\sim 10eV$), however similarly to the cryogenic detectors from above, the active mass of the detectors is often quite small. An example of an experiment using this technology for CEνNS is the CONNIE experiment at the Angra-2 reactor in Brazil [43]. The collaboration employs two Skipper-CCDs, a special type of CCD which allows multiple readouts of a single pixel, with a total active mass of 0.5 g. The experiment recently presented their results for the detection of reactor-antineutrinos with a live time of 243 days reactor on and 67 days reactor off data, placing a limit of about 80 times the standard model prediction [43].

1.5.5 High-purity germanium detectors

Lastly, one of the most prominent technologies for the detection of CEνNS is the use of high-purity germanium (HPGe) detectors. These types of detectors, which will be described in full detail in Section 2.3 and 2.3.1, use germanium crystals as semiconductor diodes to measure the ionisation which is freed in a CEνNS interaction. They offer excellent detector resolution (down to below 50 eV [4]) and energy thresholds (down to 150 eV [4]) and are used in a number of experiments, including the CONUS+ experiment, the topic of this work, and its predecessor experiment CONUS (see Section 2.2.1).

Other experiments using HPGe detectors include the nuGen experiment at the Kalinin power plant in Russia [44]. The experiment employs a 1.41 kg detector located at a distance of 11 m from the reactor core. In their latest result [44], the collaboration found no excess events in the comparison between reactor on and reactor off spectrum, but a limit on the k parameter from Lindhard theory at $k < 0.26$ with 90 % C.L. was obtained.

Chapter 2

The CONUS+ experiment

2.1 Experimental location

The CONUS+ experiment is a dedicated CEνNS experiment located at the KKL nuclear power plant in Leibstadt, Switzerland [4]. Its initial goal was the first observation of the CEνNS interaction in the fully coherent regime using reactor antineutrinos. This goal was achieved in January 2025 [45]. The CONUS+ setup is placed inside the reactor building of the KKL power plant, in the room named ZA28R027, visible in Figure 2.2. The KKL reactor itself is a 3.6 GW$_{th}$ boiling water reactor consisting of 648 fuel assemblies. It is operated at a high duty cycle and at its maximum capacity for most of the year. The reactor is switched off during a one-month outage period annually to allow for reactor maintenance works and repairs. These periods can be used for the taking of background-only data with the CONUS+ experiment and will be referred to as reactor off periods. The location of the CONUS+ experiment inside the reactor building is shown in Figure 2.1.

The experiment is positioned at a height of 25.2 m over ground and a horizontal distance of 12.54 m from the reactors central axis. The four high purity germanium detectors at the centre of the shield (see Sections 2.3.6) have a distance of (20.7 ± 0.1) m from the centre of the reactor core, resulting in an expected neutrino flux of $1.45 \times 10^{-13} s^{-1} cm^{-2}$. CONUS+ is surrounded by the concrete walls of room ZA28R027 and 3.8 cm of steel (steel containment) and 1.2 m of reinforced concrete from the reactor building itself. This results in an overburden of 7.4 m w.e., effectively reducing the hadronic part of the cosmic ray flux by two orders of magnitude [46]. Additionally, the many layers of concrete between the experimental area and the reactor core reduce radiation from the reactor in the room by several orders of magnitude to a level below 1 μSv/h on average [5].

Inside ZA28R027, CONUS+ is located in an area near the rear of the room as shown in Figure 2.2. This area is separated from the rest of the room by a wall, which allows improved cleanliness and precautions against outside contaminations as well as allowing stable

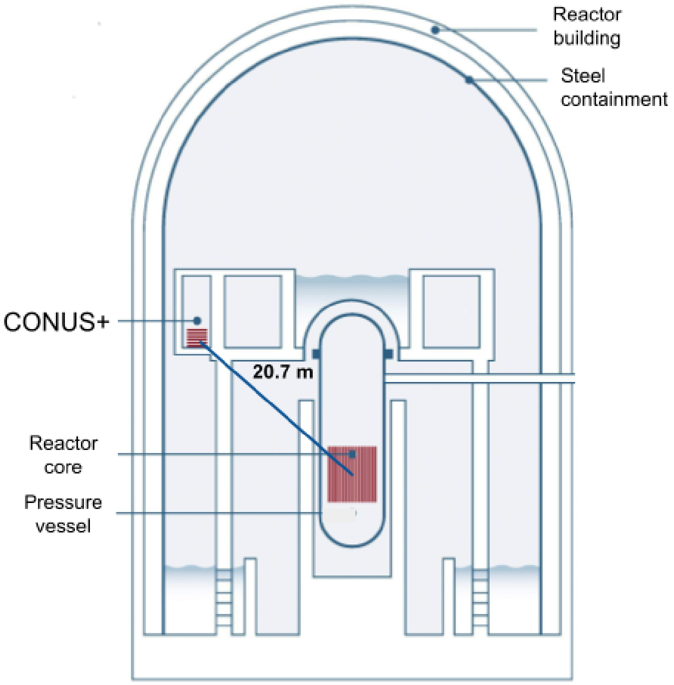

Figure 2.1. Schematic drawing of the KKL reactor building with the CONUS+ location, taken from [4]

temperatures inside the room from a continuously running AC. The CONUS+ experiment also features a direct network connection from KKL to MPIK through a local network at reactor site, used for the taking of real-time data as well as the remote operation of the experiment and access to slow control data. An important characteristic of the placement of CONUS+ is the fact that during the regular reactor outage the head of the drywell container, a vessel surrounding the reactor, is placed directly above room ZA28R027. It is made of 3.8 cm of steel and increases the overburden of the experiment during this time period by approximately 25 cm w.e.

2.2 Timeline

2.2.1 From CONUS to CONUS+

The CONUS+ experiment is based on its predecessor experiment, the CONUS experiment. CONUS was a dedicated CEνNS experiment located at the KBR nuclear power plant in Brokdorf, Germany [47]. It ran from 2018 to 2022 and was placed in the reactor building of the power plant at a distance of 17 m from the reactor core. The experiments used the C1, C2, C3 and C4 detectors, which at the time reached an energy threshold of 210 eV (before the detector upgrade detailed in Section 2.3.7). The last data collection period of the

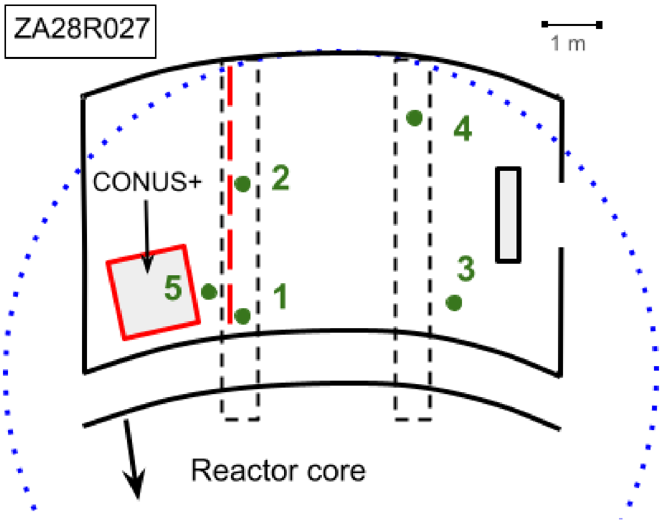

Figure 2.2. Location of CONUS+ within room ZA28R027 [5]. The red dashed line indicates the separation wall between the CONUS+ area (left) and the rest of the room. Green dots indicate the positions used in the background characterisation performed before the move to KKL. The Blue line indicates the position of the reactor drywell head during reactor outage above room ZA28R027.

experiment was run 5 from July 2021 to November 2022 [48]. As the KBR power plant was permanently shut down at the end of 2021, the whole of 2022 could be used as reactor off data collection. This much longer background measurement, as well as other substantial improvements in data collection compared to previous runs of the CONUS experiment, such as the use of the CAEN DAQ system, led to the, at the time, best limit for the detection of the CEνNS interaction at a nuclear power plant worldwide. The limit that was found was below 0.34 events kg^{-1} d^{-}1, which is approximately a factor two above the Standard Model prediction for the specifications of the CONUS experiment [48]. Figure 2.3 shows the measured spectra in both reactor on and reactor off times for the C2 detector. Furthermore, it shows three different signal predictions, each using a different model for the behaviour of the quenching factor: the Lindhard model, as well as the Lindhard model with a cubic and linear excess at low energies, favoured in [6] (see Section 2.3.2). Due to the high expected signal count rate for the Lindhard + linear model, the CONUS experiment was able to exclude this model at the time, while the Lindhard + cubic model was also disfavoured.

The permanent shutdown of the KBR power plant at the end of 2021 implied the need for the experiment to find a new location for a continued search for the CEνNS interaction. This location was found with the KKL power plant in Leibstadt, Switzerland, and planning for the upcoming move began in 2022. This included an extensive background characterisation of several potential positions for the experiment in KKL, which was undertaken in different campaigns between May 2022 and July 2023 [5] (see Section 3.2). After the com-

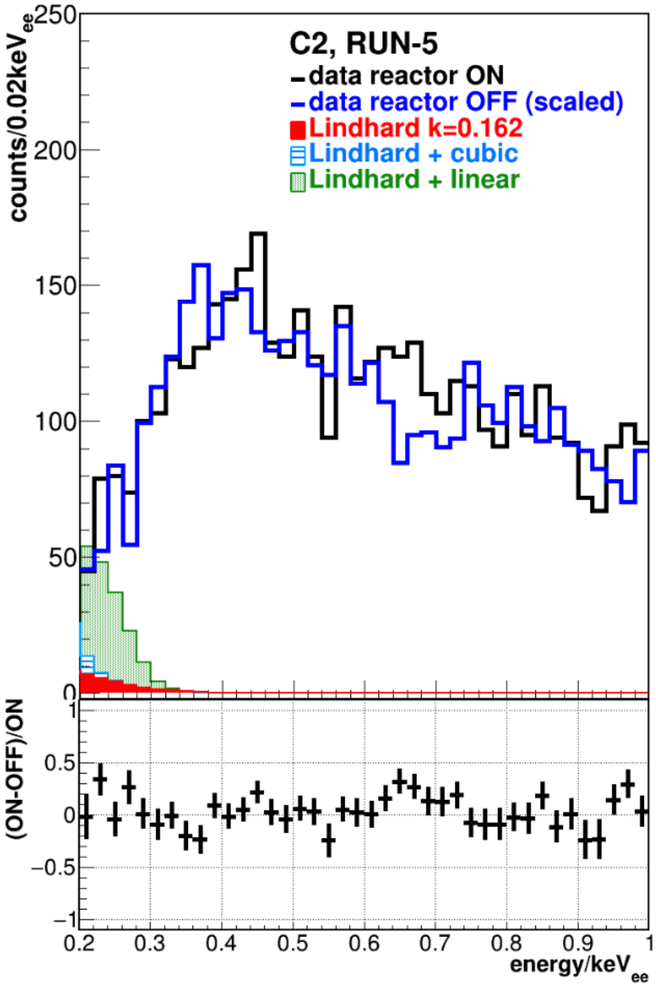

Figure 2.3. Spectra measured with the C2 detector in run 5 of the CONUS experiment. The ROI was defined as 210 eV to 1000 eV. Reactor on data is shown in black, while reactor off data is shown in blue and good agreement was in principal found between both spectra, indicating no clear sign of a measured CEνNS interaction. Additionally, three theoretical predictions for the CEνNS signature are shown. Red shows the standard prediction using the Lindhard model described in Section 2.3.2 as well as the two quenching descriptions from [6].

pletion of the run 5 data collection in December 2022 the CONUS shield was opened and the four HPGe detectors were extracted. They were sent to the Mirion company in Lingolsheim, France, a company that specialises in the construction of detectors for particle physics experiments, and built the four detectors ahead of their installation at KBR. There, they underwent several upgrades, which will be detailed in Section 2.3.7, and the Germanium crystals were refurbished. When this process was finished, the detectors were sent to MPIK for characterisation and further testing.

2.2.2 CONUS+ commissioning and first runs

The CONUS+ experiment was installed at KKL in July 2023. The installation was followed by a two-month commissioning phase, in which the complete setup, including the slow control system, was proven to be working as expected. This allowed for the start of the first physics run (Run 1) in November 2023 and finally the first collection of reactor off data during the reactor outage in May 2024. This was followed by a neutron irradiation campaign using a Cf source in order to acquire precise understanding of the energy calibration of the detectors with intrinsic neutron-induced γ-lines in their spectra. Run 1 was completed in October 2024 and included a ^{252}Cf irradiation campaign during the last two months. Afterwards, three of the four HPGe detectors were again extracted from the CONUS+ shield and replaced with three Germanium detectors with larger active mass (see Section 5). The upgraded setup is currently taking data since January 2025 recorded its first reactor off data in May of this year.

2.3 Germanium detectors

The following section describes the HPGe detectors used in the CONUS+ experiment. First, a general introduction on Ge semiconductor detectors is given, after which the four CONUS+ detectors are introduced and characterised.

2.3.1 Ge semiconductor principles

Germanium is an intrinsic semiconductor. It has a band gap of 0.67 eV at 77 K and is available in very high purities (HPGe), making it an ideal material for low-energy particle physics detectors. The small band gap allows for the easy production of electron-hole pairs in germanium by either thermal excitation of electrons or ionisation, as a result of a passing charged particle. Neutral particles, such as neutrinos, are also able to induce electron-hole pairs through processes such as CEνNS, where recoil energy is transferred to a Ge nucleus which then ionises the surrounding atoms. At the same time, phonons are produced. The number of electron-hole pairs that is created in such a process is directly linked to the energy of the particle that interacts in the germanium, and a higher energy particle produces more electron-hole pairs. Measuring the number of electrons (or charges) created in an interaction in the germanium, therefore allows the measurement of the energy of the interaction. This is the working principle of a semiconductor detector.

In order to extract and measure the created charges, an electric field is required. However, for germanium detectors, because of the small band gap, a high current (called the leakage current) is already present from thermally excited electrons. To get rid of these free charge carriers, a pn-junction must be formed. This is achieved (in the case of the CONUS+ detectors), by the deposition of a very thin layer of lithium (Li) atoms on the outside of the germanium crystal, which diffuse inwards and act as the n-type layer, defined as a layer with excess free electrons. The germanium itself, because of the presence of impurities or additional doping, is a p-type semiconductor, i.e. it features a large amount of acceptors and holes (positive charges). The contact between the p-type germanium and the n-type lithium layer causes electrons to diffuse into the p-type layer and holes to diffuse into the n-type layer, where they are each neutralised, forming a depletion region, a region with no free charge carriers, between the two materials. To increase the size of this region, a high voltage of the order of a few kV is attached to the detector in reverse bias through two electrodes: the n+ lithium layer on the outside of the crystal and an additional p+ contact. In this way, a diode is formed. In the case of an incoming particle, which interacts in the depletion region, (the active volume) and produces electron-hole pairs as described above, the created charges will then move through the applied electric field to one of the diodes where they can be readout.

In general, several types of germanium detectors with different designs are in use in the field of particle physics. The first of these, are so-called coaxial detectors, which feature a central bore in the middle of the crystal which allowing for the placement of the p+ contact (one of the electrodes) in the middle of the crystal. This is advantageous in bigger germanium crystals due to easier shaping of the electric field. These types of detectors are typically better suited for higher energy applications like material screening [49] due to an increased capacitance which increases electronic noise and disfavours measurement at very low energies as needed for CONUS+. The next type of germanium detectors are the so-called Broad-Energy Germanium detectors (BEGe). Their geometry is usually more planar compared to the coaxial detector and they feature a small p+ contact on one side of the crystal. This small contact leads to a decreased capacitance of the detector, which favours uses in low energy regimes compared to the coaxial detector. Closely related to this type of design is the so-called P-type Point Contact (PPC) germanium detector. These types of detectors have a more cylindrical shape and also feature a p+ contact on one side of the crystal. Compared to a BEGe detector however, this p+ contact is tiny in size (below 1 mm in diameter), which leads to greatly reduced electronic noise in the detector and makes them ideal for very low energy applications like the search for the CEνNS interaction. The electric field in such a PPC detector shows an extremely steep field gradient near the point contact due to its small size, which additionally allows for excellent pulse shape discrimination capabilities. For these reasons, the four detectors in the CONUS+ experiment were chosen to be PPC germanium detectors.

Figure 2.4 shows a schematic overview of a p-type point contact Ge detector. Apart from the described components of the PPC detectors, namely the p+ point contact, the Lithium layer, which acts as the n+ contact, and the depletion region in the middle of the detector, which is the active volume for measurement, a very thin insulation layer ($\sim$100 nm) is needed to avoid contact between the p+ and the n+ contacts.

Lastly, it should be mentioned that due to the very small band gap of germanium, Ge semiconductor detectors cannot be operated at room temperature and have to be cryocooled. Operation at room temperature would lead to thermal excitation of many electron-hole pairs which would lead to a very large leakage current. For this reason, the detectors are housed in cryostats, which in the case of CONUS+ are made out of copper, due to its high radiopurity. The cooling itself is conventionally achieved with liquid nitrogen, however, because of the location of CONUS+ in a nuclear power plant, this is not possible. Instead, the detectors are cooled with electrical cryocoolers.

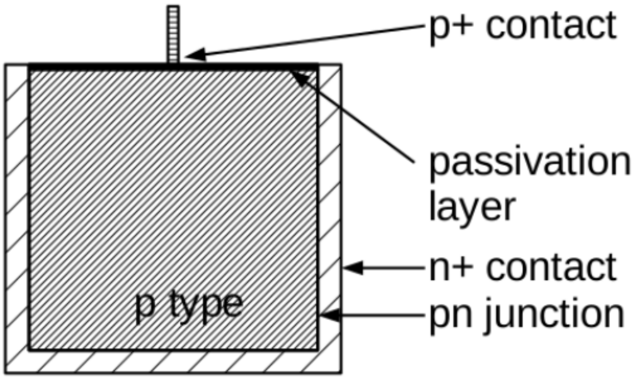

Figure 2.4. Schematic of a point contact p-type Ge detector like the ones used in CONUS+ [2]

2.3.2 Nuclear quenching

As described in the previous section, a germanium semiconductor detector in the context of a CEνNS experiment does not directly measure the energies of the incoming neutrinos but instead only accesses the recoil energies of the germanium nuclei in the interaction. As shown in Section 1.4 and Equation 1.5, this recoil energy is small as its maximum is proportional to the inverse mass of the germanium nucleus. The measurement is further complicated by the so-called nuclear quenching effect, an important characteristic of semiconductor detectors also previously mentioned in Section 1.4. The following section will explain the effect and its implications for CEνNS measurements.

When a CEνNS interaction (or any other scattering) occurs on a germanium nucleus inside the crystal, the nucleus gets a certain recoil energy E_{rec}. After the interaction, the energy of the participating nucleus is converted into two different types of energies. One part of the energy leads to the ionisation of the surrounding germanium atoms, which creates electron-hole pairs that drift to the appropriate cathode in the crystal, where they can be readout. The other part of the energy induces vibrations (phonons) in the lattice structure of the crystal, essentially heating the semiconductor by a very small amount. Although it is possible to measure these very small temperature changes by operating detectors at mK temperatures and using high-precision bolometers, for a standard germanium detector this second part is not measurable and essentially lost. Only the ionisation energy E_{ion} in the form of released charges is detected in the measurement. The ratio of the ionisation energy to the total recoil energy is known as the quenching factor q:

$$q = \frac{E_{ion}}{E_{rec}} \tag{2.1}$$

The quenching factor is energy dependent and its knowledge is one of the most important systematics for the treatment of the predicted theoretical signal prediction of CEνNS and also of the expected background components. The most well-known and largely accepted description of the behaviour of q at different energies is the semi-empirical Lindhard theory [50]. It uses one empirical parameter k:

$$q(E_{rec}) = \frac{k\ g(\epsilon)}{1 + k\ g(\epsilon)}, \tag{2.2}$$

with $\epsilon = 11.5\ Z^{-7/3}\ E_{rec}$ and $g(\epsilon) = 3\epsilon^{0.15} + 0.7\epsilon^{0.6} + \epsilon$. Z is the proton number of the target nucleus (in this case Z(Ge) = 32). The k parameter is material-dependent dimensionless scaling parameter and must be determined through measurements.

As mentioned above, the quenching factor is one of the most important systematics for CEνNS experiments using semiconductor detectors. For this reason, a dedicated quenching measurement in the context of the CONUS experiment was performed prior to the analysis of its last data collection period [7]. In this measurement, nuclear recoils between 0.4 keV and 6.3 keV were produced in a thin HPGe detector using mono-energetic neutron beams. The resulting measured nuclear quenching factors at different recoil energies are shown in figure 2.5 and are found to be consistent with Lindhard theory with k = 0.162 ± 0.004. Alternative quenching descriptions [6] have been proposed and have been tested with the CONUS and CONUS+ experiments (see Sections 2.2.1 and 4.7.4).

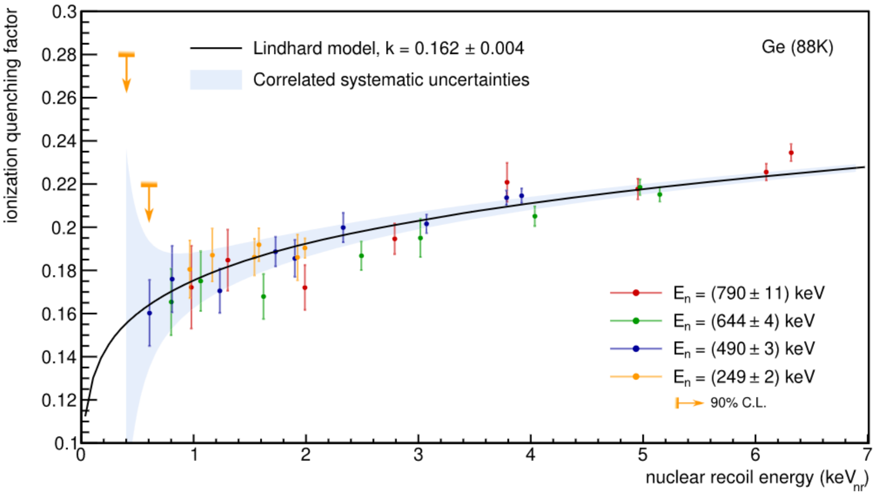

Figure 2.5. Ionization quenching factor as a function of the nuclear recoil energy [7]. The data points were obtained for four different neutron beam energies. Indicated error bars are uncorrelated uncertainties, correlated uncertainties are represented by the blue band. The data fits the Lindhard theory description with k = 0.162 ± 0.004 (stat + sys)(black curve)

The presence of nuclear quenching in the germanium crystals essentially decreases the energies which can be measured from the CEνNS interaction even further. The Lindhard model with a k parameter of 0.162 predicts $q(1\,\mathrm{keV}) = 0.125$, which means that for an initial recoil energy of 1 keV only 125 eV can be measured in the detector. This again explains the necessity for extremely low energy thresholds in these type of detectors, one of the key requirements for a successful measurement as defined in Section 1.4.

2.3.3 Signal processing in the preamplifier

The ionization charges produced during a CEνNS interaction drift toward the p+ contact through the electric field, inducing a time-dependent charge signal, Q(t), in the electrode. The characteristics of this signal depend on the trajectories of the charge carriers at the point contact, which can be calculated using the Shockley-Ramo theorem [51] (for details, see [52]). To read and analyse the signal, it must be processed.

The first component of the signal processing chain is the preamplifier, located within the cryostat and cooled together with the crystal to minimize electronic noise. The preamplifier amplifies the small signals induced by interactions in the germanium crystal without degrading their quality. It is placed as close as possible to the germanium crystal to minimize the pickup of noise from cables or the surrounding environment. The preamplifier collects the charges induced at the point contact, with the energy deposited in the crystal being proportional to the output voltage of the preamplifier. The lowest output voltage, which corresponds to the absence of signal in the crystal, is referred to as the baseline. Events in the crystal cause a stepwise increase in voltage from this baseline. These steps are recorded as pulses (or waveforms), with the maximum height of the pulse being proportional to the energy of the event. Examples are shown in Figure 2.6. The pulses are not perfectly step-like and instead feature a finite rise time, equivalent to the time it takes until all charges are accumulated, and a decay after they reach their maximum, induced by the response of the preamplifier electronics. Their shape provides additional information about the location and nature of the interaction. For example, pulses from bulk events in the main active volume of the detector differ from those originating from surface events in the outer transition layer, where weaker and inhomogeneous electric fields lead to charge loss and longer drift times. Similarly, pulses from multi-site events, in which more than one energy deposition occurs within the same event, have distinct shapes. This information can be used as the basis for pulse-shape discrimination of background events, as was previously done for the run 5 CONUS data [53].

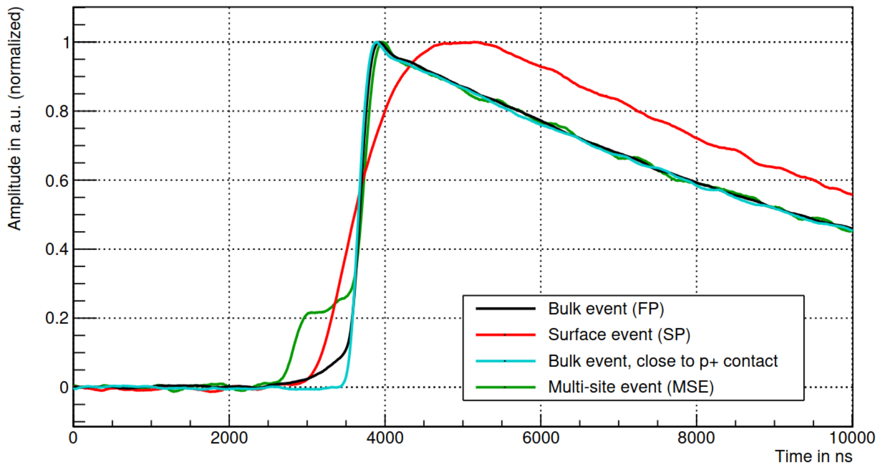

Figure 2.6. Examples of pulses generated in the CONUS+ detectors from [8]. The shape of the pulse gives information about the location of the event within the germanium crystal: Bulk events (black) are standard events happening in the main active volume of the detectors, surface events (red) happen in the transition layer of the crystal and feature slower rise times, Multi-site events (green) are events in which multiple energy depositions happen in one event, leading to one or multiple steps in the rise of the pulse.

The preamplifier used for the CONUS+ detectors is a custom-built transistor reset preamplifier (TRP), as opposed to a more traditional resistor-feedback (RC) preamplifier. The reason for this is twofold: First, the thermal noise (Johnson-Nyquist noise [54]) is lower in a TRP due to the use of a typically very large feedback resistor in an RC preamplifier. This makes the TRP more suitable for low energy applications. Second, signals from an RC preamplifier exhibit a long exponential tail due to the RC circuit and the large feedback resistor. In high-signal-rate environments, this tail can interfere with energy reconstruction, particularly if a second signal arrives before the first signal has decayed. In contrast, a TRP avoids this issue because the charges accumulated on the capacitor do not discharge between resets, keeping the baseline flat for each subsequent pulse. If the baseline becomes too large and the dynamic range of the TRP is reached, a control circuit triggers a field-effect transistor (FET), which very quickly (a few μs) discharges the capacitor. Such an event is called a TRP reset and the data during the reset is not usable. For this reason, the time of the reset events is recorded and a cut window (TRP cut) is placed after such an event in the processing of the data. The cut window is set to be between 1 to 2.5 μs, depending on the detector. The cut induces a certain amount of ”dead time” in the measurement, which later has to be accounted for.

2.3.4 Data acquisition and energy reconstruction

The next step of the signal processing chain is the data acquisition (DAQ) system, which digitises the output of the TRP at regular intervals (typical sampling rates $\sim$ 100 MS/s). The DAQ system first uses a triangular discriminator in order to identify physical events amidst electronic noise and trigger data acquisition. After triggering, the energy of each event is reconstructed using a trapezoidal shaping filter, a common shaping tool in particle physics data acquisition. The filter first gradually integrates the incoming pulse until it reaches its maximum (i.e. shaping time = 12 μs in CONUS+). It then holds the signal at a constant level for a fixed period (i.e. flat top $\sim$ 3 - 6 μs in CONUS+) in which the energy of the event is readout. Afterwards, the signal decays back to the baseline. The energy of the signal which is reconstructed in this way is given in terms of discrete digital bins called ”channels” (or ADC channels = analog digital converter channels), which are assigned to different pulse amplitudes. A calibration of the system with radioactive sources of known energy is needed to convert these channel numbers to the actual deposited energies in each event. After the correct energy has been assigned to each event, the data of each detector is stored in histograms (later called spectra). Here, one bin corresponds to a certain energy range and the counts in the bins are accumulated. These histograms are then later used for the actual analysis of the data. Section 2.3.9 will give a more detailed summary of the DAQ system used in CONUS+.

2.3.5 Energy resolution of a germanium detector

The total resolution σ of a germanium detector consists of five independent contributions: the intrinsic line width σ_{int}, the statistical uncertainty on the number of produced electron-hole pairs σ_{eh}, the uncertainty in charge collection σ_{coll}, electronic noise σ_{noise}, and environmental vibrations σ_{vib} [2].

$$\sigma_{tot}^2 = \sigma_{int}^2 + \sigma_{eh}^2 + \sigma_{coll}^2 + \sigma_{noise}^2 + \sigma_{vib}^2 \tag{2.3}$$

The two main contributions in the case of the CONUS+ detectors are σ_{eh} and σ_{noise}. In germanium, an average energy of ϵ = 2.96 eV is needed to create an electron-hole pair. Therefore, the number of electron-hole pairs produced in an interaction with an energy deposition E in the detector is

$$n = \frac{E}{\epsilon} \tag{2.4}$$

and the inherit statistical fluctuation of n lead to an uncertainty in the energy reconstruction and therefore to an increased energy resolution. This uncertainty is

$$\sigma_{eh} = \sqrt{F\epsilon E}, \tag{2.5}$$

where F is the Fano factor in germanium (F $\sim$ 0.1 - 0.15), defined as the ratio of the observed variance in the created number of electron-hole pairs and the variance predicted by Poisson statistics [55].

The influence of electronic noise on the energy resolution can be understood by looking at the energy reconstruction in the DAQ system. Here, the energy of an event is calculated by extracting the height of the pulse of the event from a constant baseline. As electronic noise will lead to small variations in the baseline, it also leads to slight variations in the extracted pulse height and therefore in the reconstructed energy. The electronic noise of a germanium semiconductor detector, specifically its voltage noise, is dominated by the input transistor of the preamplifier and directly proportional to the capacitance of the detector, which is given by

$$C = 2\pi K \epsilon_0 r. \tag{2.6}$$

Here, K is the dielectric constant of germanium, ϵ_0 is the free space permittivity, and r is the radius of the point contact electrode. The reduction of electronic noise through the reduction of the point contact size is one of the main upgrades of the CONUS+ detectors, as detailed in Section 2.3.7.

2.3.6 The CONUS+ detectors

The CONUS+ experiment uses four HPGe detectors (C2 - C5) with an additional detector (C1) being stored at MPIK for local testing. The detectors are housed in copper cryostats and connected to pulse-tubed cryocoolers (Cryo-Pulse 5 Plus by Mirion Lingolsheim) located outside of the shield (see Figure 2.7b). With these, the temperature inside the cryostats is kept at -195 to -200° C, depending on the detector. This temperature, as well as the temperature of the CP5 compressor and its power consumption, is monitored. The four CP5 cryocoolers themselves are being cooled with a liquid-cooling system consisting of two chillers which continuously pump cold water (in the case of Run 1) through the CP5 housing. The germanium detectors have a mass of 1 kg, resulting in an active volume of 0.92 - 0.95 kg per detector. Here, ”active volume” refers to the part of the germanium crystals which can be used for measurements i.e. the depletion region of the diode. The n+ lithium-diffused layer (dead layer) on the outside of the crystals does not contribute to this volume. The detectors are able to be operated continuously for long periods of time allowing for stable data taking in the KKL power plant without constant need of maintenance. Most importantly, the detectors are able to achieve excellent performances in energy resolution, noise edge and detector threshold which will be discussed in detail in Section 2.3.8.

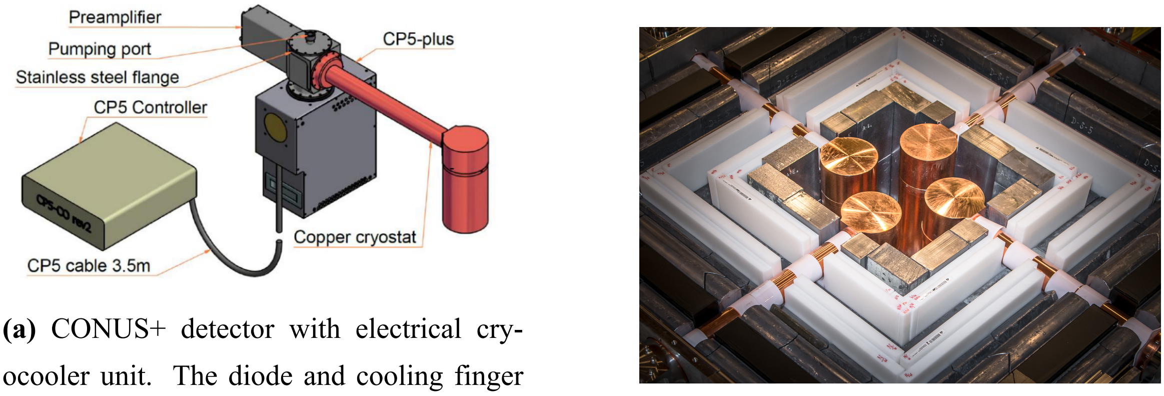

(a) CONUS+ detector with electrical cryocooler unit. The diode and cooling finger are fully enclosed by the shield, while the cryocooler sits outside the shield.

(b) The four CONUS+ detectors inside the shield.

Figure 2.7. Detectors for the CONUS+ experiment

2.3.7 Detector upgrades

As mentioned previously, the detectors used in the CONUS+ experiment underwent extensive upgrades after their use in the CONUS experiment in KBR in 2023. These upgrades were performed at Mirion Lingolsheim and mainly consist of two major improvements in the electrical components of the detectors. These changes resulted in greatly improved detector characteristics for the CONUS+ experiment.

The first change was the use of application-specific integrated circuit (ASIC) electronics in the preamplifier of the detectors. Compared to traditional electronic components, these customised chips are able to reduce electronic noise and increase the processing speed. In the context of CONUS+, they lead to faster pulses (shorter rise times), which is helpful to discriminate between small energy signals and noise at the DAQ level. The second change in the upgraded CONUS+ detectors was a reduction in the size of the point contact. As shown in Equation 2.6 and Chapter 2.3.5, the capacitance of the HPGe detectors is proportional to the size of the point contact and a reduction of its capacitance leads to a direct reduction of electronic noise. Prior to the upgrade, all CONUS detectors (C1 - C5) featured a point contact radius of $r = 1.25$ mm. After reworking of the crystals, a value of $r < 0.5$ mm was achieved in all detectors, leading to the very small theoretical capacitance $C = 0.45$ pF [8]. Furthermore, the cooling system of the external CP5 cryocooler systems was changed from air cooling with fans to water cooling, as mentioned in the previous section. This change reduces vibrations induced by the fans in the cryocoolers which can induce microphonic noise in the detectors.

2.3.8 Detector performance

The following section describes the performance of the CONUS+ detector after the upgrade described above both at the manufacturer Mirion and in the full experimental setup at the KKL power plant. The characterisation of the detectors was mainly performed by Janine Hempfling and details on the following parameters can be found in her dissertation [8].

Energy resolution

The energy resolution of the detectors was evaluated with a ^{241}Am source ($E = 59.5$ keV) and an artificial pulser signal. The values found for all detectors by Mirion (directly after the upgrade) and at KKL can be found in Table 2.1. All values in this and subsequent tables are given in terms of FWHM.

For all detectors, a decrease of the pulser resolution of at least 15 eV was achieved. To visualise this large improvement, Figure 2.8 shows the injected pulser peaks for the C2 detector before and after the upgrade. Here, the amplitude and mean of both peaks were normalised to one for an adequate comparison. Table 2.2 additionally shows the resolution achieved in the ^{241}Am peak at 59.5 keV.

Trigger efficiency

The trigger efficiency of a detector setup refers to its ability to recognize and register signals at different energies. Ideally, the setup should have a trigger efficiency of 100 % for

Table 2.1. Pulser resolution of each CONUS+ detector measured by Mirion (ΔE_{Mirion}) and in the full experimental setup at KKL (ΔE_{KKL}). These values are compared to the pulser resolution before the detector upgrade in the CONUS setup at the KBR power plant (ΔE_{KBR}) [8]. The C5 detector was mainly a prototype detector during the CONUS experiment and not used in KBR, explaining its very high resolution before the upgrade.

Detector	ΔE_{Mirion} [eV]	ΔE_{KKL} [eV]	ΔE_{KBR} [eV]
C2	51	49 ± 1	77 ± 1
C3	51	49 ± 1	64 ± 1
C4	48	50 ± 1	68 ± 1
C5	49	48 ± 1	300 - 500

Table 2.2. Resolution of the ^{241}Am peak for each CONUS+ detector measured by Mirion (ΔE_{Mirion}) and at MPIK (ΔE_{MPIK}). For this measurement the source was placed on top of the cryostat of the detectors [8].

Detector	ΔE_{Mirion} [eV]	ΔE_{MPIK} [eV]
C2	326	317.5 ± 10.3
C3	318	323.5 ± 9.3
C4	308	308.9 ± 10.1
C5	314	339.7 ± 5.3

all energies, meaning that any interaction that happens inside the detector is registered and its energy is correctly reconstructed. However, in reality this is not the case, and the trigger efficiency decreases towards very low energies. This is due to the fact, that as the energy of an interaction decreases, also the amplitude of its detector pulse over the baseline decreases. For very small energies, the pulse amplitude is so small that the DAQ system cannot distinguish between the pulse and the electronic noise on the baseline and, therefore, does not trigger. This decrease in trigger efficiency is an extremely important characteristic of germanium detectors, especially in CEνNS searches since the expected CEνNS signature is mainly focused at very low energies (see Chapter 1.1). As the decreasing trigger efficiency at low energies is tied to the electronic noise, a reduction of this noise as achieved through the reduction of the point contact size in the detector upgrade will also lead to an improvement of trigger efficiency.

Figure 2.9 shows the new trigger efficiencies measured in the CONUS+ commissioning phase at KKL after the detector upgrade and compares them to the values obtained before

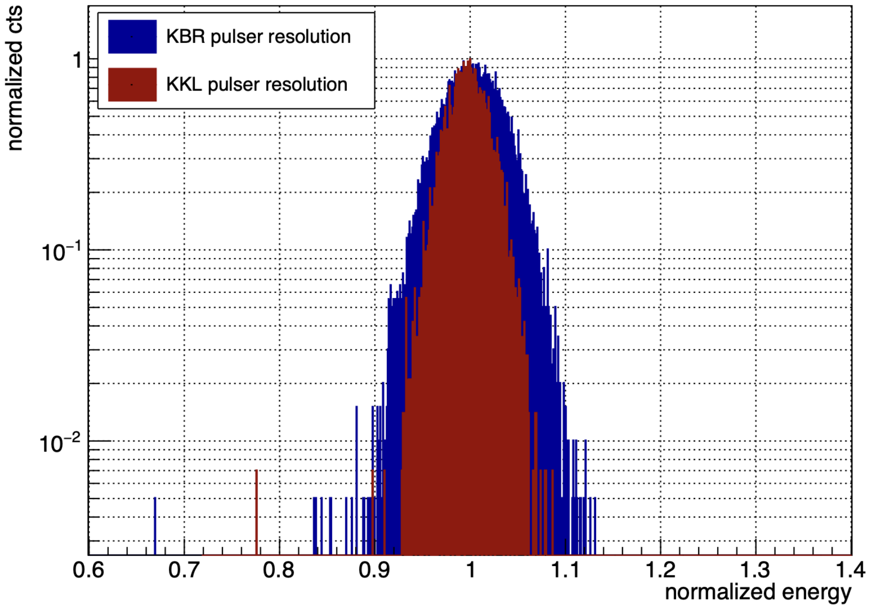

Figure 2.8. Pulser resolution of C2 before (blue) and after (red) the upgrade [8].

the upgrade. For all detectors substantial improvements were achieved, which can also be seen from Table 2.3, which gives approximate values for the energies at which efficiencies of 100 %, 50 %, and 20 % are reached in the C4 detector before and after the upgrade.

Table 2.3. Trigger efficiency values for the C4 detector before and after the detector upgrade.

	Before upgrade	After upgrade
100 % down to	∼ 500 eV	∼ 150 eV
50 % at	∼ 300 eV	∼ 85 eV
20 % at	∼ 200 eV	∼ 65 eV

Noise edge

The noise edge, which means the point in the spectrum of the germanium detectors below which the dominant component is electronic noise, is another important characteristic to determine the detection threshold. It is expected to improve with improved pulser resolution, as the width of the noise peak is the same as that of an injected pulser signal [56]. During reactor characterisation, it became obvious that the noise peak for the CONUS+ detectors featured an additional slow rising peak that extended towards energies over 1 keV [8]. This additional, unexpected noise component was identified as most likely stemming from TRP related events and false triggers by the DAQ on falling previous pulses. They can be re-

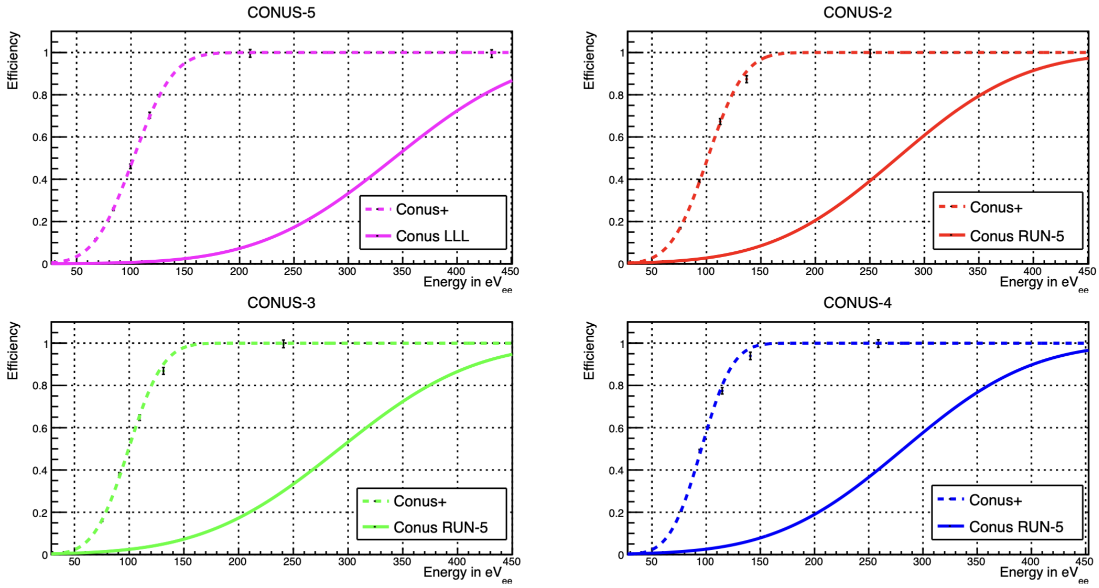

Figure 2.9. Improvement of the trigger efficiencies of all detectors used in the CONUS+ experiment. Dashed lines show values measured in the commissioning phase at KKL, while the solid lines how the values for the CONUS experiment at KBR. As C5 was not used at KBR, the solid line presents values measured at MPIK before the upgrade. [8].

moved by the TRP cut detailed in Section 2.3.3 and cutting on pulse shape parameters of the recorded pulses. After this correction, the detectors all feature an unprecedented noise edge at around 160 - 180 eV, which is in line with the measured pulser resolution from the previous section.

Energy calibration and nonlinearity

As described in Section 2.3.3, the signals in the detector are measured in the DAQ system in terms of ADC channels, which means the relative amplitude in reference to the dynamic range of the preamplifier. For analysis of the spectrum, these ADC channels have to be converted into actual energies and this is done with radioactive sources of known energy. Some of the sources used for this purpose are ^{228}Th, ^{57}Co, and ^{241}Am, as well as the intrinsic ^{68}Ge activation lines inside of the detectors (see Section 2.4.1). For the conversion from ADC channel to energy, in first order, a linear relationship is assumed:

$$E\ [keV] = a\ [keV] + b\ [\frac{keV}{Channel}] \cdot Channel \tag{2.7}$$

Here, a and b are the two calibration coefficients, which have to be measured with the aforementioned known sources. They are listed in Table 2.4 for run 1 of the CONUS+ experiment.

However, the conversion from ADC channels to energy is unfortunately not strictly lin-

Table 2.4. Calibration coefficients a and b for the low energy channels of all four detectors in run 1 of the CONUS+ experiment. a describes a constant offset of the energy calibration function (in keV), while b describes the slope of the function (see Equation 2.7).

Detector	a [keV]	b $[\frac{keV}{Channel}]$
C5	- 0.00638 $\pm$ 0.00168	0.00109 $\pm 2 \cdot 10^{-7}$
C2	- 0.00467 $\pm$ 0.00185	0.00113 $\pm 2 \cdot 10^{-7}$
C3	- 0.00385 $\pm$ 0.00156	0.00115 $\pm 2 \cdot 10^{-7}$
C4	- 0.00206 $\pm$ 0.00197	0.00113 $\pm 2 \cdot 10^{-7}$

ear, and at very low energies below 300 eV nonlinearity effects have a large influence. The effect arises in the energy reconstruction of the DAQ system and is due to too large rise times (shaping times) which were selected for the trapezoidal filter (see Section 2.3.3) in the energy reconstruction in run 1. These too large shaping times lead to slight deviations between the reconstructed energy and the actual energy of the physical signal, which manifests as non-linearities in the energy scale. They were studied by introducing artificial pulser signals in the detectors at known energies and measuring the deviation of their energy from the expected energy with a purely linear calibration. Figure 2.10 shows the measured deviations for the C2, C3 and C5 detectors. As the nonlinearity deviations are energy dependent and must be included in the final energy calibration of the data set, a fourth-order polynomial NL(E) was chosen to describe them. This fitted polynomial is then included in the energy calibration of the final data set to get a total energy calibration:

$$E\,[keV] = a\,[keV] + b\,[\frac{keV}{Channel}] \cdot Channel + NL(E) \tag{2.8}$$

2.3.9 CONUS+ DAQ system

CONUS+ uses the V1782 Octal Digital Multichannel Analyzer by CAEN [57] as its DAQ system for the readout of germanium data. This module features a sampling rate of 100 MS/s (Mega Samples per second) and a resolution of 16 bit per sample, making an accurate measurement in both time and energy possible. Additionally, it makes the recording of the pulses of each signal possible.

The DAQ system is set up such that data can be taken in two separate channels for all four detectors, which the CONUS+ experiment uses to record a low energy channel with a range up to approximately 35 keV and a high energy channel with a range of up to 500 keV. The low energy channel is used to perform the main analysis of the experiment, as it contains the region of interest for the CEνNS analysis. The high energy channel is used to check

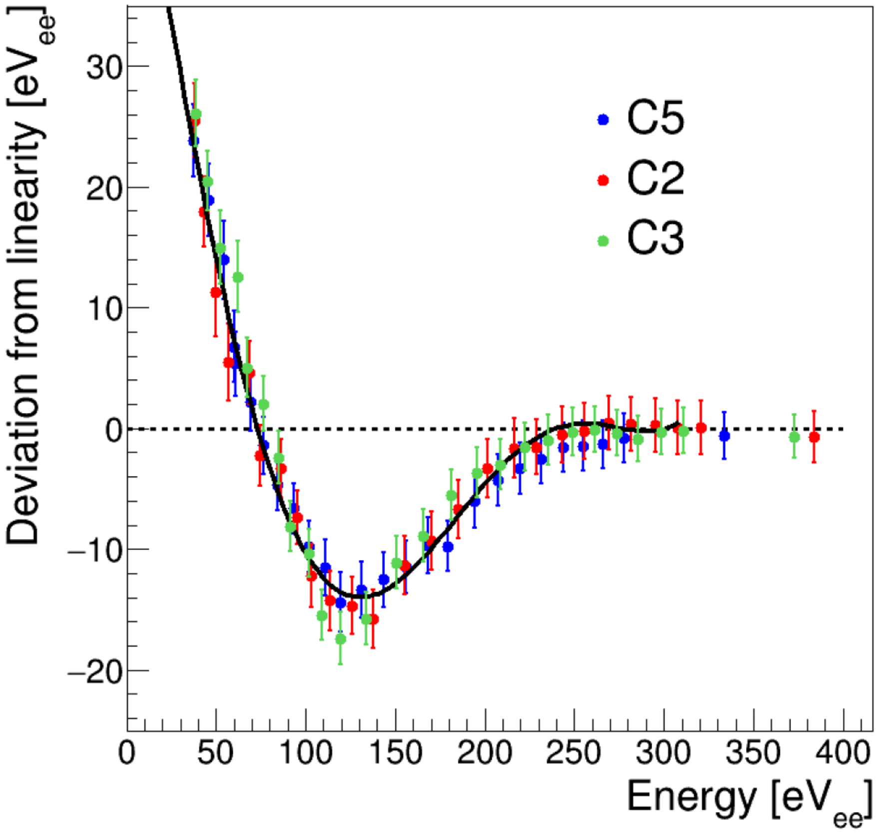

Figure 2.10. Deviation from a purely linear scale for the C2, C3 and C5 detectors. The line shows the fit function NL(E) (fourth order polynomial) chosen to describe the energy dependence of the deviation. This fit function was implemented in the energy calibration of the final data sets.

background stability of the experiment and is an important input for the background model discussed in Chapter 3. In this energy region, several gamma lines like the ones from radon decay in the detector chamber are visible which allows to put exact constraints on these background contributions in the model. As the preamplifiers of the CONUS+ detectors are optimized for their performance at low energies, the efficiency of the detector setup decreases at high energy. The specific origin of this effect is under study. These efficiency losses start at around 100 keV and increase towards higher energies. In order to still be able to make use of the channels, an efficiency correction of their recorded spectra is performed using data from muon background simulations. This procedure will be detailed in Section 3.4.2.

Apart from the V1782 system for readout of the germanium data, the experiment also uses an additional V1740D board [58] to readout the data from the muon veto PMTs and the TRP resets. This board features 64 channels which makes it ideal for the large number of PMTs and has a sampling rate of 62.5 MS/s at a resolution of 12 bit per sample.

2.4 CONUS+ shield and backgrounds

The shield design of the CONUS+ experiment is based on 20 years of experience working with low background experiments at the Max-Planck-Institute für Kernphysik (MPIK) and is specifically tailored to the different types of background expected in the setting of the KKL nuclear power plant. The following section will describe these background sources in detail, then explain the different mitigation techniques for each of these backgrounds, and finally illustrate the shield design that follows from these considerations.

2.4.1 Background sources for the CONUS+ experiment

Cosmic rays

Cosmic rays are highly energetic (charged or neutral) particles that originate from extraterrestrial sources like the Sun, the core of our galaxy, or supernovae. Of these primary cosmic rays, about 99% are the bare nuclei of common atoms and about 1% are bare electrons [9]. Of the nuclei, about 90% are protons, 9% are alpha particles, and the remaining 1% are the nuclei of heavier atoms. The exact composition of the cosmic ray spectrum varies for different energies and is shown in Figure 2.11. The energy of primary cosmic rays can reach up to 10^{11} GeV, with the most energetic particles likely originating from extragalactic sources.

High energy primary cosmic rays are able to penetrate Earth's magnetic field and can interact with its atmosphere. These interactions induce electromagnetic and hadronic showers in which many different kinds of particles are produced. Of theses secondary cosmic rays arriving at Earth's surface (excluding neutrinos), approximately 75 - 80% are muons due to their long live time of 2.2 μs. Furthermore, the spectrum consists of 5 - 10% electrons (and positrons), 5 - 10% neutrons, 1 - 5% protons, and a small quantity of pions and high-energy γ-rays (see Figure 2.12) [10]. Of these different particles, the most relevant background sources for shallow underground experiments like the CONUS+ experiment with its overburden of 7.4 m w.e. are cosmic neutrons followed by muons, because of their ability to penetrate even deep underground and their large abundance.

Cosmic ray muons

The interactions of primary cosmic rays with Earth's atmosphere are dominated by inelastic collisions in which secondary mesons are produced. An example of such an interaction is

$$p + A \rightarrow \pi^+ + \pi^- + K^+ + K^- + X \tag{2.9}$$

where a cosmic proton hits an atmospheric nucleus (like nitrogen or oxygen) and produces several pions, kaons, and additional secondary hadrons (X). The same interactions

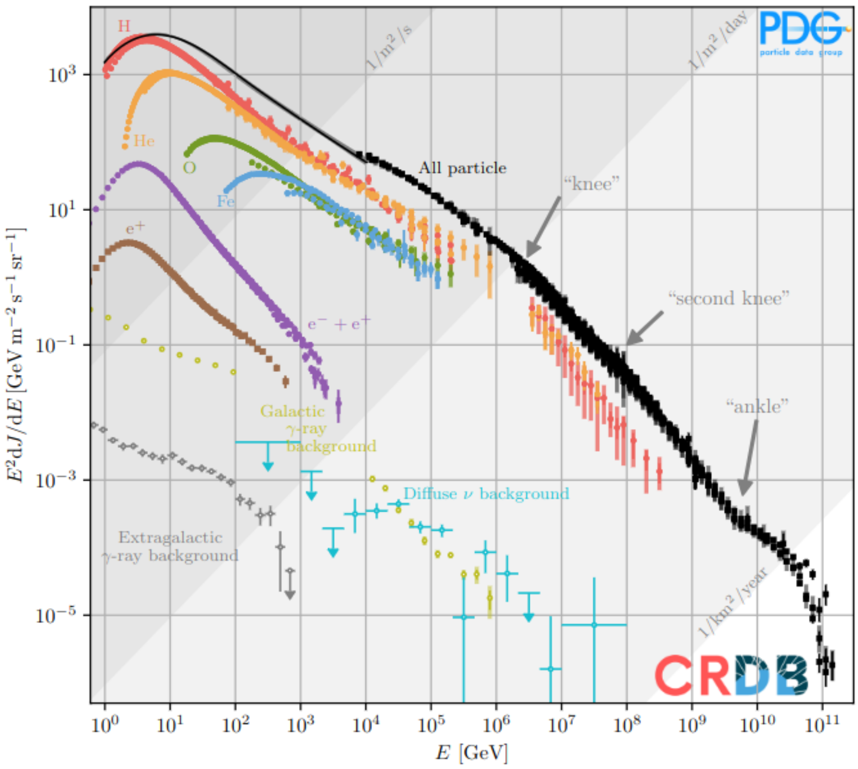

Figure 2.11. Spectrum of primary cosmic rays in units of intensity multiplied by kinetic energy squared. Points show measurements of negative muons with E > 1 GeV from different experiments. Taken from [9]

also apply for heavier cosmic ray nuclei. The charged pions and kaons are unstable ($\tau_\pi = 8.52(18) \times 10^{-17}$s, $\tau_{K_L} = 5.12(21) \times 10^{-8}$s) and therefore decay further.

$$\begin{aligned} \pi^+ \rightarrow \mu^+ + \nu_\mu \, , \; \pi^- \rightarrow \mu^+ \bar{\nu_\mu} \\ K^+ \rightarrow \mu^+ + \nu_\mu \, , \; K^- \rightarrow \mu^+ \bar{\nu_\mu} \end{aligned} \tag{2.10}$$

At higher altitudes, muon production via pion decay is dominant due to its shorter lifetime. At lower altitudes, kaon decay becomes more significant, while the probability of a secondary hadronic shower increases due to the higher atmospheric density, effectively suppressing direct muon production. Therefore, the majority of secondary cosmic ray muons are produced at very high altitudes of around 15 km [10]. Due to the muons long lifetime ($\tau_\mu = 2.1969811(22) \times 10^{-6}$s), many of them can reach sea level, making them the most abundant charged cosmic ray particle at very low altitudes (see Figure 2.12). While travelling through the atmosphere, muons primarily lose energy through ionisation of the surrounding air molecules, leading to an energy loss of about 2 GeV for muons produced at an altitude of 15 km before reaching the ground. This results in an average energy of 4 GeV of muons at sea level. The integral intensity of muons above 1 GeV in the vertical direction is 70 $m^{-2}s^{-1}sr^{-1}$ [59].

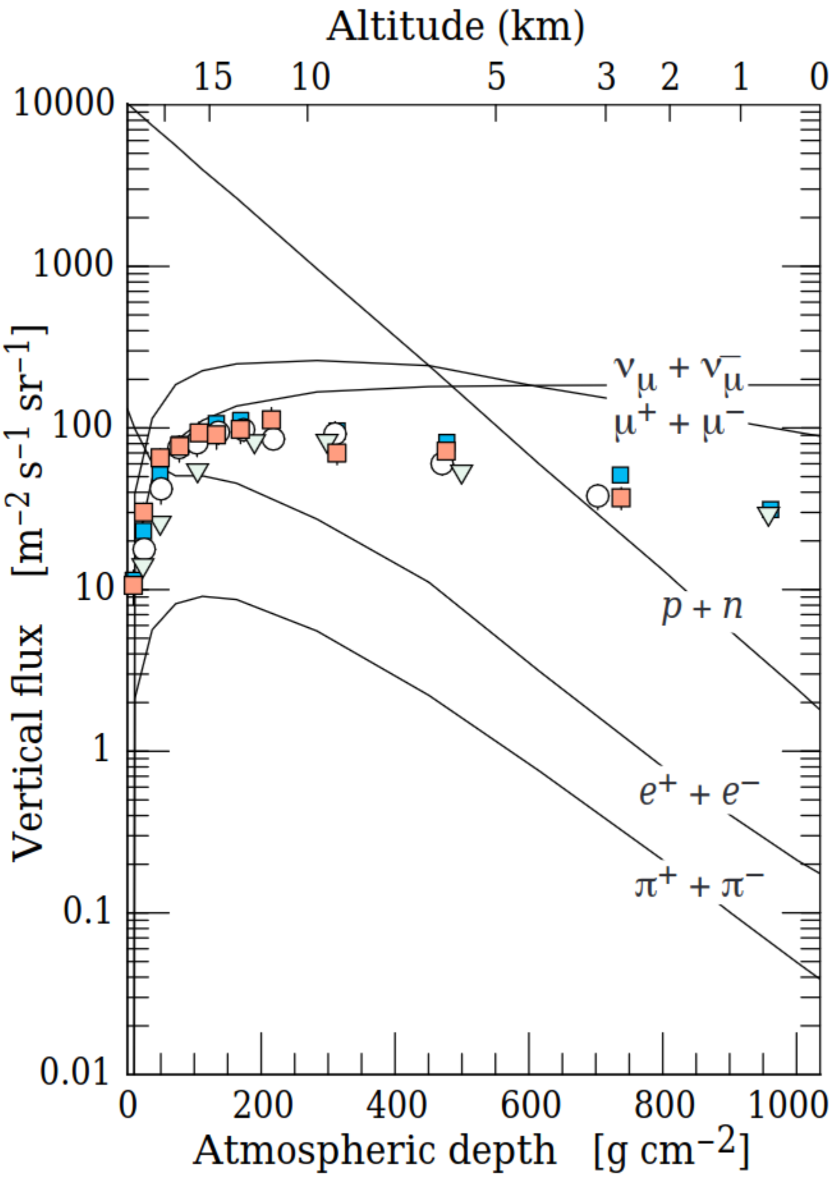

Figure 2.12. Spectrum of secondary cosmic rays at different altitudes / atmospheric depths. Extracted from [10]

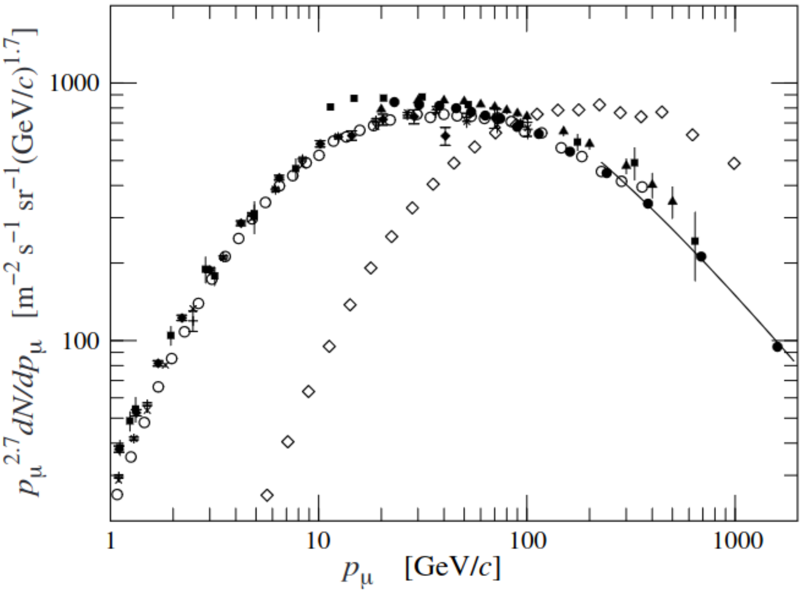

Figure 2.13. Spectrum of cosmic ray muons at sea level for $\theta = 0°$. $\diamond$ additionally shows $\theta = 75°$. Taken from [10]

Figure 2.13 shows the energy spectrum of muons at sea level for the zenith angles $\theta = 0°$ and $\theta = 75°$. Their overall angular distribution follows $\sim \cos^2$, which is characteristic for 3 GeV muons, and gets steeper for E < 3 GeV and flatter for higher energies. [10]. The disappearance of low energy muons at $\theta = 75°$ in Figure 2.13 is explained through the increased distance that the muons have to travel through the atmosphere, increasing their chance of decay. Another aspect that has to be considered is the muon charge ratio, defined as the ratio between the amount of positive muons and the amount of negative muons in cosmic rays. The interactions shown in Equation 2.9 favour the production of positively charged hadrons due to the predominantly positively charged cosmic rays. As a result, the muon charge ratio is greater than one with values of around 1.3 for muons in the range between 10 and 100 GeV. Figure 2.14 shows the dependence of the ratio on the energy of the muon.

When cosmic ray muons hit Earth, they are almost exclusively decelerated through electromagnetic interactions with the traversed matter, resulting in electromagnetic showers, pair production, and muon bremsstrahlung. Furthermore, they can produce secondary neutrons through photonuclear interactions, muon capture or deep inelastic scattering. The energy loss in the dominant electromagnetic interactions is very small, which, in combination with the long lifetime of the muon, allows them to penetrate deep underground. Figure 2.15 from [2], [60] shows the intensity of the muon flux at shallow underground sites with depths of up to 100 m w.e. As discussed before, the CONUS+ experiment has an overburden of 7.4 m w.e. consisting of the reactor building of the KKL power plant. This results in an

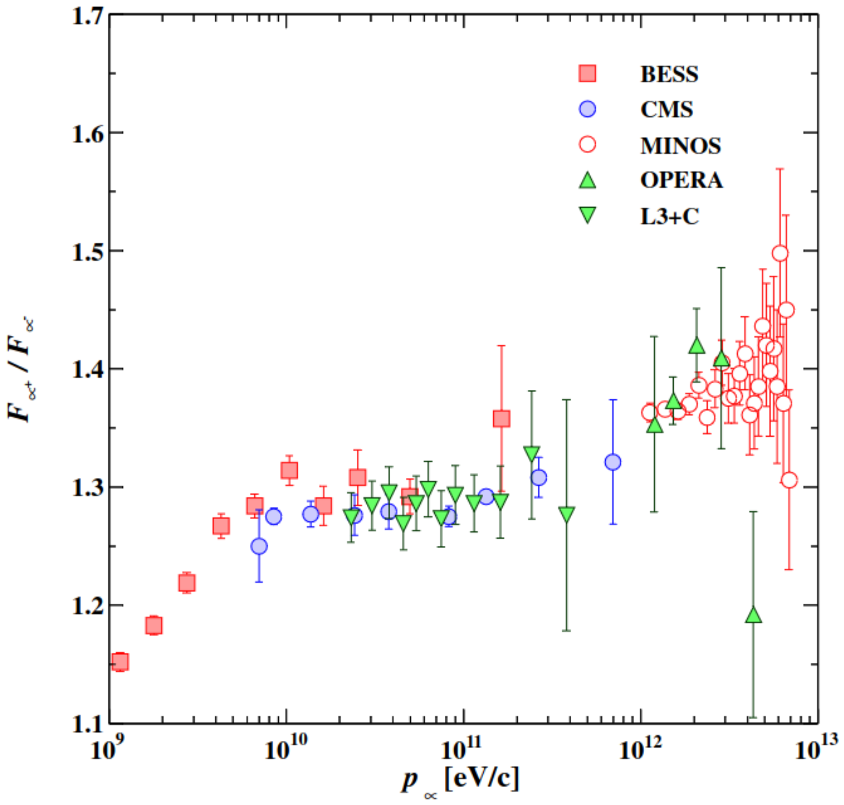

Figure 2.14. Muon charge ratio measured in different experiments. Taken from [10]

approximate muon flux of $(107 \pm 3)\ \mathrm{m}^{-2}\mathrm{s}^{-1}$ for the CONUS+ experiment. Muons passing through the reactor building and the CONUS+ shield produce electromagnetic showers and secondary neutrons, that can be registered as background in the HPGe detectors at the centre of the shield. This is especially relevant for the heavy materials of the CONUS+ shield (such as Pb), since the cross section for muon bremsstrahlung scales with the atomic number Z of the traversed material, while the cross section for muon capture (neutron production) scales with Z^4. This, paired with their high flux, makes cosmic ray muons one of the dominant background sources for the CONUS+ experiment and adequate background reduction techniques have to be employed in order to mitigate their impact.

Due to the very small energy loss of muons in matter (a 10 GeV muon loses only approximately 3.1 GeV, when passing through 25 cm of lead [61]), passive shielding is unable to reduce the muonic background. Instead, a common technique, which is also employed in the CONUS+ experiment, is the use of an active muon anti-coincidence system (or ”muon veto”) around the detector. The muon veto system consists of 18 plastic scintillator plates with a thickness of 5cm and made from EJ-200 [62]. They are arranged in two layers (an inner and an outer veto) in the shielding setup. Each scintillator plate is equipped with photomultiplier tubes (PMTs). When a muon (or a high-energy γ) passes through such a layer it deposits a certain (known) amount of energy in the scintillator which can be read out with

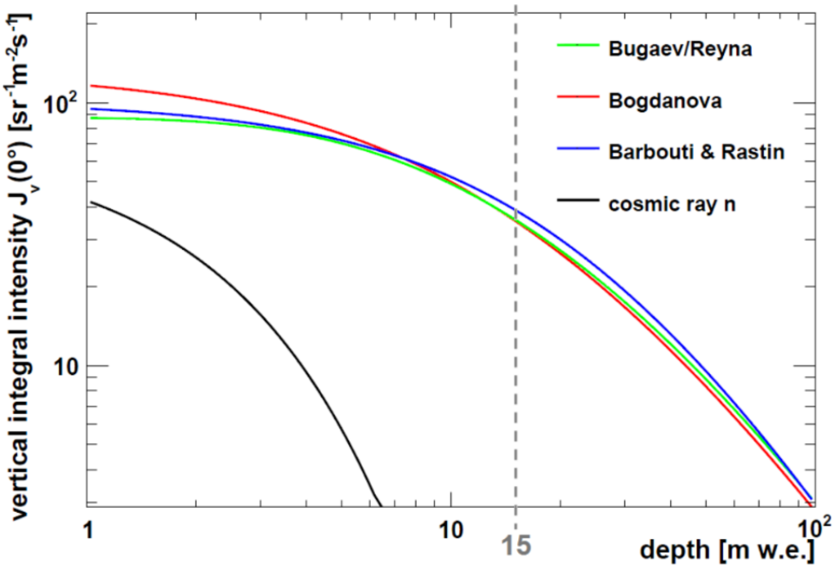

Figure 2.15. Vertical integral intensity of muons for different depths of overburden, from [2]. Different models for the calculation of the intensity are compared and show good agreement. Furthermore, the vertical integrated intensity for cosmic ray neutrons is shown.

the PMTs. If sufficient energy is deposited in the plate, the system triggers and records the time stamp of the event. In the post processing of the data, this triggered event is used to define the muon veto cut in which all events in the germanium immediately after the trigger are removed. The time for which this is done is called the ”muon veto window” and is chosen to be long enough that the shower of particles induced by the passing muon is expected to have ended. In the case of the CONUS+ experiment 450 μs were chosen. This value is very conservative but was chosen to also reduce the impact of delayed muon-induced neutrons from the shield. The procedure leads to the accumulation of dead time in the measurement, but is very effective in reducing the muon background, reaching efficiencies of up to 99%. For the trigger of the muon veto system, an energy threshold needs to be defined in such a way as to maximise the amount of rejected events (from muons and high-energy γ) and minimise the accumulated dead time.

The described method only reduces muonic backgrounds that are produced in the CONUS+ shield and has no effect on particles that are produced by muons passing through the overburden of the experiment, such as neutrons. They are separately shielded by several layers of polyethylene (PE) in the shield. Neutrons that pass through these layers are slowed down significantly and thermalised due to the very high hydrogen content in PE, leading to a high probability for elastic scattering. ^{10}B with its very high thermal neutron capture cross section of $\sim$3.8 kb [63] is then used as an additive in several PE layers to remove the thermalised neutrons.

Cosmic ray neutrons

Another prominent component of cosmic rays at Earth's surface as shown in Figure 2.12 are neutrons. These are produced through a number of processes like spallation, where a high energy primary cosmic ray particle fractures a nucleus in the atmosphere, kaon decay or neutron evaporation through the nuclear de-excitation of a nucleus. These interactions primarily occur in the upper parts of the atmosphere, leading to an exponential decrease of neutron flux in greater atmospheric depths due to the absorption and scattering of the neutrons. Due to the high cross section for neutron scattering on the surrounding nuclei, the integrated neutron flux at ground level can depend on pressure and temperature of the atmosphere, as well as on latitude, longitude, and altitude of the measurement location [64]. Figure 2.16 shows a typical neutron spectrum at sea level, measured in [11]. The spectrum consists in general of three peaks: a thermal peak at around 10^{-8} MeV, where neutrons have been slowed down to the point where they are in equilibrium with the nuclei of the atmosphere, a nuclear evaporation peak (E $\sim$ 1 MeV), and the fast neutron peak (E > 10 MeV). The flux measured in [11] was 0.0134 $\text{cm}^{-2}\text{s}^{-1}$.

As described above, neutrons exhibit high cross sections for elastic scattering on the nuclei of the materials they traverse, particularly on hydrogen. As such, neutrons are not able to penetrate very deeply underground and are attenuated with a mean length of about 200 $\text{g}\cdot\text{cm}^{-2}$ [46]. This is shown in Figure 2.15 and results in the common value of 10 m w.e. as a benchmark for an effective shielding from cosmic ray neutrons. The CONUS+ experiment is located at a depth of 7.4 m w.e. and therefore will experience some residual cosmic neutron flux at its location. These neutrons can propagate through and interact with the materials of the CONUS+ shield, again resulting in background events for the measurement. The shielding of these neutrons is again based on the use of high Z materials (lead) and borated and unborated PE layers. However, compared to the slower reactor neutrons the shielding of the CONUS+ shield is not as effective for these neutrons.

Natural radioactivity

Natural radioactivity consists of the decays of the ^{238}U and ^{232}Th series, as well as ^{40}K. These isotopes can be found in almost all materials present on Earth with concentrations of a few ppm for ^{238}U and ^{232}Th and up to 100 ppm for ^{40}K [65]. Their decay produces several types of radiation, such as α-particles and γ-rays through β-decays. While the influence of external α-particles on low background measurements is limited apart from α-emitters directly on the surface of the detectors, the production of γ-rays is more important. They can have energies of up to a few MeV, with the highest energy from commonly occurring decays being 2.6 MeV from the decay of ^{208}Tl, one of the last isotopes in the Th decay chain,

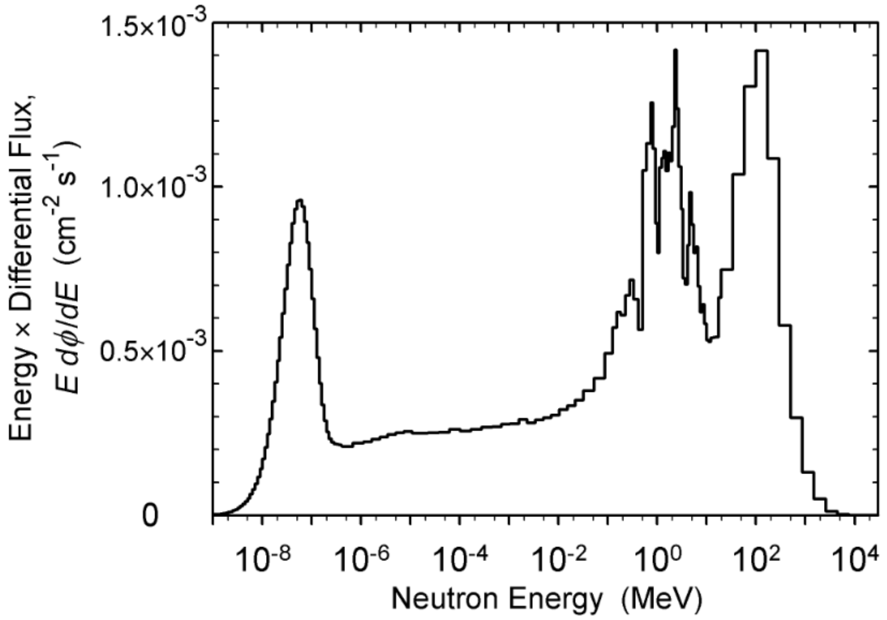

Figure 2.16. Typical spectrum of cosmic ray neutrons at sea level, measured in New York, USA from [11]

and can therefore penetrate into the HPGe detectors of the CONUS+ experiment and induce background events. Furthermore, the emitted electron in the β-decay of these isotopes can induce bremsstrahlung in the materials surrounding the detectors, which is especially problematic for CEνNS experiments since the bremsstrahlung spectrum rises towards low energies and is therefore most prominent in the region of interest for CEνNS.

In order to mitigate the influence of natural radioactivity, two concepts are used in the CONUS+ experiment and in low background experiments in general. The first is the use of lead as a shielding material for γ-rays due to its high atomic number Z (Z = 82). This leads to an increased electron density in lead that is favourable for Compton scattering to occur. The intensity of γ-rays $I(x)$ after passing through a certain length x of a material is described by Lambert's law:

$$I(x) = I_0 e^{-\mu x} \tag{2.11}$$

with the initial intensity I_0 and the attenuation coefficient μ. The attenuation coefficient for 2.6 MeV γ-rays in lead is approximately μ = 0.36 cm^{-1} [66], which results in a decrease of 99.6 % of γ-ray intensity after 15 cm of lead. The second concept is the use of radiopure materials in the the shield and detector, meaning materials that are (almost) completely free of radioactive contaminations (typically in the range of μBq/kg). The use of lead is again justified here, as it is typically very low in natural radioactivity and only commonly features ^{210}Pb, a product of the uranium decay chain which is not removed in the smelting and refining process of lead samples. Ideally, lead layers that are very close to the detectors should exhibit only small amounts of ^{210}Pb, as can be found in archaeological lead samples ($\tau_{\frac{1}{2}}$ = 22.2 y). Another material that is often used in low background experiments is copper due to its lack of any long-lived naturally occurring isotopes. Additionally, electroforming copper using electrolysis can remove impurities producing extremely pure samples.

Two isotopes that must be mentioned separately are the radon isotopes ^{222}Rn and ^{220}Rn of the uranium and thorium decay chain. Radon is a noble gas and, as such, does not chemically bond to any other isotopes in the material in which it is produced. Instead, it can move freely through the porous material and escape, leading to concentrations of radioactive radon in the air. This process is especially relevant for closed rooms, where radon can escape from concrete in the walls and accumulate. This not only leads to health concerns in high radon environments, but is also relevant for low background experiments like the CONUS+ experiment, where radon can diffuse into the shield structure and decay inside of the detector chamber. The decay products of radon, i.e. the lower parts of the uranium and thorium decay chain, can then accumulate inside the chamber and again induce background events through their own decay. In order to protect against this, the inside of the CONUS+ shield is continuously being flushed with radon-free air, i.e. air that has been stored in gas bottles for several weeks ($\tau_{\frac{1}{2}}(^{222}Rn)$ = 3.8 d). The system with its eight bottles of radon-free air is pictured in Figure 2.17.

Figure 2.17. Picture of the eight bottles (10 L, 300 b) of radon-free air in the CONUS+ room. The bottles are stored in a rack and connected with pressure reducers to a system of tubes which guide the air inside the shield. A flowmeter (not pictured) is included to check the air flux.

Cosmogenic activation of materials

Cosmogenic activation is the process by which radioactive contaminations are induced in materials due to their exposure to cosmic rays, primarily high energy neutrons. This can lead to the production of long-lived radioisotopes through interactions such as spallation or neutron capture. In the case of the CONUS+ experiment, cosmogenic activation is especially relevant for the copper parts of the shield and cryostats as well as for the germanium detectors themselves. Tables 2.5 and 2.6 give an overview of the relevant isotopes for the CONUS+ experiment and their influence on the spectrum in terms of lines from γ-rays, X-rays, which are typically produced after the isotope undergoes electron capture, or bremsstrahlung from β-decays.

Table 2.5. Most relevant cosmogenically induced isotopes in copper for CONUS+ and their impact on the CONUS+ spectrum. x denotes the presence of X-rays or β-decay for the isotope. "Above range" indicates the presence of γ-lines above the sensitive energy range of the CONUS+ measurement [12].

Isotope	Half-life [d]	Production mechanism	Relevant γ-lines	X-rays	β-decay
^{60}Co	1923.6	Neutron capture on ^{59}Co	above range	x	x
^{57}Co	271.8	Spallation of ^{63}Cu and ^{65}Cu	122 keV	x	x
^{54}Mn	312.2	”	above range	x	x

In order to protect all of the components from cosmogenic activation, it is necessary to store them in underground facilities with an overburden of more than 10 m w.e. to protect them from the impact of cosmic ray neutrons (see Figure 2.15). In cases where this is not possible, such as during transports, the exposure of the materials to cosmic rays should be tracked in order to effectively estimate the amount of contaminations present.

Reactor-correlated backgrounds

In addition to the background sources listed above, experiments at nuclear reactors are exposed to further backgrounds that are unique to their environment. The first of such backgrounds, which has to be noted, are neutrons coming from the reactor itself. These neutrons are used to induce fission in the reactor core, effectively driving heat production. Each fission reaction produces 2-3 neutrons and a constant flux is expected at experimental sites close to it. They have energies of a few MeV at most (see for example [67]) and are shielded in the CONUS+ setup through the aforementioned layers of (borated) polyethylene. The presence of reactor neutrons is especially problematic in the context of a CEνNS experiment, since they can also scatter elastically with the germanium nuclei in the detectors and are also only present in reactor on data taking, which means they can exactly mimic the signature of the CEνNS interaction.

Furthermore, reactor neutrons can activate materials through which they pass, leading to increased radioactive contaminations in and around the reactor, like the presence of ^{60}Co

Table 2.6. Most relevant cosmogenically induced isotopes in germanium for CONUS+ and their impact on the CONUS+ spectrum. x denotes the presence of X-rays or β-decay for the isotope. "Above range" indicates the presence of γ-lines above the range of the CONUS+ measurement [12].

Isotope	Half-life [d]	Production mechanism	Relevant γ-lines	X-rays	β-decay
^{60}Co	1923.6	Neutron capture on ^{59}Co	above range	x	x
^{57}Co	271.8	Spallation of ^{63}Cu and ^{65}Cu	122 keV	x	x
^{54}Mn	312.2	"	above range	x	x
^{68}Ge	271.0	Neutron capture on ^{67}Ge	10.3 keV, 1.3 keV, 0.16 keV	x	x
^{68}Ga	0.05	Decay of ^{68}Ge	9.7 keV, 1.2 keV	x	x
^{65}Zn	244.0	Neutron capture on ^{64}Zn	8.9 keV, 1.1 keV	x	x
^{3}H	4493.9	Spallation of Ge nuclei			x
^{55}Fe	1002.7	Spallation of ^{56}Fe		x	

originating from neutron activation of steel structures in the reactor building (see Section 3.2.1 for a more detailed summary). Because of this, extreme cleanliness and attention is required, when setting up and building the experiments, to ensure that none of these contaminations find their way into the experiment or onto the detectors. Lastly, the opening of the reactor vessel during reactor outage and maintenance releases small quantities of several radioactive gases, which can diffuse into the shield of the experiment, similarly to radon. They include ^{137}Xe, ^{85}Kr, and ^{3}H, and are also reduced by the radon protection system mentioned above.

2.4.2 Shield setup

Figure 2.18 shows the shield that is used in the CONUS+ experiment. It is built in an onion-like structure. consisting of several different layers, and is based on the shield design of its predecessor, the CONUS experiment [68]. The shield features four layers of lead with a thickness of 5 cm each, two layers of borated polyethylene, and two layers of plastic scintillator plates, used as an active muon veto as described in the previous section. The inclusion

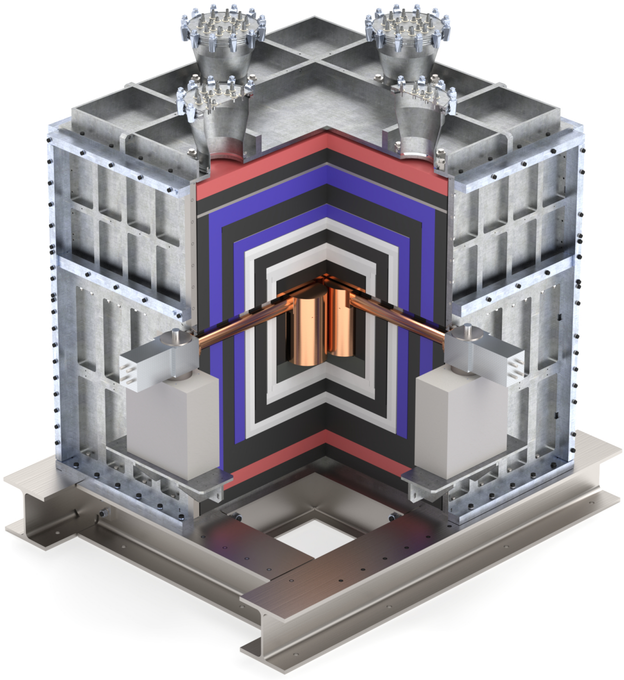

Figure 2.18. Shield design of the CONUS+ experiment, consisting of layers of stainless steel (silver), polyethylene (red), borated polyethylene (white) and lead (black). Additionally, two layers of plastic scintillator (blue) with integrated PMTs act as a double muon veto system. In the centre, the four HPGe detectors are embedded, housed in ultra low background copper cryostats. The inner detector chamber is continuously flushed with radon-free air.

of a second muon veto layer is the main difference between this shield configuration and that of the CONUS experiment, as the latter featured an additional lead layer in its place. This change was performed due to the smaller overburden of the CONUS+ experiment (7.4 m w.e. compared to 24 m w.e.) resulting in a muon flux that is approximately 2.6 times higher than for CONUS [5]. As the veto efficiency in the CONUS experiment, meaning the percentage of muons that were correctly tagged by the veto system, was found to be 97 % [12], such an increase in muon flux would lead to greatly increased background levels for CONUS+. A second muon veto layer mitigates this effect and it was shown in a dedicated study [69], that the inclusion of a second veto layer can increase the tagging efficiency to up to 99 %. Section 3.4 will feature a detailed discussion of the muon veto efficiency reached in CONUS+. The time window that was chosen for the application of the muon veto cut in run 1 of the CONUS+ experiment was 450 μs. The impact of electromagnetic showers induced by muons is typically expected to be in the order of 160μs, however the longer window was chosen to also mitigate effects from delayed muon-induced neutrons. A second advantage of the inclusion of a second muon veto layer is the reduction of high-Z materials (lead) in the

CONUS+ shield, which reduces the amount of neutrons induced by muons passing through the shield. In the thesis cited above, it was also shown that the reduced lead thickness in the new CONUS+ shield (20 cm compared to 25 cm before) is sufficient in shielding against the external γ radiation in the CONUS+ room. Additionally, the plastic scintillator used in the muon veto system contains a high amount of hydrogen, which is effective in thermalising and shielding neutrons.

The lead that is used in the shield increases in radiopurity towards the centre. The innermost layer is made from a mixture of old lead from the Freiburg Minster and refurbished lead bricks from other low background experiments. Their ^{210}Pb content was extensively measured before the installation of the CONUS experiment in Brokdorf in 2018 and was found to be below 1.7 Bq/kg on average [12]. This amounts to a ^{210}Pb content of approximately 1.4 Bq/kg in 2023, when the CONUS+ experiment was installed.

The layers of borated polyethylene between the lead layers have a boron content of 3 % relative to natural boron equivalent and the alternating placement of lead and PE was chosen to effectively moderate the neutrons induced by muons in the lead. The whole shield is encapsulated in a steel cage, which allows the shield and detector chamber to be flushed with radon-free air. This air is taken from eight 300 b air bottles stored next to the shield and guided into the shield through tubes. The bottles are exchanged every two weeks and a new set of bottles is required to have been stored for at least four weeks, allowing the radon inside of them to decay fully. Figure 2.19 shows the background suppression capabilities of the old CONUS shield setup in the KBR power plant. It can be seen that the ”passive” shield, referring to the shield without the muon-veto system, suppresses the background level by three orders of magnitude, while the addition of the muon veto adds another order of magnitude. Due to the almost identical shield setup of the CONUS+ experiment, similar background suppression levels can be expected, with a slight decrease in the effectiveness of the passive shielding, due to the omission of one lead layer, and an overall increase of the effect of the muon veto.

2.5 Additional infrastructure and data pipeline

Inside of the CONUS+ room at KKL, two desktop PCs and a Raspberry Pi are located, which handle all of the data taking of the experiment. One of the PCs, the ”DAQ PC” solely handles the germanium data taking and runs the ComPASS software that is used to control the DAQ systems. The other desktop PC, the ”environmental PC”, and the Raspberry Pi handle a number of other smaller measurements inside of the room that monitor environmental parameters, which are crucial for the stability of the germanium data taking. These measurements are combined in a dedicated slow control database, where they can be con-

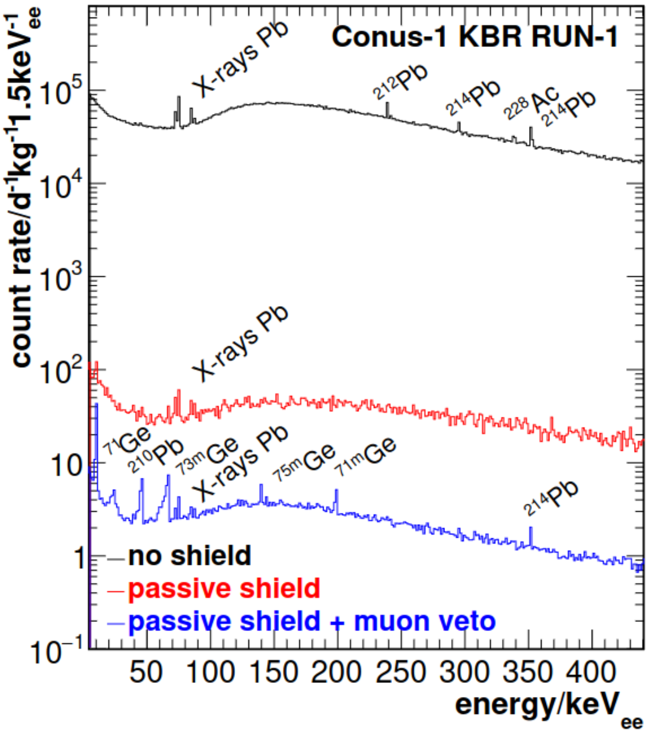

Figure 2.19. Background suppression capability of the shield setup used in the CONUS experiment in Brokdorf, measured for one HPGe detector (C1) [12]. ”Passive shield” refers to the shield setup without active muon veto. For the CONUS+ experiment one lead layer was replaced with an additional muon veto, thereby slightly decreasing the suppression of the passive shielding, while increasing the capability of the muon veto system.

tinuously monitored. More details on the stability criteria and the resulting live time of the experiment will follow in Section 4 .

The slow control database includes four temperature measurements inside the CONUS+ room. The temperature sensors are located close to the four preamplifiers of the germanium detectors, since varying or too high temperatures can induce electronic noise in this component. The temperature in the room is cooled with an AC system provided by KKL. This is necessary, due to the large heat output of the experimental setup which would heat up the room considerably without a dedicated AC and lead to power fluctuations in the cryocoolers, which could in turn induce noise in the detectors. Another aspect of the slow control system is the monitoring of the cryocooler output. This includes the values for the cryocooler power, the temperature inside the cryocooler and the achieved coldtip temperature, i.e. the temperature inside the cryostat. Furthermore, the trigger rates of the germanium measurement, the TRP reset, and the PMTs in the muon veto system are measured. This allows a quick response in the event that one of these systems fails. The radon concentration inside the room is also monitored with the use of a commercial radon detector. Lastly, a bare ^{3}He neutron counter is included in the CONUS+ setup and continuously measures the flux of thermal neutrons inside of the room.

The environmental PC and the DAQ PC are part of a local network inside of the KKL power plant. This network connects the two PCs to a server located outside of the containment area in another building on the KKL site and is completely seperated from all other networks inside the power plant. The server hosts the slow control database and serves as permanent storage for all of the data taken in the CONUS+ experiment. The environmental data is continuously pushed to this server, while the germanium data is copied once every hour, after which it is deleted off of the DAQ PC, due to limited storage on this PC. The server is connected through a VPN to the MPIK server cluster in Heidelberg and the data on the server is copied to the cluster once per day, which allows real time analysis of the data in Heidelberg. Through the VPN connection, the local network at KKL can also be directly accessed from MPIK and the DAQ and environmental PCs can be controlled through a Remote Desktop software. In this way, members of the collaboration can also access a webcam, which is connected to the environmental PC, allowing them an overview of the experimental site at all times.

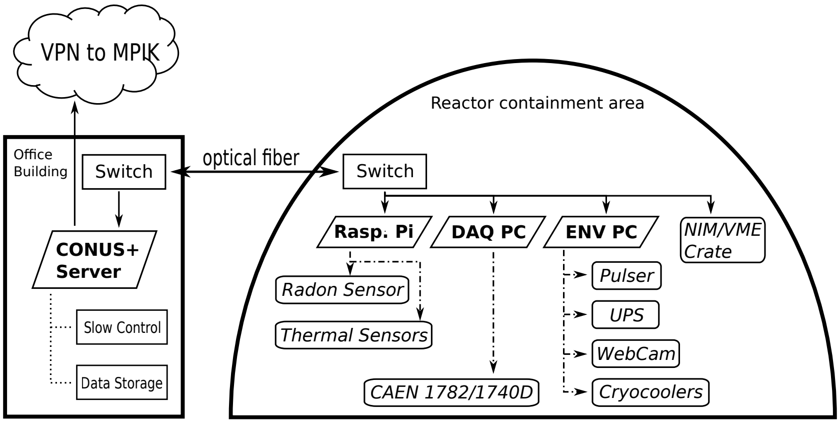

Figure 2.20. Schematic of the slow control systems and overall infrastructure of the CONUS+ experiment. A local network connects the CONUS+ server to all data taking devices in the CONUS+ room (inside the containment area) through the Raspberry Pi, the two PCs and the NIM/VME crates. The server is connected to MPIK through a VPN.

Chapter 3

Background Model

The following sections detail the first focal point of this work, which is the full decomposition of the background spectra of the three detectors used in the analysis of run 1 of the CONUS+ experiment. First, the general motivation for a detailed background model will be given and the background characterisation campaign prior to the installation of the experiment at the KKL power plant will be discussed. Next, the Monte Carlo framework and general approach to simulations will be presented. Lastly, a full overview of each component in the background, including all of the necessary inputs as well as the resulting impact on the background of the detectors, will be given, which results in a complete background model for each detector. This model will be compared to the measured spectra from the experiment.

3.1 Motivation

Complete knowledge and understanding of the background spectrum of a particle physics experiment, i.e. all of the measured events which do not originate from the desired signal, is crucial to its success. The CONUS+ experiment searches for the signature of the CEνNS interaction, which is an exponentially rising signal at very low energies below 300 eV. As explained in 1, the CEνNS interaction has a large cross-section compared to other neutrino channels, however the overall expected count rate is still very low and the total spectrum of the experiment is dominated by background sources. Understanding and modelling of these components allows for the distinction between them and the desired CEνNS signature. Quantitatively, this is taken into account in the analysis of the data, which uses a log likelihood approach to fit a model μ of the data to the actual measured spectra (see Section 4.6). This model describes the contents of each measurement bin as a sum of the expected background in this bin b_i and the expected CEνNS signal in this bin s_i:

$$\mu_i = N_b \cdot b_i + N_s \cdot s_i, \tag{3.1}$$

where N_b and N_s are some normalisation terms for each contribution. The shape of the expected signal s_i is given by theory, taking into account the neutrino flux from the reactor, the CEνNS cross section and the quenching effect (see Section 4.5). A correct background model b_i for each bin and knowledge of the normalisation factor N_b therefore ensure that the fit is able to correctly fit the factor N_s, which corresponds to the signal strength and the amount of CEνNS counts in the data.

The CONUS+ experiment has the added benefit of being able to measure around one month of reactor off data each year, during the yearly reactor maintenance period. Since the neutrinos that produce the CEνNS interaction are produced in β-decays inside the reactor and the β-emitting isotopes, which originate from neutron-induced spallation, have short half-lives, no signal is expected during these reactor off periods. The measured spectra during this time are therefore used as background-only measurements in the analysis and are fitted at the same time with a separate term in the log likelihood function. The model μ_{off} used in this term only consists of the background contributions:

$$\mu_{off,i} = N_{b,off} \cdot b_i. \tag{3.2}$$

In this way, the reactor off measurement can be used to verify the credibility of the background model also in the region of interest, where a significant contribution from the CEνNS signal to the spectrum is expected in the reactor on measurement.

3.2 Background characterisation of the CONUS+ location

Prior to the movement of the CONUS+ setup to the KKL power plant in Leibstadt, Switzerland, an extensive background characterisation campaign took place from July 2022 to May 2023. The campaign was carried out by several members of the CONUS+ collaboration, including the author of this work, and the findings were evaluated and analysed by E. Sanchez. It was the goal of the campaign to ensure the suitability of the location for the CONUS+ experiment and to get a first idea of the backgrounds that should be expected. The full details can be found in [5], and the following sections go into the most important findings of the campaign. The measured backgrounds are an important input for the background simulations detailed in the upcoming chapters.

3.2.1 Gamma rays

The gamma background in room ZA28R027 , the CONUS+ room, in KKL was studied with the p-type coaxial HPGe detector CONRAD [70]. The detector is able to measure gamma ray backgrounds up to an energy of around 10 MeV. As described in Section 2.4.1, the spectrum below 2.7 MeV is expected to be dominated by naturally occurring radioisotopes. Above this energy only gamma lines from isotopes induced by neutron capture in surrounding materials in the reactor environment are expected.

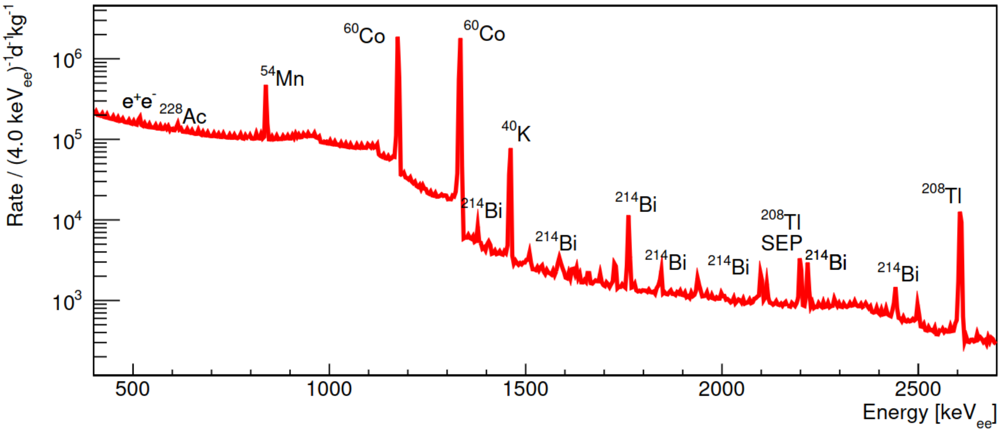

Figure 3.1. Gamma ray spectrum below 2.7 MeV measured with the CONRAD detector inside of the CONUS+ room at KKL with identification of the isotopes producing the peaks from [5]. The spectrum is dominated by naturally occurring isotopes. The most prominent contribution is from the decay of ^{60}Co. The spectrum also features a single escape peak (SEP) from ^{208}Tl, where a the γ-ray induces pair production, the produced electron and positron annihilate and one of the resulting 511 keV photons escapes the detector.

Figures 3.1 and 3.2 show the measured spectra inside the room. As expected, mainly lines from natural radioactivity are visible, such as lines from the decay of ^{214}Bi and ^{208}Tl from the uranium and thorium decay chain as well as from ^{40}K. Additionally, two very prominent peaks at 1173 and 1332 keV from the decay of ^{60}Co are visible in the spectrum. ^{60}Co is a synthetic radioisotope and does not occur naturally in significant amounts. In the context of a nuclear reactor, it is typically produced in steel structures in close proximity to the reactor core in a series of neutron captures and decays starting from stable iron isotopes. In the simplest case, starting from ^{58}Fe:

$$^{58}Fe + n \rightarrow\ ^{59}Fe$$
$$^{59}Fe \rightarrow\ ^{59}Co + e^- + \bar{\nu}_e$$
$$^{59}Co + n \rightarrow\ ^{60}Co$$

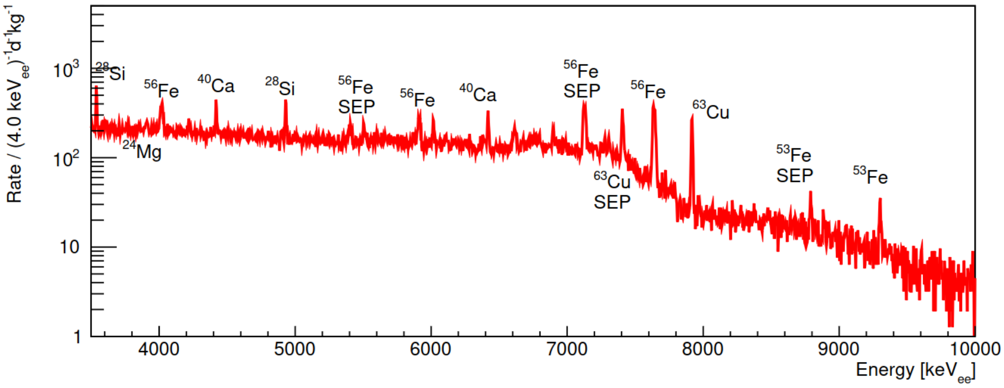

Figure 3.2. Gamma ray spectrum above 3.5 MeV measured with the CONRAD detector inside of the CONUS+ room at KKL with identification of the isotopes producing the peaks from [5]. The spectrum is dominated by isotopes that are induced from neutron capture of the reactor neutrons on the surrounding materials. The spectrum also features single escape peaks (SEP), where the gamma rays from the decay induce e^+e^- pair production and subsequent annihilation in the Ge crystal and one of the annihilation gammas escapes the crystal.

The high energy spectrum above 3.5 MeV, shown in Figure 3.2 is indeed dominated by radioisotopes induced by neutron capture in the materials surrounding the reactor core. The most prominent lines come from the decay of several iron isotopes produced by neutron capture in steel structures, similarly to the production of ^{60}Co. Additionally, several lines from neutron capture on ^{28}Si, the most abundant silicon isotope, and ^{40}Ca, the most abundant calcium isotope, can be found. Both are featured as components of the concrete structures in the reactor building. In general, the integrated count rate in the gamma spectrum above 3.5 MeV is quite low at a rate of 6 counts s^{-1} kg^{-1}, which is around 25 times lower than for the CONUS experiment at KBR [5]. The reason for this large reduction is mostly the absence of ^{15}N, which made up a large part of the high energy γ radiation for the CONUS experiment. This isotope is produced through neutron interactions with oxygen and is therefore present in the cooling cycle of a nuclear power plant, which in the case of CONUS was located close to the experimental setup. This is not the case in KKL. The reduction in high energy γ radiation also helped justify the removal of one of the lead layers of the shield which was replaced with a second muon veto layer as explained in Section 2.4.2.

The measurement with CONRAD gives a good overview of all of the gamma backgrounds that are present in the CONUS+ room. However, it is not able to distinguish the source of the gamma rays, especially the difference between radiation coming from the bulk volume of surrounding materials or radiation coming from surface contamination on these materials, for example in the form of dust particle. This latter source is of particular interest for the CONUS+ experiment since this dust can enter into the shield and detector chamber of the experiment when building up the experiment, opening the shield or handling critical components inside the room. For this reason a series of wipe tests was performed inside of the CONUS+ room, as well as at the location of CONUS in KBR prior to the deconstruction of the shield and the move to Leibstadt. The wipe tests at KBR were performed on the shield of the CONUS setup as well as inside of the opened detector chamber and the floor of the room in which CONUS was located. At KKL, the wipe tests before the installation of CONUS+ were performed at several points on the floor and walls of the CONUS+ room, as well as on the shield and inside the detector chamber after the installation, to check for potential cross contaminations introduced in the installation campaign. All wipe tests were performed with a water-soap mixture and covered an area of 100 cm^2. The tests were evaluated with the low background Ge spectrometers BRUNO and CORRADO at MPIK [71].

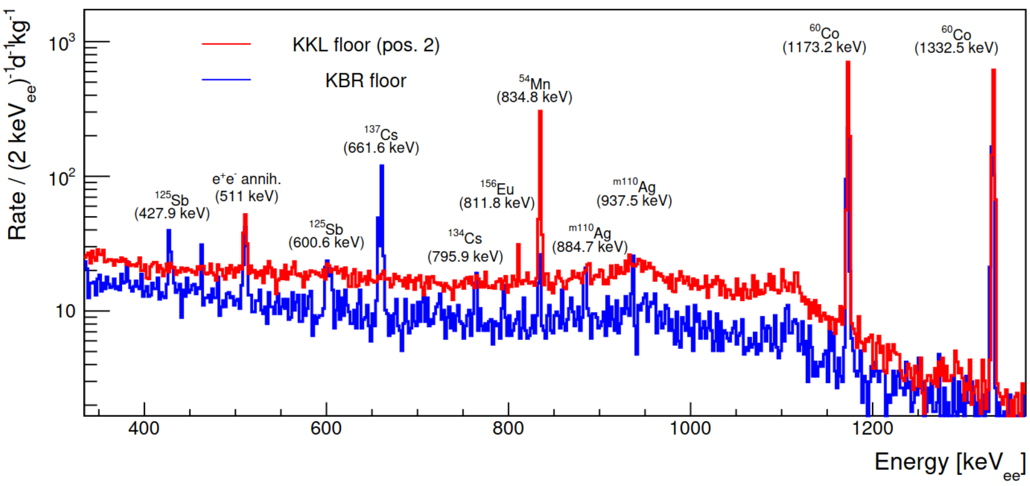

Figure 3.3. Energy spectra of two representative wipe tests taken at the CONUS and CONUS+ locations at KBR and KKL respectively. They were evaluated with the BRUNO Ge spectrometer at MPIK.

Figure 3.3 shows the result of these measurements for two representative wipe tests. The spectrum of one wipe test taken of the floor of the experimental site before the deconstruction of CONUS at KBR is shown in blue, while the red spectrum shows a wipe test taken of the floor in the CONUS+ room at KKL before the construction of CONUS+. It is apparent, that the CONUS+ experimental site features a larger amount of surface contaminations and is mainly dominated by ^{60}Co, which was already the defining feature of the low energy spectrum measured with the CONRAD detector in Figure 3.1. On the basis of these wipe tests, extreme care was taken to thoroughly clean the CONUS+ room before the installation of the experiment and large portions of the room were covered in plastic tarp during the actual operation. Additionally, all components of the shield close to the detectors and the

detectors themselves were wrapped in plastic foil during the transportation and up to the very last moment before their placement in the setup. These preparations proved to be successful as no hint of any surface contaminations is found in the data of any of the detectors.
Apart from the difference in the ^{60}Co abundance, significant differences are also found for ^{137}Cs, which was a prominent feature in the KBR spectrum and is missing at KKL, and ^{54}Mn, which is considerably more abundant at KKL. The larger ^{54}Mn peak can be explained in the same way as the previous ^{60}Co contamination, since ^{54}Mn is also produced from neutron interactions with steel parts of the reactor building. ^{137}Cs on the other hand is mainly produced as a fission product inside the fuel rods in the reactor core. Its measurement at KBR likely stemmed from the close proximity of the measurement to the cooling water system of the reactor.

3.2.2 Cosmic muons

As discussed in Section 2.4.1, cosmic ray muons are a prominent background source for shallow underground experiments like the CONUS+ experiment with its overburden of 7.4 m w.e. At such depths their impact is expected to be dominant without the use of a muon veto and even with the use of the veto system, they still play a major role.
For this reason, measurements of the muon flux were performed in the background characterisation campaign. The measurement used a small liquid scintillator detector designed and assembled at MPIK, which allows to measure muons of up to 16 MeV. It consists of a small PTFE cell filled with 120 cm^3 of liquid scintillator and the scintillation light is read out with a photo-multiplier tube (PMT). The detector is shown in Figure 3.4. The measurement was performed during a reactor outage to exclude the impact of high energy γ radiation induced by neutron activation from the reactor.

Liquid scintillator detectors like the one used in this campaign are able to distinguish between nuclear and electronic recoils based on pulse shape discrimination. With this technique, fully detailed in [72], particle identification is possible. The full gate window for a signal from the liquid scintillator is 1 μs. Interactions from electronic recoils, like from muons or natural radioactivity, will lead to signals where the majority of the detected light (and therefore the collected charge) is measured at the beginning of the signal. Contrary to this, nuclear interactions, like from neutrons, will lead to an additional slower component and therefore a larger portion of the light being acquired later in the event. Hence, the ratio between the collected charge at the beginning of the event Q_{fast} and the total collected charge Q_{tot} is greater for electronic interactions than for nuclear interactions. With this, a new variable called F$_{40}$ can be defined as the ratio between the charge collected in the first 40 ns of the signal and the total charge collected in the full 1 μs window. Figure 3.5 shows

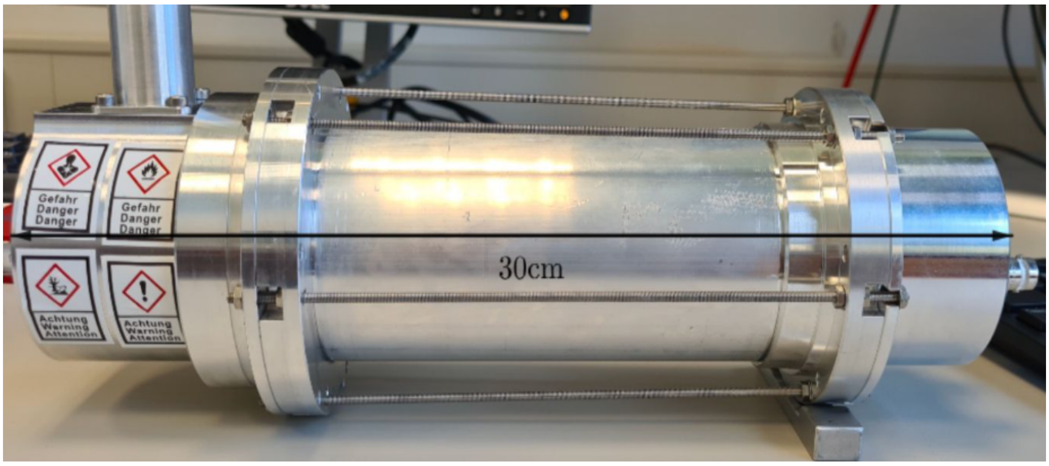

Figure 3.4. Liquid scintillator used for the measurement of the muon flux in the CONUS+ room. The detector is enclosed in an aluminium housing and connected to a CAEN V1725 analog-to-digital converter for data acquisition.

the distribution of this variable with respect to the total reconstructed energy of the event and three distinct populations can be identified. The first population at low F_{40} values comes from neutron interactions. The second population at high F_{40} values and energies below 2.7 MeV comes from natural radioactivity in the CONUS+ room. The third population at high F_{40} values and energies above 2.7 MeV are cosmic muons.
The measured muon spectrum is shown in Figure 3.6 and compared to a spectrum measured with the same detector above ground at MPIK. As MPIK and KKL are located at a very similar altitude of approximately 350 m w.e. the scaling factor between both spectra can be used to estimate the overburden in the CONUS+ room. A scaling factor of 1.9 is found, which is equivalent to an overburden of 7.4 m w.e. This value is consistent with the value expected from the structure of the reactor building (see Section 2.1). The muon flux in the room is found to be (107 ± 3) muons s^{-1} m^{-2} [5].

3.2.3 Neutrons

Neutron measurements at KKL were performed with the Extended Range Bonner Sphere Spectrometer (ERBSS) of the Paul Scherer Institut (PSI). It is based on [73] and consists of several thermal neutron sensors encased in polyethylene (or in one case Cu, referred to as ”modified sphere”) spheres with varying thicknesses. The thermal neutron sensors contain 2.3 b of ^{3}He. In the case that a neutron enters the sensor, in is captured by a helium atom and a proton and a triton (^{3}H), as well as 764 keV of energy, shared between both particles, are produced. The proton an triton drift under the influence of an applied electric field and ionise the surrounding high-pressure ^{3}He gas. The resulting ionisation electrons drift towards the anode where they produce a detectable current pulse. The different spheres

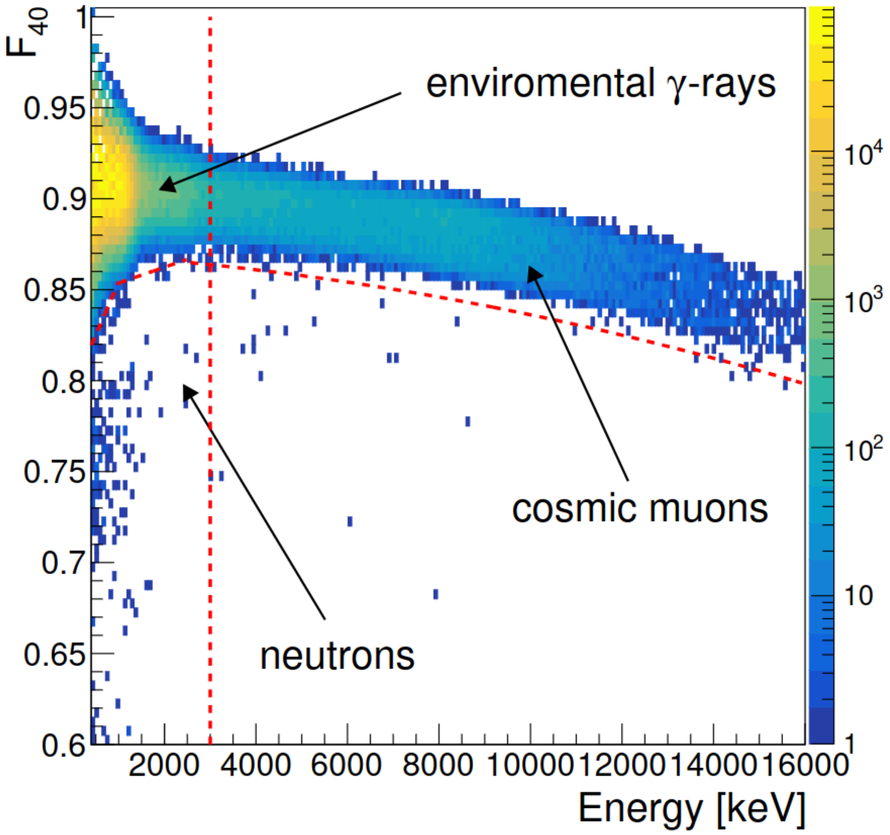

Figure 3.5. Distribution of F_{40} variable versus total reconstructed energy of the event measured in the CONUS+ room in one day. The combination of the F_{40} variable and energy allows for the distinction between three different populations of events: natural radioactivity, muons, and neutrons.

around the sensors allow for the moderation of faster neutrons, making them visible to the thermal neutron sensors. The thickness of the spheres approximately corresponds to the amount of energy that neutrons can lose when passing through the spheres and larger spheres are therefore more sensitive to faster and faster neutrons. These different sensitivities are quantified in response functions that have been acquired with Monte Carlo simulations and are shown in Figure 3.7. The data and count rates of the different Bonner spheres were evaluated using a Bayesian Parameter Estimation with a parametrised model [74] and the method was based on Monte Carlo simulations [75].

Neutrons during reactor on time

The count rates measured in the Bonner sphere arrays during reactor on times are shown in Figure 3.8. From these count rates and using the response functions of the spheres and the evaluation method described above, a neutron spectrum in the CONUS+ room can be derived. It is shown in Figure 3.9.

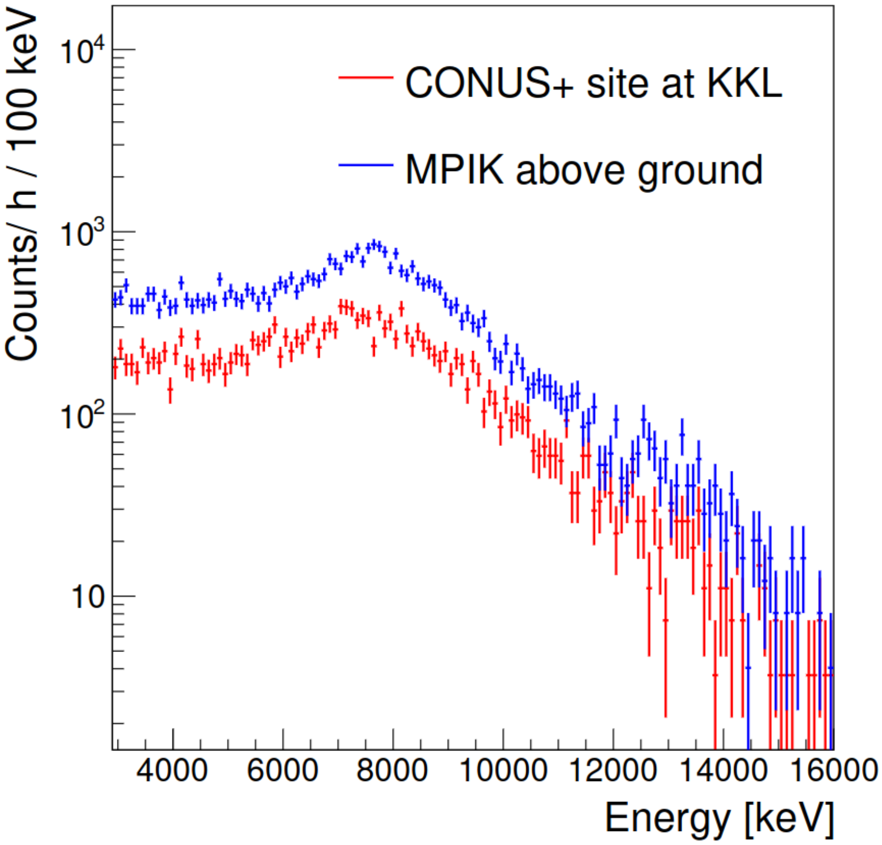

Figure 3.6. Muon energy spectra measured in the CONUS+ room at KKL and at MPIK above ground. The spectra share the same shape with a scaling factor of 1.9, which is equivalent to an overburden of 7.3 m w.e.. MPIK and KKL are located at a very similar altitude of approximately 350 m above sea level.

The spectrum is very similar in shape to that found in [12]. It is dominated by a peak of thermal neutrons in the sub-eV range and shows a steady decline towards higher energies with an additional very small peak at around 100 MeV from cosmogenic neutrons. The thermal peak and the neutrons with energies below 1 MeV generally originate from the reactor and are thermalised in the surrounding concrete walls of the reactor building. A total neutron flux of (262.3 ± 13.1) cm^{-2} (GW h)$^{-1}$ is measured. For better comparison with the reactor off neutron flux and other measurements, four energy regions in the neutron spectrum are defined: thermal neutrons $[1.0 \cdot 10^{-9}, 4.0 \cdot 10^{-7}]$ MeV, intermediate neutrons $[4.0 \cdot 10^{-7}, 0.1]$ MeV, fast neutrons [0.1, 20] MeV, and cascade neutrons [20, 1000] MeV. The fluxes in each energy region can be found in Table 3.1.

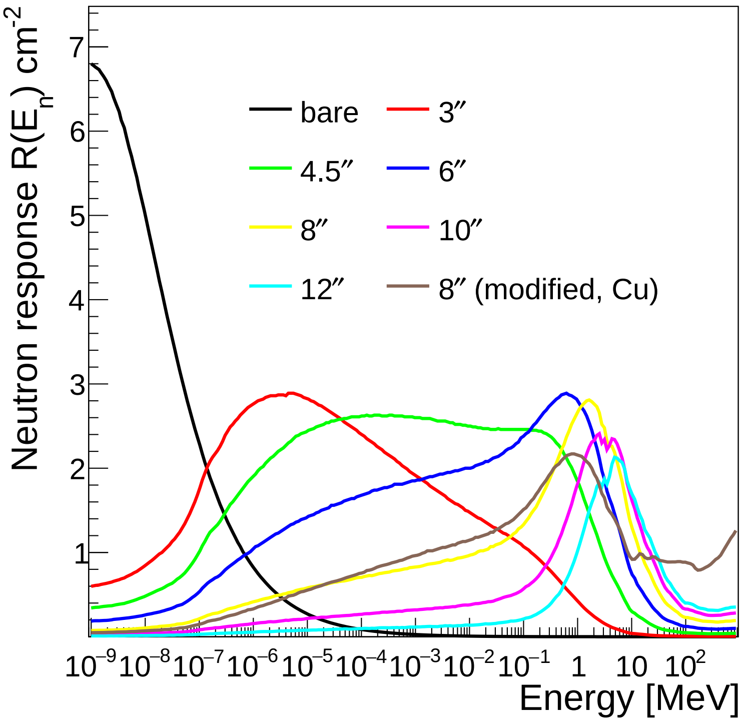

Figure 3.7. Response functions of the different Bonner spheres used in the measurement. The diameter of the spheres in inches is given, The brown line is the response function of an 8 inch sphere with an additional Cu shell.

Neutrons during reactor off time

The neutron measurement during reactor off was performed with a limited set of only four bonner spheres and one bare thermal neutron counter due to limited time and available space. The spheres that were used were the 3.5”, the 8” and the 12” sphere, as well as the modified 8” sphere and the bare counter. Additionally, the measurement was performed with all five detectors operating at the same time, placed approximately 30 cm from each other due to space constraints. The total measurement time was five days and the count rates can be found in Figure 3.10. As expected, the count rates are several orders of magnitude smaller

Table 3.1. Neutron fluxes in different energy regions. Thermal neutrons are by far the dominating part of the spectrum.

Energy region	ϕ cm^{-2} (GW h)$^{-1}$
thermal	195.7 ± 18.6
intermediate	62.4 ± 4.3
fast + cascade	4.2 ± 3.4

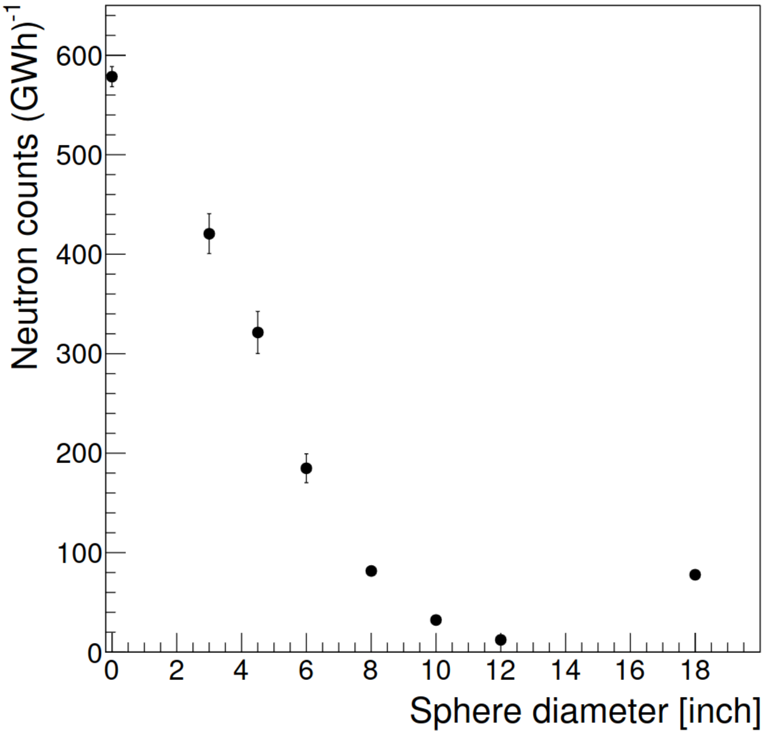

Figure 3.8. Neutron count rates in the individual Bonner spheres during reactor on as function of the sphere diameter. The rates are normalised to 1 GW h. 0 corresponds to the bare counter and 18” corresponds to the 8” modified sphere.

than in the reactor on measurement due to the absence of reactor neutrons. Nevertheless, the count rates are higher than the ones found in [12] due to the lower overburden, indicating the presence of cosmic neutrons in the room.

Unfortunately, due to the close proximity of the spheres to each other during the measurement, inducing possible backscattering between the spheres, and the short measurement time, combined with low count rates, no reliable neutron spectrum could be extracted from the bonner sphere measurement for reactor off. For this reason, a simulation-based approach was taken to generate neutron spectra in the room. In the simulations, a cosmic neutron spectrum from literature [11] taken at a comparable altitude to that of KKL was propagated through a model of the reactor building, as was previously done for other experiments [76, 77]. The resulting flux in the CONUS+ room can than later be taken as input for background simulations for the experiment. Section 3.5 will detail this approach and the results obtained in this way.

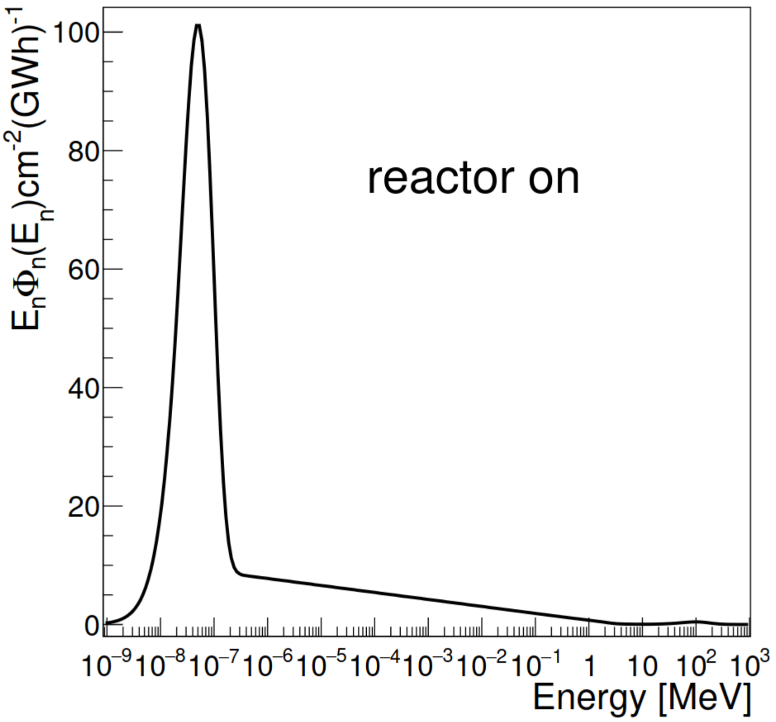

Figure 3.9. Energy distribution of neutrons in the CONUS+ room, acquired from the Bonner sphere measurement and normalised to the thermal power of the reactor.

3.3 Monte Carlo framework and approach

The Monte Carlo simulations to investigate the background sources of the CONUS+ experiment were performed with the Monte Carlo framework MaGe [78] based on Geant4 [79], [80], specifically version 10.4.3. MaGe was developed for the Majorana [81] and Gerda experiments [82], two low background experiments that searched for neutrinoless double beta decay, and as such was designed to simulate very similar low energy background sources to those present in the CONUS+ experiment. It uses the ”Livermore” physics models for electromagnetic processes and the ”Neutron High Precision Model NeutronHP” for neutron propagation. Additionally, production cuts are applied in the simulations to save computation time. MaGe provides three separate production cut realms and the simulations in this work use the ”DarkMatter” production cut realm, which is specifically tailored to high precision low energy simulations with its cuts of 5 μm and 0.5 μm for γ-rays and electrons respectively.

In Geant4, the detectors and shield of the experiment are built in as geometric models. In these models, the exact dimensions, material properties and placement of every component of the setup are specified. The simulated particles (primary particles) are started from a volume or surface that is specified in a macro file and can be located anywhere either inside or outside of the setup or in a specific part of the experiment. Typically, a very large number of

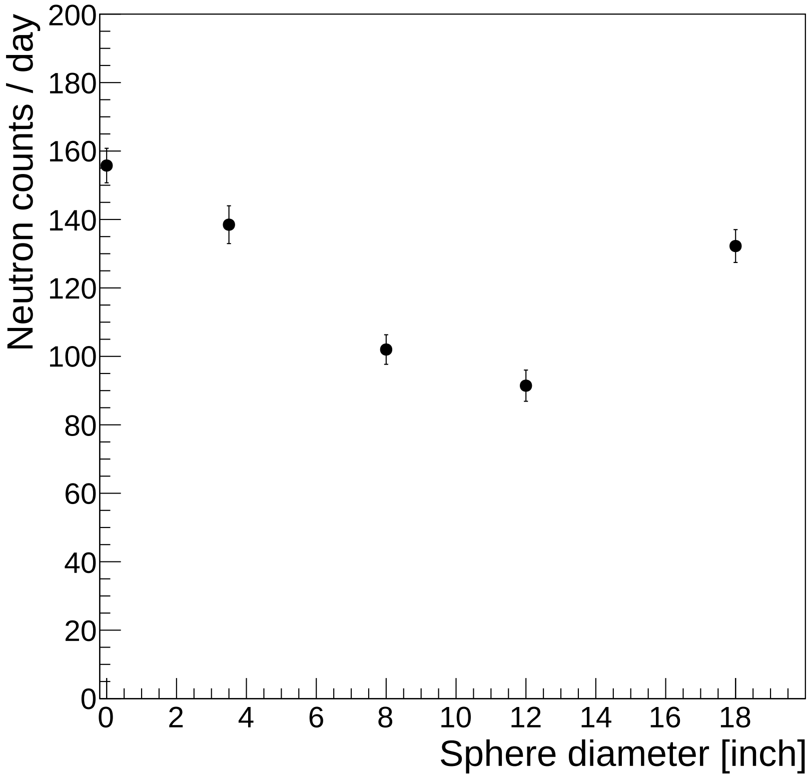

Figure 3.10. Neutron count rates in the individual Bonner spheres during reactor off as function of the sphere diameter. 0 corresponds to the bare counter and 18” corresponds to the 8” modified sphere.

primaries (on the order of 10^{10} particles) are started to accumulate a large number of statistics and their energy and angular distributions are provided in the aforementioned macro. The Germanium crystals of the CONUS+ experiment are the active detectors in the simulation and for each started primary (also called an event) a number of properties are stored as the result of the simulation. These include the energy depositions in the crystals, the type of particle responsible for the deposition, and the location of the deposition in the crystal.

The output of the simulations is saved as ROOT files [83] and further processed with a series of ROOT-based C++ scripts. In this post-processing routine, all energy depositions in one event are added up, which corresponds to the actual detected energy in the detector. Furthermore, nuclear quenching is applied to each energy deposition by neutrons and nuclei using the Lindhard model mentioned in Section 2.3.2 and charge collection inefficiencies in the crystal are considered. As described in Section 2.3.3, these inefficiencies occur for events happening in the transition layer of the detectors at the outside of the crystal. This is a thin layer in which the electric field in the crystal is weaker and not homogenous, which leads to the partial loss of charges created in interactions here. Therefore, the energy that is detected in the crystal for such events is lower than the actual energy of the interaction. In order to correct for this, the coordinates of every energy deposition in the crystal are checked in the post-processing and depositions inside of the TL are shifted to lower energies using a sigmoid-like function [47]. Due to the lower electric field in the TL, charges created here also have longer drift times to arrive at the point contact of the crystal. This leads to slower rise times of the pulses of these events, a fact that can be used for pulse shape discrimination (PSD), as background sources like γ-rays have a higher probability to interact in the outer layers of the crystal compared to neutrinos which make up the signal of the CONUS+ experiment. This approach was employed in the final result of the CONUS experiment [53] and, as of the writing of this thesis, is currently being investigated for the CONUS+ experiment. In the last step of the post-processing routine, the resulting spectra of each background contribution are folded with a Gaussian to account for the energy resolution of the detectors. The width of this Gaussian consists of the pulser resolutions listed in Table 2.1 and the energy dependent statistical uncertainty σ_{eh} (Formula 2.5). Here, a Fano factor of F = 0.11 is used.

After the results of the simulations are obtained, they are combined in the full background model B$_{total}$, which is the sum of all individual background components b$_i$. The different components can have varying impacts on the four detectors inside the CONUS+ shield (C2, C3, C4 and C5) and can also vary between reactor on and reactor off measurement , which results in a separate model for every detector and measurement phase:

$$B_{total,det}^{ON/OFF} = \sum N_{b_{i,det}^{ON/OFF}} \cdot b_{i,det}^{ON/OFF} \tag{3.3}$$

The normalisation factors N_{b_i} are determined in a number of different ways depending on the type of background that is being investigated. For cosmic rays like neutrons and muons the flux inside of the CONUS+ room is used, for certain material contaminations, like Pb^{210} in the lead bricks of the shield, values from previous screening measurements are relied on, and for the background contributions responsible for visible peaks in the CONUS+ Ge spectra, like radon and Ge^{68}, the simulation results are scaled to the appropriate line height. It is important to note, that all normalisations and general information about the composition of the background model is obtained without using data from the energy region below 400 eV in reactor on data. This is because the CEνNS signal is expected to be measured in this energy region. Blinding this region is therefore important to ensure the absence of biases in the construction of the background model.

The following sections will discuss every background source that was investigated for the CONUS+ experiment, the inputs used for their simulations and the resulting impact on the background spectra of CONUS+. The background sources will first be discussed in the context of reactor on data taking. A dedicated section will explain the experimental differences between reactor on and off measurements and how these impact the background model. Lastly, the full background model for both measurement configurations and all detectors will be presented. The specific results for each background component will mostly be shown compared to the spectrum of the C5 detector and for the specific case of C5. In the case where the background components of the specific sources are significantly different for the C2 and C3 detectors, the spectra will be shown in Appendix A.

3.4 Muon-induced background

Based on the muons flux measurements detailed in Section 3.2.2, especially Figure 3.6, the overburden of the CONUS+ experiment was found to be (7.4 $\pm$ 0.1) m w.e. This corresponds to a muon flux of (107 $\pm$ 3) s^{-1} m^{-2}. The value for the overburden can be used to get an energy distribution of the muons in the room, based on descriptions of the cosmic muon flux in shallow underground laboratories from literature. In this work, the model by Reyna [84], which gives a parametrisation for the muon spectrum at sea level, is used. It is based on a model by Bugaev et al. [85] and expands it to all zenith angles θ and low energies. The model was tested previously in the context of the CONUS experiment [12] and other low background applications at the MPIK [86]. To apply the model to shallow underground conditions at KKL, a shift of the mean muon energy is performed. Additionally, an altitude correction is applied to account for the location of KKL at 350 m above sea level. Details about the calculation of the spectrum can be found in [86]. The procedure also allows for the calculation of the angular distribution of the muons, which was found to be $I(\theta) \sim cos^2(\theta)$. The calculated energy spectrum for θ = 0 can be found in Figure 3.11.

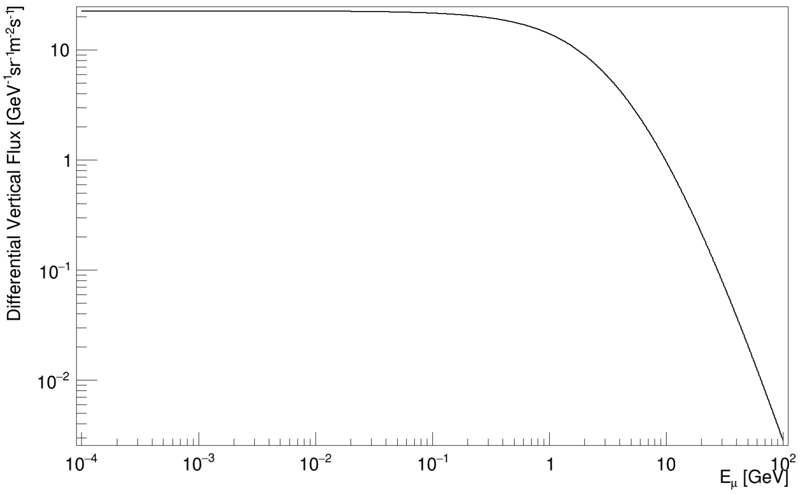

Figure 3.11. Differential vertical muon flux spectrum at an overburden of 7.4 m w.e. as in the CONUS+ room.

Taking this spectrum and the angular distribution of the muons as input, the muon flux in the room can be propagated through the CONUS+ shield and the impact on the background of the germanium detectors can be assessed. In the simulation, muons are started from five planar sources around the CONUS+ shield, which are placed at the positions of the walls and the ceiling of the CONUS+ room and have their dimensions. Muons and antimuons are simulated and the results have to be normalised to the muon charge ratio discussed in Section 2.4.1. For each ”wall”, 10^9 muons of both charges respectively are started, leading to a total of 10^{10} particles in the simulations. The obtained energy spectrum in the four CONUS+ detectors is normalised to the aforementioned measured muon flux in the room, i.e. to the number of muons that are expected to pass through each ”wall” in one day.

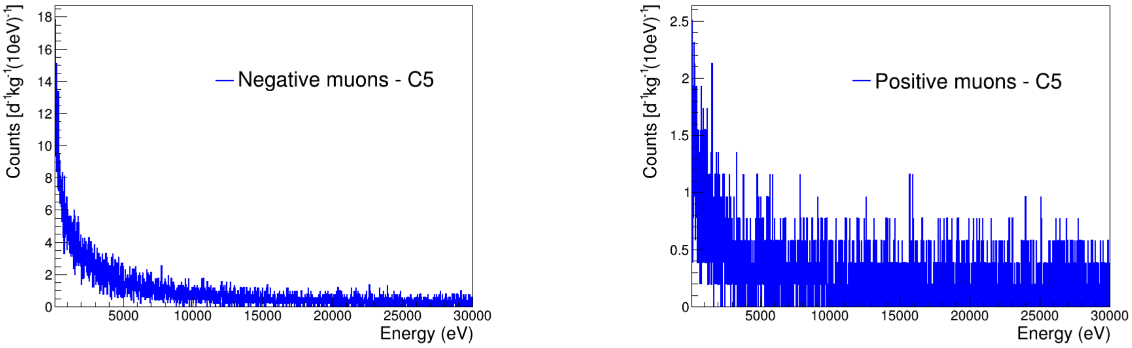

Figure 3.12. Simulated spectrum of the muon-induced background in the C5 detector without application of the muon veto. The left plot shows the background induced by negative muons, while the right plot shows positive muons.

Figure 3.12 shows the muon-induced background spectrum for the C5 detector obtained in the simulations. Due to the close proximity of the detectors to each other, all detectors share the same spectrum. It can be seen, that the impact of the negative muons is considerably higher than that of the positive muons. This is due to the ability of negative muons to be captured by atomic nuclei which is especially relevant for high Z materials like the lead in the CONUS+ shield. This capture produces secondary radiation, like neutrons, electrons or gammas, that propagate further through the shield and are measured in the germanium detectors.

As the spectra of the CONUS+ detectors are dominated by muonic background without the application of the muon veto, a comparison of the sum of the spectra in Figure 3.12 and data taken in one of the detectors in run 1 without applied veto can be used to check the validity of the simulations (see Figure 3.13). Very good agreement between both spectra is found, indicating the correctness of the approach.

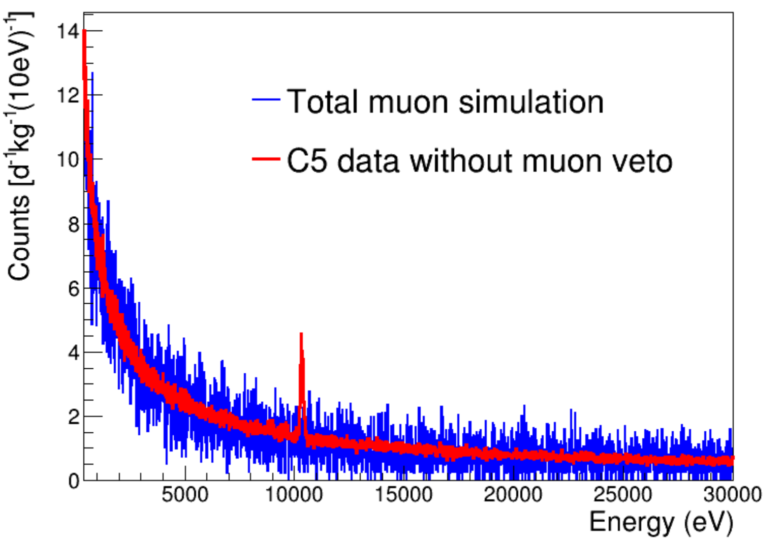

Figure 3.13. Comparison of the total simulated muon background spectrum and data taken by the C5 detector in run 1 without the application of the muon veto from 0.4 to 30 keV. Very good agreement is found. At 10.3 keV the gamma line from the decay of $^{68/71}$Ge can be seen in the data.

3.4.1 Muon veto and application to simulations

As described in Section 2.4.1 and 2.4.2, the CONUS+ experiment employs two separate layers of plastic scintillators operating as a muon veto system. The system triggers on muons or (high-energy gammas) that pass through it and deposit enough energy above a certain defined energy threshold in the plastic scintillators, which are read out with PMTs. This enables the use of a muon veto cut, where all events in the germanium happening within 450 μs after a triggered event are removed. This is vital for the background mitigation of the experiment, since the background is completely dominated by muons otherwise, as was shown in the previous section.

The background model for the four detectors must therefore also feature this cut to accurately describe the data after its application. For this work, in a first step, the efficiency of the cut in removing muon events is modelled by applying a constant reduction factor to the simulation results in Figure 3.13, as was previously validated in [12]. An indication for the value of this factor can be extracted by looking at the background reduction that is achieved by using the muon veto cut on the CONUS+ data.

Figure 3.14 shows the data collected by the C5 detector during run 1 with and without the applied muon veto cut. A clear and large reduction of the event rate in the detector can be observed, indicating again the dominance of the muon-induced events on the overall background. At the same time, it can be seen that the intrinsic γ lines in the spectrum, like

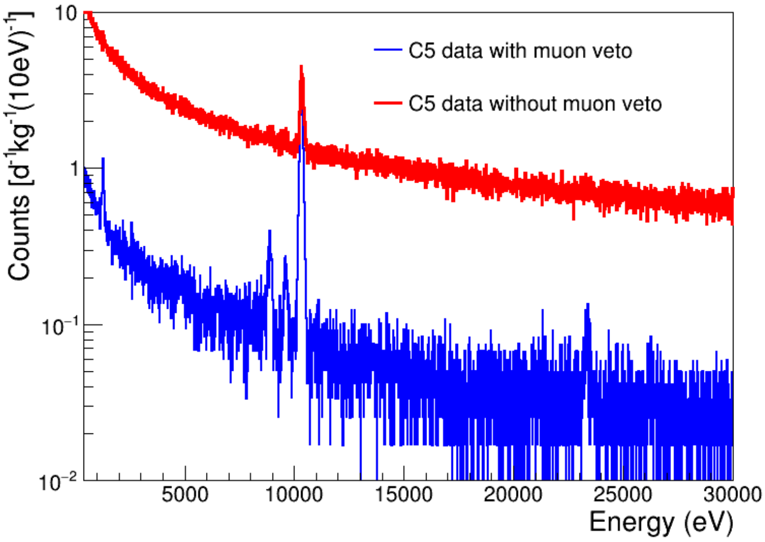

Figure 3.14. Comparison of C5 run 1 data with and without the applied muon veto cut.

the 10.4 keV $^{68/71}$Ge line are net reduced by the veto, which indicates the proper function of the system.

Table 3.2. Background reduction in the C5 detector with the muon veto cut in different energy regions. Count rates are given without error, since they are only used to get a first approximation of the muon veto cut efficiency

Energy region	Counts without veto [d^{-1} kg^{-1}]	Counts with veto [d^{-1} kg^{-1}]	Ratio [%]
(0.4 - 1) keV	562.3 ± 2	43.5 ± 1	7.7
(2 - 8) keV	1575.5 ± 3	103.1 ± 1	6.5
(15 - 30) keV	1106.7 ± 3	53.7 ± 1	4.9

Table 3.2 lists the count rates that were measured in three different energy regions in C5. It can be seen, that a consistent background reduction of over 92 % is achieved in all regions. It is also noticeable, that the background reduction is larger for higher energies, indicating a larger influence of muon-induced events in these regions. However, the background reduction cannot be directly equated with the efficiency of the muon veto cut, since the remaining background after the cut is comprised of different background sources. Therefore, we can conclude that the muon veto cut efficiency, the factor which has to be applied to the muon simulations, must at least be 92 %.

For the overall muon veto efficiency in the full background model, an efficiency of 99 % for all energies above 15 keV is estimated. This is validated by the overall agreement of the background model with the data in all detectors (see Section 3.14), as well as by the studies

carried out prior to the installation of CONUS+ in [69].
At energies below 15 keV, corrections to the muon veto cut efficiency have to be applied. These corrections come from an overall inefficiency in the tagging ability of the muon veto due to the structure of the CONUS+ shield. As detailed in Section 2.4.2, both plastic scintillator layers that act as the muon veto system are located inside of the shield. The outer veto is surrounded by by a 5 cm layer of lead and the outer steel support structure. This placement was chosen to avoid the constant triggering of the muon veto system due to the influence of high-energy gammas (see Section 3.2.1), which would lead to the accumulation of a large amount of dead time. However, with the current design is is possible that an incoming muon passes through the very outer layer of the shield, without ever passing through one of the muon veto layers (see Figure 3.15). Such muons can still interact within the outer shield and induce electromagnetic showers, which then propagate through the shield and induce events inside of the germanium detectors. If these showers do not deposit enough energy inside of the plastic scintillator layers, the veto system will not trigger although the Ge detectors registered muon-induced events, thus inducing a tagging inefficiency.

Figure 3.15. Illustration of the origin of the muon veto tagging inefficiency. An incoming muon passes through the outer layers of the shield without passing through the outer muon veto layer. In the shield, it induces an electromagnetic shower, which propagates through the shield and induces events in the Ge detectors.

This effect was studied in the simulations by tagging the primary muons that never cross one of the plastic scintillator layers and registering their energy depositions inside of the detectors. Figure 3.16 shows the results of this simulation. It can be seen that at very low energies below 1000 eV, a majority of the muon-induced events inside the germanium originate from muons that never cross any of the plastic scintillator plates of the shield. The effect generally increases towards lower energies. In the energy region between 160 and 400 eV, which is the critical part of the region of interest for CONUS+, approximately 81 % of muon-induced events come from events without a tagged muon. An adjustment of the muon veto efficiency for these energies is therefore critical.
In order to quantify the effect in a simplified way and convert it into a factor that can be

applied to the simulations, the ratio of the two plots in Figure 3.16 is studied. Computing this ratio between the spectrum of the muon-induced events with no tagged muon and the spectrum of muon-induced events with a tagged muon, gives a measure to the percentage of the total muon-induced spectrum which is caused by untagged muons (see left plot in Figure 3.17). The inefficiency in the muon veto must be proportional to this ratio. It is therefore fitted with a polynomial function of fifth order below 15 keV, where the inefficiency starts to become noticeable. The resulting fit is then normalised such that its value at 15 keV corresponds to 0.01. The values of the fit below 15 keV are than taken to be the inverse muon veto efficiency:

$$\text{Muon veto efficiency}(E) = 1 - \text{Fit Value}(E)_{\text{Normalised}} \tag{3.4}$$

In this way, it can be assured that for all energies above 15 keV an efficiency of 99 % is considered, while below 15 keV the tagging inefficiency is taken into account.

Figure 3.17 shows the result of the fit and the muon veto cut efficiency that is obtained in this way. For very low energies below 400 eV, it drops to 96.5 %. This value is still acceptable for the CONUS+ experiment and was also approximately the value that was found for the muon veto efficiency in its predecessor experiment CONUS [12]. With these values an overall good agreement in the background model of all detectors can be found as will be shown in Section 3.14.

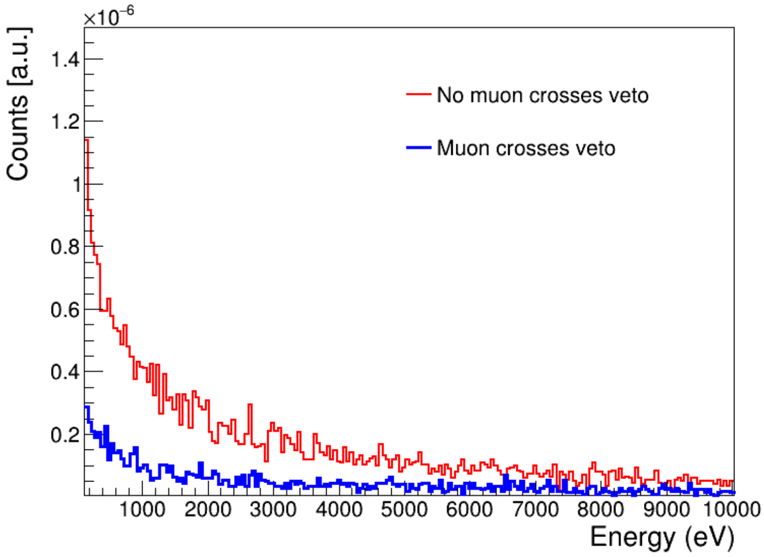

Figure 3.16. Simulated spectrum of muon-induced events from muons that do not cross a muon veto layer (red) and from muons that cross a muon veto layer (blue). At low energies below 15 keV, it can be seen that most of the events originate from muons that do not cross a plastic scintillator plate. These events are not triggered in the veto system and therefore induce an inefficiency at low energies.

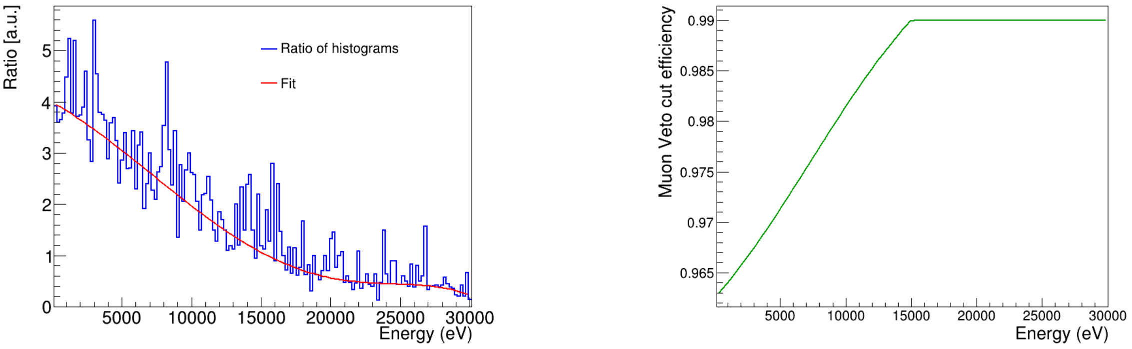

Figure 3.17. Left: Polynomial fit to the ratio of the spectrum of muon-induced events with no tagged muon to the spectrum of muon-induced events with a tagged muon. Right: Resulting muon veto efficiency. For very low energies the efficiency drops to 96.5 %

Figure 3.18 shows the muon simulation result with the applied fitted muon veto efficiency from Figure 3.17. The resulting spectrum is approximately flat in the energy range between 5 and 30 keV and features an exponential rise towards low energies. The reason for this exponential rise becomes obvious when taking a closer look at the types of particles that cause energy depositions in the germanium crystals in the muon simulations. For this, the muon simulation result is split into two parts, shown in Figure 3.19, one hadronic part, where energy depositions in the crystal come from neutrons induced by muons passing through the high-Z material of the shield, and an electromagnetic part, consisting of energy depositions from electrons and photons. The figure shows, that at very low energies, especially in the region of interest for the CEνNS, the hadronic component of the muon spectrum is dominant. At higher energies the elctromagnetic component of the spectrum increases, which will be discussed in more detail in the next section.

Overall, the background contribution from cosmic muons is one of the dominant background sources in the ROI of the CONUS+ experiment. This is shown in Table 3.3, which lists the contributions in the energy range from 400 to 1000 eV (partially in the ROI) and compares it to the overall background rate here after the application of the muon veto cut. The error on these values stems from the uncertainty of the overall muon flux in the room, which mainly comes from uncertainties in the exact overburden of the room. These were evaluated by using slightly different values for the overburden in the calculation of the flux from [84].

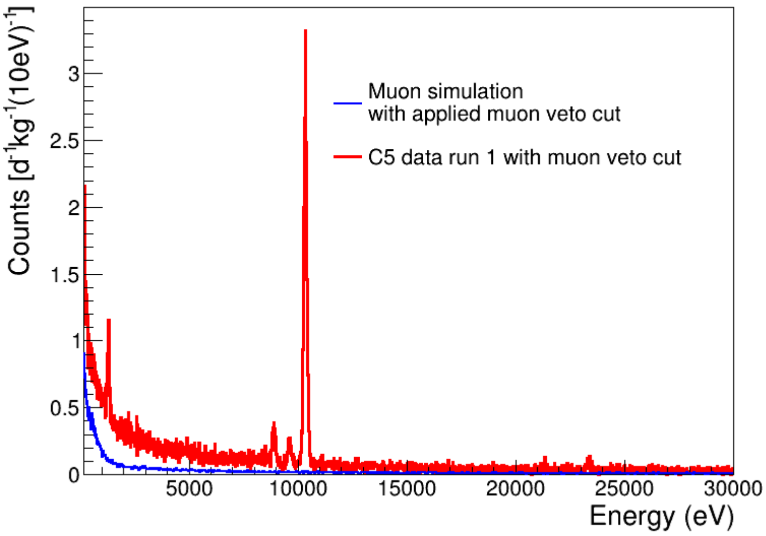

Figure 3.18. Muon simulation result with the applied muon veto efficiency from Figure 3.17 compared to the data taken with the C5 detector in run 1. In the shown energy range the muon spectrum is flat at higher energies and rises exponentially towards low energies. This rise is due to the presence of neutrons that are induced by the muons in the high-Z materials of the CONUS+ shield.

3.4.2 Efficiency correction of the High E channels with muon simulations

Up to this point, only data taken in the low energy channels of the CONUS+ experiment, ranging from 0 to 30 keV, were considered. However, as mentioned in Section 2.3.3, the experimental setup employed in Leibstadt is also able to measure germanium data with energies over 30 keV, in principle reaching energies of up to a few hundred keV. The problem with this data, is that large efficiency losses were observed for all four detectors in these channels, which can be seen from Figure 3.20. The loss of efficiency is especially apparent when comparing the data taken in these channels without applied muon veto cut to the result of the muon simulations from Figure 3.12 in Figure 3.21. The data without applied muon veto cut is almost 100 % made up of muon-induced events, and the simulation result should therefore describe the data well, as was previously found for the CONUS experiment (see [12]). The comparison shows good agreement up to energies of approximately 50 keV, but significant efficiency loss above, which increases towards higher energies. The reason for this loss of efficiency is likely due the dynamic range of the preamplifier. Events with high energies lead to large pulses above the baseline of the preamplifier output. If these pulses are too high, the end of the dynamic range of the preamplifier is reached, leading to saturation and the reset via the TRP described in Section 2.3.3. As mentioned previously,

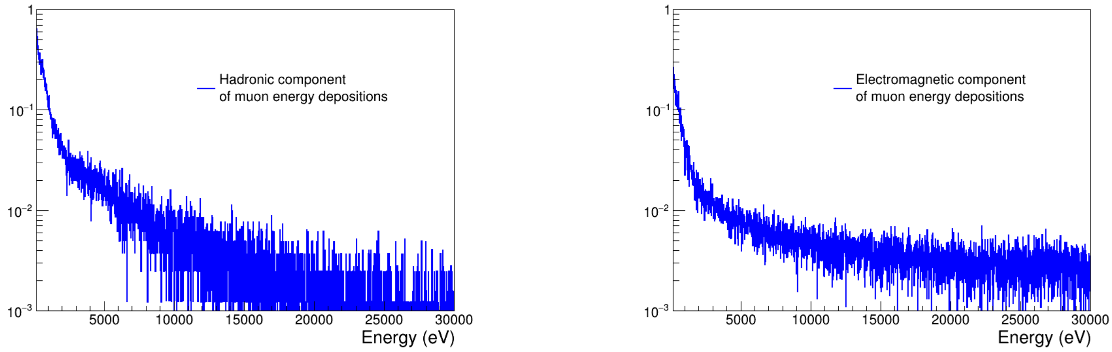

Figure 3.19. Muon simulation result split into hadronic (left) and electromagnetic (right) component. The distinction is made by the type of particle directly responsible for the energy deposition in the detector.

Table 3.3. Contribution to the background count rates in the three detectors from muons in the energy region from 400 to 1000 eV. The slightly different count rates for the muon contribution originate from different dead layer thicknesses between the detectors. The difference in the percentages of the total background in each detector arise from the presence of different other background sources depending on the detector.

Detector	Count rate in [400, 1000] eV (d^{-1} kg^{-1})	Percentage of total background (%)
C5	15.2 ± 0.3	38.4 ± 0.7
C2	16.5 ± 0.3	31.5 ± 0.6
C3	16.5 ± 0.3	33.4 ± 0.6

the high energy channels are not the main data taking channels for the CONUS+ experiment (the CEνNS ROI is fully covered in the low energy channels) and are mainly used to gain additional information about the background composition of the data. As such the electronics of each detector (mainly preamplifier settings) have been optimised for the low energy channels. Investigations into the efficiency loss in the high energy channels are currently ongoing to fix this issue for upcoming runs.

For run 1, the efficiency loss is corrected using the muon simulation directly. It is known that the data taken in the high energy channels without application of the muon veto cut should follow the muon simulations. Therefore, the result of the simulations is divided by the data bin-by-bin for each high energy channel. In this way, a correction factor can be assigned to each bin of the data, and the resulting correction function can be applied also to data with muon veto cut to mitigate the loss of efficiency. This method, while giving good results and producing workable spectra, is not an exact reproduction of the true high energy spectra, due to statistical fluctuations in the data (and the model) and the presence of gamma ray lines in the measured data. To decrease the impact of this effect, the obtained correction function is smoothed with a sufficiently large bin number.

The result of the correction can be seen in Figure 3.22. The spectra now follow the shape that is expected from studies in [12]. The goodness of the method can also be verified by the branching ratios of the three radon gamma lines in the spectrum, as will be done in Section 3.7. Unfortunately, the method introduces large uncertainties in the count rates for bins over 300 - 320 keV. This is due to the limited statistics in these bins in the original data sets (see Figure 3.20), which leads to large fluctuations in the correction function. As a result, only energies up to 300 keV are used for analysis and information about background sources in the following.

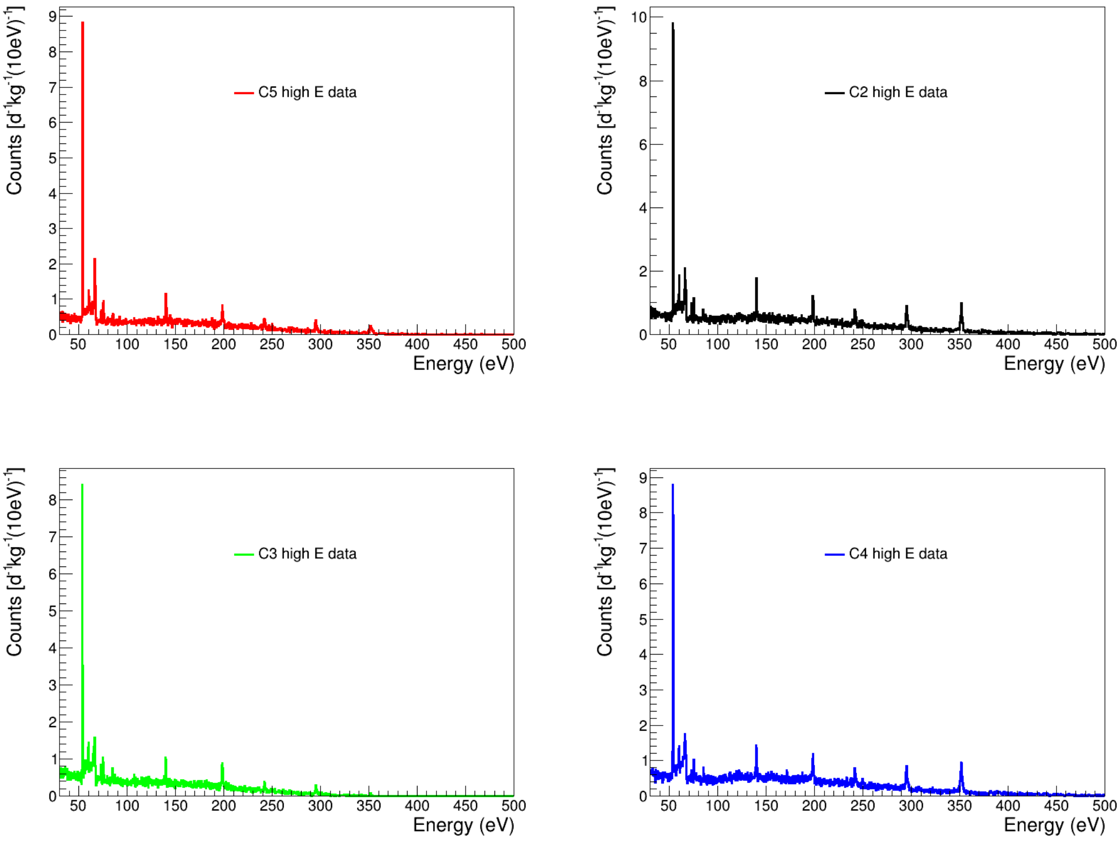

Figure 3.20. Data taken during run 1 in the high energy channels of the four detectors with muon veto cut applied. Clear efficiency losses are visible starting above energies of approximately 100 keV. The efficiency loss is especially visible for the C5 and C3 detectors.

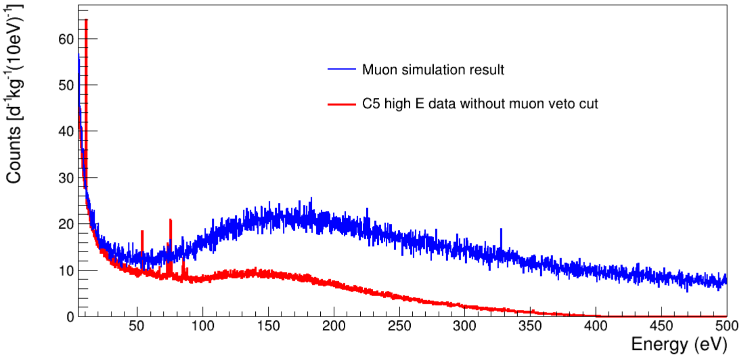

Figure 3.21. High E data measured in the C5 detector without muon veto cut compared to the result of the muon simulation presented in the previous sections. The data without muon veto cut should be completely dominated by muon-induced events and the simulations should therefore describe the data.

3.5 Cosmic neutron background

For most neutrino experiments cosmic ray neutrons are effectively shielded by an overburden >10 m w.e.. However, as described in Section 2.1, the CONUS+ experiment features an overburden of only (7.4 ± 0.1) m w.e. Therefore, a detailed investigation into cosmic neutrons as a possible source of background for the CONUS+ experiment is necessary. As input for the simulations, in a first step the spectrum and flux of cosmic neutrons in the CONUS+ room is needed.

3.5.1 Cosmic neutron flux in the CONUS+ room

Section 3.2.3 described the efforts to measure the neutron flux present in the CONUS+ experimental location inside of the KKL reactor building. These measurements were performed with a set of Bonner sphere arrays in two separate campaigns, one during normal reactor operation and one during the reactor outage in May of 2023. However, both of these measurements were unable to determine a precise spectrum for the cosmic neutron component, as previously explained in Section 3.2.3. Consequently, the following chapter and considerations rely on simulations to acquire a spectrum of cosmic neutrons in the CONUS+ room as was previously done for other experiments [76, 77]. For the future of the experiment, efforts are being taken to perform another dedicated measurement either directly in the experimental location or on the outside of the reactor building to confirm the following results.

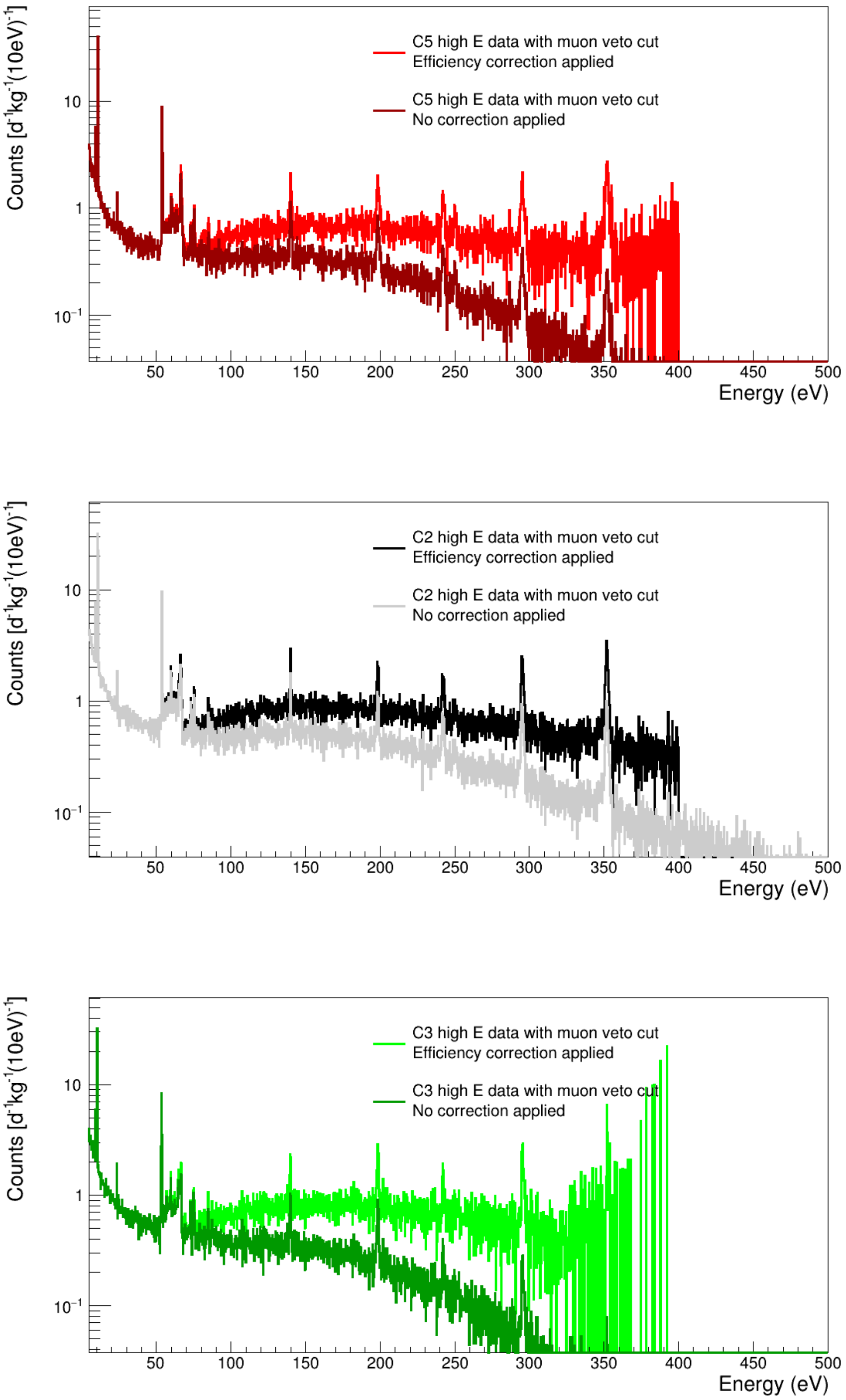

Figure 3.22. Corrected high energy spectra of the three detectors used in the analysis of run 1. The spectra match the expected shape after the efficiency correction with the muon simulation results. The method introduces large uncertainties in the bins above 300 keV due to the limited statistics in the original data. Therefore, only the spectra up to 300 keV are used for analysis.

Simulation of cosmic neutrons through the overburden of the KKL reactor building

The first input for a simulation of the cosmic neutron flux inside the CONUS+ experimental room is a spectrum of the cosmic neutron flux at the location of KKL in Leibstadt, Switzerland. Unfortunately, such a measurement is not available in the literature and therefore a cosmic neutron measurement from a comparable location has to be used. In this work, the measurements in [11] are used. In their work, Gordon et al. performed measurements of the cosmic neutron flux at five different locations in the continental United States, all differing in their altitude. On of these locations was Yorktown Heights, NY with an altitude of 170 m over sea level. The spectrum that was measured at this location is shown in Figure 3.23. As described in Section 2.4.1, the spectrum shows the three characteristic peaks associated with a cosmic neutron spectrum. A total neutron flux of 0.0134 $\mathrm{cm^{-2}\ s^{-1}}$ is measured. Due to the difference in altitude between the measurement location (167 m) and Leibstadt, Switzerland (350 m) a correction is applied to this flux, arriving at an estimated flux of $(0.0142 \pm 0.020)\ \mathrm{cm^{-2}\ s^{-1}}$ to be used in the following simulation. The correction also takes into account the different locations of the measurements in terms of latitude and longitude. No change in the principal shape of the spectrum is expected [11].

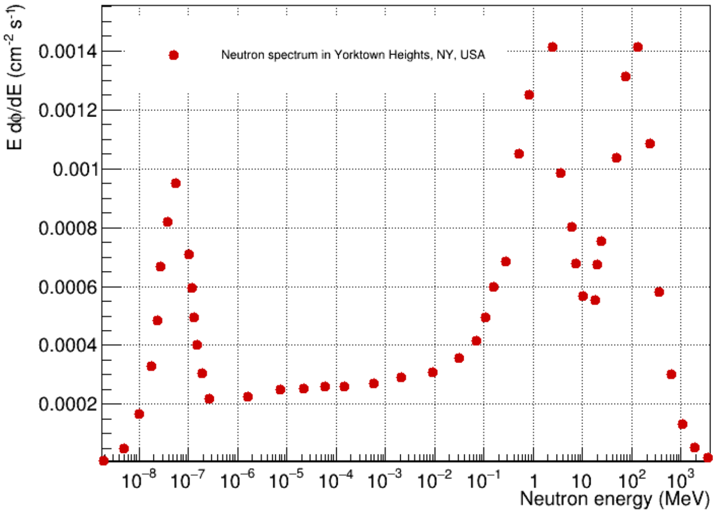

Figure 3.23. Neutron spectrum measured in Yorktown, NY, USA in [11]. The spectrum shows the characteristic thermal, evaporation and cascade peaks described in 2.4.1.

In addition to the neutron spectrum, the simulation require a detailed model of the KKL reactor building to correctly propagate them through the different materials of the dome. The model was built in Geant4 from drawings and schematics of the building provided by KKL and is shown in Figure 3.24. The important features for the propagation of the neutrons through the model are the materials above and around the room and their densities. The concrete used in the model is assumed to be a standard concrete with a density of 2.5 $\frac{g}{cm^3}$, while the steel is assumed to have a density of 7.85 $\frac{g}{cm^3}$. The outer wall of the the reactor building is made of a reinforced concrete, as is standard practice for nuclear power plants, to protect against impacts and seismic activity. It is known that this reinforced concrete is made from standard concrete with additional steel elements, however the exact composition is not known. Due to the effective overburden of (7.4 $\pm$ 0.1) m w.e., which is observed in the CONUS+ experiment (see Section 2.1 and Section 3.4), the density of the reinforced concrete can be estimated to be (5.2 $\pm$ 0.1) $\frac{g}{cm^3}$.

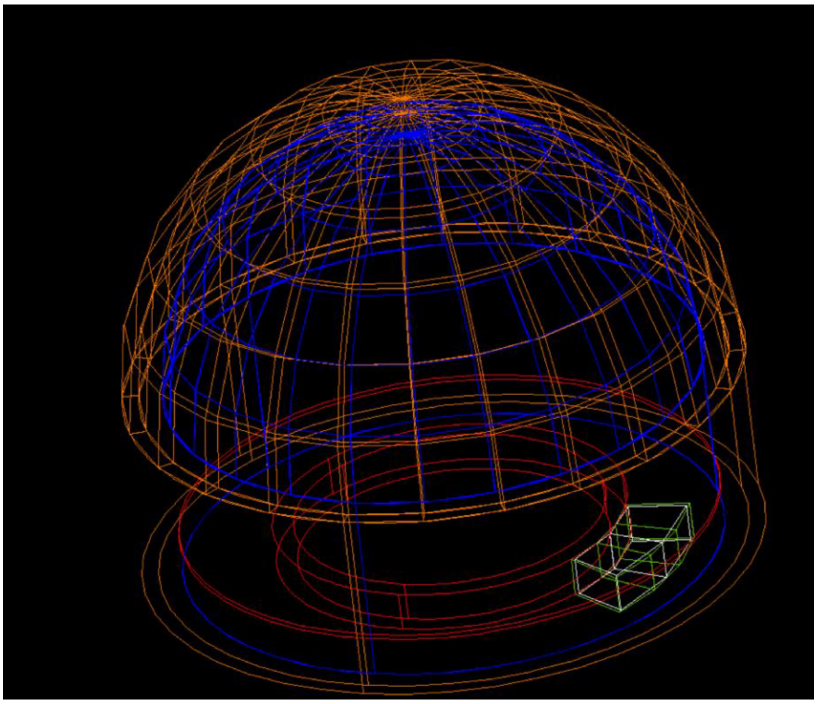

Figure 3.24. Model of the KKL reactor building built in Geant4. Only the structure above the CONUS+ room is simulated. The materials that are used are: Standard concrete (red), reinforced concrete (orange) and steel (blue). The CONUS+ experimental room is shown in green.

In the simulations, neutrons with the energy distribution from Figure 3.23 and isotropic angular distribution are started from a plane above the reactor building model. In the model the neutrons and their energies are registered when they pass through a half-sphere vacuum volume that is placed at the position of the CONUS+ shield. The results are shown in Figure 3.25.

The total flux of neutrons that arrives in the CONUS+ room is found to be (0.9 $\pm$ 0.2) cm^{-2} d^{-1}. The uncertainty on this value comes from the original uncertainty of the assumed outside flux at the KKL location, as well as from uncertainties in the exact composition of the reinforced concrete in the KKL reactor building. For this purpose, several simulations were performed, where the density of this material was changed slightly within

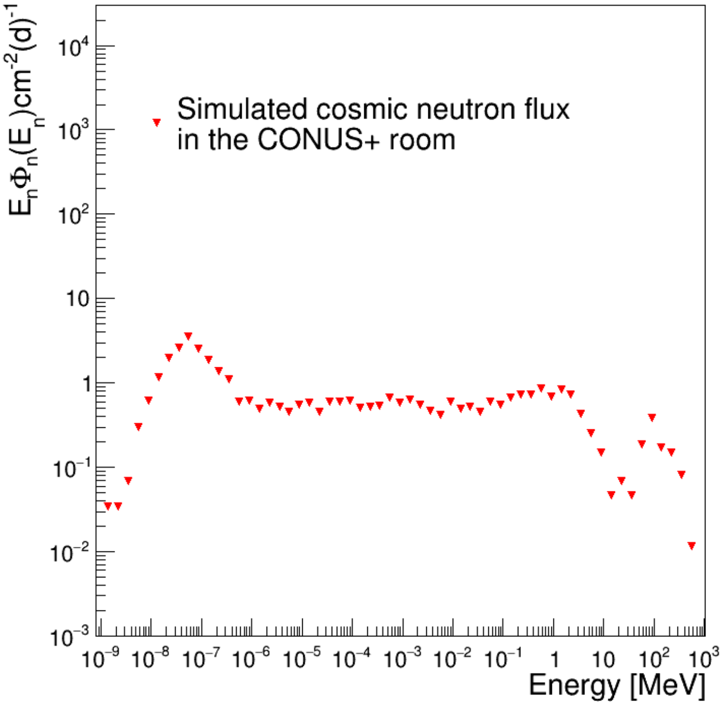

Figure 3.25. Flux of cosmic neutrons in the CONUS+ room from simulations of neutrons passing through the reactor building.

the constraints of the observed overburden of (7.4 ± 0.1) m w.e.. The shape of the spectrum is consistent with other simulated neutron spectra in similar shallow depth experiments, like in [76]. As expected, the flux is greatly reduced compared to the outside flux in Figure 3.23 by around two orders of magnitude, however, a small flux remains. This is especially critical, since a fraction of very fast neutrons ($E > 10$ MeV) originating from the cascade peak remain in the CONUS+ room, as can be seen from Figure 3.25. These neutrons have the potential to penetrate deep into the CONUS+ shield and lead to considerable background for the experiment as will be shown in the following section.

3.5.2 Impact on background

To quantify the effect of the remaining cosmic neutrons, a final simulation is performed, where neutrons with the energy spectrum in Figure 3.25 and isotropic angular distribution are started from a half-sphere around the CONUS+ shield. Because of the close proximity of the four detectors and the isotropic distribution of the neutron flux, an equal contribution is again considered for all detectors as in the case of the muons. Figure 3.26 shows the result of these simulations in comparison to the C5 data for the low and high energy channels. The neutron spectrum in the detector features a flat tail at high energies and an exponential rise towards low energies, especially in the ROI of the CEνNS search. As such they make up up to 50 % of the background of the separate detectors here, which can be seen from Table 3.4, which shows the background contribution in the energy range from 400 to 1000 eV. The cosmic neutrons are therefore one of the dominant background sources for the CONUS+ experiment due to the low overburden of the reactor building at KKL. It is important to again point out, that the impact of the neutron background was determined from outside cosmic neutron spectra taken from literature and not from direct measurements in the room itself. This explains the rather large uncertainty of approximately 15 % on the values found in Table 3.4. As such, a future dedicated measurement of the cosmic neutron spectrum at the CONUS+ location would be desirable to confirm these results and their validity.

Table 3.4. Contribution to the background count rates in the three detectors from neutrons in the energy region from 400 to 1000 eV.

Detector	Count rate in [400, 1000] eV (d^{-1} kg^{-1})	Percentage of total background (%)
C5	21.6 ± 3.1	50.3 ± 7.2
C2	21.6 ± 3.1	41.3 ± 5.9
C3	21.6 ± 3.1	43.8 ± 6.2

3.6 Muon-induced neutrons in the overburden

The previous section discussed neutrons originating as secondary particles from cosmic rays, while Section 3.4 discussed the prompt impact of muons that pass through the CONUS+ shield. However, these muons can also induce neutrons when passing though the overburden of the reactor building via various different interactions described in Section 2.4.1. So far these neutrons were not discussed in any of the previous two sections and their impact on the CONUS+ background must be considered and evaluated closely.

For this, muons were propagated through the model of the KKL reactor building (shown in Figure 3.24) in a first step. The procedure is analogous to the one described in the previous section for the cosmic neutrons and the neutron flux arriving in the CONUS+ room is tracked again. The spectrum of the muons was again calculated from [84], this time for zero overburden and at the approximate altitude of KKL, and is shown in Figure 3.27. The neutron flux arriving in the room is shown in Figure 3.28. In the spectrum, two of the three characteristic neutron peaks described in Section 2.4.1, the thermal and evaporation peak, are visible again. The evaporation peak is induced directly by muons passing through the

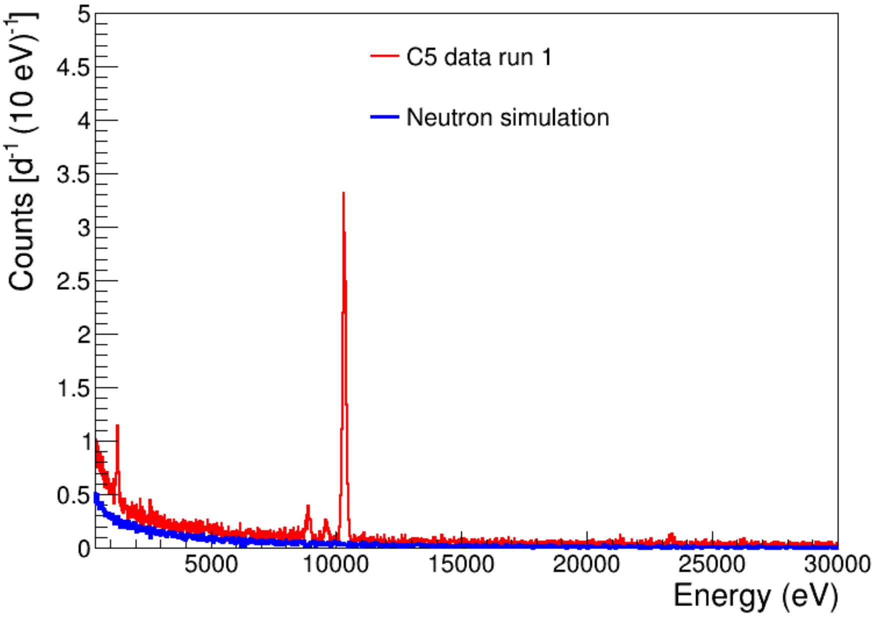

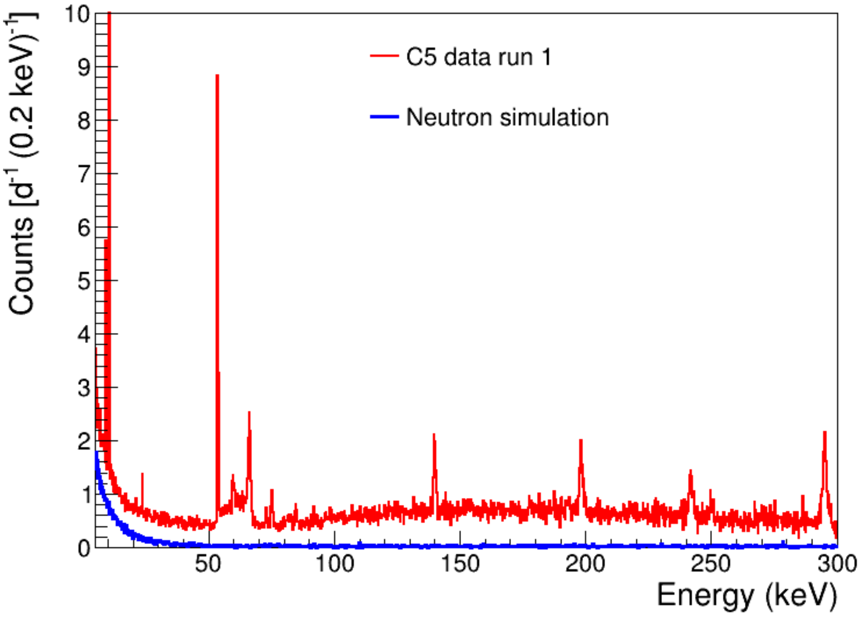

Figure 3.26. Neutron simulation result compared to the data taken in run 1 of the CONUS+ experiment with the C5 detector in the low energy channel up to 30 keV (top) and the high E channel (bottom). The neutrons feature an exponential rise towards very low energies and their spectrum flattens towards higher energies.

reactor building, while the thermal peaks appears through the energy loss of these neutrons in the materials. Additionally, a small cascade peak at around 100 MeV is visible. The total flux of muon-induced neutrons is around one order of magnitude smaller than the flux of cosmic neutrons in the room.

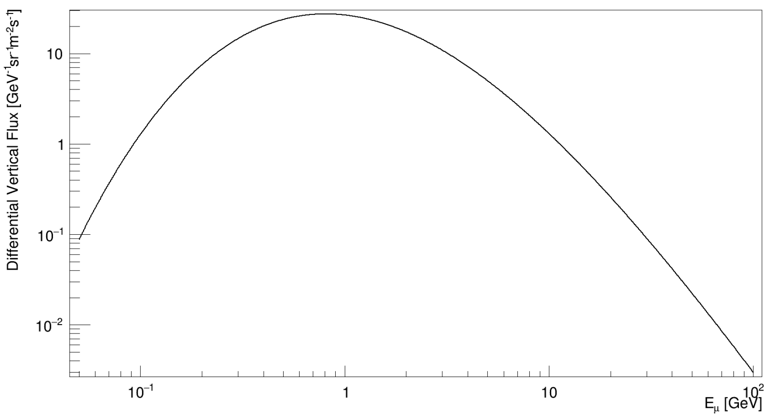

Figure 3.27. Spectrum of muons on the outside of the KKL reactor building. These muons are propagated through the model of the reactor building.

The spectrum from Figure 3.28 is used as input for the next simulation, where these neutrons are started from a half-sphere around the CONUS+ shield with an isotropic angular distribution, equivalent to the treatment of cosmic neutrons in the previous section. The result, both in the low and high energy channel of C5 is shown in Figure 3.29, while Table 3.5 shows the respective contribution to the background in the energy region from 400 to 1000 eV. The impact of muon-induced neutrons from the overburden of the reactor building is around one order of magnitude smaller than that of cosmic neutrons, however, their impact especially in the ROI at very low energies is not negligible, making up around 5 % of the background in the mentioned region. The error on the values shown in Table 3.5 comes from the uncertainty of the initial muon flux on the outside of the reactor and the overburden and exact material composition of the reactor building. This was again evaluated by doing several simulation with slightly varying overburden and material densities in the model of the reactor building.

3.7 Radon in the detector chamber

As explained in Section 2.4.2, the inside of the CONUS+ shield is continuously being flushed with radon-free air through a system of eight 300 b bottles that are stored in the CONUS+ room. However, as seen from the measured spectra of the high energy channels in run 1 in Figure 3.20 and the corrected spectra in Figure 3.22, several gamma ray lines are still visible in the range from 150 to 400 keV. Of these lines, three originate from the

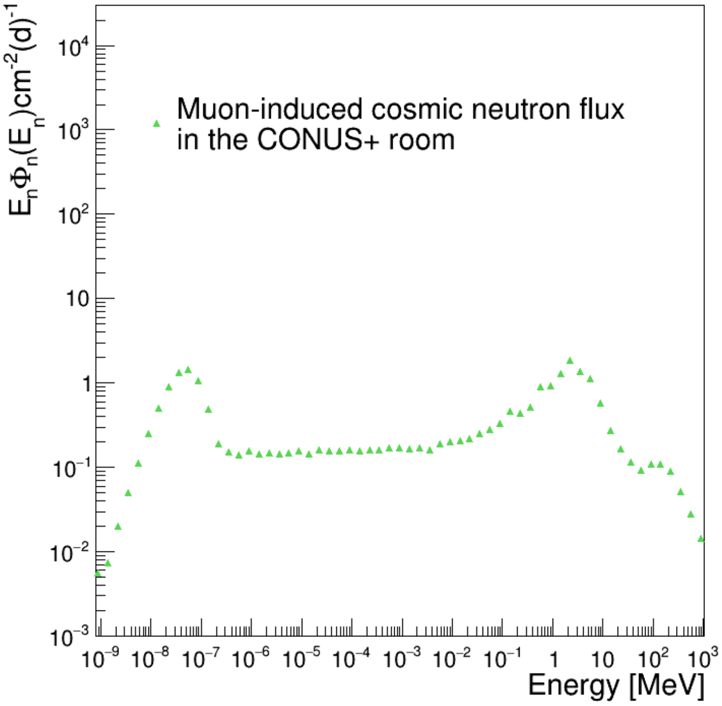

Figure 3.28. Muon-induced neutron flux in the CONUS+ room from simulation. The thermal and evaporation peak are present again, while a small cascade peak at 100 MeV is also visible.

decay of daughter isotopes of radon, indicating a remaining presence of radon in the detector chamber. These lines come from the decay of ^{214}Pb, a daughter nucleus in the decay chain of ^{222}Rn. Table 3.6 lists their energies and relative intensities.

The count rates of the respective lines in the reactor on data of run 1 are shown in Table 3.7. The count rates are calculated by first performing a gaussian fit to the line in the spectrum as shown in Figure 3.30. The result of the fit, namely the mean μ and standard deviation σ, is then used to define a region of interest (ROI) around the mean with a width of 2.5 times the FWHM of the Gaussian. Additionally, two background regions to the left

Table 3.5. Contribution to the background count rates in the three detectors from muon-induced neutrons in the energy region from 400 to 1000 eV.

Detector	Count rate in [400, 1000] eV (d^{-1} kg^{-1})	Percentage of total background (%)
C5	2.2 ± 0.1	5.1 ± 0.2
C2	2.2 ± 0.1	4.2 ± 0.2
C3	2.2 ± 0.1	4.4 ± 0.2

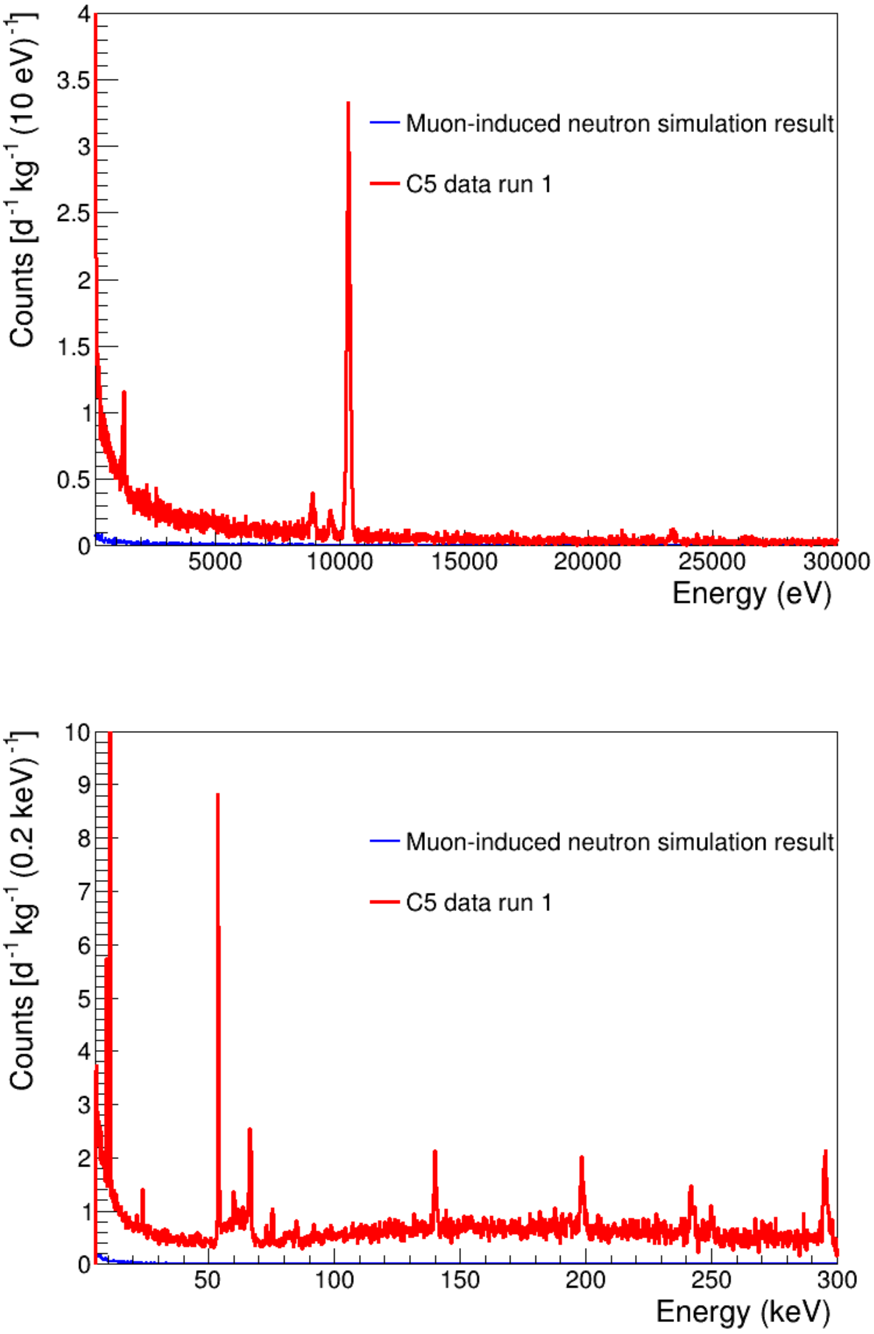

Figure 3.29. Simulation result for muon-induced neutrons compared to the data taken in run 1 of the CONUS+ experiment with the C5 detector in the low energy channel up to 30 keV (top) and the high E channel (bottom). The impact of these neutrons is small compared to the contributions from prompt muons and cosmic neutrons, however a small contribution at very low energies (in the ROI for CEνNS) is visible. The impact at energies above 30 keV is negligible, as the background decreases strongly towards higher energies, as was the case for the cosmic neutrons

Table 3.6. γ-ray lines from radon decay chain in the CONUS+ high energy channels. Information on the energy and relative intensities are taken from [15]

Isotope	Energy [keV]	Relative intensity [%]
^{214}Pb	241.995 ± 0.004	7.26 ± 0.04
^{214}Pb	295.224 ± 0.002	18.47 ± 0.11
^{214}Pb	351.932 ± 0.002	35.72 ± 0.24

and the right of the ROI (BG$_{left}$ and BG$_{right}$) are defined in order to subtract the background from the count rate in the line. The width of these background regions is half the width of the ROI each. The count rate in the line is then defined as:

$$\text{Counts(ROI)} - \frac{\text{Counts(BG}_{left}) + \text{Counts(BG}_{right})}{\text{Width(BG}_{left}) + \text{Width(BG}_{right})} \cdot \text{Width(ROI)} \qquad (3.5)$$

The count rates of the 242 keV and 295 keV line show good agreement when compared to the expected relative intensities listed in Table 3.6, which validates the efficiency correction with the muon simulation result for this energy range. The values for the 352 keV line are consistently too low compared to the expected intensity, which is due to the unreliability of the method for energies larger than 300 keV. As explained in Section 3.4.2, this is due to the limited statistics in the original data in this energy region, making a correct reconstruction with this method impossible.

It can also be seen, that the detectors do not have the exact same levels of radon background, indicated by the different count rates in individual lines between them. This is to be expected, since the daughter isotopes of radon, namely ^{214}Pb, which is responsible for the lines, is not airborne as opposed to the original radon. This means that the daughter isotopes will not necessarily spread out homogeneously in the detector chamber and instead might gather at certain points. This leads to slightly differing contributions in each detector.

For the simulation of this component, the relevant daughter isotopes of radon (^{214}Pb and ^{214}Bi) are placed on surfaces inside the detector chamber, primarily on the floor of the chamber and the endcaps of the detectors. The contamination is placed homogeneously and the result is later scaled to be in accordance with the measured count rates in the the three lines listed in Table 3.7 for each detector. As ^{214}Pb decays into ^{214}Bi with a probability of 100 % and has a short half-life of only 26 minutes, an equal number of ^{214}Pb and ^{214}Bi isotopes are started in the simulation. The result of the simulations for the C5 detector is shown in Figure 3.31, while the results for C2 and C3 are shown in A.1 and A.2. It can be seen that the contribution of radon to the background in the high energy range is one of the largest, featuring a distinctive bump in the between 150 and 200 keV which dominates the

Table 3.7. Count rates of the radon induced lines in the high energy channels of the three detectors used in the run 1 analysis. The values for the count rates in the 352 keV line (marked with *) are not completely reliable, since at these high energies the efficiency correction with the muon simulation fails due to the low number of statistics in the original data, as explained in Section 3.4.2. The uncertainties given for the count rates only considers the poissonian uncertainty from the extracted value. For the case of the 352 keV line, this uncertainty is too small and an additional term from the efficiency correction should also be included for a more complete picture.

Detector	C5	C2	C3
Energy in data [keV]	242.085 ± 0.024	241.967 ± 0.029	242.158 ± 0.020
Count rate [d^{-1} kg^{-1}]	5.77 ± 0.14	8.49 ± 0.29	7.64 ± 0.07
Energy in data [keV]	295.229 ± 0.012	295.275 ± 0.016	295.468 ± 0.008
Count rate [d^{-1} kg^{-1}]	16.63 ± 0.31	20.70 ± 0.40	19.8 ± 0.29
Energy in data [keV]	352.033 ± 0.006	351.922 ± 0.011	352.177 ± 0.001
Count rate [d^{-1} kg^{-1}]	24.61 ± 0.45 (*)	26.77 ± 0.47 (*)	20.08 ± 0.38 (*)

shape of the spectrum. Despite this, the contribution of radon in the low energy channel is very small, especially in the region of interest for the CEνNS search. This is shown in Table 3.8. The final normalisation of the radon simulation was largely based on the count rate of the 295 keV lines in each detector.

Table 3.8. Contribution to the background count rates in the three detectors from radon in the detector chamber in the energy region from 400 to 1000 eV.

Detector	Count rate in [400, 1000] eV (d^{-1} kg^{-1})	Percentage of total background (%)
C5	1.9 ± 0.1	4.4 ± 0.1
C2	2.8 ± 0.1	5.3 ± 0.1
C3	2.6 ± 0.1	5.3 ± 0.1

3.8 Cosmogenic activation

As described in Section 2.4.1, cosmogenic activation describes the process in which radioactive isotopes are produced in materials which are exposed to cosmic rays through processes such as neutron capture. Before and during the building of the CONUS+ experiment, the

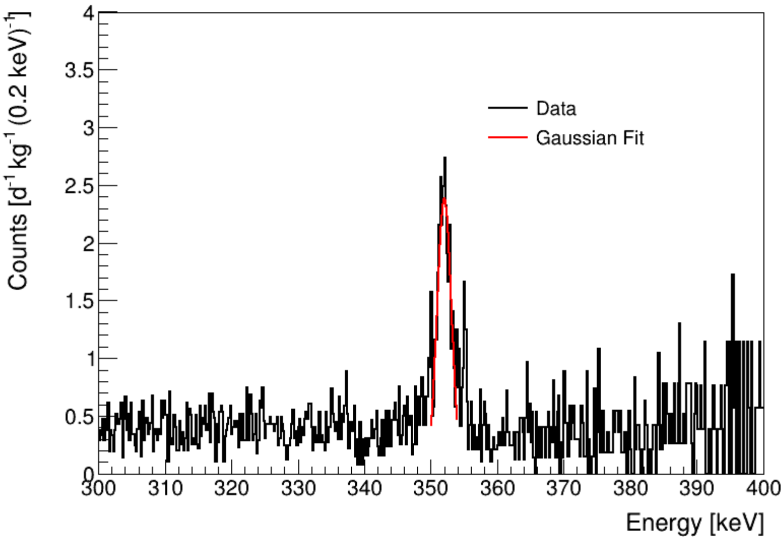

Figure 3.30. Example of Gaussian fit to the 352 keV ^{214}Pb line in C5 reactor on data

materials used in the shield and detectors were carefully monitored and shielded from cosmic ray exposure by placing them primarily in the low level laboratory (LLL) at MPIK with an overburden of 15 m w.e.. Nevertheless, periods of exposure could not be completely prevented during the transports of the materials and the stay of the detectors at Mirion Lingolsheim for their upgrades and refurbishing after the end of the CONUS experiment (see Section 2.3.7). For this reason, it is possible that backgrounds and γ-ray lines from cosmogenically activated isotopes are present in the CONUS+ data. The following chapter will carefully analyse this aspect for both the copper parts of the cryostats and the germanium crystals themselves.

3.8.1 Germanium crystals

The relevant isotopes that can be created from cosmogenic activation in the germanium crystals are listed in Table 2.6. Lines from three of these isotopes are visible in the low energy data taken in run 1 of the CONUS+ experiment: ^{68}Ge / ^{71}Ge with lines at 10.37 keV and 1.3 keV, ^{68}Ga with lines at 9.7 keV and 1.2 keV, and ^{65}Zn with lines at 8.96 keV and 1.1 keV. Due to the energy resolution of the detectors the lines around 1 keV from the three isotopes cannot be distinguished from each other and appear as one peak at around 1.2 - 1.3 keV.

^{68}Ge and ^{71}Ge

The dominant line in the low energy background of CONUS+ is the 10.37 keV line emitted by the decay of ^{68}Ge and ^{71}Ge. These isotopes are produced in the germanium crystal

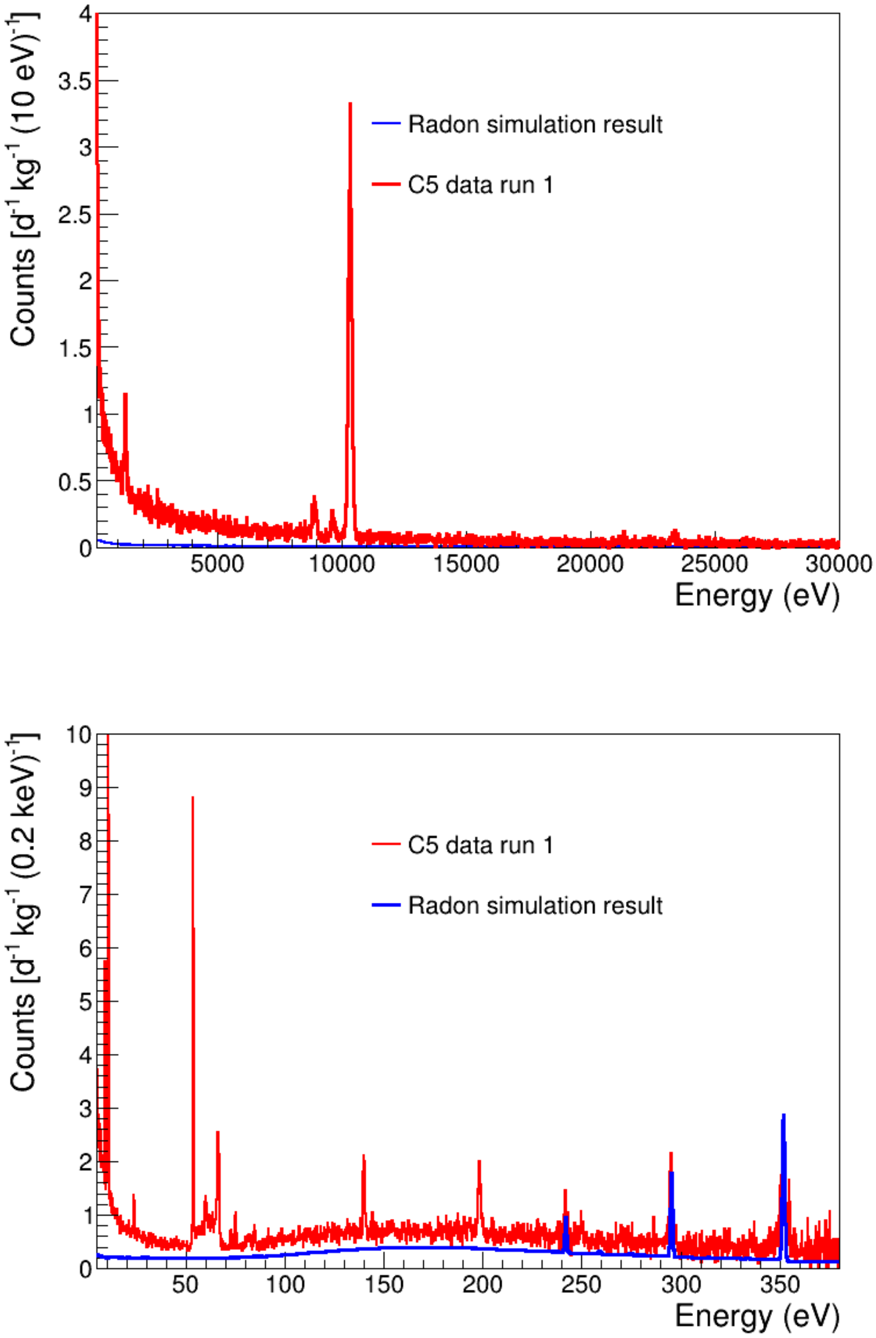

Figure 3.31. Simulation result for radon in the detector chamber compared to the data taken in run 1 of the CONUS+ experiment with the C5 detector in the low energy channel up to 30 keV (top) and the high E channel (bottom). The impact of radon is small in the low energy channel and the ROI but is considerable and one of the largest contributions in the high energy range.

through interactions with neutrons. In the case of ^{68}Ge, a neutron with an energy above $\sim$ 20MeV scatters off of a germanium nucleus and induces spallation:

$$^{70}Ge + \text{fast neutron} \rightarrow^{68} Ge + 3n \tag{3.6}$$

These fast neutrons typically only originate from cosmic rays which is why any ^{68}Ge contamination in the crystals stems from exposure at Earth's surface. Contrary to this, ^{71}Ge is produced by thermal neutron capture on ^{70}Ge, which means that this isotope can still be induced even in shallow underground depths like the location of CONUS+ through the thermalisation of cosmic neutrons in the overburden and in the shield, as well as from muon-induced neutrons. This distinction between the two isotopes, as well as their different half-lives ($\tau_{71} = 11.4d$, $\tau_{68} = 278d$) allows the disentanglement of their respective contributions to the 10.37 keV line in the data, as was previously done for data of the CONUS experiment in [2, 12] by analysing the changing count rate in the line over the measurement period.

Both isotopes emit the 10.37 keV line from K shell transitions induced by electron capture (EC). Similarly, another line with an energy of 1.3 keV is produced from L shell transitions in both isotopes This line is also visible in the CONUS+ data, however due to the energy resolution of the detectors, it cannot be distinguished from the L shell lines of ^{68}Ga and ^{65}Zn. The branching ratio for the transitions used in Geant4 (version 4.10) is 0.865 for the K shell line and 0.113 for the L shell line. In previous works (see [2]), excellent agreement between the branching ratio in the MC and literature was found.

As the lines from the decay of both isotopes are exactly the same and thus the shape of their contribution to the CONUS+ background is the same, only ^{68}Ge was considered in the simulations for this work. Similarly to the radon contributions in the previous chapter, the simulation output was then scaled so that the count rate in the 10.37 keV line matches the count rate observed in the data for each detector. These count rates are listed in Table 3.9 and were again calculated with the method described in the previous chapter.

For the simulation of the background contribution the ^{68}Ge atoms were placed homogeneously in each germanium crystal. The result of the simulation for the C5 detector in reactor on data of run 1 can be seen in Figure 3.32. Results for the C2 and C3 detectors can be found in A.3. It can be seen that apart from the two lines that were discussed a third γ-ray line can be observed in the simulated spectrum at extremely low energies of around 160 eV. This is the M shell transition line of the two isotopes [87], which was previously unobserved in the CONUS experiment due to its higher threshold of 210 eV. The line was previously observed in the CDMS low ionisation threshold experiment (CDMSlite), which uses germanium detectors to search for weakly interacting massive particles (WIMPs) [88]. The line offers the unique possibility of an additional intrinsic germanium line which could be used for effective energy calibration at very low energies. In this way, non-linearity effects in this energy regime can be studied much more closely. The CONUS+ experiment is currently investigating this possibility using the C8 detector, one of the new 2.4 kg germanium detectors (see Section 5.1) at MPIK. Depending on the energy threshold of the detector, the M shell line is a prominent contribution to the background in the low end of the ROI of the CONUS+ experiment, which can be seen from Tables 3.15 - 3.20. Apart from this, the background contribution of ^{68}Ge and ^{71}Ge is almost negligible in the ROI.

Table 3.9. Count rates of the 10.37 keV line from K shell transitions of ^{68}Ge and ^{71}Ge in the CONUS+ detectors in reactor on data in run 1

Detector	C5	C2	C3
Energy in data [keV]	10.34 ± 0.03	10.34 ± 0.04	10.35 ± 0.03
Count rate [d^{-1} kg^{-1}]	49.78 ± 1.03	51.44 ± 1.05	48.64 ± 1.02

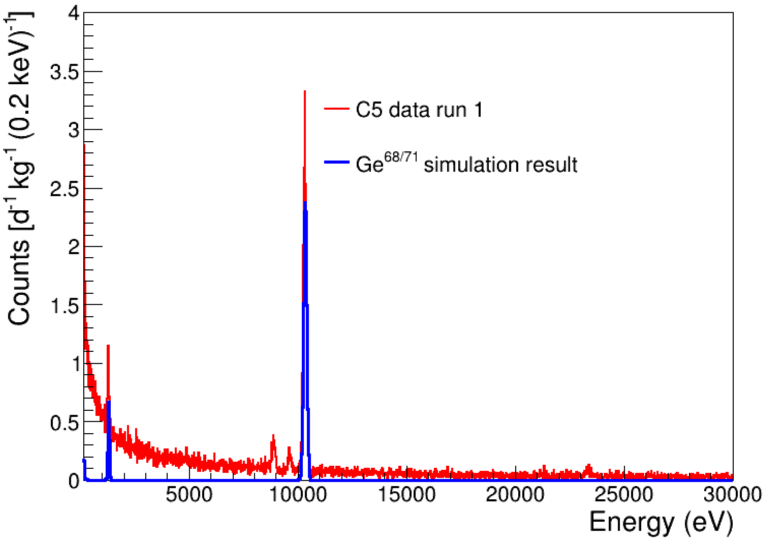

Figure 3.32. Simulation result for the background contribution of ^{68}Ge and ^{68}Ge in the C5 detector in reactor on data of run 1.

^{68}Ga

^{68}Ga is the decay product of ^{68}Ge and decays instantly via electron capture (10.86 %) and positron emission (89.14 %). Just like ^{68}Ge and ^{71}Ge, it produces two X-ray lines from its K and L shell transitions. These have energies of 9.69 keV (visible in data) and 1.19 keV (included in the broad line at 1.3 keV, due to detector resolution). Additionally, the decay of ^{68}Ga produces γ-rays and electrons which contribute to the continuous background of the detectors. For the simulations, the same approach as in the previous chapters is used; the count rates in the 9.69 keV line in all three detectors are listed in Table 3.10. Figure 3.33 shows the result of the simulation of the respective background contribution in the C5 detector in reactor on in run 1. Results for the C2 and C3 detectors can again be found in A.3. Just like in the case of ^{68}Ge and ^{71}Ge, the spectrum is dominated by the K and L shell transition lines. The impact on the ROI at very low energies is negligible.

Table 3.10. Count rates of the 9.69 keV line from the K shell transition of ^{68}Ga in the CONUS+ detectors in reactor on data in run 1

Detector	C5	C2	C3
Energy in data [keV]	9.62 ± 0.03	9.63 ± 0.04	9.63 ± 0.03
Count rate [$\mathrm{d}^{-1}\ \mathrm{kg}^{-1}$]	2.48 ± 0.37	1.87 ± 0.25	2.13 ± 0.28

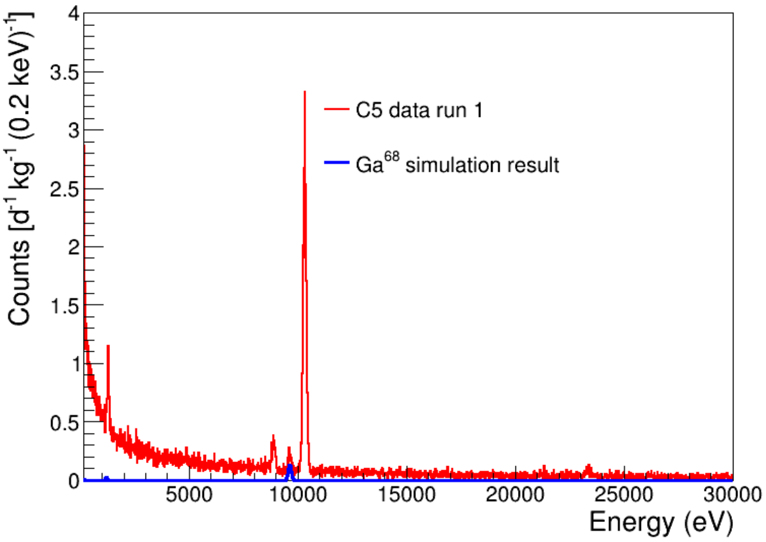

Figure 3.33. Simulation result for the background contribution of ^{68}Ga in the C5 detector in reactor on data of run 1

^{65}Zn

The last of the visible lines in the low energy spectrum of the three CONUS+ detectors comes from ^{65}Zn. This isotope is again created through spallation reactions with fast neutrons during exposure of the germanium crystals to cosmic rays:

$$^{70}Ge + \text{fast neutron} \rightarrow ^{65}Zn + 2n + He \tag{3.7}$$

Just like the previous discussed isotopes, ^{65}Zn also features a K shell transition line at 8.96 keV, which is visible in the CONUS+ spectra, and a L shell line, which is contained in the broad peak at 1.3 keV in the measured spectra. ^{65}Zn decays via electron capture into ^{65}Cu with a half-life of 244d. The count rates in the K shell line can be found in Table 3.11 and the simulation result can be found in Figure 3.34 for the C5 detector and in A.3 for C2 and C3.

Table 3.11. Count rates of the 8.96 keV line from the K shell transition of ^{68}Ga in the CONUS+ detectors in reactor on data in run 1

Detector	C5	C2	C3
Energy in data [keV]	8.92 ± 0.03	8.91 ± 0.04	8.92 ± 0.03
Count rate [d^{-1} kg^{-1}]	2.56 ± 0.63	6.18 ± 0.67	5.22 ± 0.73

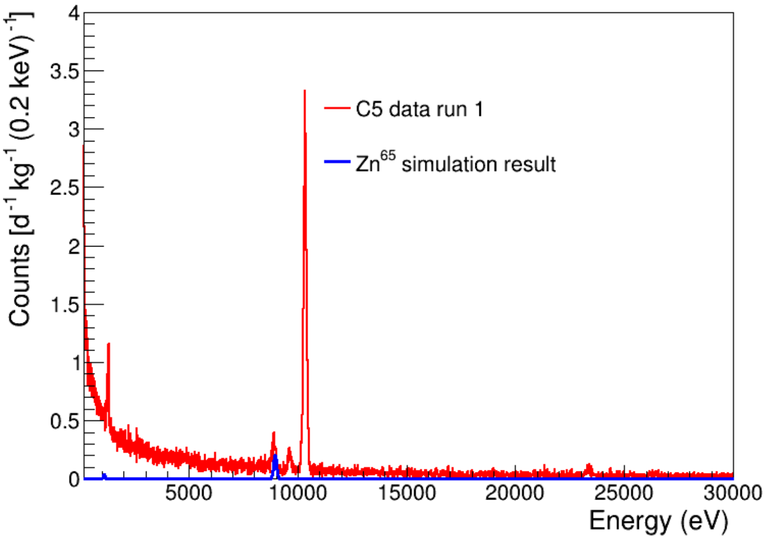

Figure 3.34. Simulation result for the background contribution of ^{65}Zn in the C5 detector in reactor on data of run 1

Cosmogenic isotopes with no visible line background in the data

Several cosmogenically induced isotopes in the germanium crystals have no visible lines in the spectrum of the CONUS+ detectors, either because of too low count rates or because of the absence of lines in the energy range of CONUS+ in general. Due to the absence of lines coming from these isotopes, the procedure of the previous sections is not valid for including them in the background model. Instead, their approximate abundance in the germanium crystals has to be calculated from the production rates and half-lifes listed in Table 3.12. To

Table 3.12. Production rates of different cosmogenically induced isotopes with no visible lines in the CONUS+ spectrum in germanium. Values in the table are taken from [12]

Isotope	Half-life [d]	Production rate in germanium [atoms d^{-1} kg^{-1}]]
^{57}Co	271.8	7.6 ± 3.9
^{60}Co	1923.6	3.9 ± 1.5
^{54}Mn	312.2	2.6 ± 1.7
^{55}Fe	1002.7	5.8 ± 2.6
^{3}H	4493.9	77 ± 21

calculate the expected number of atoms N(n) of a certain isotope after n days of exposure to cosmic rays, the following formula can be used:

$$N(n) = \frac{R \cdot m}{\lambda}(1 - e^{-\lambda n}) \tag{3.8}$$

Here, R is the production rate of the isotope in atoms per day per kg, $\lambda = \frac{ln2}{\tau_{1/2}}$ where $\tau_{1/2}$ is the half-life of the isotope, and m is the mass of the germanium crystal in kg. The activity of the isotope can then be calculated by multiplying the number of atoms by λ (in 1/s). For the number of days on which the detectors have been exposed to cosmic rays, 100 days is assumed. This is consistent with the time that the detectors spent at Mirion, Lingolsheim for their upgrades (see Section 2.3.7) and the transport to Leibstadt. Furthermore, this is also consistent with the values for the four detectors of the CONUS experiment before its installation at the KBR power plant (see [12]).

The first of the isotopes without visible lines in the CONUS+ spectra is ^{57}Co, which can be produced by neutron spallation similarly to the production of ^{65}Zn. It has a half-life of 271.8 days and decays via β-decay to the excited state of ^{57}Fe. This state then deexcites via the emission of a 122.06 keV γ (85.49 %) and a 14.42 keV γ (9.18 %) to the ground state. Additionally, a single γ with the combined energy of 136.47 keV can be emitted in a direct deexcitation to the ground state with a branching ratio of 10.71 %. Furthermore, K shell transmissions in the isotope lead to X-rays with energies of 6 to 7 keV. In the case of a ^{57}Co decay occurring in the germanium crystals, the different single peaks of the discussed lines are not visible due to the time resolution of the detectors. This leads to a single summation peak at 143.5 keV, which is the sum of all previously discussed energies. In the case that the 122 keV γ escapes the detector and is not measured an additional peak at 21.5 keV (= 14.42 keV + (6 to 7) keV) can also be visible. This peak has a considerably smaller detection efficiency due to the high probability of an interaction for the original 122 keV γ. The

probability that the 14.42 γ or the X-rays escape the detector is negligible.
The described 143.5 keV line is not visible in the data of the three detectors during run 1, as shown in Figure 3.35.

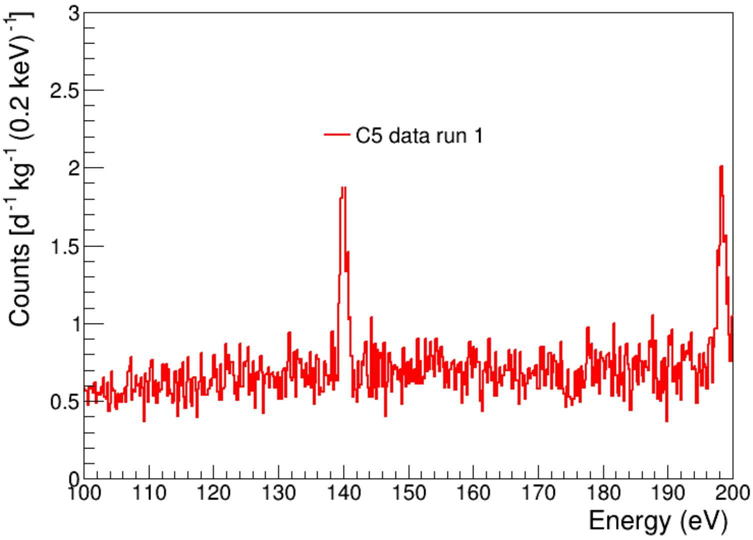

Figure 3.35. Data taken in the C5 detector between 100 and 200 keV. No line at 143.5 keV is visible. The line at 140 keV comes from the decay of a metastable germanium state, ^{75m}Ge.

Another cosmogenic isotope which was investigated was ^{55}Fe, which decays via electron capture and emits a K shell line at 6.54 keV and additionally a γ at 126 keV with an extremely small branching ratio of 10^{-7}. This isotope has a low production rate in germanium compared to the previously discussed isotopes (see Table 3.12), due to the fact that a considerable number of nucleons have to be released to create it from a typical germanium nucleus, which requires very high energy interactions. For this reason, no lines are visible in the spectrum.
A similar case is made for ^{54}Mn, which decays via electron capture with a half-life of 312 days and emits a K shell line at 5.99 keV. The production rate in germanium is again too small to have a considerable impact on the background of the detectors.
^{60}Co is also created in the germanium crystals during cosmic ray exposure. It has a half-life of 5.27 years and decays via β-decay to ^{60}Ni. The decay has a Q value of 318.13 keV, which means that the electrons from the decay can have an impact on the background spectrum of the detectors. Furthermore, two γ-rays at 1173 and 1333 keV are created in the decay. These lines lie outside of the energy range of the CONUS+ detectors, but can still contribute to the background due to their Compton continuum. As was the case for ^{54}Mn and ^{55}Fe, the production rate in germanium is small for ^{60}Co at a value of (3.9 ± 1.5) atoms per day per

kg when exposed to cosmic rays at Earth's surface (see Table 3.12).

Lastly, the impact of ^{3}H in the crystals was tested. ^{3}H can generally be produced in nuclear reactions by the hadronic component of cosmic rays and decays via β-decay with a half-life of 12.3 years. It's end point is 18.6 keV, which is in close vicinity to the ROI of the CONUS+ experiment. As listed in Table 3.12, the production rate of ^{3}H is the highest of all the cosmogenically activated isotopes in germanium at a value of (77 ± 21) atoms per day per kg.

The simulation result for the four discussed isotopes with no visible lines in the germanium crystals are shown in Figure 3.36. The activities were calculated from Table 3.12 and Formula 3.8 assuming an exposure of 100 days.

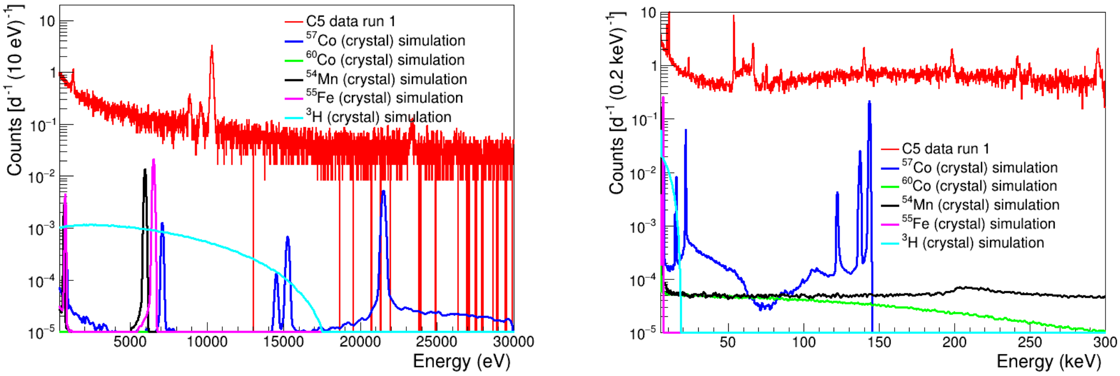

Figure 3.36. Background contributions from cosmogenically activated isotopes in the germanium crystals without visible lines. Their corresponding activities were calculated from Table 3.12 and Formula 3.8 assuming an exposure of 100 days.

Metastable germanium states

Apart from the mentioned radioactive isotopes, a number of metastable states can be produced in neutron capture on germanium nuclei. These are ^{71m}Ge, ^{73m}Ge, and ^{75m}Ge. A metastable state is a long-lived excited state of a nucleus; the nucleus is not in its ground state but the state also does not decay immediately. Instead these states can have half-lifes of up to several days in the case of the listed germanium states. When the metastable state finally decays, it transitions into its ground state and can emit one or several γ-rays, which are visible in the background of the CONUS+ detectors. The decay paths of the three states are shown in Figure 3.37. Although, the metastable states are induced by neutron capture of either thermalised cosmic neutrons or muon-induced neutrons, the states do not appear in the simulations of the respective sources as these long-lived states are not produced in Geant4.10. They are therefore considered in separate simulations and again scaled to the

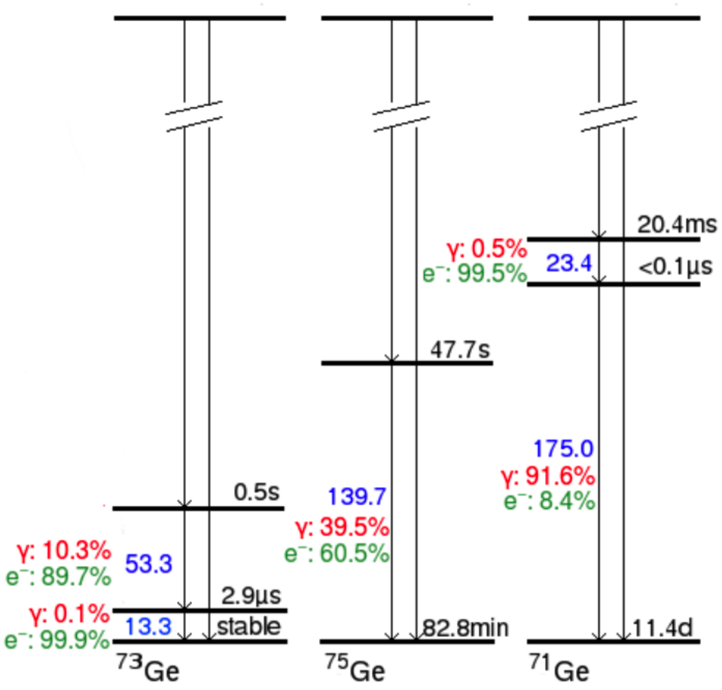

Figure 3.37. Decay scheme of the three metastable states in germanium.

respective count rates found in the CONUS+ data. The figures shown in the following sections again focus on the C5 detector. Simulation results for C2 and C3 can be found in A.4.

^{71m}Ge is an excited state of ^{71}Ge. It decays to the ground state via the emission of two γ-rays with energies of 23.4 and 175.0 keV respectively. Additionally, a summation peak at 198.4 keV is visible in the data. Figure 3.38 shows the background contribution of this decay to the spectrum of the C5 detector in reactor on measurement in run 1.

^{73m}Ge, an excited state of ^{73}Ge, also decays via the emission of two γ-rays with energies of 13.3 and 53.3 keV. The resulting spectrum features a double-peak structure with a peak at 53.3 keV and a second peak at 66.6 keV, the summation peak (see Figure 3.40). Between the two lines, a rising background can be observed which is a consequence of the very short half-life of only 2.9 μs between the emission of both gammas. This means that the emission of the 13 keV γ-ray very often happens within the decay of the pulse of the original 53.3 keV event. The second pulse is then observed in the DAQ system as an increase on top of the first pulse. Depending on the exact time of the second event and how much the first pulse already decayed this can lead to an increase of the maximum pulse height, which corresponds to the reconstructed energy of the event. In this way, all energies between 53 and 66 keV can be registered in the decay of ^{73m}Ge as shown in the left hand plot in Figure 3.39. If the second pulse arrives sufficiently late within the decay time of the first pulse, the whole event will still be registered with an energy of 53 keV, which is shown in the right

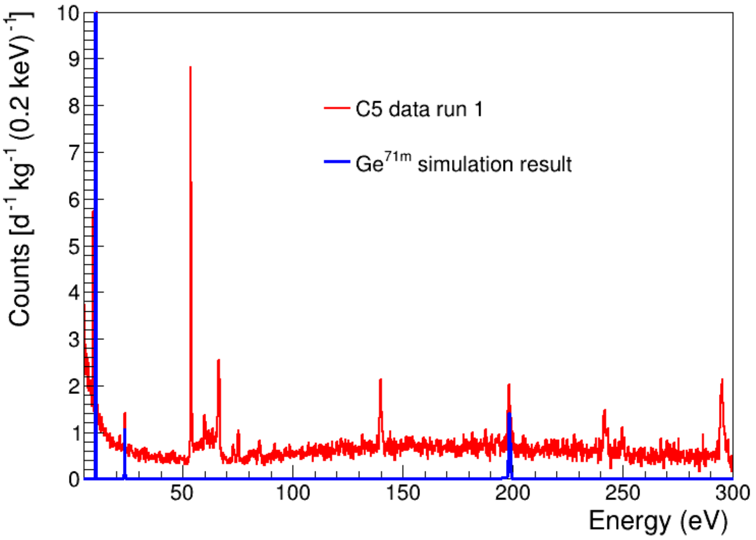

Figure 3.38. Simulation result for the background contribution of the metastable state ^{71m}Ge in the germanium crystal of the C5 detector in reactor on during run 1.

hand plot in Figure 3.39. In rare cases it can also happen that the emission of the 13.3 keV γ happens very late, which leads to a small peak in the spectrum. Figure 3.40 shows the background contribution of this metastable state to the spectrum of the C5 detector during reactor on in run 1.

Lastly, ^{75m}Ge is considered. As shown in Figure 3.37 it decays to its ground state vie emission of a 139.7 keV γ-ray, which is also visible in the CONUS+ spectra. The resulting background contribution is shown in Figure 3.41.

3.8.2 Contributions of copper

The most important copper parts to be considered in this section are the copper parts closest to the germanium crystals: the cryostats and the crystal holders. These parts have a total mass of approximately 2 kg.

Of the cosmogenically activated isotopes that were discussed for germanium in the previous section, three isotopes are also relevant for the copper parts of the CONUS+ setup: ^{57}Co, ^{60}Co, and ^{54}Mn. The same decay schemes and emissions as in germanium apply in copper with small corrections in the case of ^{57}Co. Here, the previously discussed summation peak at 143 keV is unlikely to be seen from decays happening in copper parts of the setup since the X-rays and 14.42 keV γ-rays have too little energy to reach the active volume of the germanium diodes. Instead, the single γ peak at 122 keV is most likely to be seen. However, as was the case for the summation peak in germanium, this peak is also not observed in any of the CONUS+ detectors. An important difference in the case of cosmic activation of

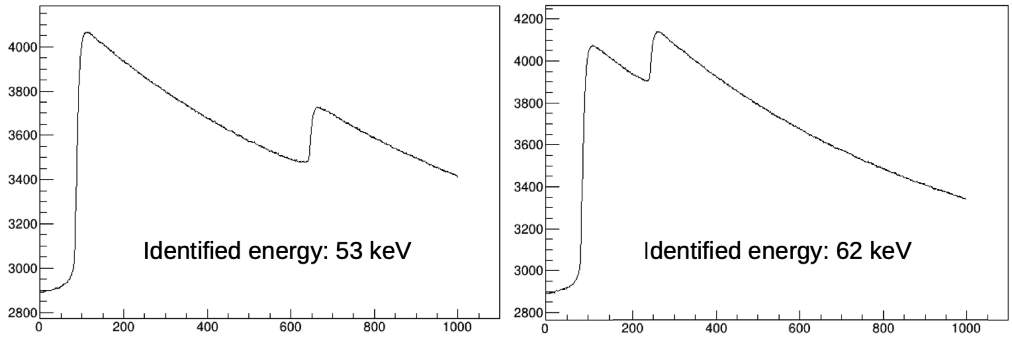

Figure 3.39. Explanation of the shape of the double-peak structure visible in the spectrum of ^{73m}Ge. Left: After the first event (the emission of the 53 keV γ) the second event (13.3 keV) happens in very close succession. The energy of the whole event is reconstructed at the maximal height of the recorded pulse, leading to a value between 53 and 66 keV. Right: The second pulse arrives later, after the first pulse has already sufficiently decayed. The highest point in the pulse is still the maximum of the first pulse, the reconstructed energy is therefore just the energy of the first γ.

these isotopes in copper as opposed to germanium are their much higher production rates as can be seen from Table 3.13. This is due to their closer similarity to copper in terms of mass number, meaning that fewer nucleons have to be freed from the nucleus in a spallation reaction with cosmic rays. Therefore, a considerably higher abundance of these isotopes in copper should be expected for similar lengths of cosmic ray exposure. This effect is somewhat mitigated by the distance of the copper parts to the germanium diodes in the setup, meaning that higher activities in these parts do not necessarily lead to backgrounds that are much higher than those from activities in the germanium crystals themselves. Formula 3.8 can again be used to calculate estimated activities in the cryostats. Here, an exposure of 100 days is assumed again. Figure 3.42 shows the background contribution of these three isotopes in comparison to C5 data taken in run 1 during reactor on. It can be seen that the contribution from comic activation in the copper parts to the background in the detectors is small compared to the total background in the detector.

Table 3.13. Production rates of different cosmogenically induced isotopes with no visible lines in the CONUS+ spectrum in copper. Values in the table are taken from [12]

Isotope	Half-life [d]	Production rate in copper [atoms d^{-1} kg^{-1}]]
^{57}Co	271.8	55 ± 19
^{60}Co	1923.6	46 ± 26
^{54}Mn	312.2	16 ± 7

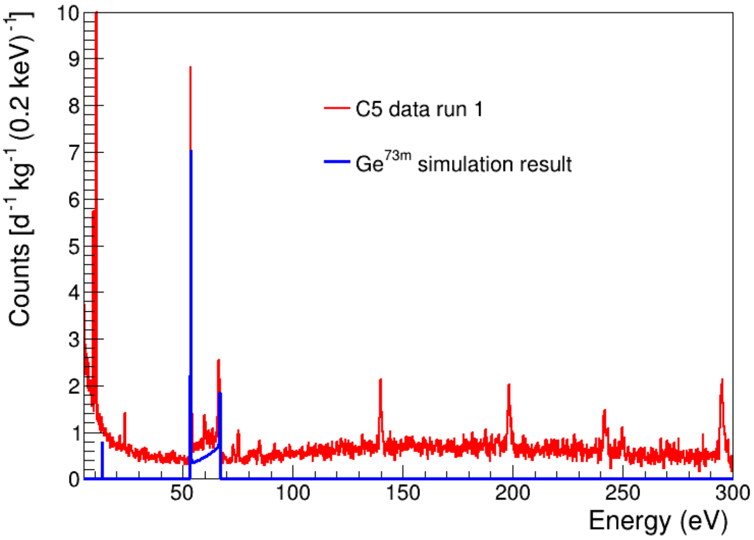

Figure 3.40. Simulation result for the background contribution of the metastable state ^{73m}Ge in the germanium crystal of the C5 detector in reactor on during run 1.

3.9 ^{210}Pb in lead

^{210}Pb is a naturally occurring radioactive isotope of lead. It generally poses a significant challenge to all kinds of low background experiments due to the popularity of lead as a shielding material against γ-rays. It is a decay product of the ^{238}U series and can be accumulated in lead samples in the smelting process and the production of lead bricks, leading to contaminations of several thousands of Bq/kg being common in standard lead. In the field of low background physics, such as for the CONUS+ experiment, the use of low background lead, meaning lead with a low ^{210}Pb content is generally favoured, especially for lead parts close to the detectors. These low-background lead samples can often achieve ^{210}Pb contaminations down to 1 Bq/kg, with the cleanest lead being found in archaeological samples. Examples of such archeological lead include lead found on sunken roman galleys in the mediterranean [89] or lead from old church roofs. The latter was also used for the innermost layer of lead bricks in the CONUS and CONUS+ experiments, which partially consists of old lead from the Freiburg minster [12].

Figure 3.43 shows the decay chain of ^{210}Pb. It first decays into ^{210}Bi via β-decay (Q = 0.06 MeV), which in turn decays into ^{210}Po with a half-life of 5 days via β-decay (Q = 1.16 MeV). Both of these decays are highly relevant backgrounds for the CONUS+ experiment. ^{210}Po decays via α-decay into the stable ^{206}Pb. This decay is not as relevant for the background model due to the extremely small interaction length of α particles. Only a contamination directly on the surface of the germanium detectors could possibly lead to visible

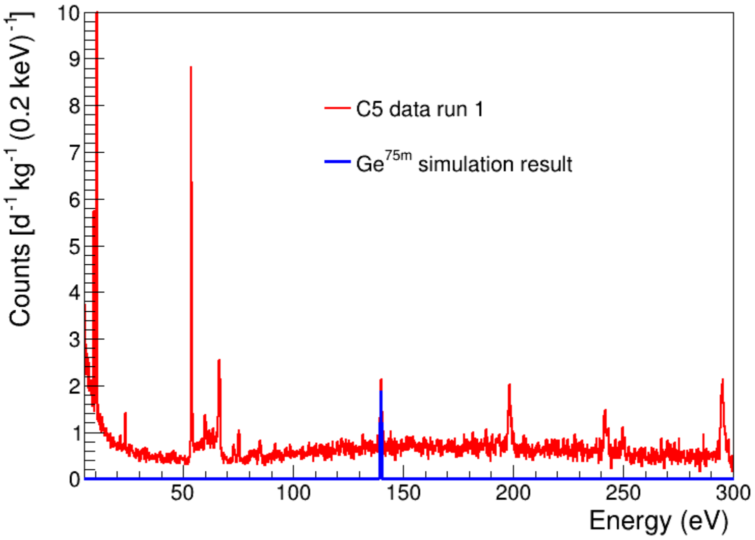

Figure 3.41. Simulation result for the background contribution of the metastable state ^{75m}Ge in the germanium crystal of the C5 detector in reactor on during run 1.

background from this decay.

3.9.1 ^{210}Pb in the shield

The shield setup of CONUS+, as described in Section 2.4.2, consists of several layers of lead. For the consideration of the effect of ^{210}Pb in these layers on the background of the four detectors only the contaminations inside of the first layer play a significant role due to the self-shielding of the inner lead layers. Before the installation of the original CONUS experiment, the lead bricks used in the shield setup were extensively screened using the GIOVE material screening station at the MPIK in Heidelberg [49]. On average, a ^{210}Pb activity of < 1.7 Bq kg^{-1} was found for bricks used in the innermost layer. These measurements were performed in 2017. Using the half-life of ^{210}Pb of 22 years, the activity of these bricks in 2023, before the installation of CONUS+ in Leibstadt, can be estimated to be < 1.4 Bq kg^{-1}. This value is used for the simulation of the background contribution of ^{210}Pb in the shield. The results can be found in Figure 3.44. In the right hand plot, the contribution of the different sides of the shield to the overall total ^{210}Pb shield background can be seen. It is not surprising, that in this comparison the sides closest to the individual detectors, in this case the bottom of the chamber and side 1 (for C5), make up the biggest part of the total. The overall contribution of ^{210}Pb in the shield to the spectrum of the detectors is small (see left hand plot in Figure 3.44), especially compared to the main background contributions like cosmic muons and neutrons. In the ROI for the CEνNs search of CONUS+, it contributes only approximately 0.2 % of the total background in the separate detectors.

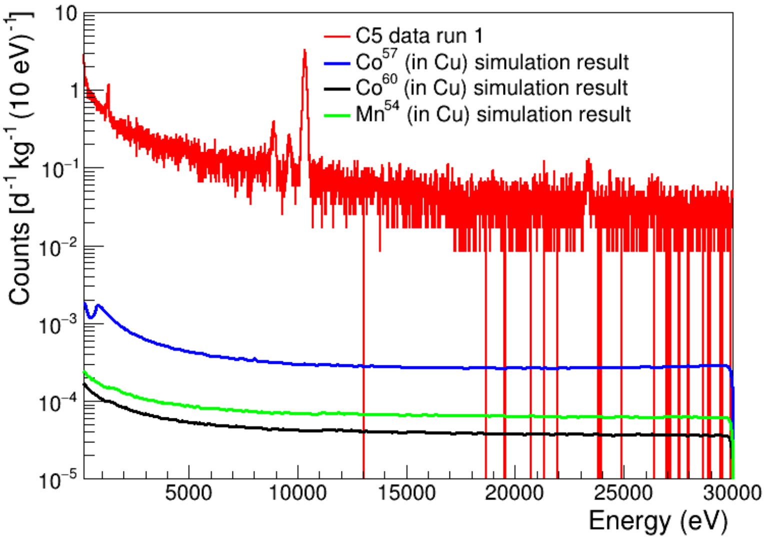

Figure 3.42. Background contributions from cosmogenically activated isotopes in the copper parts of the setup. Their corresponding activities were calculated from Table 3.12 and Formula 3.8 assuming an exposure of 100 days.

3.9.2 ^{210}Pb in the cryostat

In the background decomposition of the predecessor experiment CONUS in [12], it was found that a significant part of the background of the four detectors (up to 50 %) was comprised of ^{210}Pb within the cryostat. Several potential sources of these contaminations were identified, with the most likely candidates being solder used in the assembly of the insides of the cryostat and surface contaminations directly on the germanium diode. Soldering wire is known to often contain large ^{210}Pb contents of up to 50 kBq/kg, while surface contaminations on the diodes can accumulate during the construction of the detectors from depositions from radon decay from the surrounding air. The most prominent signature pointing to the presence of ^{210}Pb in the cryostat was the presence of the 46.5 keV line from the decay of ^{210}Pb, which, at the time, was observed in all detectors. This line cannot be generated by ^{210}Pb decays outside of the cryostat due to the shielding of the cryostat itself. Figure 3.45 shows this line in the C1 detector in the CONUS experiment. In addition of the effect of the β-decays in the ^{210}Pb chain, the α-decay of ^{210}Po can also cause background contributions in case the contamination is located on the passivation layer of the crystal, the isolation between the p and n contact of the diode (see Section 2.3). On all other sides of the detector, the dead layer with its thickness in the order of 0.5 mm is enough to shield α-particles from the decay with their range of <20 μm. Compared to the dead layer, the passivation layer is much thinner of the order of 100 nm, and is therefore not enough to shield these α particles entirely.

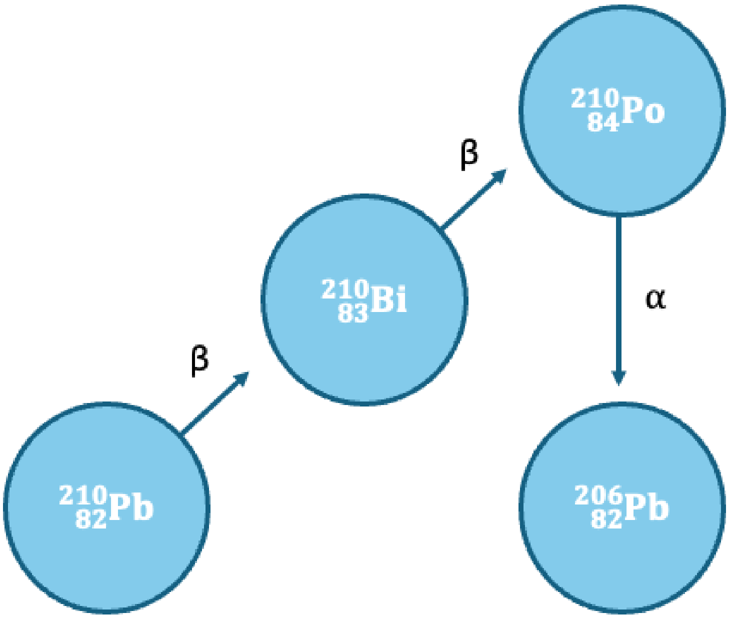

Figure 3.43. Decay chain of ^{210}Pb.

The 46.5 keV line is not visible in any of the four detectors in the CONUS+ experiment as is shown in Figure 3.46 for the C5 detector. This points to an absence or at least to a great reduction of ^{210}Pb in the cryostat compared to the previous CONUS experiment. It can be assumed that this is due to improved procedures in the assembly of the new detectors during the detector upgrade (see Section 2.3.7) in 2023 at Mirion, Lingolsheim, which is possible because of the previous experience of working on the original CONUS detectors. This is a trend which was already visible in the CONUS detectors themselves as is discussed in Section 5.6.2 of [2]. Here, it could be seen that the ^{210}Pb contamination in the cryostat of the C1 detector, which was the first detector that was built for CONUS by Mirion, was considerably higher than that of the other three detectors. Additionally, great care was taken in the selection of an appropriate soldering wire before the CONUS+ detector upgrade, where several commercially available types of solder were screened for their ^{210}Pb content and the sample with the lowest content was chosen for the upgrade.

For the background model of CONUS+, an upper limit on the amount of ^{210}Pb on the germanium diode is placed by estimating an upper limit on the counts in the 46.5 keV lines based on the statistical uncertainty in the relevant bins of the measured spectra. In this way an upper limit of $< 10\ \mu$Bq is calculated. The resulting spectrum is shown in Figure 3.47.

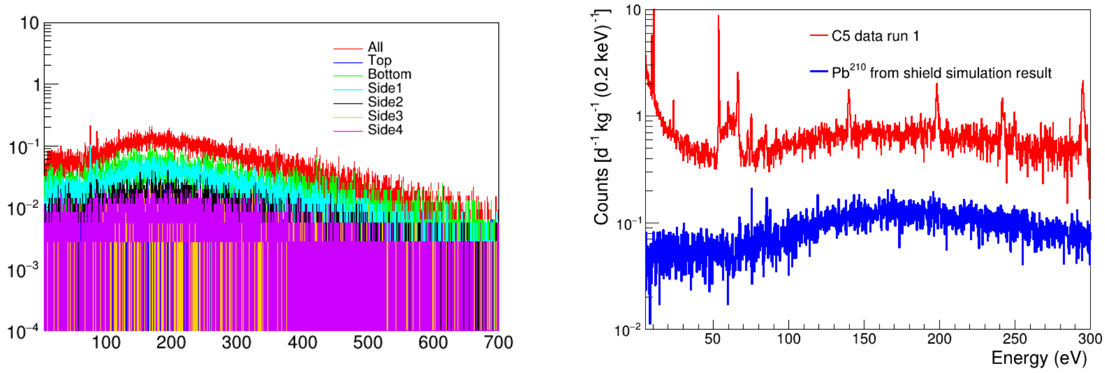

Figure 3.44. Simulation result for ^{210}Pb in the innermost shield layer. Left: Contribution from different sides to the total ^{210}Pb background from the shield. Right: Comparison of total to the spectrum of the C5 detector in reactor on measurement in run 1.

3.10 Additional contaminations inside the cryostat

In the study of the complete background model, which will be detailed in Section 3.14, it was found that after including all investigated background components for the C2 and C3 detectors a background contribution was still missing. The missing counts for both detectors in different energy regions are shown in Table 3.14. The missing count rates in all energy ranges are consistent in both reactor on and off measurement, indicating the presence of an additional background source like a material contamination with a long half-life which was previously not considered. Furthermore, all the γ-lines in the spectrum are accounted for by the described cosmogenic activities in Section 3.8 and radon, meaning that the missing background component does not produce any lines in the CONUS+ spectrum from 0.16 to approximately 350 keV.

Table 3.14. Missing count rates in the background model of the C2 and C3 detectors for different energy ranges.

Energy range	Missing rate in C2 (counts $\mathrm{d}^{-1}\,\mathrm{kg}^{-1}$)	Missing rate in C3 (counts $\mathrm{d}^{-1}\,\mathrm{kg}^{-1}$)
$[0.4, 1]$ keV	~ 4	~ 4
$[2, 8]$ keV	~ 19	~ 16
$[15, 30]$ keV	~ 15	~ 13
$[30, 100]$ keV	~ 40	~ 32
$[100, 250]$ keV	~ 40	~ 33

In order to find the cause of this missing background a number of different hypotheses were tested, most of which like a slightly higher muon or neutron flux in the room can be

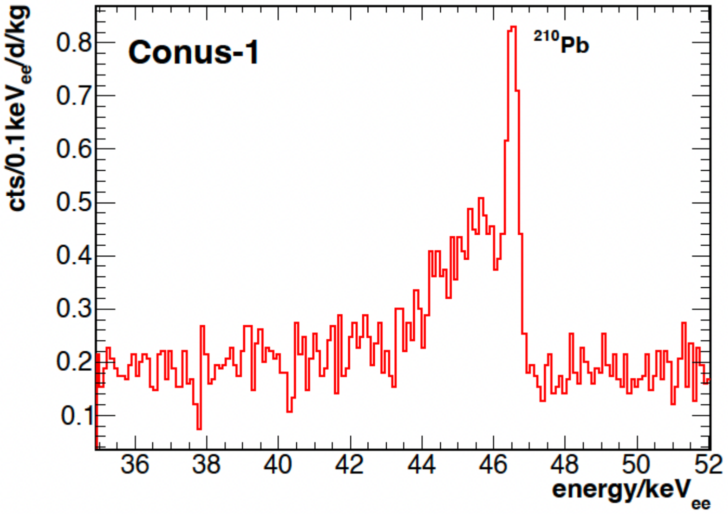

Figure 3.45. 46.5 keV line from the decay of ^{210}Pb in the cryostat in the C1 detector in the CONUS experiment from [2].

easily excluded due to the shape of the missing background. In the end, it was found that both the shape and the count rates of the missing component can be very well described by the presence of an additional β-decaying isotope in the detector cryostats in close proximity to the germanium crystals on the side of the passivation layer. A number of possible isotopes were tested including ^{210}Pb, which can be excluded due to the absence of the 46.5 keV line as described in the previous section.

The most likely isotope which was found to induce the necessary shape in the background spectra and feature no lines in the energy range of CONUS+ was found to be ^{60}Co. As seen from Table 3.13, its life-time is several times larger than the ones of the other commonly cosmogenically activated isotopes in copper at approximately six years. meaning that a small contamination from previous exposures to cosmic rays could be present in copper parts very close to the germanium crystals of C2 and C3. It was found that an activity of only approximately 5 μBq of ^{60}Co is enough to induce the missing background shape and count rates, making it a very likely candidate. The resulting spectrum of this background source is shown in Figure 3.48.

3.11 Leakage test background

During the decomposition of the background spectra of C2 and C3 an additional missing background at low energies (below 1 keV) was identified, which was equally large in both reactor on and off measurements. These two detectors were part of the previous CONUS experiment at the KBR power plant in Brokdorf. During the life time of CONUS, in particular

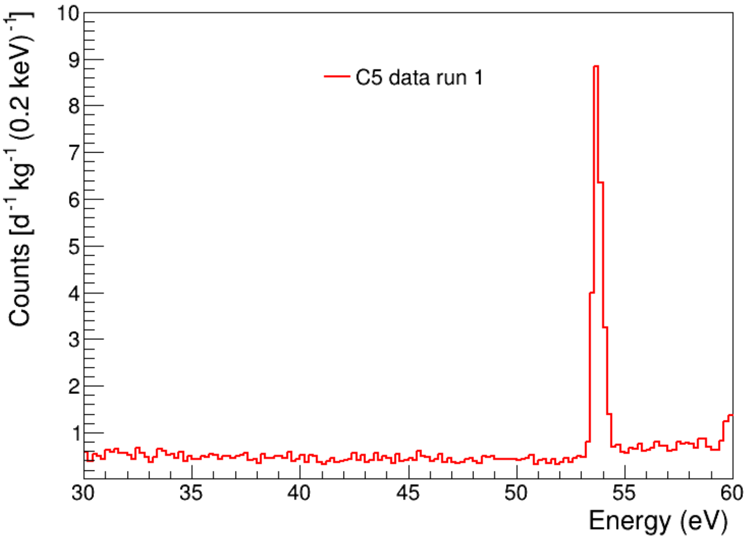

Figure 3.46. High energy data taken during run 1 of the CONUS+ experiment with the C5 detector. No line at 46.5 keV is visible, pointing to the absence of ^{210}Pb from the inside of the cryostat.

before the start of run 5, its last data taking period, the KBR power plant performed a leakage test in the containment area of the reactor building. In such a test, the tightness of the containment structure is tested by setting the whole containment vessel under an overpressure in order to check for leaks of the containment structure to the outside. Due to potential damage of this overpressure to the CONUS detectors, the vacuum inside the cryostats of the four detectors was replaced by pure gaseous argon. After removal of the argon and a return to regular data taking conditions, it was observed that the background of the four detectors was increased in the energy range below 10 keV by up to a factor 2 [48]. This new background was consistent over time and also present during reactor off data taking. At the time, large efforts were undertaken to identify the source of this new background by performing rest-gas analyses on the four detectors and testing several different hypotheses in simulations. No hint to any new radioactive contamination was found and no possible explanation could be identified in the simulations. As a consequence, the background models for the CEνNS analysis of run 5 of the CONUS experiment included an analytical function to describe the new background source, thereafter called the ”leakage test background”. The function was not directly included in the background model and was instead included in the likelihood analysis of the data by introducing two new parameters which were then fitted in the minimisation of the likelihood function. Different functions were tested and it was found that an exponential increase towards low energies best describes the additional background:

$$b_{Leak}(E) = \theta_1 \cdot e^{-\theta_2 \cdot E} \tag{3.9}$$

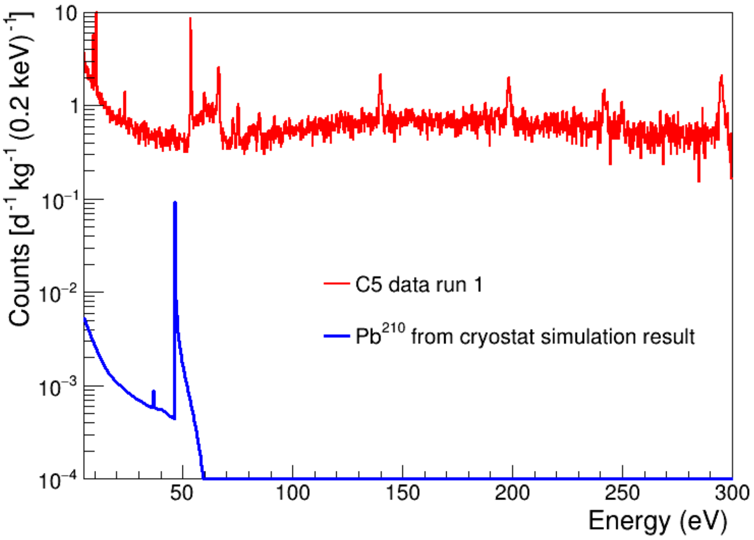

Figure 3.47. Simulation result of the ^{210}Pb contamination on the germanium diode of C5 with the calculated upper limit on the activity of 10 μBq.

The parameters θ_1 and θ_2 were the two parameters included in the likelihood function for run 5 of the CONUS experiment. Gaussian pull terms were placed on them based on additional data taken with another DAQ system which ran in parallel to the main CAEN DAQ system of CONUS. This leakage test background is a likely candidate for the missing background in C2 and C3 as it follows the same shape and is also consistent during reactor on and off time. For this reason the same function in Equation 3.9 was used to model an additional background contribution in both reactor on and off data for these two detectors. Compared to its impact in the CONUS experiment, the leakage test background is not as large in run 1 of the CONUS+ experiment, resulting in a reduced impact for energies above 1 keV. Nevertheless, the added background is needed in order to fully understand the background of the C2 and C3 detectors as will be seen in Table 3.17 - 3.20.

3.12 Reactor backgrounds

The last category of background contributions which have to be considered for the background model of the CONUS+ detectors are reactor backgrounds. These are contributions which are directly induced by the nuclear reactor of the KKL power plant and they can be correlated to the operation mode of the reactor. In cases where the reactor backgrounds are positively correlated with the reactor power (like for reactor neutrons), these contributions are especially important to consider, since they can potentially mimic the CEνNS signature in the measured spectra and be mistaken for the desired signal.

Two main backgrounds have to be taken into account in the following: neutrons from the re-

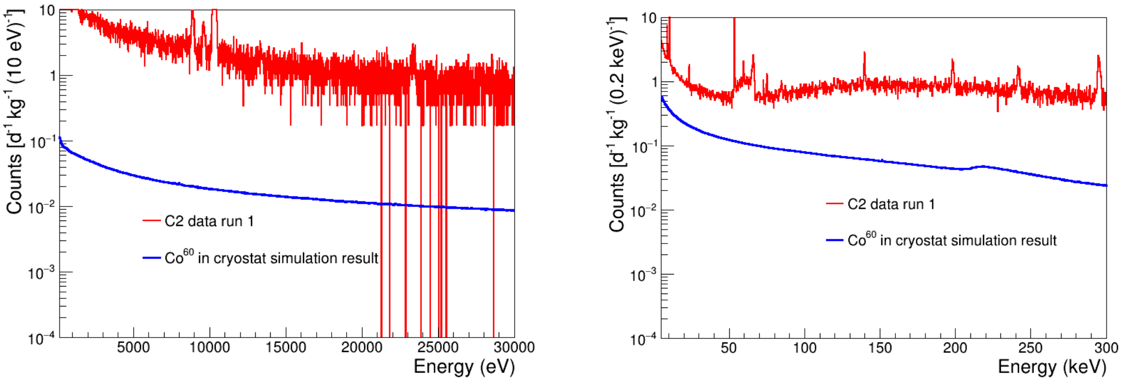

Figure 3.48. Simulation result of a 5 μBq ^{60}Co contamination in close proximity to the germanium crystal of C2. The spectrum matches the missing background component in the C2 and C3 background model.

actor, which are present only during active operation of the detector, and certain inert gases which are released when the reactor is opened during reactor off times.

3.12.1 Reactor neutrons

As described in Section 2.4.1, a constant flux of reactor neutrons is expected at locations in close proximity to a nuclear reactor. These neutrons are produced in fission reactions inside the fuel elements of the reactor and are needed to maintain the power production of the reactor core.

These neutrons can be especially problematic for the CEνNS search of the CONUS+ experiment since they can also scatter elastically off of the Germanium nuclei of the CONUS+ detectors. In this way, they can exactly mimic the signature of the expected neutrino signal. They are also only present during reactor on measurements, which can make their distinction challenging. For the CONUS experiment at the KBR power plant in Brokdorf, Germany, it was found that the impact of reactor neutrons is negligible in all energy regions due to the extremely powerful neutron suppression capabilities of the shield and its layers of polyethylene and borated polyethylene [12]. However, as detailed in Section 3.2.3, the neutron flux found at KKL is considerably larger than the one found at KBR and the impact of this background is therefore simulated again in the following.

Figure 3.9 shows the spectrum of neutrons measured during reactor on times with the Bonner sphere array of PSI. It can be assumed from the measurements during reactor off times, as well as the simulations in 3.5.1, that this spectrum is almost entirely composed of reactor neutrons due to their large abundance compared to the very small flux of cosmic neutrons in the room for all energies below approximately 20 MeV. The small peak that can be seen at around 100 MeV is due to cosmic neutrons, which have already been considered in Section 3.5. Additionally, the uncertainty on this peak in the measured spectrum in reactor on times is large (see 3.1). Consequently, the spectrum up to 20 MeV will be used as input for a simulation where 10^{10} neutrons are started isotropically from a half-sphere around the CONUS+ shield with a radius of 1.5 m. This number of neutrons is approximately equal to the expected number of neutrons in five days.

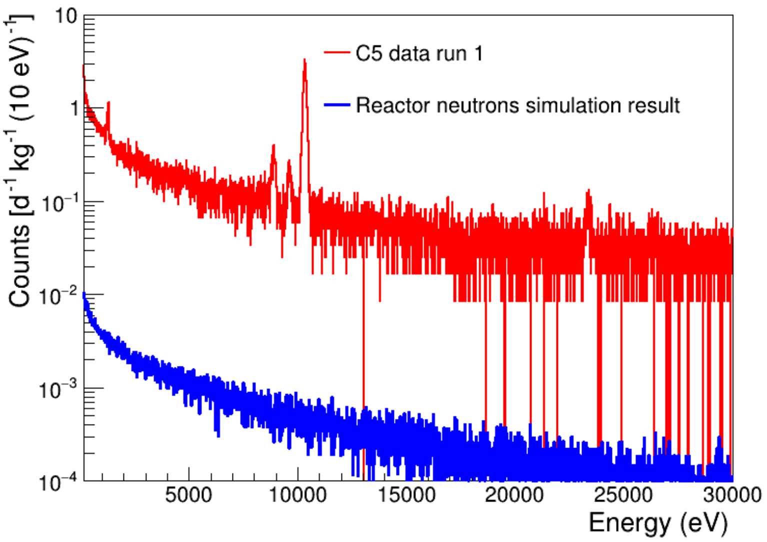

Figure 3.49. Simulation result of the reactor neutrons compared to the C5 spectrum during reactor on measurement.

Figure 3.49 shows the result of these simulations in comparison to the spectrum of C5 during reactor on in run 1. As expected, a very similar spectral shape to the one found for the background contribution of comic neutrons is found with a distinct increase towards low energies. However, the contribution is very small compared to that of cosmic neutrons which is approximately two orders of magnitude bigger. The reactor neutrons contribute around (0.2 ± 0.1) counts d^{-1} kg^{-1} in the energy region between 0.4 and 1 keV, which is well below 1 % of the total background in this region. Their impact is still sub-dominant, however it is about 20 times larger than what was found in the CONUS experiment, which is consistent with the higher reactor neutron flux in the CONUS+ location. The impact between 160 eV and 400 eV, where the CEνNS signal is present, is also (0.2 ± 0.1) counts d^{-1} kg^{-1}. Compared to the signal itself, which is expected to be around 1 to 1.5 counts d^{-1} kg^{-1} depending on the detector (see Table 4.12), the influence of reactor neutrons is therefore also still subdominant.

3.12.2 Inert gases

The second reactor background considered in the CONUS+ background model are inert gases (noble gases) produced in the reactor core. These gases can be produced as radioactive isotopes and escape the reactor core when it is opened during reactor maintenance. They can then diffuse into the CONUS+ shield, similarly to radon, and can therefore effect the background model of reactor off data as well as that of reactor on data in the case of long-lived isotopes. The most important of these radioactive gases are ^{3}H, ^{85}Kr, and ^{135}Xe. In addition, ^{41}Ar, is also produced and can escape, however, it features a very short half-live of 1.8 h and therefore has negligible impact on CONUS+ data.

^{3}H can be produced in reactor cores as a direct product of fission reactions of ^{235}U, although this production is rare. More importantly, it can be produced through direct interactions of neutrons with boron used as a neutron control material:

$$^{10}B + n \rightarrow \ ^{3}H + 2\alpha \tag{3.10}$$

Additionally, it can be produced from neutron capture on deuterium.
^{3}H decays via β-decay without emission of a γ-rays. Its endpoint energy is 18.6 keV making it especially relevant for low energy experiments like CONUS+. Furthermore, it has a half-live of 12 years, meaning that a ^{3}H contamination can be present in the air of the containment area of the reactor long after the opening of the reactor core.

^{85}Kr can be produced in reactor cores as a direct fission product from ^{235}U, ^{239}Pu, and other fissile isotopes ($\sim$ 0.3 % per fission). It decays via β-decay to ^{85}Rb, which is stable, and has a half-life of 11 years. In very rare cases ($\sim$ 0.43 %) it can decay to an excited state of ^{85}Rb, which emits a γ-ray of 514 keV (above the sensitive energy range of CONUS+).

Lastly, ^{135}Xe can also be produced as a direct fission product of fissile isotopes ($\sim$ 0.3 % per fission). However, the dominant production mechanism is from the decay of ^{135}I, which has a higher yield ($\sim$ 6.5 % per fission). It decays via β-decay to ^{135}Xe, which has a half-life of 9 hours. This short half-life means that the impact of ^{135}Xe is largely confined to the first few days after the opening of the reactor core. ^{135}Xe can decay to an excited state of ^{135}Cs, which decays to the ground state by emitting a γ-ray with an energy of 250 keV. This line is visible in the CONUS+ data for all detectors, primarily in the spectra taken during reactor off measurement.
The activities of these radioactive isotopes in the air of the containment area are constantly being monitored by KKL in order to ensure safe working conditions inside the reactor build-

ing. Unfortunately, it was not possible to gain access to this information and the exact impact on the CONUS+ background had to be assessed differently. In simulations, all three gases were distributed homogeneously inside the detector chamber of the setup. For ^{135}Xe, the resulting simulated spectrum was scaled such that the count rate in the 250 keV line is equivalent to that found in the spectra for the different detectors in both on and off measurement. Since both ^{85}Kr and ^{3}H feature no lines in the CONUS+ energy range, their contribution was estimated based on the known yield of the separate isotopes per fission compared to that of ^{135}Xe. The resulting background contributions are shown in Figure 3.50 for the C5 detector during reactor off measurement. For comparison, the result for reactor on measurement in C2 and C3 is shown in A.5 and A.6. It can be seen that the contributions from ^{135}Xe and ^{85}Kr are very small compared to the total background count rate, while the contribution from ^{3}H is noticeable for energies below 18 keV.

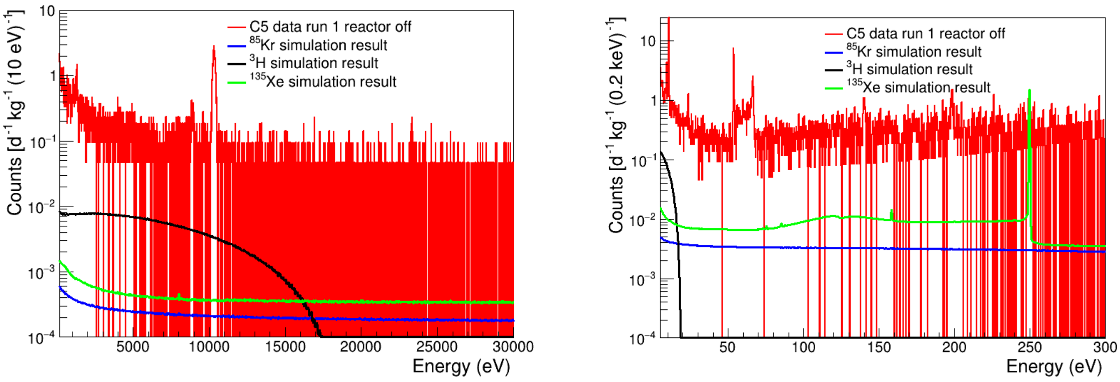

Figure 3.50. Simulation result of ^{3}H, ^{85}Kr, and ^{135}Xe and their impact on the background of the C5 detector in reactor off measurement during run 1.

3.12.3 High energy γ radiation

As seen from Section 3.2.1 and Figure 3.2, the CONUS+ room features high energy γ radiation produced from neutron activation of materials in the reactor building. In order to test the possible impact of this radiation on the background of the four detectors, 10^{10} γ particles with an energy of 10 MeV were started from a point source (a ”particle gun”) on the outside of the CONUS+ shield in the direction of the centre of the shield in MaGe. No impact in the detectors was found in the simulations, indicating the ability of the shield to effectively shield all γ radiation.

3.13 Model differences between reactor on and off measurement

In the discussion of the background components of the CONUS+ experiment in the sections above, only the background during reactor on measurement was considered so far. However, as described in Section 3.1, the background model also needs to be able to describe the spectra measured during the reactor outage in order to verify the model and perform the likelihood analysis on both on and off spectra.

In order to build a correct model for the reactor off spectra, the differences in the experimental setup during this time have to be considered.

3.13.1 Impact of drywell lid

As described in Section 2.1, the major difference in the CONUS+ experimental location between reactor on and off measurement is the placement of the drywell lid directly above the CONUS+ room. The lid, which is part of the pressure vessel which houses the reactor core, is removed during reactor maintenance in the yearly outage period. It has a thickness of 3.8 cm and is made of steel, effectively adding an additional overburden of 0.3 m w.e. to the experimental location. As can be expected, this has consequences for the flux of both cosmic muons and neutrons arriving in the room. In order to quantify this effect, the model of the reactor building introduced in Section 3.5.1 and shown in Figure 3.24 was again used for simulations. In the model, the drywell lid was approximated as a flat steel disc with a radius of 3 m and the appropriate thickness of 3.8 cm. As previously described, muons and neutrons with the appropriate energy spectra and angular distributions were again started from outside the reactor building and the muons and neutrons arriving in the room were tracked.

The simulations show a reduction of 19% in the neutron flux and 3% in the muon flux compared to the situation without the drywell lid. Consequently, these background contributions have to be reduced by 19 and 3% compared to the values and spectra presented in Sections 3.5 and 3.4. Additionally, simulations were performed in which high energy gammas of 10 MeV were started from the position of the lid above the CONUS+ room to assess the effect that possible radioactivity from the lid could have on the experiment. No impact on the CONUS+ background was found due to the excellent shielding from the concrete ceiling and the CONUS+ shield itself.

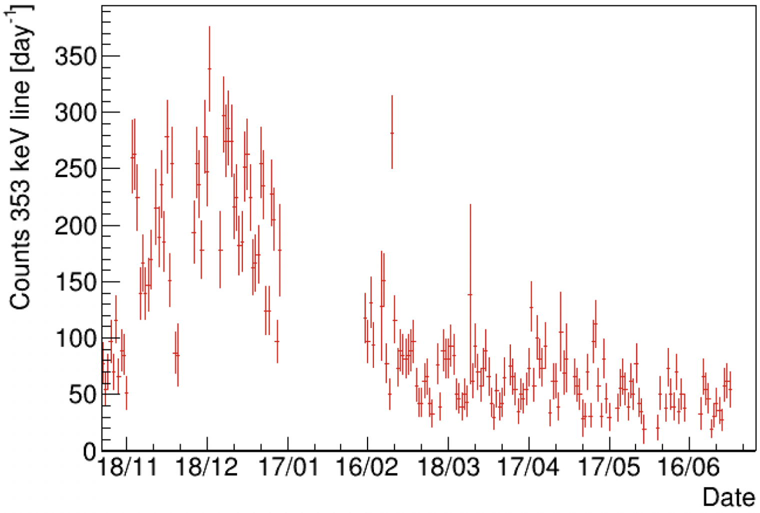

Figure 3.51. Evolution of the radon contamination in the detector chamber shown through the count rate in the 353 keV line in C2. The reactor off measurement was in May, where the radon contamination was considerably lower than for most of the on measurement.

3.13.2 Reduced radon contamination in off measurement

Figure 3.51 shows the evolution of the radon contamination in the detector chamber of the CONUS+ experiment, represented by the count rate in the 353 keV line in the C2 detector over time. The evolution of the line clearly shows lower radon contaminations during the reactor off measurement (May of 2024) compared to most of the reactor on measurement (before May). The reason for this lower radon concentration later in run 1 was better understanding and fine-tuning of the radon-free air flushing system, which was gradually acquired in the early stages of the experiment. Consequently, the radon contribution in the reactor off spectra of the CONUS+ detectors has to be scaled down in order to describe the data. The correct scaling is again found by comparing the count rates in the radon induced lines between simulation and data, as described in Section 3.7.

3.13.3 Reactor-correlated background sources

The last difference between reactor on and off measurement is the difference in background sources directly originating from the reactor (Section 3.12). While the reactor neutrons described in Section 3.12.1 are completely absent from the reactor off spectra, the impact of the inert gases can be higher during this time. This is due to the fact that these gases are only released when the reactor core is opened for maintenance at which point they enter the containment area and can diffuse into the CONUS+ shield. The main change between reactor on and off measurement can be observed in the contribution from ^{135}Xe due to its short half-life of only 9 hours. This means that the background coming from this isotope is mainly relevant in the first few days after the opening of the reactor and therefore considerably higher in the reactor off spectra. The difference in contributions coming from ^{85}Kr and ^{3}H is negligible due to their long half-lifes.

3.14 The full background model

The previous sections have explained and discussed all possible background sources for the CONUS+ experiment. First, the results of a number background characterisation measurements which were performed prior to the installation of CONUS+ at KKL were presented. The results of these measurements as well as knowledge about material contaminations and the precise understanding of the experimental setup were then used as input to perform Monte Carlo simulations in order to assess the impact of all known background sources. In a last step, the results of these simulations have to be added up and compared to the actual measured data to verify the validity of the presented model.
Figures 3.52 - 3.57 show the complete background model for the C5, C2, and C3 detectors in both reactor on and off measurement with all individual components discussed in the previous chapters. It can be seen that the overall background model in red shows very good agreement with the measured data in black. Additionally, Tables 3.15 - 3.20 show the full decomposition of the background model in different energy regions for all three detectors in reactor on and off measurement. The values for the lowest energy region up to 400 eV are not listed for reactor on data since this energy region is where the CEνNS signal is expected to appear. This region was blinded to avoid introducing biases ahead of the analysis detailed in the next chapter. The decomposition shows that at energies below 1 keV in the region of interest of CONUS+ the most prominent background contributions come from cosmic rays, namely muons and neutrons, which make up about 70 - 80% of the total background. At high energies above 100 keV, the influence of cosmic neutrons and muon-induced neutrons decreases significantly, while the impact of the electro-magnetic component of the muonic background is still relevant. At these energies, the background contribution from radon inside the detector chamber is dominant which is especially visible in the decomposition of the reactor on background spectra, where radon flushing was not as effective.

The comparison between data and model in the different energy regions listed in Tables 3.15 - 3.20 for all detectors in reactor on and off and the excellent agreement in Figures 3.52 - 3.57 show the success of the discussed Monte Carlo simulations and methods in decomposing and understanding the background of the CONUS+ experiment. The only energy region where deviations between model and data are observed in some detectors (e.g. C5 off, C3 on) is the [100, 250] keV region. These deviations likely occur because of the efficiency corrections of the high energy channels, detailed in 3.4.2. For a more simplified comparison between data and model for the different detectors, Figure

As discussed in Section 3.1, the understanding and decomposition of the CONUS+ background allows for the use of the background model in the analysis of the CONUS+ data and the final likelihood fit in order to achieve the goal of the experiment and find the CEνNS signal.

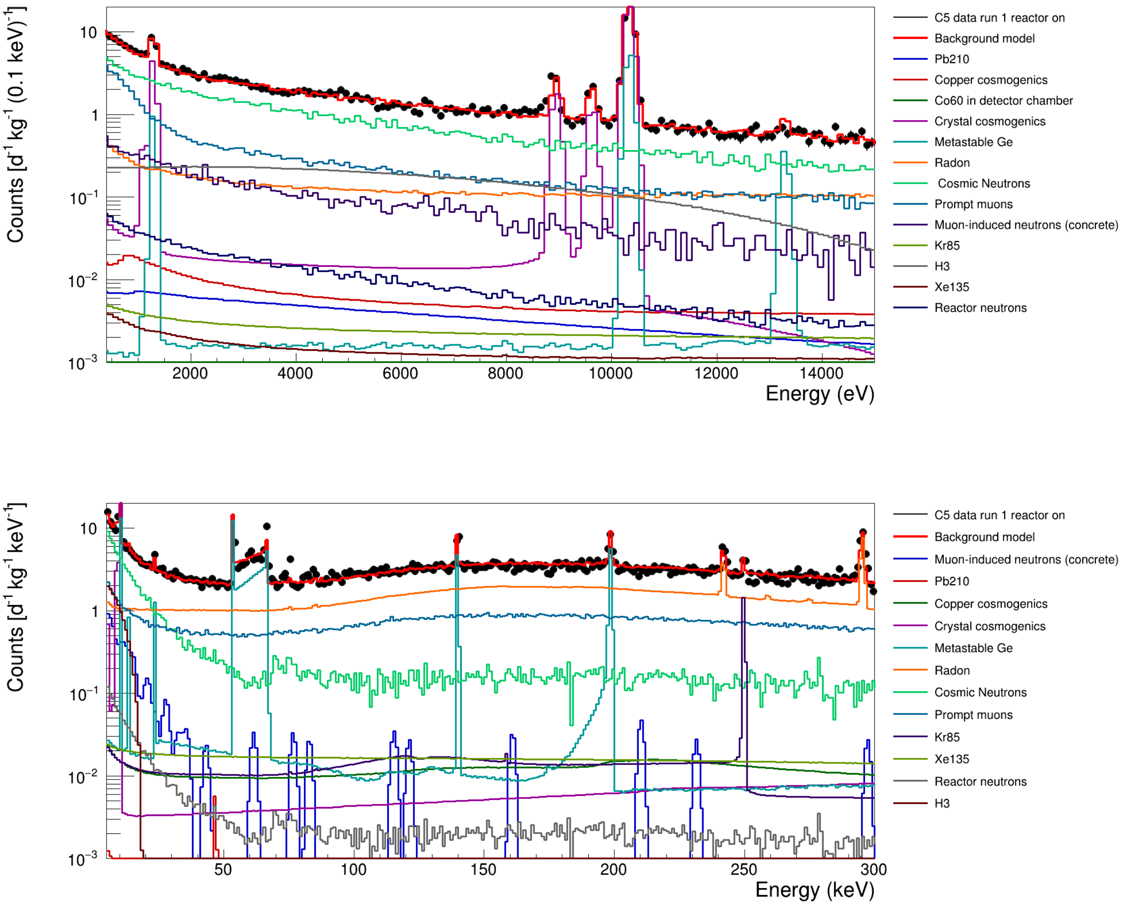

Figure 3.52. Complete background model and separate components for the C5 detector in reactor on measurement.

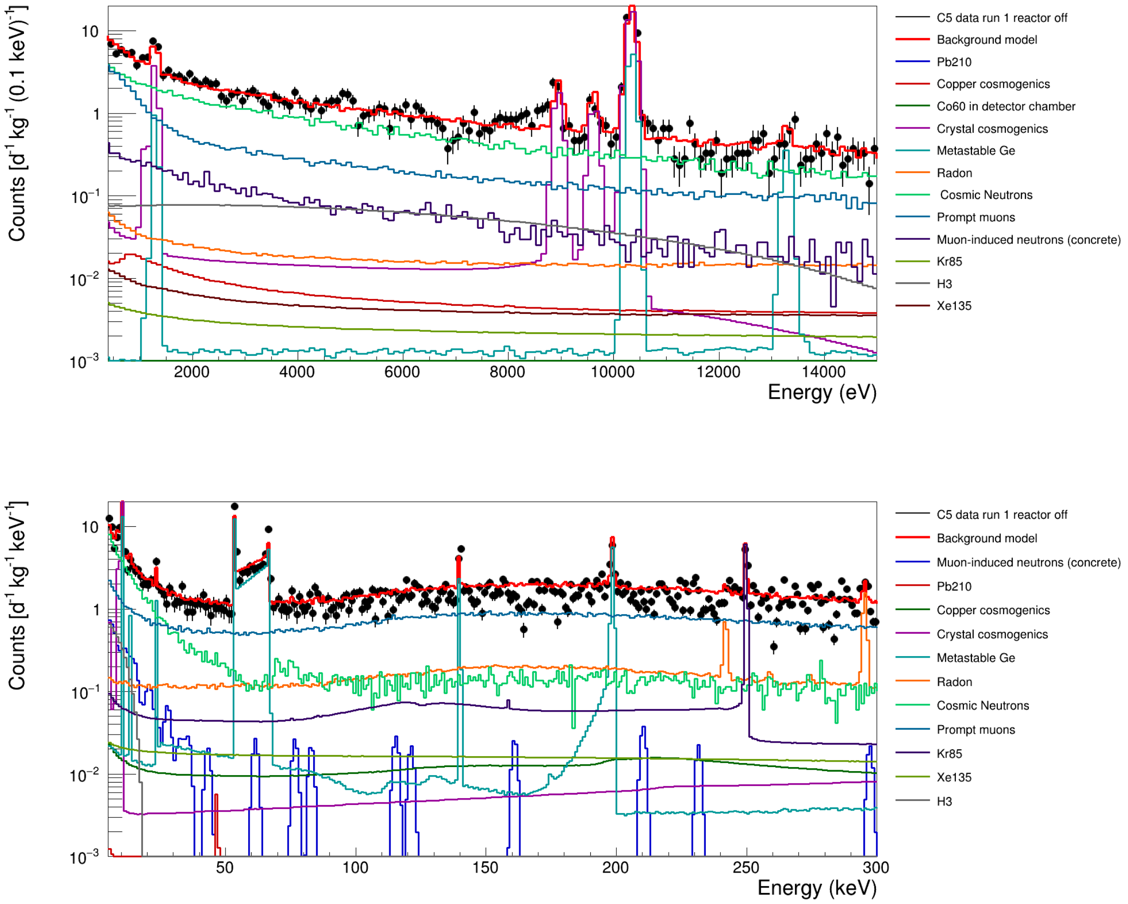

Figure 3.53. Complete background model and separate components for the C5 detector in reactor off measurement.

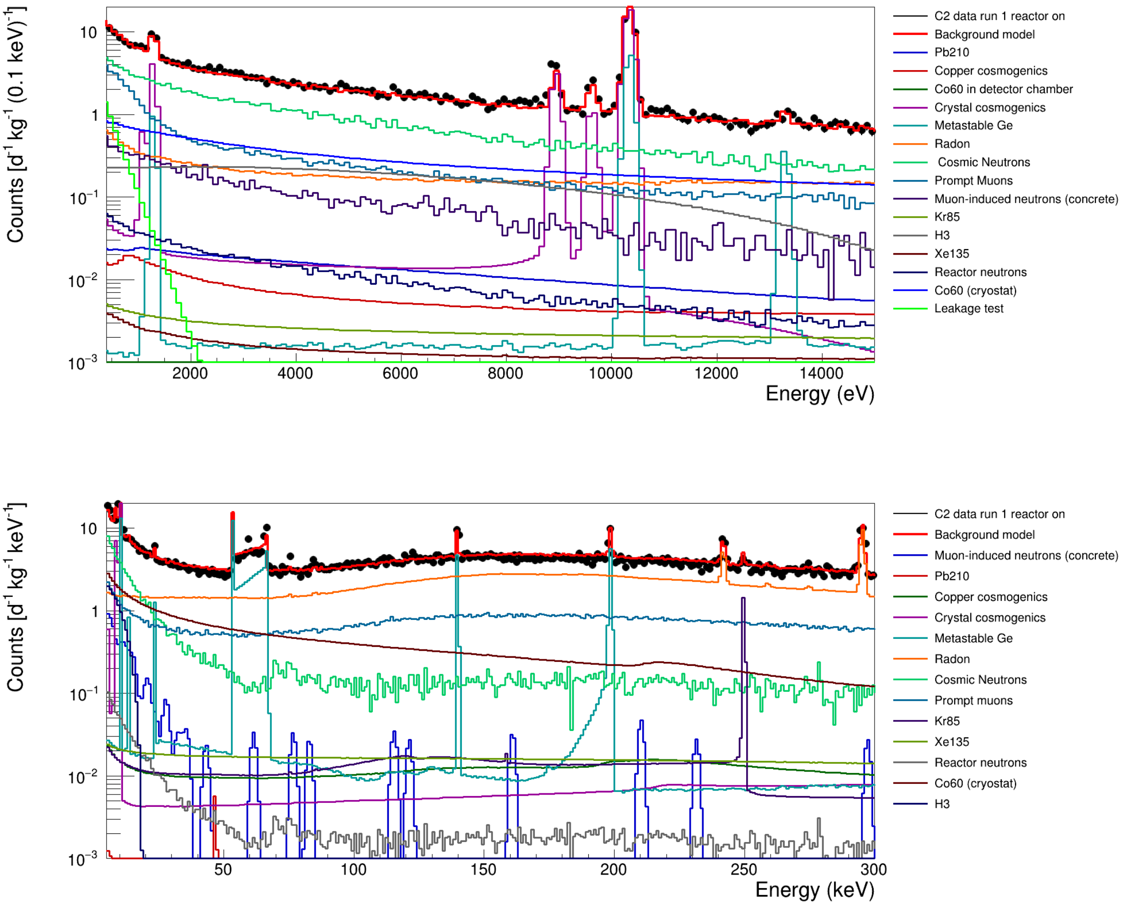

Figure 3.54. Complete background model and separate components for the C2 detector in reactor on measurement.

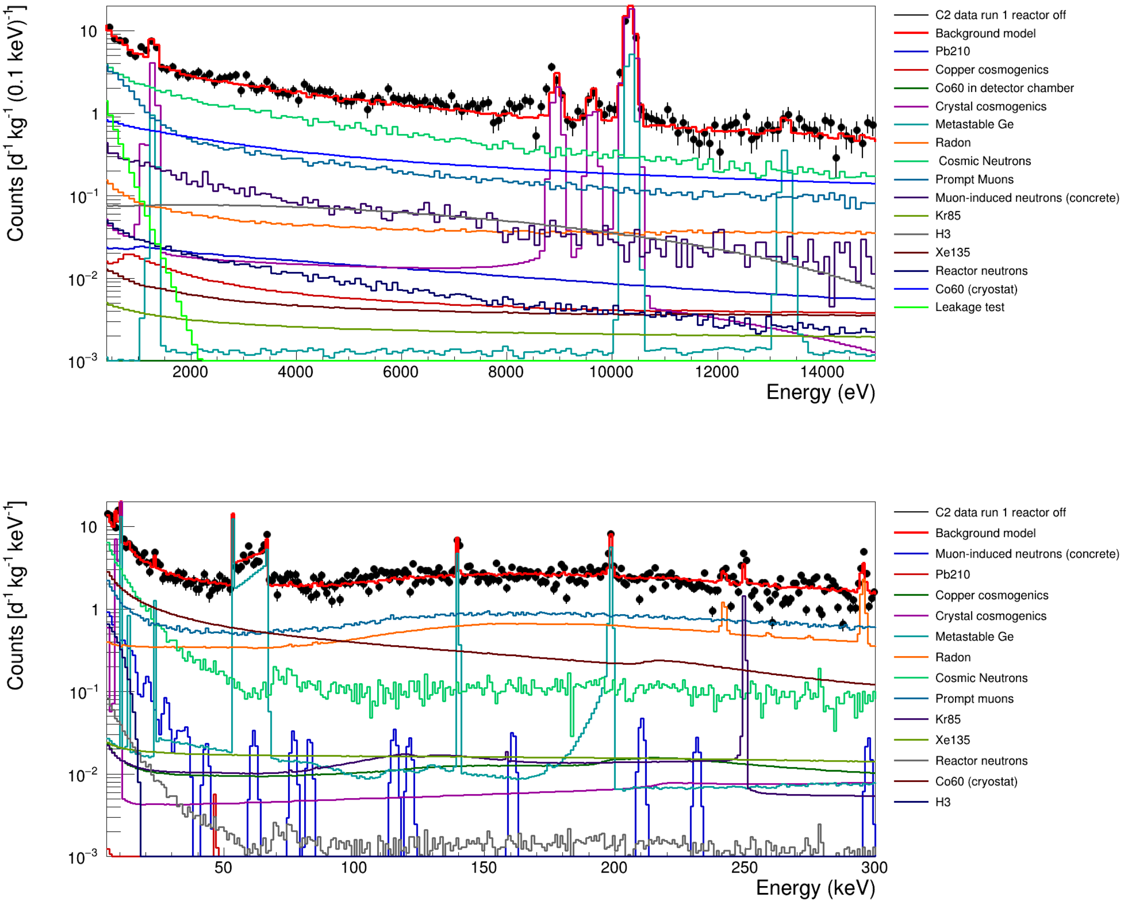

Figure 3.55. Complete background model and separate components for the C2 detector in reactor off measurement.

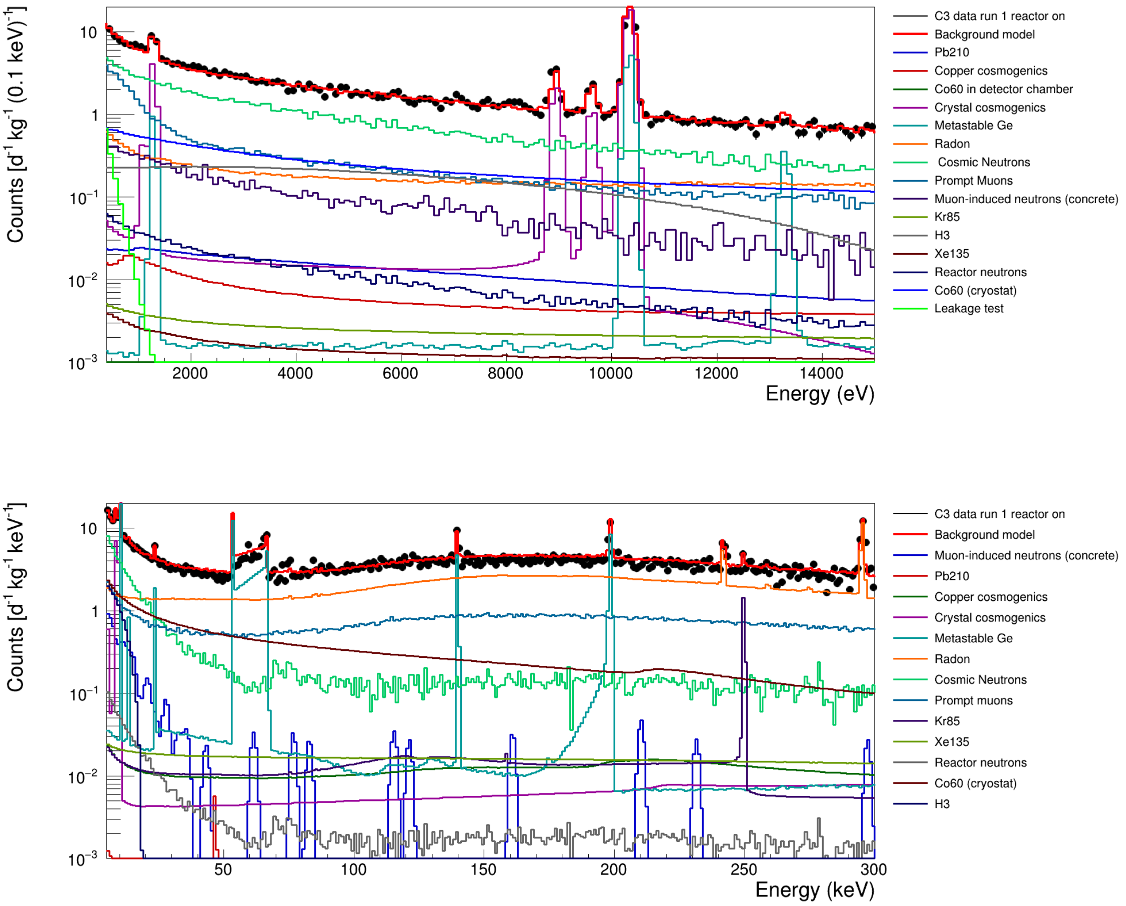

Figure 3.56. Complete background model and separate components for the C3 detector in reactor on measurement.

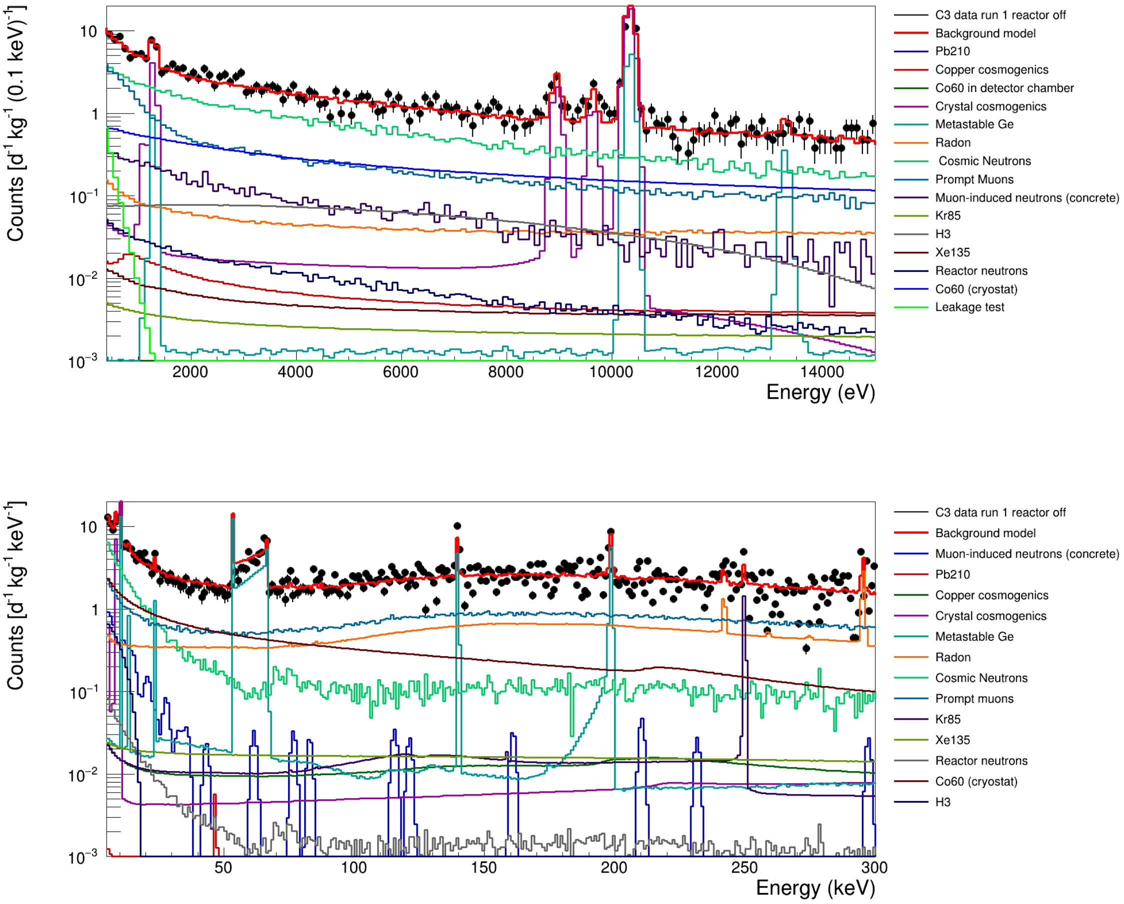

Figure 3.57. Complete background model and separate components for the C3 detector in reactor off measurement.

Table 3.15. Deconstruction of the background model of the C5 detector in reactor on in different energy regions with comparison to data. Values for the lowest energy region are not listed for reactor on data, since in this energy region the expected CEνNS signal is expected. In this way, no biases are introduced ahead of the analysis in the following chapter.

C5 Run 1 - Reactor ON						
Energy ranges	Detector threshold - 0.4 keV	$[0.4, 1]$ keV	$[2, 8]$ keV	$[15, 30]$ keV	$[30, 100]$ keV	$[100, 250]$ keV
Bkg. model [d^{-1} kg^{-1}]	-	42.9 ± 3.1	103.8 ± 8.3	48.6 ± 2.2	204.5 ± 4.6	529.6 ± 9.1
Data [d^{-1} kg^{-1}]	-	42.9 ± 0.6	103.6 ± 0.9	51.4 ± 0.7	220.9 ± 1.4	512.5 ± 2.1
Cosmic neutrons	-	50.3 %	56.4 %	30.6 %	7.1 %	4.5 %
Reactor neutrons	-	0.7 %	0.7 %	0.4 %	0.1 %	0.1 %
Muon-induced neutrons (overburden)	-	5.2 %	6.0 %	3.3 %	0.6 %	0.4 %
Cosmic muons	-	35.5 %	15.3 %	19.5 %	17.6 %	23.9 %
Cu cosmogenics	-	0.3 %	0.4 %	1.0 %	1.1 %	2.5 %
Ge cosmogenics	-	0.2 %	0.4 %	0.1 %	0.1 %	0.2 %
Metastable Ge states	-	< 0.1 %	0.1 %	2.9 %	21.7 %	2.7 %
^{210}Pb (shield and cryostat)	-	0.3 %	1.6 %	7.6 %	9.9 %	16.4 %
Radon	-	4.5 %	7.5 %	28.1 %	33.6 %	51.7 %
Inert gases from reactor	-	3.3 %	11.9 %	1.4 %	0.9 %	1.2 %

Table 3.16. Deconstruction of the background model of the C5 detector in reactor off in different energy regions with comparison to data.

C5 Run 1 - Reactor OFF						
Energy ranges	$[0.17, 0.4]$ keV	$[0.4, 1]$ keV	$[2, 8]$ keV	$[15, 30]$ keV	$[30, 100]$ keV	$[100, 250]$ keV
Bkg. model [d^{-1} kg^{-1}]	23.6 ± 1.5	35.8 ± 2.9	75.4 ± 6.4	32.3 ± 1.6	135.8 ± 3.2	283.7 ± 4.8
Data [d^{-1} kg^{-1}]	23.5 ± 1.1	33.4 ± 1.3	74.8 ± 2.0	30.7 ± 1.3	133.0 ± 2.7	242.6 ± 3.6
Cosmic neutrons	44.6 %	52.9 %	62.5 %	41.0 %	8.3 %	6.6 %
Muon-induced neutrons (overburden)	5.0 %	5.5 %	6.6 %	4.4 %	0.8 %	0.7 %
Cosmic muons	46.3 %	45.4 %	20.6 %	31.5 %	28.2 %	48.9 %
Cu cosmogenics	0.1 %	0.3 %	0.5 %	1.7 %	1.8 %	5.3 %
Ge cosmogenics	1.7 %	0.7 %	0.4 %	0.2 %	0.2 %	0.3 %
Metastable Ge states	0.2 %	< 0.1 %	0.1 %	4.6 %	39.0 %	4.4 %
^{210}Pb (shield and cryostat)	0.1 %	0.4 %	1.8 %	12.2 %	16.4 %	34.6 %
Radon	0.7 %	0.8 %	1.4 %	6.5 %	7.7 %	15.1 %
Inert gases from reactor	1.0 %	1.7 %	6.0 %	2.7 %	2.8 %	5.9 %

Table 3.17. Deconstruction of the background model of the C2 detector in reactor on in different energy regions with comparison to data. Values for the lowest energy region are not listed for reactor on data, since in this energy region the expected CEνNS signal is expected. In this way, no biases are introduced ahead of the analysis in the following chapter.

C2 Run 1 - Reactor ON						
Energy ranges	$[0.18, 0.4]$ keV	$[0.4, 1]$ keV	$[2, 8]$ keV	$[15, 30]$ keV	$[30, 100]$ keV	$[100, 250]$ keV
Bkg. model [d^{-1} kg^{-1}]	-	50.4 ± 3.1	127.3 ± 8.6	70.5 ± 2.6	272.7 ± 5.5	678.2 ± 12.1
Data [d^{-1} kg^{-1}]	-	52.3 ± 0.7	130.6 ± 1.0	71.0 ± 0.8	281.3 ± 1.5	643.2 ± 2.3
Cosmic neutrons	-	42.8 %	44.8 %	22.2 %	4.9 %	3.2 %
Reactor neutrons	-	0.6 %	0.6 %	0.3 %	0.1 %	0.1 %
Muon-induced neutrons (overburden)	-	4.4 %	4.7 %	2.4 %	0.5 %	0.3 %
Cosmic muons	-	32.8 %	12.3 %	14,1 %	13.8 %	18.9 %
Cu cosmogenics	-	0.2 %	0.3 %	0.7 %	0.9 %	2.0 %
Ge cosmogenics	-	0.3 %	0.7 %	0.1 %	0.1 %	0.2 %
Metastable Ge states	-	< 0.1 %	0.1 %	2.0 %	17.2 %	2.2 %
^{210}Pb (shield and cryostat)	-	0.5 %	1.7 %	6.1 %	7.8 %	13.0 %
Radon	-	5.5 %	8.5 %	28.9 %	37.5 %	58.4 %
Inert gases from reactor	-	2.8 %	9.5 %	1.0 %	0.9 %	1.0 %
^{60}Co in cryostat	-	8.7 %	14.8 %	21.8 %	13.9 %	6.3 %
Leakage test background	-	5.6 %	0.1 %	-	-	-

Table 3.18. Deconstruction of the background model of the C2 detector in reactor off in different energy regions with comparison to data.

C2 Run 1 - Reactor OFF						
Energy ranges	$[0.18, 0.4]$ keV	$[0.4, 1]$ keV	$[2, 8]$ keV	$[15, 30]$ keV	$[30, 100]$ keV	$[100, 250]$ keV
Bkg. model $[\mathrm{d}^{-1}\ \mathrm{kg}^{-1}]$	30.8 ± 2.1	45.2 ± 3.3	97.5 ± 6.8	51.2 ± 2.3	189.7 ± 4.8	388.3 ± 6.4
Data $[\mathrm{d}^{-1}\ \mathrm{kg}^{-1}]$	30.6 ± 1.3	45.3 ± 1.5	105.4 ± 2.4	52.2 ± 1.7	201.0 ± 3.3	386.0 ± 4.5
Cosmic neutrons	32.5 %	39.0 %	44.4 %	24.1 %	5.5 %	4.1 %
Muon-induced neutrons (overburden)	3.6 %	4.0 %	4.7 %	2.6 %	0.6 %	0.5 %
Cosmic muons	40.1 %	36.2 %	13.8 %	18.5 %	19.1 %	31.6 %
Cu cosmogenics	0.1 %	0.2 %	0.4 %	1.0 %	1.2 %	3.3 %
Ge cosmogenics	1.0 %	0.5 %	0.8 %	0.1 %	0.2 %	0.2 %
Metastable Ge states	0.1 %	$<$ 0.1 %	0.1 %	2.7 %	23.9 %	3.6 %
^{210}Pb (shield and cryostat)	0.1 %	0.2 %	1.3 %	7.2 %	10.9 %	21.7 %
Radon	1.2 %	1.5 %	2.5 %	9.4 %	12.5 %	23.3 %
Inert gases from reactor	0.7 %	1.2 %	4.3 %	1.5 %	1.0 %	1.6 %
^{60}Co in cryostat	6.5 %	9.9 %	18.4 %	29.6 %	19.4 %	10.5 %
Leakage test background	14.3 %	6.5 %	0.1 %	-	-	-

Table 3.19. Deconstruction of the background model of the C3 detector in reactor on in different energy regions with comparison to data. Values for the lowest energy region are not listed for reactor on data, since in this energy region the expected CEνNS signal is expected. In this way, no biases are introduced ahead of the analysis in the following chapter.

C3 Run 1 - Reactor ON						
Energy ranges	$[0.16, 0.4]$ keV	$[0.4, 1]$ keV	$[2, 8]$ keV	$[15, 30]$ keV	$[30, 100]$ keV	$[100, 250]$ keV
Bkg. model [d^{-1} kg^{-1}]	-	49.2 ± 3.5	123.4 ± 8.4	66.9 ± 2.6	256.4 ± 5.2	658.9 ± 11.3
Data [d^{-1} kg^{-1}]	-	48.8 ± 0.6	123.3 ± 1.0	66.7 ± 0.8	261.7 ± 1.5	606.6 ± 2.3
Cosmic neutrons	-	44.2 %	47.4 %	23.6 %	5.4 %	3.3 %
Reactor neutrons	-	0.6 %	0.6 %	0.3 %	0.1 %	0.1 %
Muon-induced neutrons (overburden)	-	4.6 %	5.0 %	2.6 %	0.5 %	0.4 %
Cosmic muons	-	33.8 %	13.0 %	15.0 %	15.1 %	20.0 %
Cu cosmogenics	-	0.2 %	0.3 %	0.8 %	1.0 %	2.1 %
Ge cosmogenics	-	0.4 %	0.8 %	0.1 %	0.1 %	0.2 %
Metastable Ge states	-	< 0.1 %	0.1 %	2.2 %	18.9 %	3.0 %
^{210}Pb (shield and cryostat)	-	0.5 %	1.8 %	6.4 %	8.5 %	13.8 %
Radon	-	5.4 %	8.6 %	29.4 %	39.3 %	59.3 %
Inert gases from reactor	-	2.9 %	10.0 %	1.0 %	0.8 %	1.0 %
^{60}Co in cryostat	-	7.4 %	13.0 %	19.2 %	12.5 %	5.5 %
Leakage test background	-	1.5 %	0.1 %	-	-	-

Table 3.20. Deconstruction of the background model of the C3 detector in reactor off in different energy regions with comparison to data.

C3 Run 1 - Reactor OFF						
Energy ranges	$[0.18, 0.4]$ keV	$[0.4, 1]$ keV	$[2, 8]$ keV	$[15, 30]$ keV	$[30, 100]$ keV	$[100, 250]$ keV
Bkg. model [d^{-1} kg^{-1}]	30.9 ± 2.1	42.0 ± 3.2	93.2 ± 7.4	48.0 ± 2.2	182.9 ± 4.0	381.2 ± 5.9
Data [d^{-1} kg^{-1}]	31.1 ± 1.3	42.5 ± 1.5	98.4 ± 2.3	49.6 ± 1.6	182.6 ± 3.1	387.6 ± 4.5
Cosmic neutrons	33.7 %	41.6 %	47.6 %	25.4 %	6.0 %	4.2 %
Muon-induced neutrons (overburden)	3.8 %	4.3 %	5.0 %	2.7 %	0.7 %	0.6 %
Cosmic muons	42.6 %	37.7 %	15.8 %	19.5 %	21.2 %	31.5 %
Cu cosmogenics	0.1 %	0.2 %	0.4 %	1.1 %	1.3 %	3.3 %
Ge cosmogenics	1.4 %	0.5 %	0.4 %	0.1 %	0.2 %	0.2 %
Metastable Ge states	0.2 %	< 0.1 %	0.1 %	2.9 %	26.2 %	3.6 %
^{210}Pb (shield and cryostat)	0.1 %	0.2 %	1.4 %	7.5 %	11.9 %	21.6 %
Radon	1.2 %	1.6 %	2.7 %	9.9 %	13.8 %	23.2 %
Inert gases from reactor	0.7 %	1.3 %	4.6 %	1.7 %	1.1 %	1.6 %
^{60}Co in cryostat	5.6 %	8.7 %	16.2 %	25.8 %	17.6 %	8.6 %
Leakage test background	9.8 %	1.9 %	0.1 %	-	-	-

Chapter 4

First CEνNS observation at a nuclear reactor

The following sections detail the CEνNS analysis of run 1 of the CONUS+ experiment at KKL. The methodology is based on the analysis performed for the previous runs of the CONUS experiment at KBR (see [2, 48, 68]) and uses the background model presented in Chapter 3. First, the data sets for the analysis are defined using data cuts based on the quality of the data, as well as taking into account the stability of the background levels and environmental parameters of the experiment. This is followed by the definition of the region of interest, as well as a description of the expected CEνNS signal from theoretical inputs and reactor parameters. Lastly, the likelihood function for the final fitting of the model to the data is defined, which is used to extract the result of the analysis.

This work focuses on the CEνNS result of CONUS+, the main goal of the experiment. In parallel, the run 1 data is also being analysed with respect to possible BSM channels, as explained in Section 1.3.1. An upcoming publication will detail the findings and deduced limits in these new interactions.

4.1 Definition of data sets

This work presents the CEνNS analysis of run 1 of the CONUS+ experiment, which lasted from November of 2023 to July of 2024. Within this period, one regular reactor outage in May of 2024 is included. In August of 2024 a neutron irradiation was performed, where a ^{252}Cf source with an activity of approximately 135 kBq was placed in close proximity to the CONUS+ shield. This source is used to gain better and more precise knowledge about the energy calibration of the CONUS+ detectors, which will be explained in closer detail in Section 4.3. The period of activation and the following weeks are not used in the analysis of run 1 due to increased background levels.

4.1.1 Selection cuts and dead-time

Rejection of time periods based on noise level

The expected signal from the CEνNS interaction in the germanium crystals is an exponential increase at very low energies, typically below 300 eV, at a rate of 1 - 1.5 counts per day depending on the detector (see Figure 4.14). At these low energies, electronic noise plays a crucial role in understanding the shape of the spectrum. Figure 4.1 shows the influence of electronic noise on the low energy spectrum of the C5 detector in run 1. It is visible as a sharp increase in the count rate below 150 eV and can be estimated to have a Gaussian shape.

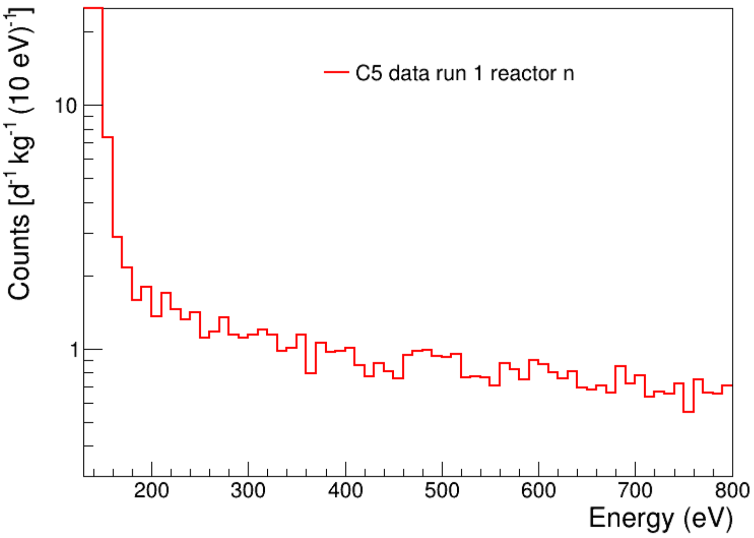

Figure 4.1. C5 run 1 reactor on data from 120 to 800 eV. Below 150 eV a large increase in the count rate can be seen, this is the noise peak. The region above 150 eV is well described by the background model of the detectors as shown in Section 3.14.

The region of interest for the CEνNS analysis (see Section 4.4) is chosen to begin above the noise peak of the detectors to avoid influence of the noise on the part of the spectrum used for analysis. The stability of the noise peak in both rate and width is therefore of great interest for the CONUS+ experiment, not only for the definition of the ROI but also to assure that no noise events leak into it due to unstable noise conditions. These events would distort the shape of the spectrum in the ROI. For this reason, time periods with increased noise have to be rejected and cannot be included in the analysis of the data.

In order to quantify the noise level in each detector, the ”noise integral” is defined as the integrated count rate from zero to some higher energy, such that most noise events are included (approximately 150 eV). The integral as well as the width of the peak are monitored continuously and compared to other environmental data in the Slow Control system of the experiment, like room temperature and cryocooler power, which can influence the amount of noise in the detectors. Based on this, a rejection criterium is defined for certain time periods: a period is rejected in case the noise integral deviates from the average by more than 20% or if the resolution of the noise peak deviates from the average by more than 5eV.

Figure 4.2 shows the mentioned parameters for all four detectors during the whole of run 1. For C5, C2 and C3 most periods pass the rejection cut and feature variations in the noise integral below 10 %. In the case of C5 and C2, only two short period in December 2023 and January 2024 have to be rejected, while for C3 two additional periods in the first month of data taking and during the reactor outage were excluded.

For the C4 detector shown in the lower right of the figure, large inconsistencies are found in both the noise integral and the width of the peak (illustrated through the FWHM) during the whole of run 1. This issue is likely to have originated from intrinsic problems in the inner detector electronics and is currently under investigation at MPIK. For this reason, the C4 detector was excluded from the CEνNS analysis presented in this chapter. The total collected exposure for each of the remaining three detectors used in the analysis is listed in Table 4.1.

Table 4.1. Total collected exposure of the three detectors used in the CEνNS analysis in both reactor on and off periods.

Detector	Exposure ON [kg d]	Exposure OFF [kg d]
C5	112.3	20.0
C2	111.2	19.8
C3	103.3	19.9
Total	326.8	59.7

Data cuts

In the processing of the CONUS+ data, several cuts are applied. These cuts aim to reduce the amount of background events in the detectors while keeping the CEνNS signal intact. The cuts generally induce a certain amount of dead-time, meaning measurement time which is lost for the analysis of the data. The amount of dead-time is recorded so that the live time of the measurement can later be corrected in the processing of the data.

The first of these cuts is the muon veto cut. This cut, as previously explained in Section 2.4.1, is based on output from the muon anti-coincidence system implemented in the shield of CONUS+. An energy threshold based on the amount of deposited energy from a muon passing through the plastic scintillator plates is defined and the system triggers whenever the PMTs in the corners of the plates register an event with an energy higher than the threshold.

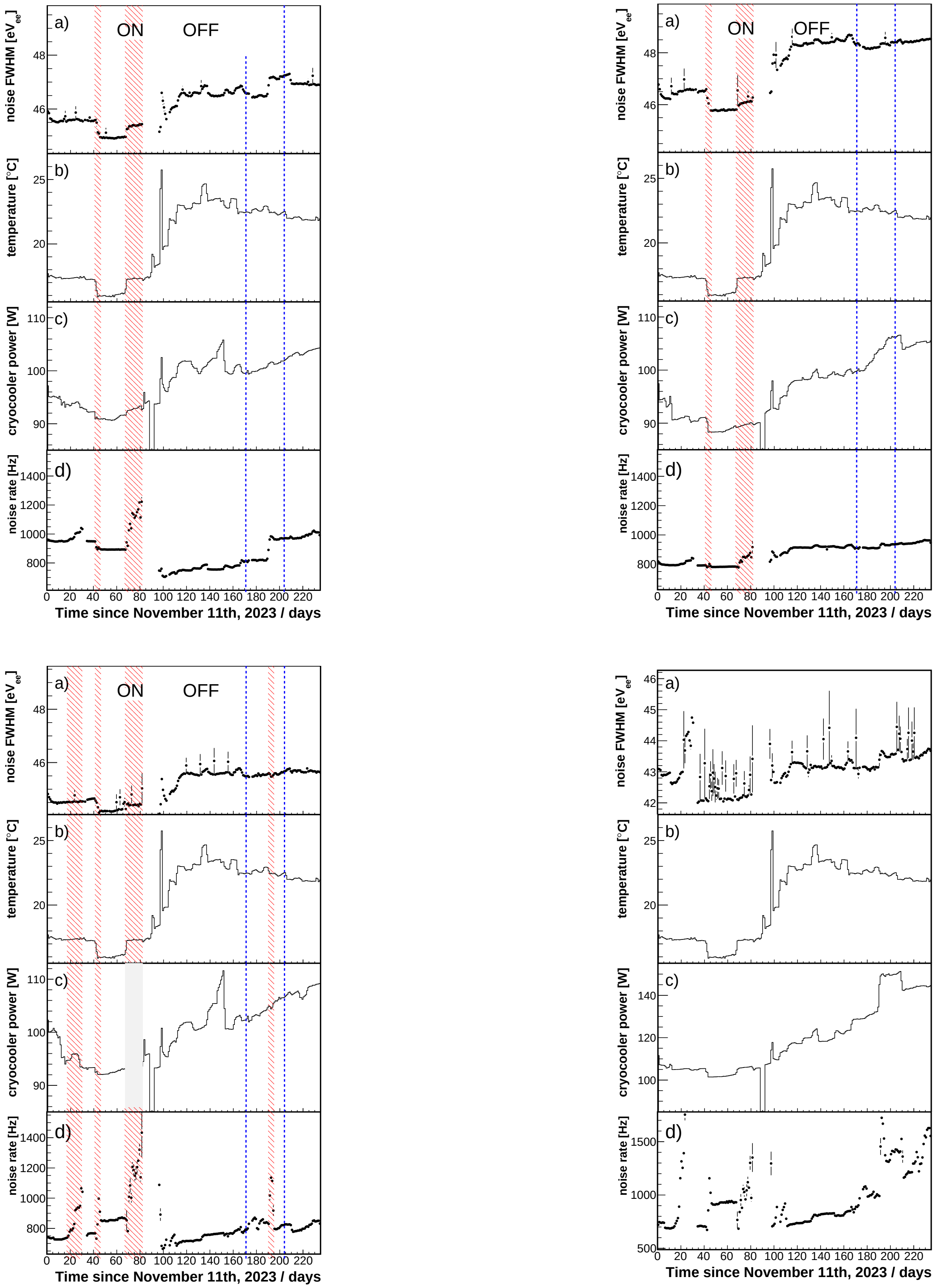

Figure 4.2. Noise and environmental parameters for the four detectors of the CONUS+ experiment: C5 (upper right), C5 (upper left), C3 (lower left), and C4 (lower right). Periods with red shading for the C5, C2 and C3 detectors are excluded due to large variations in the noise integral. The reactor off period is marked between the blue lines. The C4 detector is completely excluded from the analysis due to consistently large variations in both its noise integral and noise peak FWHM. The figures (except for the C4 figure) are extracted from [13].

As the time stamps of all events in the Germanium crystals are recorded, events immediately after such a muon event can be removed in the offline data processing routine. The amount of time which is removed after each muon event, the muon veto window, is defined such that the full shower induced by the passing muon is expected to have subsided. For the CONUS+ detectors the window is defined to be 450 μs. The average trigger rate in the muon veto is (274 $\pm$ 1) Hz in reactor on and (214 $\pm$ 1) Hz in reactor off periods. The reduction of the rate can be explained by the influence of high energy gammas induced by neutron capture from reactor neutrons in the material of the reactor building. These gammas cannot penetrate the shield completely and reach the germanium crystals but can reach the outer layer of the muon veto system, where they can deposit enough energy to trigger the system. The corresponding dead-times in both periods are 12.3 % in reactor on and 9.6 % in reactor off.

Secondly, the transistor reset (TRP) cut, already mentioned in Section 2.3.3, is placed on the data. For this cut, inhibit signals are generated whenever the dynamic range of the preamplifier reaches saturation. A certain time window, the TRP window, is again cut after such an inhibit signal to ensure a stable baseline is reached before the next event is recorded and to remove unwanted spurious events generated in the germanium detectors shortly after the reset. The TRP window is 1 to 2.5 ms, depending on the detector. The dead time induced by this cut is calculated together with the aforementioned muon-veto dead time due to large correlations between muon veto triggers and TRP resets. On its own it is estimated to be around 0.5-2.1%, depending on the detector.

Third, a cut based on the time-difference distribution (TDD) of the germanium events is placed on the data. For this cut, the distribution of time between two events in the germanium crystals is plotted as shown in Figure 4.3 for the C5 detector in run 1. The cut was first proposed in [90], where it was shown that germanium events with time differences below a certain threshold are most likely to be microphonic events induced by mechanical vibrations or spurious events, while events above the threshold are poisson-distributed physical events. Events below the threshold are cut to increase the quality of the data. For CONUS+ the cut is placed at 10^{-1}s for the low energy channels of all detectors.

Lastly, an anti-coincidence cut between the Germanium detectors is performed. In this cut, events in all detectors within a 5 ms window after an event in one detector are removed. This can be done because the probability of a neutrino interacting within several detectors is negligible, while other background sources like muon-induced neutrons are likely to scatter and interact multiple times with different detectors.

The rejection efficiencies of all selection cuts are listed in Table 4.2 for two energy ranges. The total dead time of all cuts is between 12.8% and 14.4% depending on the detector.

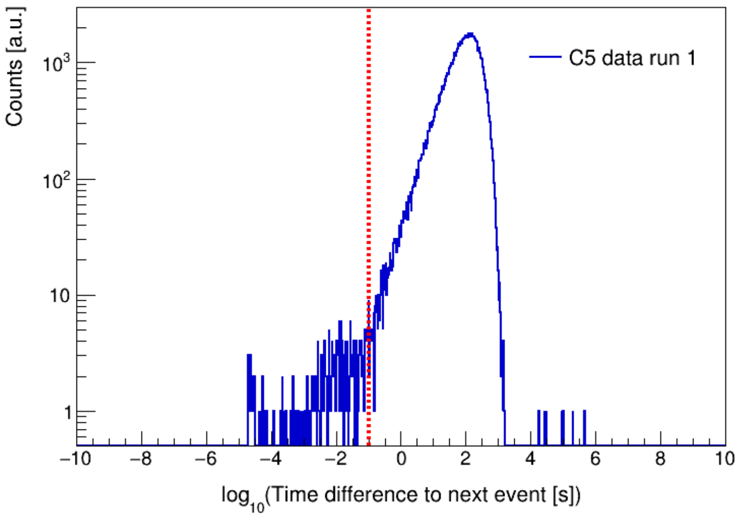

Figure 4.3. Time-difference distribution of events in the C5 detector in run 1. The red dashed line indicates the TDD cut placed at 10^{-1}s. Below this value are microphonic and spurious events, while above it are poisson-distributed physical events.

4.2 Background and performance stability

In order to assess the data taking stability of the experiment the stability of the background data in energy ranges above the influence of the CEνNS interaction is studied. Figures 4.4, 4.5, and 4.6 show the evolution of the count rates for the [0.4, 1] keV interval, the [2, 8] keV interval, and the 10.37 keV $^{68/71}$Ge line are shown. Only statistical uncertainties are given. Overall, all points agree within the uncertainties and no correlation to any of the quantities given in Figure 4.2, especially to cryocooler power and temperature, are found.

Looking at the [2,8] keV background stability, a trend can be observed, where the count rate, in the example of the C2 detector, rises from values around 120 counts d^{-1} kg^{-1} to around 160 counts d^{-1} kg^{-1} at the end of 2023. The count rate then falls again and stabilises in spring of 2024. This trend seems to be correlated to the amount of radon in the detector chamber as shown through the count rate in the 352 keV line in Figure 3.51 and therefore to the quality of the air flushing and can also be understood quantitively. Looking at Table 3.17, the background contribution in this energy range from gases in the detector chamber is 18%, which corresponds to around 23 counts d^{-1} kg^{-1}. Figure 3.51 shows that from the start of the experiment to the end of 2023, where the maximum of the count rate is reached, the amount of radon approximately triples in the detector chamber. Assuming that the same behaviour is true for the other gases in the detector chamber, their background contribution can also be expected to triple. This would correspond to an increase of 46 counts d^{-1} kg^{-1}, explaining the increased count rate in Figure 4.5.

Table 4.2. Rejection efficiencies of selection cuts for all detectors in run 1. The cuts are applied consecutively, meaning the muon veto cut is performed first and the efficiency of the TRP cut refers to the remaning data after the muon veto cut etc.

$[0.4-1.0]$ keV$_{ee}$						
Detector	**C5**		**C2**		**C3**	
Reactor period	On	Off	On	Off	On	Off
Muon veto cut	99.3%	99.3%	99.8%	99.8%	99.8%	99.8%
TRP cut	35.9%	39.6%	43.4%	44.0%	43.9%	46.5%
TDD cut	0.1%	0.1%	0.2%	0.5%	0.2%	0.1%
Detector anti-coincidence cut	6.8%	6.6%	4.3%	4.8%	7.2%	6.8%
Total	99.6%	99.6%	99.9%	99.9%	99.9%	99.9%
$[2-18]$ keV$_{ee}$						
Detector	**C5**		**C2**		**C3**	
Reactor period	On	Off	On	Off	On	Off
Muon veto cut	98.9%	98.9%	98.6%	98.6%	98.7%	98.9%
TRP cut	19.7%	25.0%	3.9%	5.5%	6.1%	6.7%
TDD cut	0.1%	0.1%	0.1%	0.1%	0.1%	0.1%
Detector anti-coincidence cut	6.5%	7.0%	4.3%	4.3%	6.7%	6.5%
Total	99.2%	99.2%	99.1%	99.1%	98.9%	99.1%

Another important quantity to judge the stability of the experiment is the stability of the detector performances. The first of these is the trigger efficiency of the detectors, which was previously introduced in Section 2.3.7 and shown in Figure 2.9 for all detectors in run 1. To describe the trigger efficiency and also implement it in the likelihood analysis of the experiment, the shape of the curves is described by the following function:

$$\epsilon_{trig} = 0.5 \ \cdot \ (1 + erf(\frac{E-\mu}{\sigma})). \tag{4.1}$$

Here, E is the measured energy, erf denotes the error function, and μ and σ are two parameters of the error function: μ is the position of ϵ_{trig} = 0.5, and σ is the width of the efficiency increase, or in other words a measure for the sharpness of the increase. The stability of these two parameters over the course of run 1 is shown in Figure 4.7. Overall, the values only vary within a few eV over the whole time period and are therefore assumed to be stable. The average best fit parameters, which will be used in the likelihood analysis as pull terms for the likelihood function are shown in Table 4.3.

Lastly, the stability of the muon veto is an important quality for the overall stability of the experiment due to the large muon flux in the CONUS+ experimental location. The

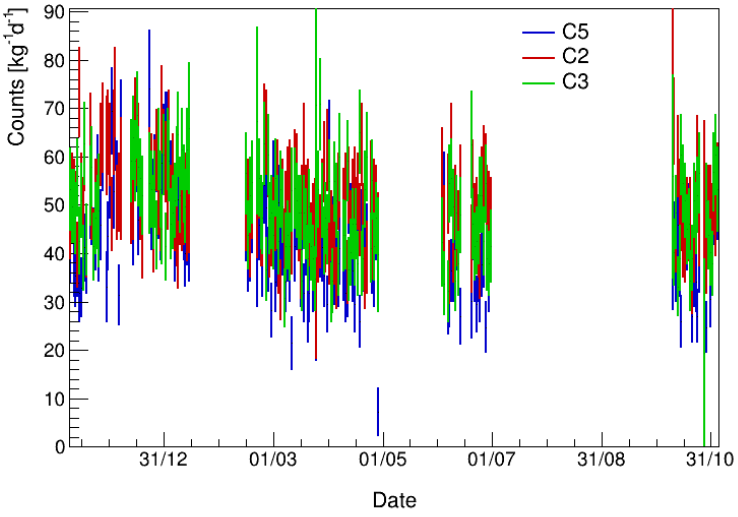

Figure 4.4. Count rate in the 0.4 to 1 keV energy region for all detectors over the course of reactor on data taking of run 1.

Table 4.3. Best fit values for the two parameters of the trigger efficiency function for all detectors in the CEνNS analysis.

Detector	μ [keV]	σ [keV]
C5	0.109 ± 0.001	0.054 ± 0.002
C2	0.106 ± 0.001	0.051 ± 0.001
C3	0.099 ± 0.001	0.053 ± 0.002

rate of the muon veto from the beginning of the experiment to shortly before the reactor outage in 2024 in shown in Figure 4.8. The rate is stable over the whole period, and shows no major deviations from the average. The seasonal variation of the muon flux on Earth due to variations in atmospheric pressure and temperature has been previously measured by different experiments (see for example [91]), where it was found to be between 1 and 2% on Earth's surface. These small variations have no impact on the CONUS+ data taking.

4.3 Energy scale calibration

The stability of the energy calibration scale is closely monitored during the whole run. As previously explained in Section 2.3.8, the γ-lines from the decay of $^{68/71}$Ge at 10.37 and 1.3 keV are used for this purpose and fitted with a Gaussian to find their exact position in the detector spectrum in ADC channels. This position is then converted to their respective energies and the parameters a and b of Equation 2.7, the calibration coefficients, can be

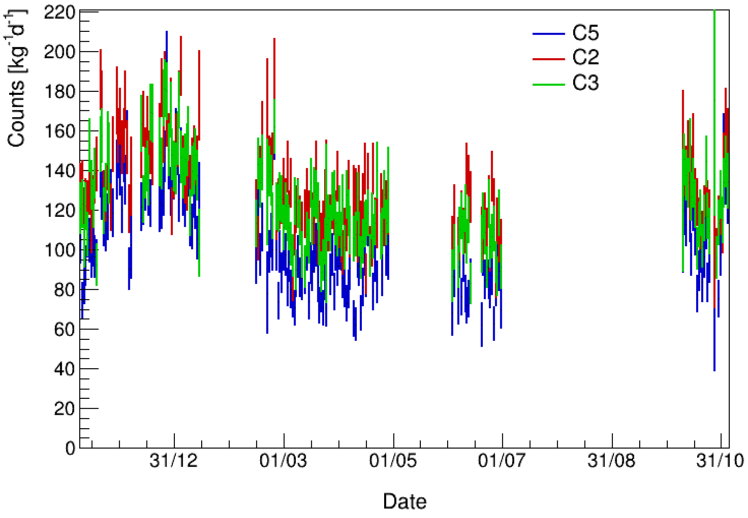

Figure 4.5. Count rate in the 2 to 8 keV energy region for all detectors over the course of reactor on data taking of run 1.

extracted. The best fit coefficients for run 1 of CONUS+, prior to the Cf irradiation in August of 2024 are listed in Table 4.4.

Table 4.4. Calibration coefficients a and b for run 1 of the CONUS+ experiment, prior to the californium irradiation in August of 2024 for the low E channels.

Detector	a [keV]	b [keV/ch]
C5	-0.00392 ± 0.00250	$0.00109 \pm 2.87 \cdot 10^{-7}$
C2	-0.00302 ± 0.00261	$0.00113 \pm 3.07 \cdot 10^{-7}$
C3	-0.00333 ± 0.00244	$0.00115 \pm 2.98 \cdot 10^{-7}$

The uncertainties on the a and b coefficients give the uncertainty on the energy calibration of the experiment. Using for example the values found for the C5 detector in Table 4.4, an uncertainty in the energy calibration uncertainty for Ch_{ADC} = 400 is 2.62 eV, while it is 5.5 eV for Ch_{ADC} = 10000. It is apparent that for small energies (or channels) the uncertainty on the a coefficient is dominant, while the uncertainty on b becomes dominant at higher energies (or channels).

In order to improve on the uncertainty of the energy scale, the CONUS+ experiment performed a californium irradiation campaign in August of 2024, at the end of run 1. In this irradiation campaign, a powerful 135 kBq source of ^{252}Cf was placed in the CONUS+ room in close proximity to the shield. To visualise the setup, Figure 4.9 shows the californium source during the irradiation campaign of the predecessor experiment CONUS at the KBR

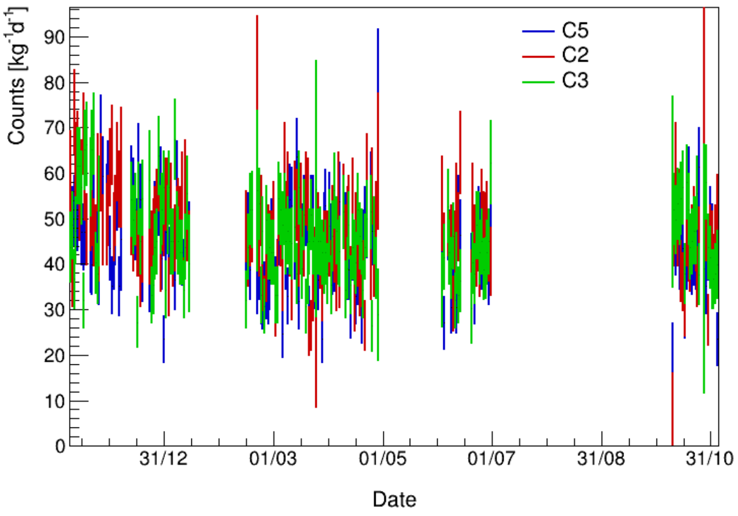

Figure 4.6. Count rate in the 10.37 keV $^{68/71}$Ge line for all detectors over the course of reactor on data taking of run 1.

power plant. The setup during run 1 of CONUS+ is the same. ^{252}Cf has a half-life of 2.6 years and decays primarily to ^{248}Cm via α-decay at a probability of 97% [92]. In 3% of cases, it decays via spontaneous fission producing a number of emitted neutrons. Additionally, the ^{248}Cm produced in the α-decay also has an 8% probability to decay via spontaneous fission and produce a number of emitted neutrons [93]. A strong ^{252}Cf sources such as the one used for CONUS+ therefore is a very powerful neutron source. These neutrons are used in the irradiation campaign to artificially enhance the amount of $^{68/71}$Ge isotope in the four germanium crystals in the shield and thereby increase the count rate in the 10.37 keV (K-shell) and 1.3 keV (L-shell) lines in the spectra (see Section 3.8.1). This enhanced count rate can then be used to get more precise gaussian fits to the peaks and therefore get more accurate values for the calibration coefficients a and b. The campaign ran for two weeks in August of 2024, after which the count rate in the K-shell line was increased by a factor 4 - 10, depending on the detector. The best fit values for the calibration coefficients after the campaign are listed in Table 4.5.

Table 4.5. Calibration coefficients a and b for run 1 of the CONUS+ experiment after the californium irradiation in August of 2024 for the low E channels.

Detector	a [keV]	b [keV/ch]
C5	-0.00638 $\pm$ 0.00168	0.00109 $\pm$ $1.97 \cdot 10^{-7}$
C2	-0.00467 $\pm$ 0.00185	0.00113 $\pm$ $2.23 \cdot 10^{-7}$
C3	-0.00385 $\pm$ 0.00115	0.00115 $\pm$ $1.93 \cdot 10^{-7}$

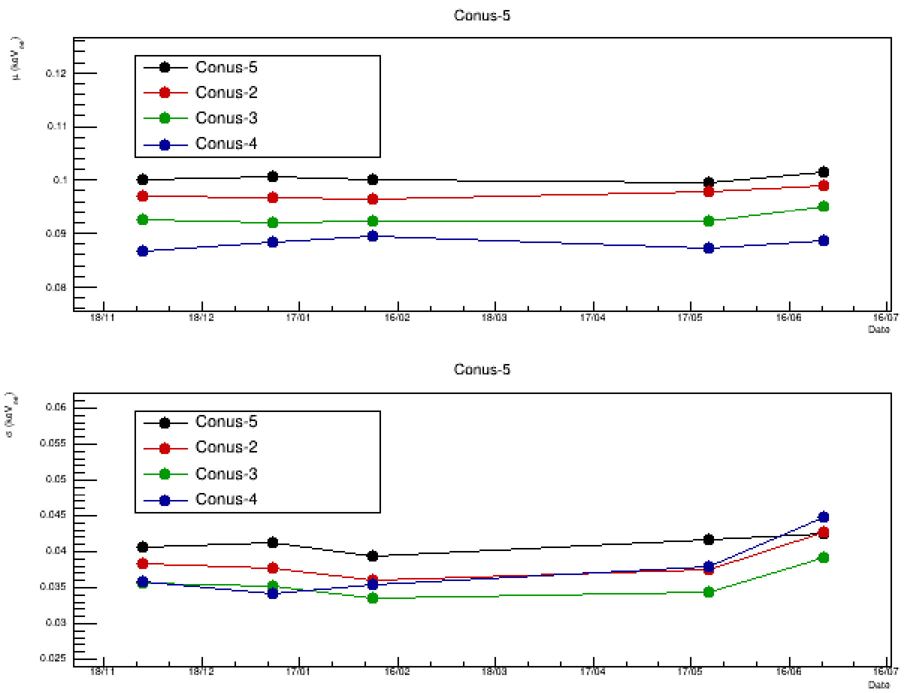

Figure 4.7. Stability of the two trigger efficiency parameters μ and σ during run 1 of the CONUS+ experiment. In total five measurements were performed.

The table shows a noticeable improve in the uncertainties of a and b compared to Table 4.4. Using again the example from above for the C5 detector, the energy calibration uncertainty for Ch$_{ADC}$ = 400 is 1.76 eV, while it is 3.68 eV for Ch$_{ADC}$ = 10000.
Lastly, the stability of a and b over the whole of run 1 is shown in Figure 4.10. Both coefficients are stable during the ful time period.

4.4 Definition of thresholds and region of interest

The region of interest (ROI) for the CEνNS search with CONUS+, meaning the energy range which is used for the analysis of the data, must be defined in such a way that the CEνNS event rate in it is maximised and the influence of the noise peak is negligible. For this reason, an energy threshold is defined which acts as the lower end of the ROI. The definition of this threshold takes into account the measured trigger efficiency in each detector, as well as the position of the noise edge in the spectrum. Due to the characteristically low energy signature of the CEνNS interaction (see Section 4.5) a very low energy threshold is one of the most important aspects of a CEνNS experiment and its lowering can be responsible for great improvements in sensitivity. The CONUS+ experiment uses the following definition to set its energy threshold:

E_{th} = Point in the spectrum at which the electronic noise (fitted with a gaussian) is smaller

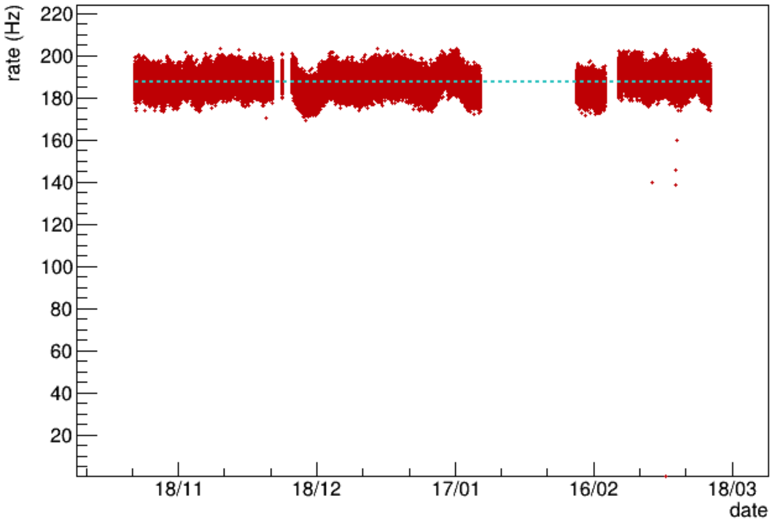

Figure 4.8. Stability of the muon veto rate during run 1 of the CONUS+ experiment. An average rate of 188 Hz is found.

or equal to 10 % of the expected CEνNS signal.

The fit of the noise spectrum also takes into account the maximum variation of the noise peak, which is monitored continuously (see Section 4.1). The definition ensures, that the ROI extends to low energies, where the CEνNS signal is expected to be strongest, while also ensuring that the impact of electronic noise is not too large. To correctly identify this point, the electronic noise is fitted with a Gaussian. Figure 4.11 illustrates this definition for the C3 detector as an example. Table 4.6 lists the thresholds for the C2, C3 and C5 detectors found in this way. Due to the binning of the data in 10 eV bins, the energy thresholds for the analysis always have to be multiples of 10 eV. This means that thresholds which are found with the definition above are always rounded up to the nearest multiple of 10 eV. Previous definitions of the threshold in the CONUS experiment also required that the trigger efficiency of each detector is larger than 20% at the energy threshold. This definition is naturally fulfilled for CONUS+ because of the very good trigger efficiency, which only falls to 20% below energies of approximately 70 eV, depending on the detector.

Compared to the CONUS experiment, the predecessor of CONUS+, great improvements in the energy thresholds of the detectors have been achieved. The previous thresholds were 210 eV for all detectors. This improvement is possible because of the detector upgrades, mainly the enhancement in trigger efficiency at low energies and the reduction of electronic noise, detailed in Section 2.3.7.

The upper edge of the ROI has to be chosen in such a way that it covers all events from the CEνNS interaction, while also including a certain range of background-only data.

Figure 4.9. Picture of the setup during the californium irradiation campaign of the CONUS experiment at the KBR power plant. The source is contained in the white plastic cylinder. The setup during the irradiation of CONUS+ is the same.

This is done to ensure that the likelihood fit, which is detailed in Section 4.6, can use the background-only data to correctly scale the background model to the data. At the same time, the ROI should not be influenced by any γ-lines, which the fit might find difficult to handle because of uncertainties in the gaussian folding of the MC model or the total count rate in the line. For the CONUS+ experiment, the 1.3 keV line from the L-shell transmissions in neutron-induced germanium contaminations in the crystal (see Section 3.8.1) is relevant for the definition of this upper edge. The experiment chose to set the upper edge of the ROI for the CEνNS analysis for all detectors at 800 eV. In this way, no influence of the 1.3 keV line is expected in the ROI. At the same time, the ROI includes all significant CEνNS events, which are expected to reach up to maximally 350 eV (see Section 4.5), and includes

Table 4.6. Energy thresholds for all four detectors in run 1 of the CONUS+ experiment. For C4, no threshold is listed, since the detector was not used in the final analysis due to issues with its stability.

Detector	Energy threshold [eV]
C5	170
C2	180
C3	160
C4	-

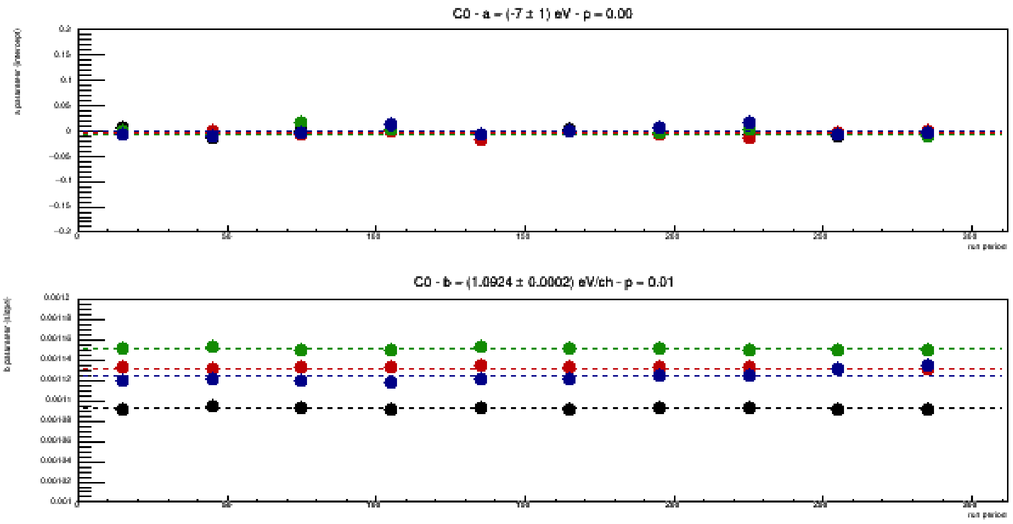

Figure 4.10. Stability of the calibration coefficients a (top) and b (bottom) during run 1 of the CONUS+ experiment.

background-only data from 350 eV to 800 eV.

4.5 Signal expectation

The signal expectation from CEνNS in the germanium detectors of CONUS+ is calculated through the use of the initial cross section (see Equation 1.2), the neutrino spectrum from the reactor including the fission fractions in the reactor core, and properties of the detectors, like nuclear quenching, trigger efficiency and active mass. The calculation is based on code written by T. Rink and was performed by E. Sanchez.

For the cross section, specifically for the nuclear form factor, the Helm parametrisation is chosen [94, 95]. No uncertainty is assumed for the from factor due to the small neutrino energies of the nuclear reactor leading to a form factor F = 1 (see Section 1.1). A 2% uncertainty is placed on the weak mixing (Weinberg) angle [96] at a value of $\sin^2\theta_w = 0.238 \pm 0.005$. The overall uncertainty on the cross section is 3.2%.

The antineutrino spectrum is calculated using the data-driven procedure presented in [97]. In this work, the authors put forward a method for reactor neutrino experiments to predict their respective antineutrino spectra directly using data from the Daya Bay experiment [98], based on the fission fractions of the different fissile isotopes in the reactor and the spectrum of neutrinos emitted by the respective isotope. The fission fraction of a certain fissile isotope is the relative contribution of the isotope to the total number of fissions in the reactor at a given time and it varies during the run time of a nuclear reactor cycle. At the beginning of the cycle, fission is dominated by ^{235}U, which decreases over time. Neutron captures on the uranium and subsequent β-decays produce Pu isotopes, mainly ^{239}Pu and ^{241}Pu, and their

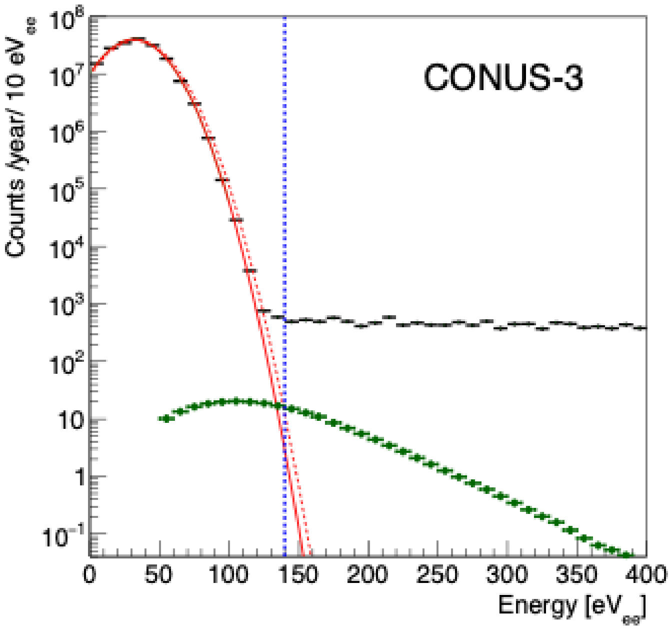

Figure 4.11. Illustration of threshold definition for the C3 detector. The threshold is defined as the point where the gaussian fit of the electronic noise (red) intersects with 10 % of the theoretically predicted CEνNS spectrum (green). C3 data is shown in black. The maximum deviation of the noise peak during the run is also considered (red dashed line).

share of the total fission events increases. At the end of a cycle, contributions from ^{235}U can fall below 50%, making Pu the dominant fissile isotope [99]. The fission fractions over the course of run 1 of the CONUS+ experiment were provided by the KKL power plant. Additionally, the thermal power of the reactor, which is shown in Figure 4.12, is needed to scale the spectrum appropriately. Overall, uncertainties on the antineutrino spectrum add up to 4.6% of the total event rate.

The antineutrino spectrum (see red graph in Figure 4.13) is convolved with the CEνNS cross section and detector effects are taken into account. This means that the resulting spectrum has to be scaled with the active mass of each detector and multiplied with its trigger efficiency. Lastly, for the use in the likelihood fit, the nuclear quenching previously described in Section 2.3.2 is applied to the data. For this, the Lindhard model with a k parameter of (0.162 ± 0.004) as measured in [7] is used. This finally leaves the expected CEνNS spectrum as it would be measured in each detector of the CONUS+ experiment, which is shown for the C5 detector in run 1 with a live time of 119 days in Figure 4.14. As previously described, the expected shape is an exponential increase towards low energies, which again illustrates the need for extremely low energy thresholds and the potential for improved sensitivities that a better energy threshold brings. The total number of expected CEνNS events during run 1 of the experiment are listed in Table 4.7.

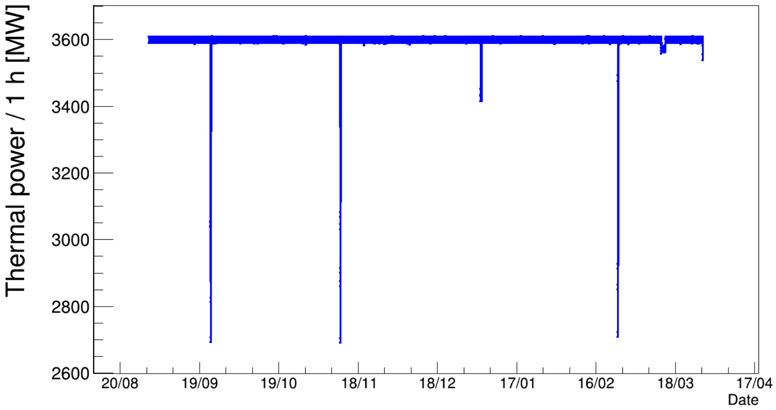

Figure 4.12. Thermal power of the KKL power plant during large parts of run 1 of the CONUS+ experiment. The reactor runs almost consistently at full power with 3.6 GW. Short periods of power reduction are visible.

Table 4.7. Expected total number of CEνNS events during run 1 of CONUS+ for each detector.

Detector	Energy threshold [eV]	Exposure reactor on [kg d]	Predicted CEνNS counts in run 1
C5	170	112.3	116^{+20}_{-18}
C2	180	111.2	96^{+16}_{-14}
C3	160	103.3	135^{+23}_{-20}
Total	-	326.8	345^{+34}_{-30}

4.6 Likelihood function

4.6.1 Maximum likelihood method

In order to fit the model of the CONUS+ data, meaning the sum of background model and signal prediction, to the actual measured data, the CONUS+ experiment uses a maximum likelihood approach. The following section explains the basics of this method. The information presented here is largely based on [100].

Generally, the maximum likelihood method is a procedure to find and estimate parameters $\vec{\lambda}$ in a model which best describe a measurement. For measured values x_1, ..., x_n, which are distributed according to a probability density $f(x, \vec{\lambda})$, the likelihood function L is defined as:

$$L(x, \vec{\lambda}) = \prod_{i=1}^{n} f(x, \vec{\lambda}) \tag{4.2}$$

Here, the measured values are considered fixed, while the parameters are variables. Ac-

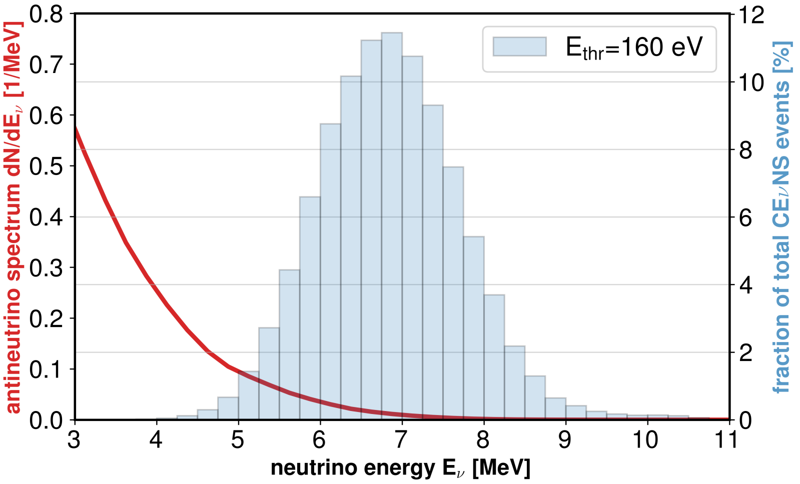

Figure 4.13. Anti-electronneutrino spectrum of the KKL power plant as seen by one of the CONUS+ detectors with an energy threshold of 160 eV. The red graph is the the antineutrino spectrum, while the blue histogram shows the fraction of CEνNS events in the detector induced by neutrinos with this energy. the fractions have their maximum at around 7 MeV, meaning that neutrinos with 7 - 7.5 MeV contribute about 20% of the total CEνNS interactions. The fraction falls towards lower energies due to the trigger efficiency of the detectors.

cording to the maximum likelihood principle, the best estimate $\vec{\lambda}_{ML}$ for the parameters is the one that maximises the likelihood function:

$$\vec{\lambda}_{ML} = \text{arg max} L(x, \vec{\lambda}) \tag{4.3}$$

In order to save computation time, the log-likelihood function $\mathcal{L}(x, \vec{\lambda})$ is often used as it has the same maxima as the regular likelihood function:

$$\mathcal{L}(x, \vec{\lambda}) = \ln\, L(x, \vec{\lambda}) = \sum_{i=1}^{n} \ln f(x, \vec{\lambda}) \tag{4.4}$$

The best estimator is therefore given by solutions to the equations

$$\frac{\delta}{\delta \lambda_j} \mathcal{L}(x_i, \lambda_j) = 0. \tag{4.5}$$

For a histogram with relatively few entries per bin as in the case of the CONUS+ spectra, the number of entries N$_i$ in bin i are usually described in terms of poisson statistics. Given a model of the data, the expectation value for the number of entries in bin i predicted by this model is $\mu_i(\vec{\lambda}) = \bar{N}_{tot} p_i$, with the predicted number of total events $\bar{N}_{tot}$ and the probability for an event to appear in bin i, p_i. Considering a poisson distribution the likelihood function can then be written as:

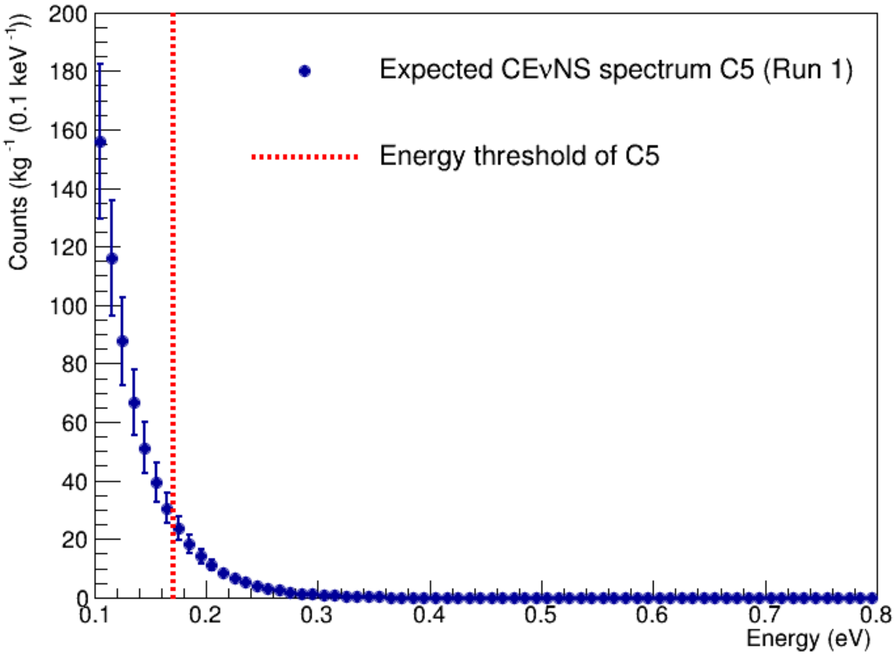

Figure 4.14. Expected CEνNS spectrum in the C5 detector in run 1 after an reactor on live time of 119 d. The red dashed lines shows the energy threshold of C5 at 170 eV.

$$L(N_1, ..., N_n; \vec{\lambda}) = L(\vec{\lambda}) = \prod_{i=1}^{n} \frac{\mu_i(\vec{\lambda})^{N_i}}{N_i!} e^{-\mu_i(\vec{\lambda})}. \tag{4.6}$$

Using again the log-likelihood function and dropping independent terms, yields

$$\mathcal{L}(\vec{\lambda}) = \sum_{i=1}^{n} N_i \ln(\mu_i) - \mu_i - \ln(N_i!). \tag{4.7}$$

Information about the model and the free parameters of the model are encoded in μ_i, while the data is represented through N_i, the number of events in the bin. The parameters maximising this function are the best estimators of the model.

4.6.2 Gaussian pull terms

Many of the free parameters in the log-likelihood fit of the CONUS+ data are not completely free and have instead been measured beforehand. These include for example the active mass of the detectors and the two trigger efficiency parameters. In order to correctly account for this prior knowledge about the parameters, the log-likelihood function for CONUS+ includes Gaussian pull terms of the form

$$\ln(\text{Pull term}) = \frac{(\theta_i - \bar{\theta}_i)^2}{\sigma_{\theta_i}}. \tag{4.8}$$

Here, θ_i is one of the parameters of the model, $\bar{\theta}_i$ is the value that was previously measured for this parameter, and σ_{θ_i} is the uncertainty of the measurement. Using such a pull term for all parameters with prior knowledge and subtracting it from the log-likelihood function penalises the function for values of θ_i which are too far away from $\bar{\theta}_i$, quite literally "pulling" the fit result to the previously measured value. In the case that two parameters of the likelihood function are correlated, a more general form for the pull term using the covariance matrix of both parameters can to be used:

$$\ln(\text{Pull term}) = (\theta_i - \bar{\theta}_i)^T\ \text{Cov}_{ij}^{-1}\ (\theta_j - \bar{\theta}_j). \tag{4.9}$$

Here, θ_i and θ_j are two correlated parameters of the likelihood function. Such a pull term introduces additional mixed terms between the two parameters, which are weighted by the off-diagonal elements of the covariance matrix.

4.6.3 Likelihood function for CEνNS analysis

The full likelihood function for the CEνNS analysis of the CONUS+ data is

$$\begin{aligned} -2\log\mathcal{L} = &-2\log\mathcal{L}_{\text{ON}} - 2\log\mathcal{L}_{\text{OFF}} \\ &+ \sum_{ij}(\theta_{\mathbf{i}} - \theta_{\mathbf{i}})^{\mathbf{T}}\ \text{Cov}_{\mathbf{ij}}^{\mathbf{-1}}\ (\theta_{\mathbf{j}} - \theta_{\mathbf{j}}) \\ &+ \sum_i \frac{(\theta_i - \bar{\theta}_i)^2}{\sigma_{\theta_i}}\,. \end{aligned} \tag{4.10}$$

$\mathcal{L}_{\text{ON}}$ and $\mathcal{L}_{\text{OFF}}$ are the binned likelihood functions for reactor on and off periods for a single detector. Gaussian pull terms for correlated parameters, namely the trigger efficiency parameters, and uncorrelated parameters, like the active mass of the detectors, the reactor neutrino flux and the uncertainty on the energy scale calibration of the spectra, are included. The analysis uses the negative log-likelihood (NLL) as opposed to the positive function, because of convenience in the selection of the optimisation algorithm, which are often designed to minimise functions instead of maximising them. The use of twice the NLL is also advantageous for likelihood ratio tests, which can be used to test the validity of the best fit. Here, Wilks' theorem states that the distribution

$$q = -2\ \ln(\frac{L(\text{null})}{L(\text{Best fit})}) \tag{4.11}$$

follows a χ^2 distribution, allowing a probabilistic interpretation of q and therefore a comparison between the goodness of the best fit to that of the null hypothesis. Similarly, a profile likelihood scan can be performed. Here, the parameter of interest, the CEνNS signal strength s in the case of CONUS+, is fixed to certain value, while the other parameters, the nuisance parameters ϕ, remain free. Then, several fits are performed with different fixed value for the parameter of interest and they are compared to the best fit likelihood value in the case of a free parameter of interest. Again, the q-values are calculated:

$$q_{\text{prof}} = -2\ \ln(\frac{L(\text{Fixed s})}{L(\text{Best fit})}) \tag{4.12}$$

Plotting this q value over the range of scanned s values gives an additional way of estimating the confidence interval of the best fit in case a signal is found or constructing an upper limit in case no signal is found.

$\mathcal{L}_{\text{ON}}$ and $\mathcal{L}_{\text{OFF}}$ are described by Equation 4.7. Every detector has its own NLL function, which are minimised in one combined fit. The parameters of the fit are generally separate for each detector, i.e. every detector has its own active mass and its own trigger efficiency parameters, however the CEνNS signal strength parameter s is shared between all detectors. The models μ_i^{ON} and μ_i^{OFF} for bin i in the spectrum of each detector are

$$\begin{aligned} \mu_i^{ON} &= (s \cdot t_{ON} \cdot \theta_2 \cdot n_i^s + b \cdot n_{i,ON}^b) \cdot c_{dt} \cdot \frac{\theta_3}{m_{act}} \cdot t_{ON} \\ \mu_i^{OFF} &= b \cdot n_{i,OFF}^b \cdot c_{dt} \cdot \frac{\theta_3}{m_{act}} \cdot t_{OFF}, \end{aligned} \tag{4.13}$$

where n_{ON}^b and n_{OFF}^b (scaled with b) are the MC background model for reactor on and off and n^s (scaled with the signal parameter s) is the predicted CEνNS spectrum. The model takes into account the live time of the experiment (t_{ON} and t_{OFF}), the active volume of the detector (m_{act}), the dead time correction (c_{dt}), the neutrino flux (θ_2) and a multiplication factor (θ_3), summarizing uncertainties of the detector response. The models as written in Equation 4.13 do not include the additional energy calibration uncertainty parameter and the four quenching uncertainty parameters for better readability. They will be explained in detail in the next section.

The models in Equation 4.13 are fitted to the CONUS+ run 1 data using the numerical minimization and function optimization library Minuit [101]. The framework for the analysis was initially developed by J. Hakenmüller for the CONUS experiment and adapted and rewritten to match the specifications and requirements of the CONUS+ experiment in the context of this work.

4.6.4 Overview of fit parameters

The following section will list all of the separate fit parameters appearing in Equation 4.13 and explain their function and role in the likelihood fit in detail. Table 4.8 gives a summary of all parameters.

Signal strength s

The signal strength parameter s is the parameter of interest for the CEνNS analysis of CONUS+. It scales the expected signal spectrum n^s (see Section 4.5), which means that the best fit value of s directly dictates the number of CEνNS counts that the fit finds in the data. The signal spectrum n^s is normalised to one, meaning that the actual value of s has no physical meaning. The parameter is shared between all three detector in the combined analysis.

Neutrino flux θ_2

The neutrino flux at the location of the CONUS+ experiment is included as a separate parameter from s and is used as an additional normalisation factor which scales the expected signal n^s. The value is pulled to the known value of $(1.45 \pm 0.01) \times 10^{13}\ \mathrm{s}^{-1}\ \mathrm{cm}^{-1}$.

Background model scaling b

The background model n^b was presented in Section 3.14. Each detector has its own background model histogram for both reactor on and off data. The b parameter is used to scale the background model in the likelihood function and every detector has a separate b parameter which is applied to both the on and off model. As the background model was specifically designed to describe the background of each detector and very good agreement between data and model is found the b parameter is pulled to one. Its uncertainty σ_b is calculated from the statistical uncertainty of the model in an energy region above the ROI of the CEνNS analysis. The [2, 8] keV region was chosen for this and the relative uncertainty is 1 - 2% depending on the detector.

Trigger efficiency parameters

The two trigger efficiency parameters which define the shape of the error function describing the trigger efficiency curves of each detector (see Section 2.3.8 and 4.2) are included in the likelihood as part of the detector response parameter θ_3. The trigger efficiency is read in as a function in the likelihood framework and directly applied to the background model and the signal prediction in the fit. Each detector has its own efficiency parameters, which are pulled to the previously measured values in Table 4.3. The pull term also includes a correlation term between the two parameters as these are highly correlated.

Energy calibration uncertainty

The detector response also includes an additional parameter dE which accounts for the uncertainty in the energy calibration of the four detectors which was discussed in Section 4.2. The parameter is applied to the background and signal models and is able to shift both of their energy scales by a small amount in negative or positive direction. The value, which is again separate for all detectors, is pulled to zero and the pull term includes the previously determined energy calibration uncertainty.

Active mass m_{act}

The active mass of each detector is not directly needed to describe the model for the CONUS+ data. However, it is used in the geometry implementation of the CONUS+ detector model in the MC simulations and hence is included here as a normalisation parameter as part of θ_3. The values for each detector are pulled to their known active masses. Their uncertainties are small, in the order of 1%.

Quenching uncertainty parameters

The last parameters of the likelihood function of CONUS+ are the four quenching uncertainty parameters. As the Lindhard quenching with k = (0.162 ± 0.04) is already applied to the signal prediction spectrum used in this likelihood analysis before the fit, the k parameter itself as well as uncertainties on the quenching model cannot be directly fitted in this version of the likelihood procedure. Instead, the likelihood framework includes an additional function namely a polynomial of fourth order which is able to vary the shape of the signal expectation within the uncertainty of the quenching measurement in [7]. The four parameters of the polynomial q_0, q_1, q_2, and q_3 are pulled so that the overall polynomial $f(q_{1-4}) = 1$ over the whole ROI, which corresponds to the measured quenching value. This means that q_1 is pulled to one, while the other three parameters are pulled to zero.

Table 4.8. Overview of parameters of the likelihood function in the CEνNS analysis of CONUS+. Each detector has 10 independent parameters and the signal strength s is shared for all detectors. The combined fit of all detectors therefore has 31 free parameters. The neutrino flux is a separate parameter for all three detectors, due to possible influences of different baseline lengths.

Parameter description	Number of parameters	detector dependent	pull term
Signal strength s	1	no	no
Neutrino flux	1 per detector	yes	yes
Background scaling b	1 per detector	yes	yes
Trigger efficiency	2 per detector	yes	yes
Calibration uncertainty	1 per detector	yes	yes
Active mass	1 per detector	yes	yes
Quenching uncertainty	4	no	yes

4.7 CEνNS result

4.7.1 Single detector results

In a first step, the data sets of the three detectors are fitted separately using the likelihood approach and function described in the previous sections. Although the final CEνNS result of run 1 of the CONUS+ experiment will mainly focus on the combined analysis of all three detectors, the results for the separate detectors will already give an indication of the final result and can be used as a final check of the model and the likelihood method before the combined fit. In this way, it can be checked if all best fit values for the pulled parameters are in agreement (within uncertainties) of the previously measured values and if all detectors are in agreement with each other.

C5

Figure 4.15 shows the result of the likelihood fit to the C5 data in run 1 for both reactor on and off periods. In both cases, good agreement is found between data and model, which in the case of reactor on data is comprised of the background model and the CEνNS signal for the reactor on data and just the background model for reactor off data.
The best fit values for the parameters of the likelihood function for C5 are listed in Table 4.9. All of the parameters which featured Gaussian pull terms in the likelihood function (see Table 4.8) show good agreement to their previously measured values, which can be found

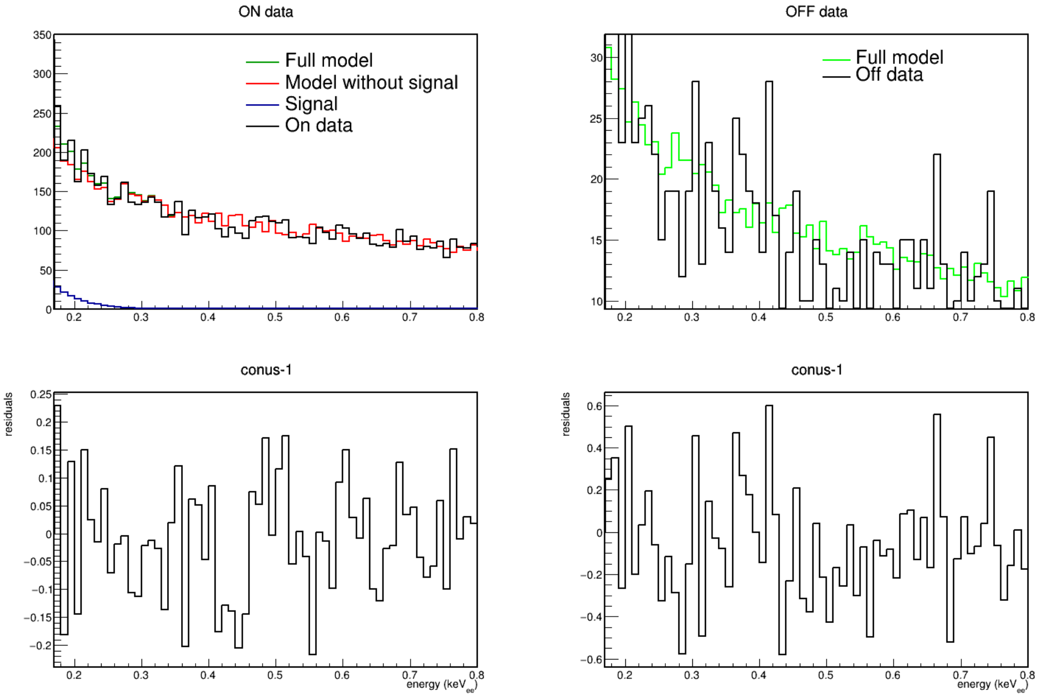

Figure 4.15. Result of the likelihood fit of C5 data in run 1. The upper left plot shows the fit to reactor on data, and the upper right plot shows the fit for reactor off data. The lower plots show the respective residuals. Very good agreement between data and model is found in both fits.

in the previous sections. Specifically, the background scaling parameter b is found to be in very good agreement with unity, indicating the validity of the background model. Furthermore, the fit finds a CEνNS signal with a signal scaling parameter of s = $(2.28 \pm 1.11) \cdot 10^{-16}$. By integrating the CE$\nu$NS signal found by the fit in Figure 4.15, it is found that this value corresponds to (117 ± 57) CEνNS counts in the reactor on measurement of C5. The number of counts is in excellent agreement with the expected number of counts of (116 ± 20) (see Table 4.7).

C2

As for the C5 detector, the fit result for C2 is shown in Figure 4.16, while its best fit parameters are listed in Table 4.10. Good agreement between data and full model, as well as sensible best fit parameters are found again. The detector prefers a CEνNS signal, although at a lower significance than the C5 detector, which might be due to its higher threshold. Integrating the fitted signal spectrum yields (69 ± 47) CEνNS counts in the reactor on data of the C2 detector.

Table 4.9. Best fit parameters for the single detector fit of C5. Pull value refers to the previously measured values for each parameter which are used in the Gaussian pull terms of the likelihood function.

Parameter	Best fit value	Pull value
Signal strength s	$(2.28 \pm 1.11) \cdot 10^{-16}$	-
Neutrino flux	$(1.45 \pm 0.10) \cdot 10^{13}$ cm^{-2} s^{-1}	$(1.45 \pm 0.10) \cdot 10^{13}$ cm^{-2} s^{-1}
Background scaling b	1.01 ± 0.02	1.00 ± 0.021
Trigger efficiency μ	(109 ± 1) eV	(109.0 ± 0.7) eV
Trigger efficiency σ	(54 ± 4) eV	(54.3 ± 2.4) eV
Calibration uncertainty	(2.65 ± 1.35) eV	(0 ± 5) eV
Active mass	(0.94 ± 0.01) kg	(0.94 ± 0.01) kg
Quenching uncertainty p_1	1.00 ± 0.05	1.00 ± 0.05
Quenching uncertainty p_2	$(-4.67 \pm 2.00) \cdot 10^{-5}$	(0.00 ± 0.05)
Quenching uncertainty p_3	$(6.00 \pm 2.07) \cdot 10^{-5}$	(0.00 ± 0.05)
Quenching uncertainty p_4	$(-3.82 \pm 5.61) \cdot 10^{-6}$	(0.00 ± 0.05)

C3

Lastly, Figure 4.17 and Table 4.11 show the result of the likelihood fit for the single detector fit of C3. The detector shows the same behaviour as the previous two detectors, while finding the highest number of CEνNS counts in its data with the highest significance at (186 ± 66) counts. This can again be explained by the energy threshold of C3 which was 160 eV in run 1, making it the lowest threshold of the four detectors.

In order to summarise the results of the single detector fits, Table 4.12 gives an overview of the CEνNS count rates found in run 1 of the CONUS+ experiment for each detector. In general, all detectors prefer a signal and the results are in agreement with the Standard Model prediction within their 1σ uncertainty.
While all three detectors see hints of the signal, none of them are able to exclude the null hypothesis at a significance of 3σ on their own as shown in the table. Additionally, the values listed here only include the uncertainty extracted from the error of the s parameter in the likelihood fit and do not include further systematic uncertainties. Thus, the uncertainties on the single detector results should be considered higher, which will further decrease

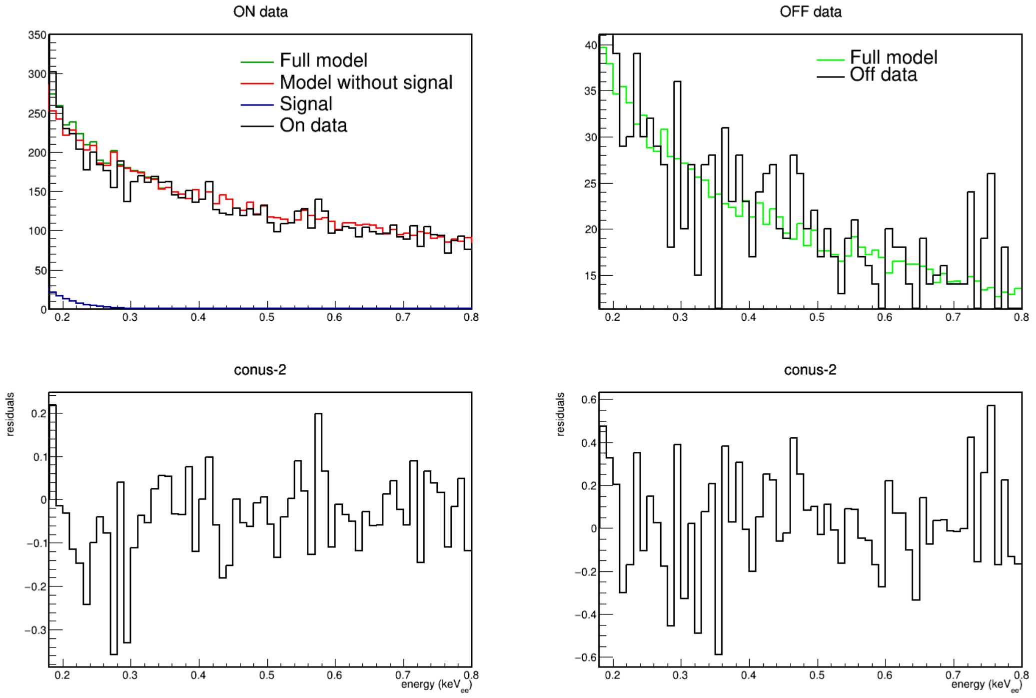

Figure 4.16. Result of the likelihood fit of C2 data in run 1. The upper left plot shows the fit to reactor on data, and the upper right plot shows the fit for reactor off data. The lower plots show the respective residuals. Very good agreement between data and model is found in both fits.

the significance of the single detector results. They are therefore not enough to claim an observation of CEνNS at reactor site and the combined fit of all three detectors has to be considered.

4.7.2 Combined detector result

The final CEνNS result of run 1 of the CONUS+ experiment is acquired with a combined fit of all three detectors used in the analysis. In this procedure, one likelihood function, the sum of the single-detector likelihood functions, is used to fit the on and off spectra of the detectors at the same time. All detectors share one signal scaling parameter s, which can then be used to extract the total number of CEνNS counts.

Figure 4.18 visualises the result of the combined fit. Here, the excess in the data compared to the fitted background model, meaning the background model including the different b parameters and trigger efficiency parameters from the combined fit, is plotted for energies below 350 eV. Due to the different energy thresholds of the detectors, bins above 180 eV feature the sum of data from all three detectors, while lower energy bins only feature data from detectors with matching energy thresholds. The data is additionally normalised to 1

Table 4.10. Best fit parameters for the single detector fit of C2. Pull value refers to the previously measured values for each parameter which are used in the Gaussian pull terms of the likelihood function.

Parameter	Best fit value	Pull value
Signal strength s	$(1.63 \pm 1.12) \cdot 10^{-16}$	-
Neutrino flux	$(1.45 \pm 0.10) \cdot 10^{13}$ cm^{-2} s^{-1}	$(1.45 \pm 0.10) \cdot 10^{13}$ cm^{-2} s^{-1}
Background scaling b	0.98 ± 0.01	1.00 ± 0.024
Trigger efficiency μ	(106 ± 1) eV	(106.0 ± 1.0) eV
Trigger efficiency σ	(51 ± 1) eV	(51.2 ± 1.3) eV
Calibration uncertainty	(12.4 ± 1.6) eV	(0 ± 5) eV
Active mass	(0.95 ± 0.01) kg	(0.95 ± 0.01) kg
Quenching uncertainty p_1	1.00 ± 0.05	1.00 ± 0.05
Quenching uncertainty p_2	$(-6.01 \pm 4.46) \cdot 10^{-4}$	(0.00 ± 0.05)
Quenching uncertainty p_3	$(4.69 \pm 4.28) \cdot 10^{-4}$	(0.00 ± 0.05)
Quenching uncertainty p_4	$(-2.47 \pm 4.99) \cdot 10^{-5}$	(0.00 ± 0.05)

kg detector mass. In this way, the first two bins of the data, where only C3 data (first bin) or C3+C5 data (second bin) enter, can be plotted together with the rest of the bins. The excess in data is compared to the standard model signal prediction for a 1 kg Germanium detector with an exposure of 119 d at the experimental conditions of the CONUS+ experiment.
The figure clearly shows an increase in the data - model excess at energies below 350 eV and the excess closely follows the expected CEνNS signal prediction. All data points lie within 1σ deviation from the predicted signal spectrum. Figure 4.19 shows the corresponding excess of the data compared to the model for the upper part of the ROI, meaning for energies between 350 and 800 eV. Here, no influence from the CEνNS signal is expected and no excess is found accordingly. This is illustrated by the distribution of the deviation of the data points around zero, found in the right-hand plot of Figure 4.19.

Figures 4.18 and 4.19 clearly indicate the presence of the CEνNS signature in the run 1 data of CONUS+. For further illustration, Figures B.1 and B.2 show the result of the combined fit in terms of the sum of the background model compared to the total data set of run 1, in accordance to the figures shown for the single detector fit results. Table 4.13 shows the best fit parameters of the combined detector fit. The fit finds a signal scaling parameter s = $(2.68 \pm 0.58) \cdot 10^{-16}$, which translates to (395 ± 86) CEνNS counts. However, the uncertainty of this value is only based on the uncertainties of the best fit parameters of

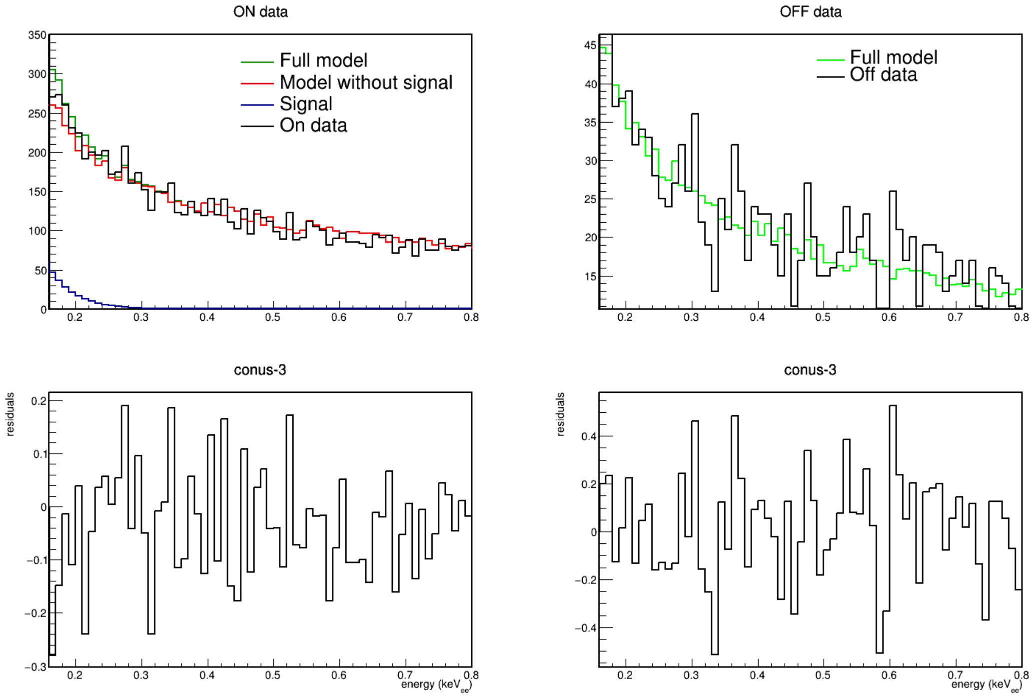

Figure 4.17. Result of the likelihood fit of C3 data in run 1. The upper left plot shows the fit to reactor on data, and the upper right plot shows the fit for reactor off data. The lower plots show the respective residuals. Very good agreement between data and model is found in both fits.

the likelihood fit and does not include several systematic uncertainties. These have to be included to correctly assess the error on the final CONUS+ CEνNS result.

Systematic uncertainties

The following studies of systematic uncertainties were performed by K. Ni. For this and as a general cross check, a second likelihood function (Likelihood B) was introduced. The principles of this likelihood are the same, however there are some key differences between it and the likelihood fit presented in the previous chapter (Likelihood A). The main difference is the treatment of the quenching parameter k of the Lindhard model, which in Likelihood A is fixed to be $k = 0.162$, while it is a parameter of the likelihood function with a Gaussian pull term in Likelihood B. Additionally, Likelihood B uses a different minimisation algorithm compared to Likelihood A and a slightly different implementation of the non-linearity correction.

The first of the systematic uncertainties which were investigated was the impact of the background model. As detailed in Chapter 3, several of the components of the model include non-negligible systematic uncertainties, which translate to uncertainties of the model. The main uncertainties in the ROI are the 6% uncertainty on the muon contribution, coming

Table 4.11. Best fit parameters for the single detector fit of C3. Pull value refers to the previously measured values for each parameter which are used in the Gaussian pull terms of the likelihood function.

Parameter	Best fit value	Pull value
Signal strength s	$(3.17 \pm 1.14) \cdot 10^{-16}$	-
Neutrino flux	$(1.45 \pm 0.10) \cdot 10^{13}$ cm^{-2} s^{-1}	$(1.45 \pm 0.10) \cdot 10^{13}$ cm^{-2} s^{-1}
Background scaling b	1.00 ± 0.01	1.00 ± 0.028
Trigger efficiency μ	(99 ± 1) eV	(99.1 ± 1.0) eV
Trigger efficiency σ	(51 ± 2) eV	(51.1 ± 1.6) eV
Calibration uncertainty	(4.26 ± 1.52) eV	(0 ± 5) eV
Active mass	(0.94 ± 0.01) kg	(0.94 ± 0.01) kg
Quenching uncertainty p_1	1.00 ± 0.05	(1.00 ± 0.05)
Quenching uncertainty p_2	$(3.41 \pm 4.40) \cdot 10^{-4}$	(0.00 ± 0.05)
Quenching uncertainty p_3	$(-2.51 \pm 4.39) \cdot 10^{-4}$	(0.00 ± 0.05)
Quenching uncertainty p_4	$(1.61 \pm 5.00) \cdot 10^{-5}$	(0.00 ± 0.05)

from the error on the initial muon flux in the CONUS+ room, the 14% uncertainty on the neutron contribution, from the initially assumed neutron flux on the outside of KKL, and an estimated 10% uncertainty on the leakage test background component in the C2 and C3 detectors. In order to test the impact of these uncertainties on the likelihood result, the background model was varied within the listed uncertainties, while keeping the total count rate between 400 and 1000 eV constant, and the likelihood fit was performed again with the varied model. This process was repeated several thousand times to attain a distribution of likelihood values. The distribution, which is shown in the left-hand figure of 4.20, was fitted with a Gaussian and the standard deviation of this Gaussian is the additional systematic

Table 4.12. Overview of the measured CEνNS counts in the single detector fits of run 1 of the CONUS+ experiment and comparison to the SM prediction

Detector	Threshold [eV]	Predicted SM CEνNS counts	Measured CEνNS counts
C5	170	116 ± 20	117 ± 57
C2	180	96 ± 16	69 ± 47
C3	160	135 ± 23	186 ± 66

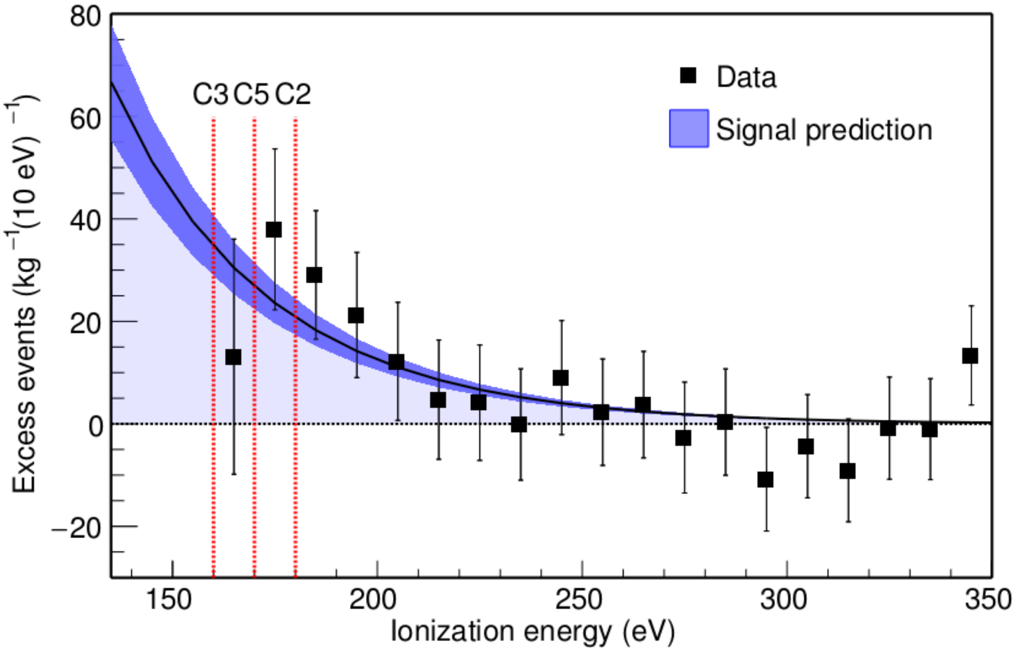

Figure 4.18. Combined result of run 1 of the CONUS+ experiment. The plot shows bin-by-bin excess in the measured data compared to the background model normalised to 1 kg detector mass. The background model includes all relevant best fit parameters from the combined fit. Red-dashed lines show the energy thresholds of the three detectors: Above 180 eV, data of all thee detectors is included. The [170 eV, 180 eV] bin includes data from C3 and C5. The [160 eV, 170 eV] bin only includes C3 data. The signal prediction for a 1 kg Germanium detector with the characteristics of the CONUS+ detectors and an exposure of 119 days is shown in blue. Uncertainties on the data points are statistical uncertainties from the data and model.

uncertainty from the background model. This uncertainty was found to be ±40.

In the same way, the systematic uncertainty due to the implementation of the non-linearity correction of the energy scale was studied. As explained in Section 2.3.8, the non-linearity correction of the energy scale, which is applied in the data processing for CONUS+ is based on the fitting of the non-linearity deviation at different energies with a polynomial. The choice of this function and its parameters introduce an additional systematic uncertainty to the result. To assess this uncertainty, the measured non-linearity deviations shown in Figure 2.10 were varied within their measurement uncertainties and were then fitted again. The thus newly obtained fit function was then used to calibrate the data and the likelihood fit was performed again. This process was again repeated several thousand times and the distribution of likelihood values can be found in the right-hand figure of 4.20. In this way an

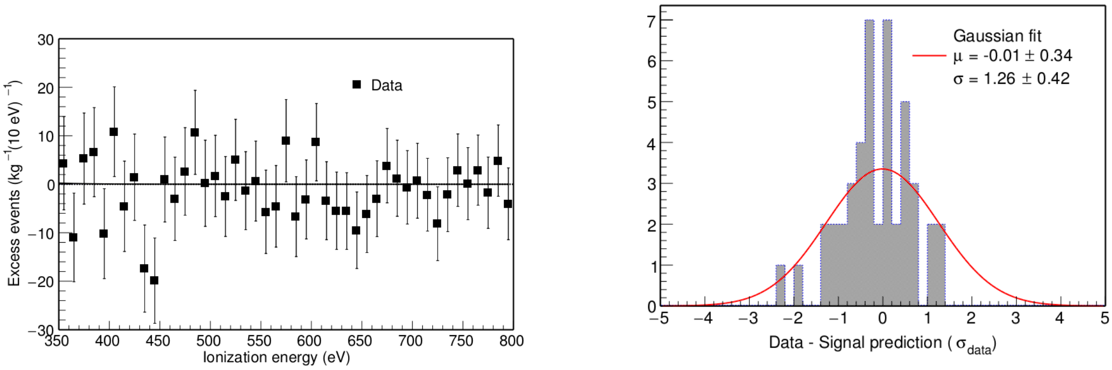

Figure 4.19. Left: Excess of data compared to model for energies above 350 eV, in accordance to Figure 4.18. Right: Deviation of the data from zero in units of the data uncertainty. A gaussian is fitted through the distribution and the mean of the gaussian is found to be compatible with zero. Thus, no significant excess is found between 350 and 800 eV, where no signal is expected.

additional systematic uncertainty of ±47 was obtained.

Lastly, the systematic uncertainty from the chosen likelihood implementation itself was studied. For this, Likelihood B also fitted the combined data of the three CONUS+ detectors and found (402 ± 84) CEνNS counts. The difference of the central values of both likelihoods ±7 is introduced as an additional systematic uncertainty on the value of Likelihood A.

The three additional systematic uncertainties are added to the initial uncertainty of the likelihood fit in quadrature to yield the final uncertainty of the CONUS+ CEνNS result. In this way the final result on the number of CEνNS counts in run 1 of the CONUS+ experiment is found to be **(395 ± 106)**. This result is consistent with the standard model CEνNS prediction of (345 ± 34) within 0.5σ C.L.. Furthermore, the CONUS+ experiment is able to reject the null hypothesis at **3.7σ C.L.**.
With this measurement, the CONUS+ experiment becomes the first CEνNS experiment to measure the interaction for neutrinos produced in nuclear reactors and the first experiment to measure CEνNS for neutrinos with energies below 10 MeV, which therefore interact full coherently. This result was first published in [13]. As detailed in Section 1, this measurement is an important milestone in the field of neutrino physics and opens the possibilities for future high precision measurements of the interaction, which in turn allow the investigation of many possible BSM channels and theories in the neutrino sector.

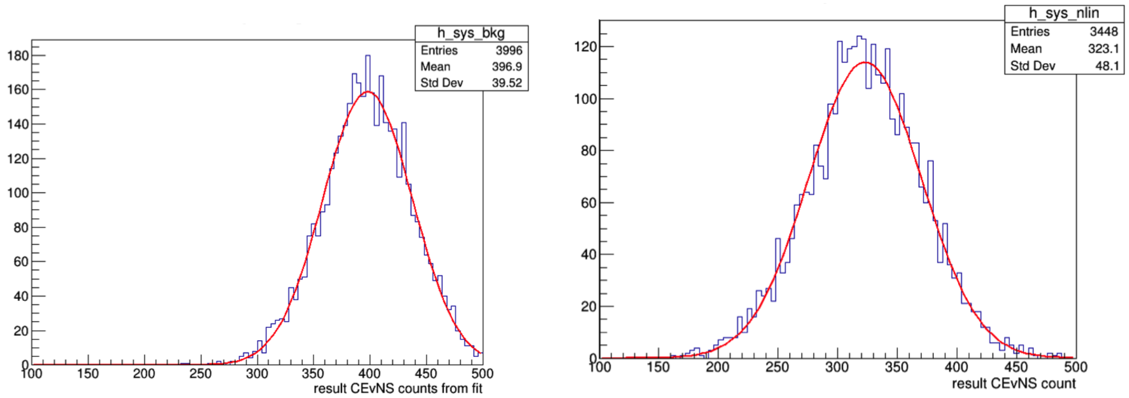

Figure 4.20. Distribution of likelihood values obtained from varying the background model of the detectors within the uncertainties of the main contributions (left) and varying the fit function used for the implementation of the non-linearity correction (right). The distribution is fitted with a Gaussian and a standard deviation of 40 (background model) and 47 (non-linearity) is found respectively.

4.7.3 Checks with different data sets

To verify the validity of the acquired CONUS+ run 1 CEνNS result, several cross checks with different data sets were performed.

The first of these tests used only reactor on data with low radon concentrations in the detector chamber and therefore low radon background contributions in the detector data. As discussed in Section 3.12.2, the radon contribution is somewhat correlated to reactor operations due to the better radon flushing in the reactor off measurement and this test is therefore valuable in checking the treatment of the radon contamination. The data set used for this low radon reactor on encompasses 161 kg d and includes data starting from March of 2024 (see Figure 3.51). The radon contribution in the reactor on background model, as well as the contribution from the other inert gases, was scaled down appropriately. The likelihood fit finds (148 ± 63) CEνNS counts, which is consistent with the SM prediction at (160 ± 16).

Additionally, a slightly extended data set, where 36 additional kg d of exposure from the very end of run 1 were added, was investigated. This additional exposure comes from a period of reactor on data after the reactor outage in May of 2024 and was initially not included in the original data set of run 1. Running the likelihood fit with this extended data set, yields (479 ± 97) CEνNS counts. The expected number of CEνNS counts in this extended exposure is (381 ± 38). The result is therefore consistent with the SM prediction.

4.7.4 Alternative quenching descriptions

As described in Section 2.3.2, the CONUS+ experiment uses the Lindhard model to describe the nuclear quenching in the germanium crystals with a k parameter of k = 0.162 ± 0.004, which was measured in [7] and leads to the signal prediction in Figure 4.18. Alternative quenching descriptions are also tested with the CONUS+ data, as described in the supplemental material of [48] including a linear and cubic functional model to explain an increased quenching factor compared to the Lindhard model found in [6] for very low energies. Figure 4.21 shows the comparison of the CONUS+ excess to the expected signal prediction from these two quenching descriptions. The linear functional model predicts a CEνNS count rate of (2600 ± 300) events, while the cubic model predicts a rate of (550 ± 50) events. Both descriptions are in conflict with the CONUS+ data. The figure also includes an additional data point at 200 eV which was extracted from Figure 4 of [14]. Here, the authors offer a model-independent CEνNS description and approximate the signal with an exponential with two parameters, an amplitude at 200 eV ($A_{0.2}$) and a decay constant. The favoured value for $A_{0.2}$ is shown within a 2σ contour in a 2-dimensional plot of the two parameters. For the data point in Figure 4.21, this favoured value was scaled down to the exposure of the CONUS+ experiment and a correction based on the difference in the neutrino flux compared to the reactor and position in [14] was applied. As expected, the obtained data point matches the linear functional quenching model, which was favoured by the authors, but can be clearly ruled out by the CONUS+ data. As previously mentioned in Section 2.2.1, the linear functional model was already excluded with data from run 5 of the previous CONUS experiment.

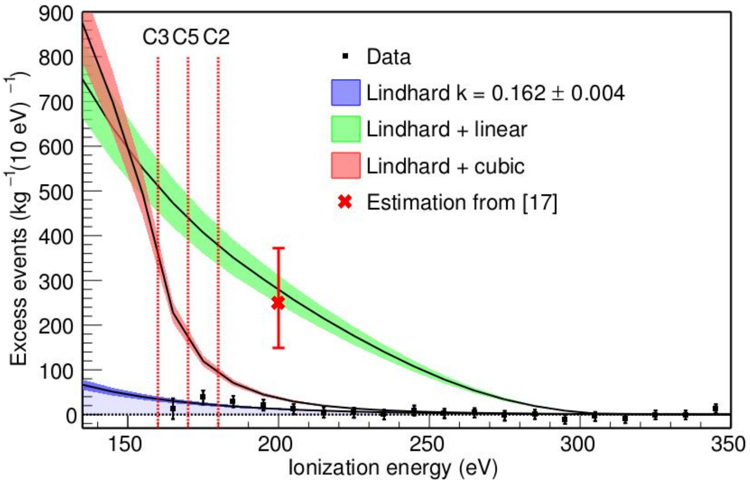

Figure 4.21. Comparison of the CONUS+ excess as plotted in Figure 4.18 to signal predictions from alternative quenching descriptions from [6]. An additional data point at 200 eV is included and was extracted from Figure 4 in [14].

4.7.5 Comparison to other CEνNS measurements

Table 4.14 shows a comparison of the CONUS+ run 1 result to other CEνNS measurements achieved so far. The accelerator measurements were all performed by the COHERENT collaboration, while the two measurements using solar neutrinos were performed by the XENONnT and PandaX experiments. As noted, the CONUS+ result is the first reactor neutrino measurement and therefore the first measurement in the fully coherent regime. The use of different target nuclei in the different experiments allows the precise study of the CEνNS cross section, specifically its quadratic enhancement with the number of neutrons in the target isotope. All listed measurements are in agreement with the SM prediction for the expected count rate, except for the germanium measurement of the COHERENT experiment. Here, a slightly lower rate then expected was measured, although the discrepancy was not found to be highly significant. The deficit was not confirmed with the CONUS+ germanium measurement presented in this work.

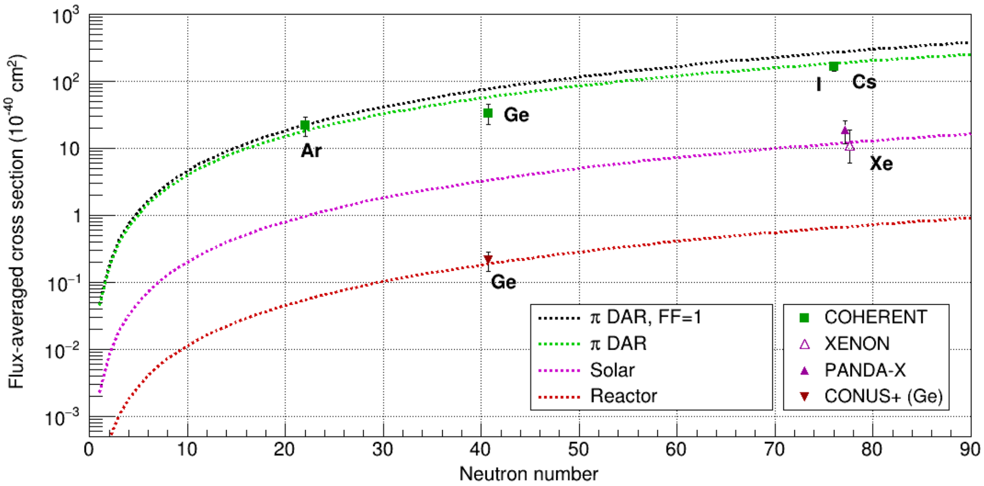

Figure 4.22. Comparison of all CEνNS measurements listed in Table 4.14 to the predicted flux-averaged cross section from the Standard Model. The calculated cross sections and the framework for the creation of this plot were provided by Kate Scholberg of the COHERENT collaboration. The CONUS+ experiment measured a cross section of $(0.215 \pm 0.071) \cdot 10^{-40}$ cm^{-2}. For the π DAR source, two separate predictions are plotted: one considering a fully coherent interaction (FF=1, black line) and the more realistic case of a smaller form factor (green line) as is expected for this neutrino source.

Figure 4.22 shows a comparison of the CEνNS measurements listed in Table 4.14 to the flux-averaged cross section predicted by the Standard Model. Here, the flux-averaged cross section is defined as:

$$\langle\sigma\rangle = \frac{\int_0^{E_\nu^{\text{max}}} \phi(E_\nu)\,\sigma(E_\nu)\,dE_\nu}{\int_0^{E_\nu^{\text{max}}} \phi(E_\nu)\,dE_\nu} \tag{4.14}$$

where:

- $\phi(E_\nu)$ is the neutrino flux spectrum of the specific source (π DAR, Reactor, Solar) where the Solar spectrum considers the ^{8}B neutrinos and the reactor spectrum is based on an extrapolation of the Huber-Müller model [105, 106],
- $\sigma(E_\nu)$ is the total cross section at energy E_ν,
- E_ν^{max} is the the end-point of the neutrino flux spectra depending on the source.

No uncertainties on the SM cross section are considered in the SM predictions shown in this plot. The definition is independent of detector characteristics like energy thresholds and detection efficiencies, which are instead considered in the measured data points corresponding to the different CEνNS measurements. By selecting the predicted SM flux-averaged cross section at the appropriate neutron number and multiplying it by the data/prediction ratios found in the last column of Table 4.14 a measured cross section can be assigned to each of the measurements. The CONUS+ run 1 result is equivalent to a measured flux-averaged cross section of $(0.215 \pm 0.071) \cdot 10^{-40}$ cm^{-2}.

Table 4.13. Best fit parameters for the combined fit of all detectors. Pull value refers to the previously measured values for each parameter which are used in the Gaussian pull terms of the likelihood function.

	Parameter	Best fit value	Pull value
All	Signal strength s	$(2.68 \pm 0.58) \cdot 10^{-16}$	-
	Quenching uncertainty p_1	1.00 ± 0.05	(1.00 ± 0.05)
	Quenching uncertainty p_2	$(-6.85 \pm 4.39) \cdot 10^{-5}$	(0.00 ± 0.05)
	Quenching uncertainty p_3	$(9.57 \pm 4.45) \cdot 10^{-5}$	(0.00 ± 0.05)
	Quenching uncertainty p_4	$(2.99 \pm 5.00) \cdot 10^{-6}$	(0.00 ± 0.05)
C5	Neutrino flux	$(1.44 \pm 0.10) \cdot 10^{13}$ cm^{-2} s^{-1}	$(1.45 \pm 0.10) \cdot 10^{13}$ cm^{-2} s^{-1}
	Background scaling b	0.98 ± 0.01	1.00 ± 0.02
	Trigger efficiency p_1	(109 ± 1) eV	(109 ± 1) eV
	Trigger efficiency p_2	(54 ± 2) eV	(54.3 ± 2.4) eV
	Calibration uncertainty	(-1.87 ± 1.44) eV	(0 ± 5) eV
	Active mass	(0.94 ± 0.01) kg	(0.94 ± 0.01) kg
C2	Neutrino flux	$(1.45 \pm 0.09) \cdot 10^{13}$ cm^{-2} s^{-1}	$(1.45 \pm 0.10) \cdot 10^{13}$ cm^{-2} s^{-1}
	Background scaling b	0.98 ± 0.01	1.00 ± 0.02
	Trigger efficiency p_1	(106 ± 1) eV	(106 ± 1) eV
	Trigger efficiency p_2	(51 ± 2) eV	(51.2 ± 1.3) eV
	Calibration uncertainty	(1.35 ± 1.72) eV	(0 ± 5) eV
	Active mass	(0.95 ± 0.01) kg	(0.95 ± 0.01) kg
C3	Neutrino flux	$(1.46 \pm 0.09) \cdot 10^{13}$ cm^{-2} s^{-1}	$(1.45 \pm 0.10) \cdot 10^{13}$ cm^{-2} s^{-1}
	Background scaling b	0.99 ± 0.01	1.00 ± 0.02
	Trigger efficiency p_1	(99 ± 1) eV	(99 ± 1) eV
	Trigger efficiency p_2	(51 ± 2) eV	(51.1 ± 1.6) eV
	Calibration uncertainty	(3.07 ± 1.57) eV	(0 ± 5) eV
	Active mass	(0.94 ± 0.01) kg	(0.94 ± 0.01) kg

Table 4.14. Comparison of the CONUS+ run 1 result with other CEνNS measurements.

Source	Target	ν energy [MeV]	flux [cm^{-2}s^{-1}]	data	data/SM prediction
Accelerator [102]	Cs	$\sim 10-50$	$5{\cdot}10^7$	306 ± 20	0.90 ± 0.15
Accelerator [21]	Ar	$\sim 10-50$	$2{\cdot}10^7$	140 ± 40	1.22 ± 0.37
Accelerator [22]	Ge	$\sim 10-50$	$5{\cdot}10^7$	21 ± 7	0.59 ± 0.21
Sun [103]	Xe	< 15	$5{\cdot}10^6$	11 ± 4	0.90 ± 0.45
Sun [104]	Xe	< 15	$5{\cdot}10^6$	4 ± 1	1.25 ± 0.52
Reactor	Ge	< 10	$1.5{\cdot}10^{13}$	395 ± 106	1.14 ± 0.36

Chapter 5

Next steps in the CONUS+ experiment

With the result of run 1, and a measured count rate of (395 ± 106) CEνNS events, the CONUS+ experiment is the first experiment to measure the CEνNS interaction for neutrinos produced at a nuclear reactor and in the fully coherent regime. This measurement is a big milestone in the ongoing field of CEνNS and neutrino experiments. However, the CEνNS channel offers many future benefits and potential for studying of SM and BSM physics as explained in Section 1.3. These benefits often, especially in terms of cross-checks of the standard model and discovery of new physics, lie in precision measurements of the CEνNS cross section. For this reason, it is the future goal of the CONUS+ experiment to provide such precision measurements in order to improve the understanding in this field and be at the forefront of CEνNS experiments.

5.1 Detector upgrade

Run 1 of the CONUS+ experiment was officially finished in September of 2024 after the successful californium irradiation campaign to improve the energy calibration uncertainty of the detectors. After this, the CONUS+ shield was opened in October of 2024 and several upgrades of the setup were performed.

The main upgrade is the replacement of three of the four 1 kg germanium detectors (C5, C2 and C4) with new 2.4 kg germanium detectors (C6, C7 and C9). The detectors were again produced by Mirion Lingolsheim and are equivalent to the old smaller detectors in terms of electronics and design. Figure 5.1 shows a comparison of the old and new detector setup inside the CONUS+ shield. In order to fit the new bigger detectors with their bigger cryostats into the detector chamber, the endcap of the cryostat sits at an angle on the cooling finger.

The new detectors lead to an increase in the total crystal mass from the previous 4 kg to now 8.2 kg. As the expected signal rate of a CEνNS experiment scales linearly with the

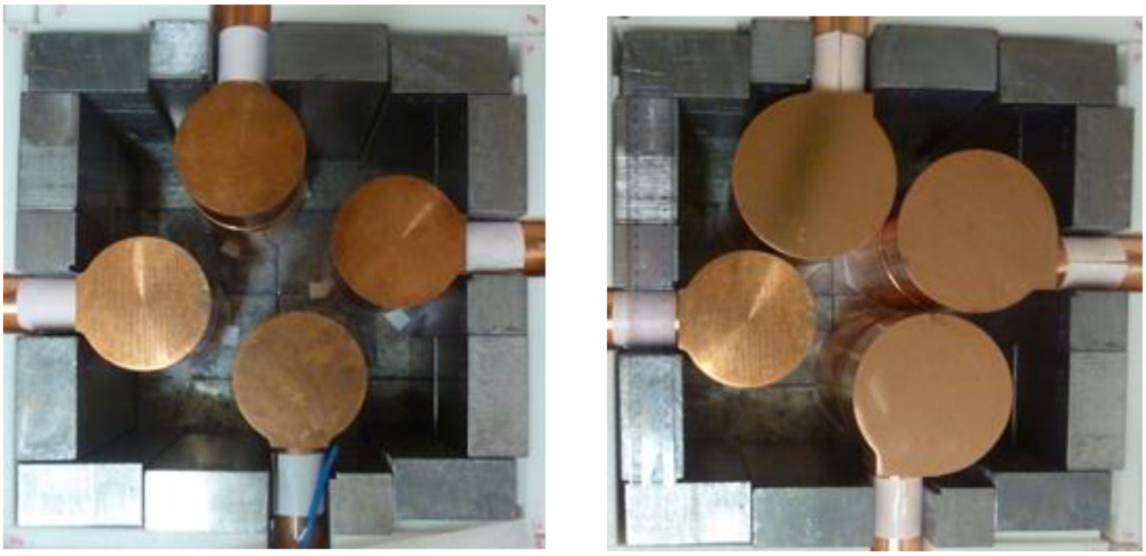

Figure 5.1. View of the CONUS+ detectors in the opened shield. Left: Old setup in run 1 with four 1 kg detectors. Right: New setup for run 2 with three new 2.4 kg detectors.

detector mass due to the homogenous scattering probability for neutrinos in the detector, this leads to a factor 2.05 increase in the amount of expected neutrino events. The expected statistical gain is illustrated in Figure 5.2. The new setup still features one of the old smaller detectors, namely the C3 detector. It was decided to keep this detector for run 2 of the experiment in order to have a point of comparison to the run 1 data set. By still including C3, it can be checked whether the background levels in the experiment change after the opening of the shield through the introduction of outside contaminations. The C3 detector was chosen since it featured the best performance in run 1 of the experiment (see Section 4.7.1). In future runs, the C3 detector will also be replaced with an additional 2.4 kg detector C8, which is currently being stored at MPIK and used for auxiliary measurements here.

Apart from the new 2.4 kg detectors, several additional improvements were made to the CONUS+ setup in the campaign in October/November 2024. Among these was the changing of the cooling liquid in the cooling system of the CP5 cryocoolers (see Section 2.3.6). Previously, water had been used here, and an additive was included in the water to decrease the chance of corrosion in the CP5 cryocoolers. This additive at times lead to accumulation of particles at critical points of the cooling circuit, which reduced the flow of cooling water through the system and lead to an increase in the CP5 temperature, which can induce noise in the detectors. For this reason, a new coolant, the commercially available SP 12 EVO [107], was chosen. This coolant is regularly used as a coolant for car motors and other standard application and is known for its long life time and is easy to acquire.

Further small improvements were made in the shield of the CONUS+ experiment. Here,

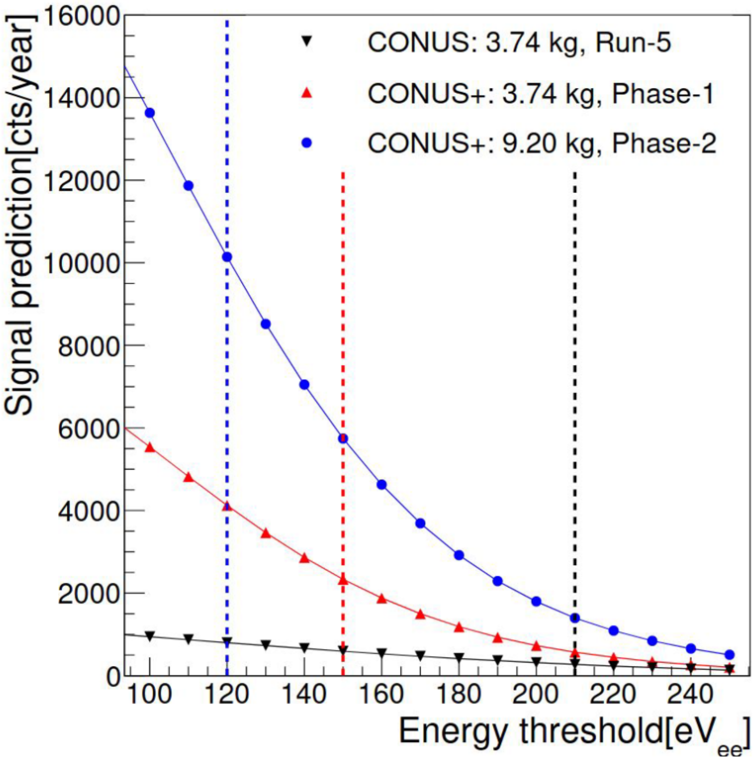

Figure 5.2. Projected count rate for the CONUS setup, the CONUS+ setup in run 1, and the CONUS+ setup in run 2 assuming four 2.4 kg detectors. Three possible thresholds are marked at 210 eV (CONUS), 150 eV (approximately CONUS+ run 1), and 120 eV.

two defunct PMTs in the muon veto system were replaced with new working PMTs. Additionally, the radon tightness of the shield was enhanced through the use of teflon paper at the entry points of the four cooling fingers into the shield.

5.2 Stability and detector performance

The new CONUS+ run 2 setup has been running continuously since November of 2024 and has already measured data during the reactor maintenance period in May of 2025. The following sections will give an overview of the detector performance and stability at the time of writing of this work.

5.2.1 Performance of new detectors

Trigger efficiency

Figure 5.3 shows the measured trigger efficiency of two of the new detectors (C6 and C7) at KKL alongside the trigger efficiency of the old C3 detector still in the CONUS+ setup. The C9 detector is not shown because it is currently not taking data. The reason for this will

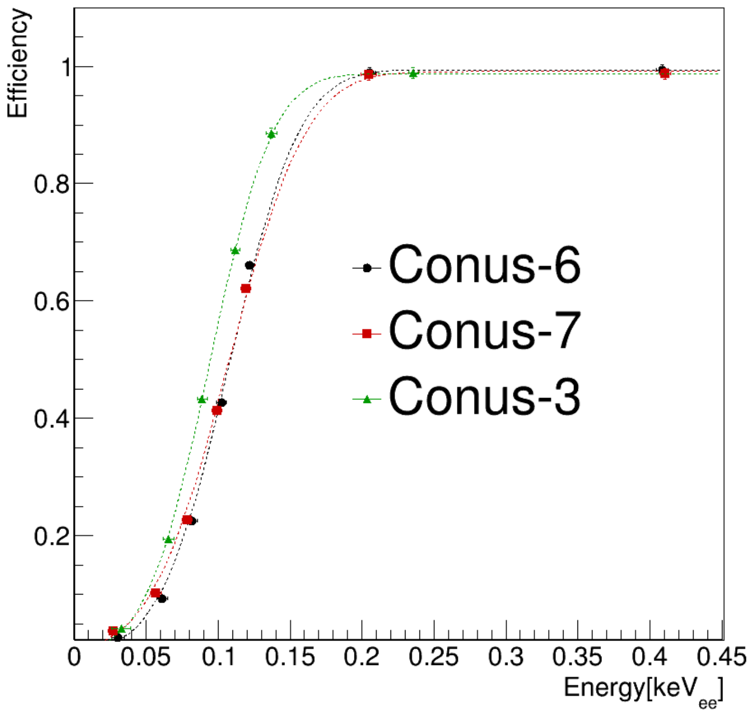

Figure 5.3. Trigger efficiency measurement for the new C6 and C7 detectors at KKL alongside the trigger efficiency of the old C3 detector.

be explained in Section 5.2.2.

The two new detectors show excellent trigger efficiencies at low energies which are comparable to the efficiency curve of C3. In general, they are slightly worse and the curve is shifted approximately 10 - 20 eV to the right. Nevertheless, they still show approximately 80% efficiency at 150 eV and reach efficiencies of over 20% down to approximately 70 eV, which was one of the requirements in the threshold of the detectors. This value is completely sufficient for the CEνNS search of the CONUS+ experiment, as the run 1 setup showed that the threshold definition is dominated by the position of the noise edge in the spectrum (see Section 4.4). The two parameters of the error function describing the trigger efficiency curves of C6 and C7 are listed in Table 5.1. Additionally, their evolution over the course of run 2 is shown in Figure 5.4.

Energy resolution

Table 5.2 shows the pulser resolution of the new CONUS+ detectors C6 and C7 as measured in the latest pulser measurement at KKL on 26.06.25. Both new detectors feature excellent resolutions comparable to those of C3 and the other detectors in run 1 (see Table 2.1). As the pulser resolution is one of the main indicators on the noise level in the detector and the

Table 5.1. Best fit values for the two parameters of the trigger efficiency function for C6 and C7 in run 2 of the CONUS+ experiment. As explained in Section 4.2, μ gives the position of $\epsilon_{trig} = 0.5$, and σ is the width of the efficiency increase, or in other words a measure for the sharpness of the increase.

Detector	μ [keV]	σ [keV]
C6	0.108 ± 0.001	0.049 ± 0.005
C7	0.107 ± 0.001	0.057 ± 0.002

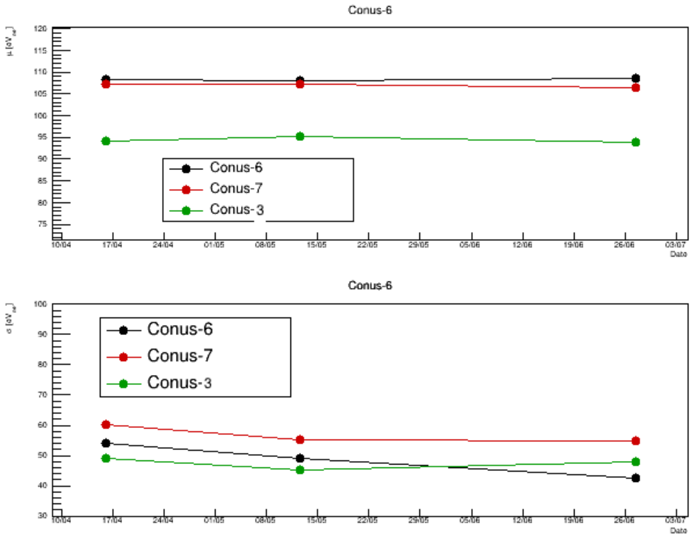

Figure 5.4. Evolution of the two trigger efficiency parameters for C3, C6 and C7 during run 2. Both values vary only slightly in the order of ~2 eV.

position of the noise edge in the spectrum, the small resolutions of the new detectors suggest a similarly low or even slightly lower energy threshold than the previous detectors in run 1.

Energy calibration

The energy scale calibration of the new detectors is performed in the same way as for the old detectors in run 1 by using the intrinsic germanium γ-lines in the spectrum. The values for the calibration coefficients a and b are shown in Table 5.3 and their stability over the course of the ongoing run is shown in Figure 5.5.

5.2.2 Run 2 data taking

The official start of run 2 of the CONUS+ experiment was the 20th of February 2025 after the successful commissioning phase of the new detectors in KKL. Since then the experiment has taken approximately 116 days of reactor on and 14 days of reactor off data as of the writing

Table 5.2. Result of latest pulser resolution measurement in run 2 for the C3, C6, and C7 detectors, performed on 26.6.25. ΔE_{Pulser} refers to the FWHM of the pulser signal in the spectra of each detector.

Detector	ΔE_{Pulser} [eV]
C3	52.8 ± 0.4
C6	49.8 ± 0.3
C7	48.1 ± 0.3

Table 5.3. Calibration coefficients a and b for all four detectors in run 2 of the CONUS+ experiment. a describes a constant offset of the energy calibration function (in keV), while b describes the slope of the function (see Equation 2.7).

Detector	a [keV]	b $[\frac{keV}{Channel}]$
C3	$- 0.00496 \pm 0.00437$	$0.00109 \pm 5 \cdot 10^{-7}$
C6	$- 0.00300 \pm 0.00218$	$0.00108 \pm 3 \cdot 10^{-7}$
C7	$- 0.00241 \pm 0.00437$	$0.00110 \pm 3 \cdot 10^{-7}$

of this work. The amount of off data which was taken in the reactor maintenance outage in May of 2025 is slightly reduced compared to the amount of off data in run 1 due to a power outage in the CONUS+ room and setup in the second half of May 2025. This unexpected power outage lead to the failure of the high voltage crates as well as the cooling of the four detectors and to their subsequent shut down. The recovery of the detector involved pumping the cryostats to reinstate the vacuum conditions within them which had deteriorated due to the missing cooling. The detectors are continuously running again since the beginning of June 2025. The amount of off data still amounts to a higher exposure compared to run 1 due to the larger detector masses in run 2.

During run 2 data taking up to this point, the C9 detector, one of the three new 2.4 kg detectors, shows unstable conditions and features reoccurring signal losses. The behaviour is currently being analysed in cooperation with Mirion Lingolsheim. For this reason the C9 detector is excluded from all figures shown in this section and no C9 data is included in run 2 as of now.

5.2.3 Noise rate and stability

Figure 5.6 shows the width of the noise peak, the noise rate, the cryocooler temperature and the cryocooler power for the three detectors in run 2 of the experiment from the start of

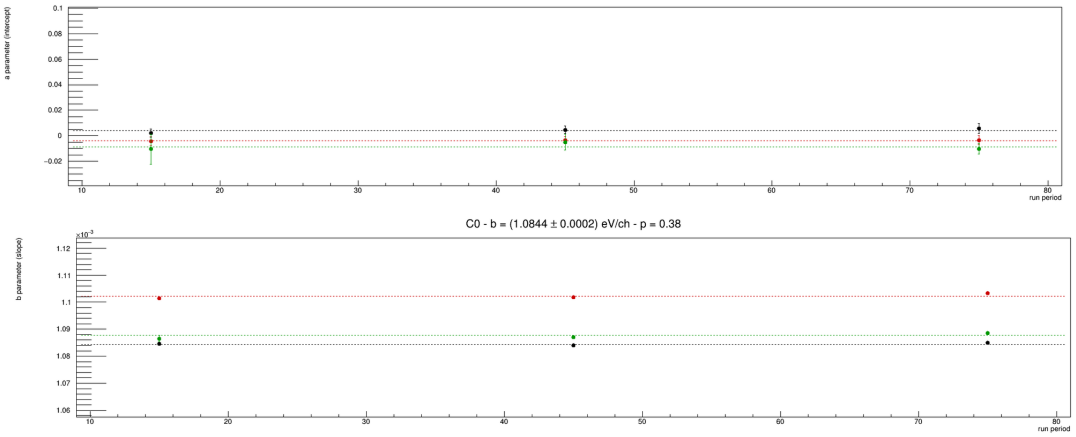

Figure 5.5. Evolution of the calibration coefficients a and b for C3, C6 and C7 during run 2.

run 2 up to the power loss during the reactor outage in May 2025. As described in Section 4.1.1, time periods with variations of the noise level above 10% are cut from the data in the analysis. In the shown period, all time periods pass this rejection criterium. It is noticeable, that all three detectors show a steady increase in the cryocooler power over that time frame, with the two new bigger detectors featuring an increase of around 10 W and C3 featuring an increase of around 3 W. This power increase does not coincide with an increase in the noise level which again shows the ability of the new water cooling system to reduce the correlation between the two.

5.3 New data sets

As described in Section 5.2.2, the experiment has so far collected 116 days of reactor on and 14 days of reactor off data. Table 5.4 shows the corresponding exposure in all three detectors and in total.

Table 5.4. Total collected exposure of the three detectors in run 2 in both reactor on and off periods.

Detector	Exposure ON [kg d]	Exposure OFF [kg d]
C3	116	14
C6	278	34
C7	278	34
Total	672	82

As can be seen from the table in comparison to the collected exposure in run 1 in Table 4.1, run 2 has so far accumulated approximately 1.6 times as much reactor on exposure and 1.4 times as much reactor off exposure. Assuming in first order a scaling of the experimental

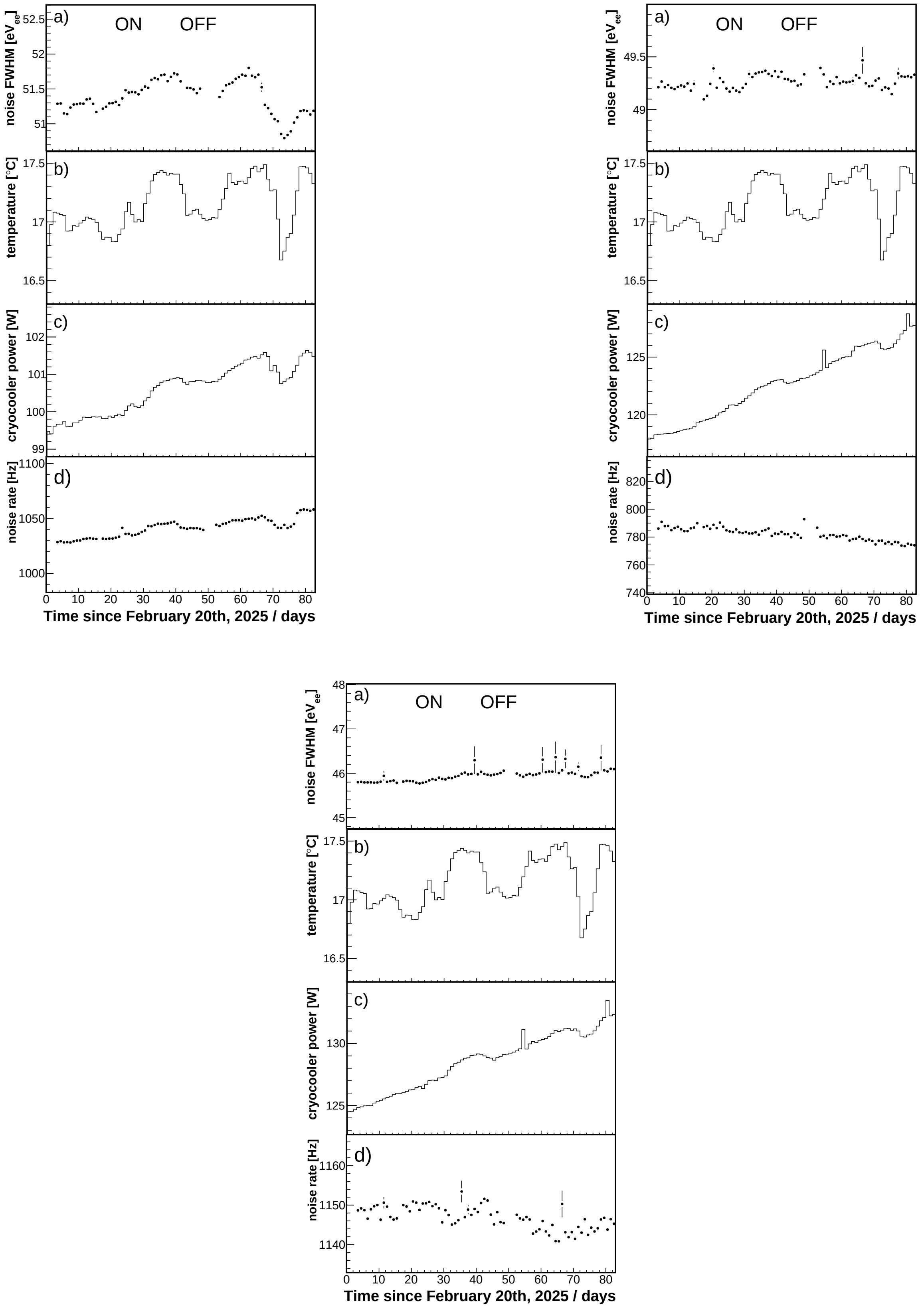

Figure 5.6. Noise and environmental parameters for the three detectors currently operating in run 2 of the CONUS+ experiment: C3 (upper left), C6 (upper right), and C7 (lower middle).

sensitivity with $\frac{1}{\sqrt{\text{Exposure}}}$, this increased exposure corresponds to an improvement of 21% in sensitivity. This very simple assumed scaling neglects the impact of systematic uncertainties in the sensitivity and only takes statistical uncertainties into account, which is why a full sensitivity study for run 2 has to be performed.

5.3.1 Background level and stability

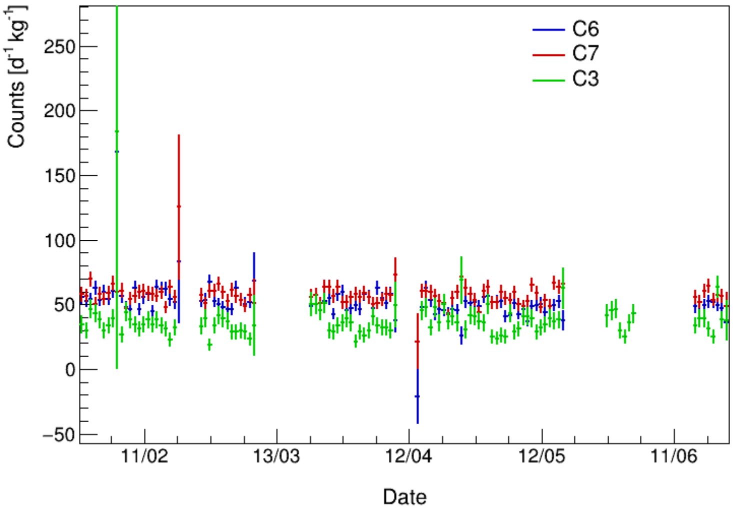

Figure 5.7. Evolution of count rate in the 10.4 keV $^{68/71}$Ge line in all three detectors over the course of run 2.

Figures 5.7, 5.8, and 5.9 show the evolution of the background count rates in the 10.4 keV $^{68/71}$Ge line, the [0.4,1] keV energy range, and the [2,8] keV energy range over the course of data taking in run 2 up to the writing of this thesis. Good stability is observed for all ranges. In the case of the 10.4 keV $^{68/71}$Ge line it can be seen that the count rates which are normalised to the detector mass agree well between the three separate detectors. This is to be expected, since the amount of $^{68/71}$Ge in the germanium crystals scales approximately with the total volume and therefore the mass of the crystals. For the two energy ranges shown in 5.8 and 5.9 a general reduction of the total integrated count rate and therefore the overall background level in the two new bigger detectors C6 and C7 compared to the old C3 detector is shown. This reduction in the overall rate can be explained partially by considering the difference between volume and surface scaling in different background contributions. As opposed to the $^{68/71}$Ge line, most of the background sources listed in the full background decomposition of the run 1 detectors including the major contributions from cosmic muons and neutrons are expected to scale with the surface area of the detector and not with the volume. This is because interactions of these background sources primarily occur at the

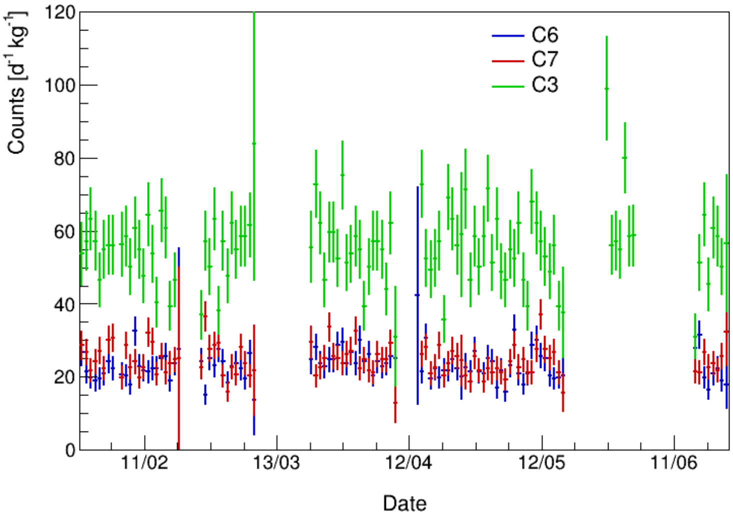

Figure 5.8. Evolution of integrated count rate between 400 and 1000 eV in all three detectors over the course of run 2.

surface of the detector. As a result, the count rate normalised to the mass of the detectors, as plotted in the figures, is expected to scale with the ratio of surface area to volume. This ratio is approximately 1.4 times bigger for the 1 kg detector than for the 2.4 kg detectors. The remaining discrepancy between the count rates could be explained by impacts from the new detector geometry and increases in the dead and passivation layers of the crystals. Additionally, the new detectors do not feature the leakage test background component and the additional ^{60}Co component which were found for C3 (see Tables 3.19 and 3.20) which make up around 10% of the C3 background in these regions. A detailed background model for the new detectors in run 2 is again needed for future analysis of the data in order to fully understand the new levels.

In addition to such a complete background study, the CONUS+ experiment will also implement pulse shape discrimination for data taken in run 2 of the experiment. As previously briefly mentioned in Section 2.3.3, the shape of the pulses created by interactions in the germanium crystals of the experiment and recorded in the DAQ system encode information about the location of the interaction in the crystal. Of special interest are the so-called ”slow pulses” which stem from interactions happening inside the outer transition layer of the crystal and feature longer rise times compared to pulses happening inside the bulk volume of the crystal due to inhomogeneous electric fields in the transition layer. These pulses can be identified through a fit and cut from the data, since interactions in the transition layers are considerably more likely to have originated from a background event (for example a low energy γ) than from a neutrino interaction. In this way the background levels of the detectors can be reduced. This procedure was already shown to be applicable to the CONUS

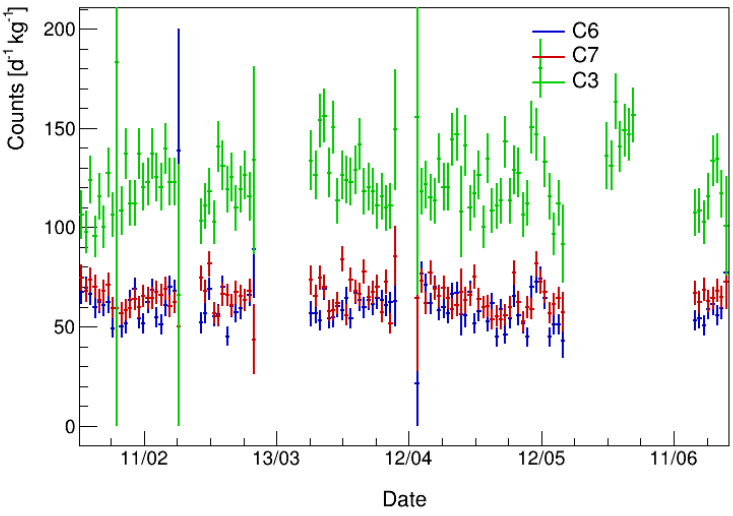

Figure 5.9. Evolution of integrated count rate between 2 and 8 keV in all three detectors over the course of run 2.

detectors in [52] and was used for the final CONUS run 5 result [48].

5.4 Sensitivity study

In order to assess the potential of the new detector setup in run 2 of the CONUS+ experiment, a preliminary sensitivity study was conducted by E. Sanchez. The study makes several simplifying assumptions which are necessary at this early stage of run 2 before a full analysis and background model are established.

For the study ”mock data” (or toy Monte Carlos) were produced. Here, the background model of the C5 detector in run 1 as well as the CEνNS signal prediction were used to estimate the mean bin values in the energy spectra for different reactor on exposures. Figure 5.10 shows such a generated data set for an assumed reactor on measurement time of 365 days. The statistical uncertainty on each bin is assumed to be poissonian around the mean value calculated from the exposure and the count rate in each bin is varied within that uncertainty. In this way, many different data sets can be produced for one assumed measurement time in order to assess statistical fluctuations in the final sensitivity. Additionally, this approach allows for the scaling of the background seen in the detectors by simply scaling the predicted background rate from the background model by some factor. In this way, the actual conditions of run 2, where a significantly lower background level is observed for the C6 and C7 detectors (see previous section) can be accounted for. Furthermore, the low energy threshold of the detectors can be changed arbitrarily.

To predict the sensitivity of the experiment 100 data sets at varying exposures between

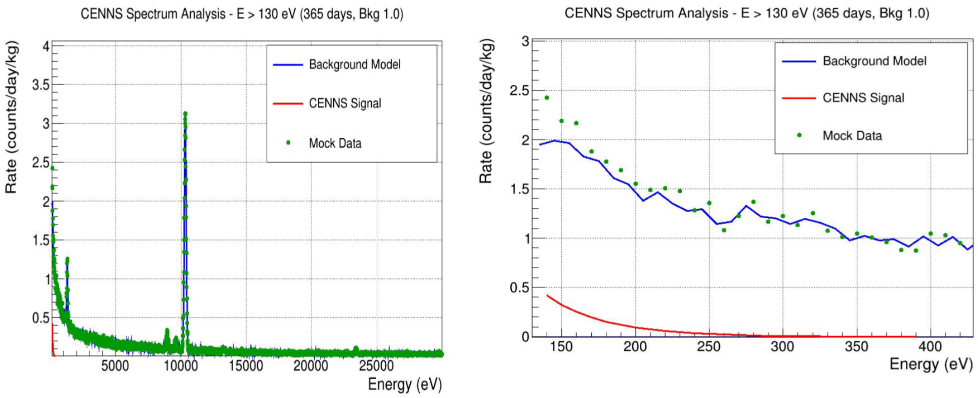

Figure 5.10. Toy Monte Carlo for 365 days of reactor on measurement time, assuming the same background level as for the C5 detector in run 1 (indicated by ”Bkg 1.0”).

50 and 1000 kg days and at three different low energy thresholds (140 eV, 160 eV, 180 eV) were produced. For each of these data sets a likelihood fit and profile likelihood ratio test (as explained in Section 4.6.1) was performed and the significance of the rejection of the null-hypothesis was extracted.

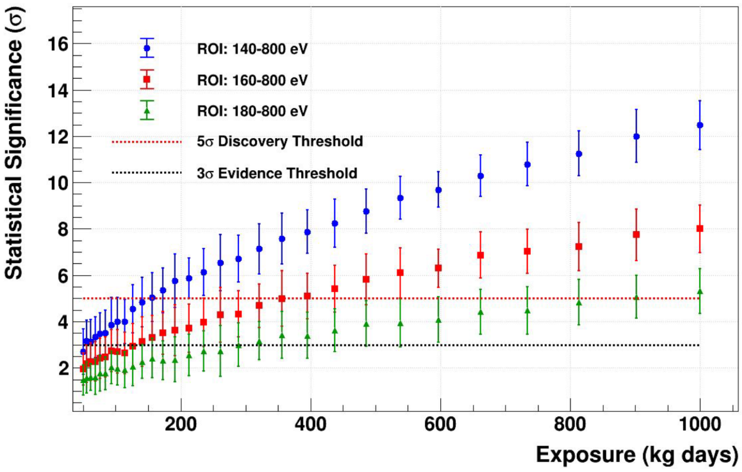

Figure 5.11. Predicted statistical sensitivity of the CONUS+ setup for three different energy thresholds at different exposures.

Figure 5.11 shows the predicted sensitivities for different exposures and the impact of the low energy thresholds on them. For this a background scaling of one is assumed, meaning the same background as in the C5 detector in run 1 is assumed for all detectors in run 2. It can be seen that in the optimal case of an energy threshold of 140 eV a significance of 5σ is already reached after an exposure of 156 kg days, while it is reached after 395 kg days for a threshold of 160 eV, and after 902 kg days is the most conservative case of 180 eV.

In order to get a more complete and realistic picture of the situation and also study the impact of the background level in run 2, three scenarios were imagined:

1. Conservative scenario: Energy threshold = 180 eV: Background ratio to run 1 = 1.0

2. Realistic scenario: Energy threshold = 160 eV: Background ratio to run 1 = 0.7

3. Optimistic scenario: Energy threshold = 140 eV: Background ratio to run 1 = 0.5

Figure 5.12 shows the projected statistical significances for these scenarios. It can be seen that a 5σ significance is reached after 902 kg days in the conservative scenario, 290 kg days in the realistic scenario and, and already after 84 kg days in the optimistic scenario. It is worth pointing out, that while the final energy thresholds of run 2 have not yet been defined, it is likely that they will be at least as good as the ones of run 1. Furthermore, as seen from Figures 5.7, 5.8, and 5.9, the average background level of the three detectors in run 2 is likely close to 50% of that in run 1, meaning that the run 2 result might end up somewhere between the realistic and optimistic scenario plotted above.

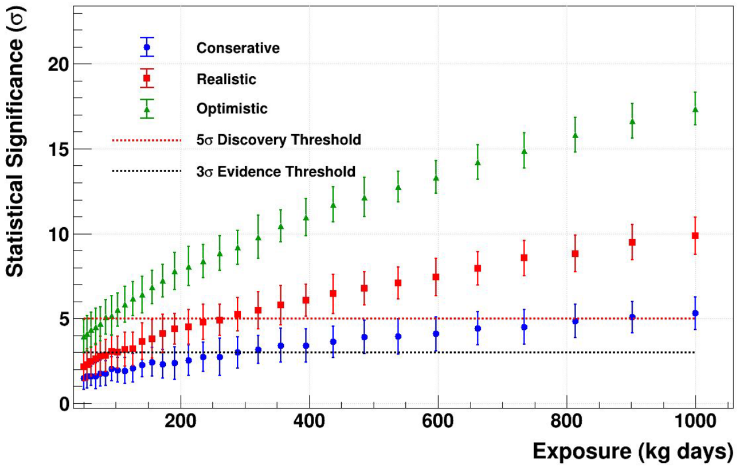

Figure 5.12. Predicted statistical sensitivity of the CONUS+ setup for the three listed scenarios.

This preliminary sensitivity study shows the great potential of the run 2 setup of CONUS+ for a precision measurement of the CEνNS interaction. However, as mentioned in the opening of the section, the study made a few simplifying assumptions. Firstly, the background spectrum of the C5 detector in run 1 was assumed by using its background model. This will lead to different results in the likelihood fits compared to the analysis of the actual run 2 data, since especially the spectra of C6 and C7 might differ (also in shape) from the run 1 C5 spectrum. Secondly, the study always assumed one shared low energy threshold between all three detectors which might not be the case for the run 2 analysis as seen from the previous run 1 analysis. Thirdly, the method presented here only takes reactor on measurements into account. By including additionally the reactor off measurements the precise knowledge about the background model can be greatly improved and the likelihood fit has more statistics, as these measurements are also fitted. The major simplification of this sensitivity study is however that it only assumes statistical uncertainties as represented by the poissonian uncertainty of the count rate in each bin of the energy spectra. As was seen in run 1 (see Section 4.7.2), the statistical uncertainty extracted from the likelihood fit is only one part of the total uncertainty of the final result. Major contributions also come from the statistical uncertainty of the background model and the non-linearity implementation of the energy scale, as well as in small parts from the chosen fit method. A full sensitivity study would have to include these effects, however they are hard to predict at the current stage. In run 1, it was seen that the inclusion of the systematics increased the uncertainty of the final CEνNS result from ±86 to ±106, an increase of approximately 20%.

Chapter 6

Conclusions

The CONUS+ experiment [4] is the successor to the CONUS experiment [48] and was built in order to achieve the first detection of the CEνNS interaction in the fully coherent regime, using antielectron neutrinos from a nuclear power plant. This goal was achieved in January 2025, when the experiment first published its result from its run 1 campaign, where a neutrino signal was measured at a count rate of (395 ± 106) with an exposure of 347 kg days, which is consistent with the SM prediction within 1σ and allows the rejection of the background-only hypothesis at a 3.7σ confidence level [13]. This work was focused on the establishment of a full background decomposition of the CONUS+ run 1 data, a crucial step towards the complete understanding of the data, as well as on the final likelihood analysis of it. The findings of this thesis therefore directly enabled and provided the successful first result of the CONUS+ experiment. In the following, the main topics will be summarised and highlighted.

The CONUS+ experiment is located at the KKL nuclear power plant in Leibstadt, Switzerland. Here, the experiment was placed inside of the reactor building of the power plant at a distance of 20.7 meters from the reactor core, resulting in an expected neutrino flux of $1.45 \cdot 10^{13}$ cm^{-2} s^{-1} at full reactor power [5]. In run 1, which lasted from November 2023 to August 2024 and included one reactor outage in May 2024, the experiment operated four HPGe detectors with an active mass of $\sim$1kg each. All of them feature excellent pulser resolutions below 50 eV FWHM and very good trigger efficiencies of almost 100 % down to 150 eV, which was achieved due to several upgrades performed by Mirion Lingolsheim before the start of the experiment [8]. Consequently, all detectors reach very low detection thresholds between 160 and 180 eV, an important characteristic in the search for CEνNS, since he expected signal is an exponentially rising signature at energies below 300 eV.

Inside of the reactor building, the four CONUS+ detectors are placed inside of an elaborate shield setup, consisting of several layers of lead, polyethylene and plastic scintillators as muon vetos, in order to protect them from different kinds of radiation which can induce background in the detectors. Despite the very good shielding capabilities of the CONUS+ shield, which reduces the background count rate by approximately four orders of magnitude, the resulting spectra are not background-free. They are, in fact, still dominated by background events, due to the rare nature of neutrino interactions. As such, the understanding and complete decomposition of the background is necessary for the experiment in order to establish a working background model, which can then later be used as input for the likelihood function in the final analysis of the data. For this reason, Monte Carlo simulations were used to investigate all possible background sources for the experiment. For these simulation, the MaGe framework [78] was used. It is based on Geant4 and was specifically developed and validated for the Majorana and Gerda experiments, two low background neutrino experiments which deal with similar background sources as the CONUS+ experiment. In this framework, a detailed model of the CONUS+ detectors and shielding was set up and the simulations were started from different volumes, either inside or outside of the shielding, depending on the appropriate position for the background source. After the results of the simulations were acquired, a post processing procedure was applied in which detector specific properties like the nuclear quenching and the detector resolution were applied to them. Information from the measured spectra in energy ranges above the influence of the expected CEνNS signal (above 400 eV), as well as measurements from the background characterisation campaign of the CONUS+ experimental site, are then used to correctly normalise the simulation output and add the different contributions together to acquire a fully working model accurately describing the data.

It was found, that in the low energy region of CONUS+ (below 1 keV), the dominant background sources are muons and neutrons from cosmic rays. They make up approximately 70 - 80% of the total background in both the [400, 1000] eV and [160/170/180, 400] eV region depending on the detector. The rest of the background in these low energy ranges is made up of a mixture of other components like radon in the detector chamber, cosmogenically activated isotopes in the copper parts of the cryostat and the germanium crystal itself, ^{210}Pb, and ^{60}Co and the leakage test background for the C2 and C3 detectors. With increasing energies, the composition of the background spectra changes significantly. The cosmic neutron component, the most dominant component at low energies, decreases significantly and other background sources like radon isotopes become more dominant. In the high energy regions of the experiment (energies above 100 keV) the most relevant background sources are radon, cosmic muons, and ^{210}Pb from the innermost lead layer of the shield. The background model was first developed for reactor on data and afterwards adapted to also fit the reactor off measurements. These adaptations mainly include different cosmic muon and neutron fluxes in the CONUS+ room due to the reactor drywell lid, which is placed on top of the CONUS+ room during reactor outages. The new fluxes are 3% and 19% lower respectively, resulting in lower background count rates from these components in reactor off measurements. Nevertheless, the two components remain the biggest contributions at low energies. Other adaptations in the reactor off background model include more effective radon flushing of the CONUS+ shield, which results in lower radon contaminations, and differing impact from radioactive noble gases during reactor outage. Additionally, the reactor neutron background, which was evaluated to have a small impact on reactor on data (one order of magnitude below the expected CEνNS signal), also disappears during reactor off data taking.

The resulting background models, i.e. the sums of all different background contributions for each detector and each data taking period (reactor on and off), were found to describe the measured spectra very well. The model works especially well at low to medium energies (below 30 keV), including in the energy range below 1 keV, where the region of interest for CONUS+ was later defined. At higher energies (above 100 keV) in the high energy channels of the measurement, smaller deviations of around 10% can be observed. The reason for these deviations is likely the efficiency correction of these channels which was applied with the help of the simulated muon spectra and proved to be slightly imprecise at high energies due to missing statistics. Nevertheless, the achieved background decomposition and model and especially its power at low energies is perfectly suitable for the use in the analysis of the CONUS+ data.

The second focal point of this work was the full likelihood analysis of the CONUS+ run 1 data sets. For this reason, the relevant data sets including selection and stability cuts were first defined. Due to instabilities in the noise spectrum in the C4 detector, one of the four detectors in run 1, this detector had to be excluded from the analysis. With the remaining setup of three detectors, an exposure of 347 kg days could be achieved in run 1. For the analysis procedure, the CONUS+ experiment uses a negative log likelihood (NLL) approach, in which a likelihood function consisting of the background models and the signal expectation are scaled, including several parameters describing detector characteristics. The background models used here are the models which were developed in the first part of this thesis and each detector and each data taking period has its own model. The signal expectation was calculated from the neutrino spectrum of the reactor (calculated using an approach suggested by the DayaBay collaboration), which was convolved with the CEνNS cross section and the expected quenching response in the detectors. Other detector characteristics, like their active mass, were also considered. The parameters of the likelihood function include several detector specific quantities, like the trigger efficiency parameters and active mass, which were constrained to previously measured values using Gaussian pull terms in the likelihood function. The most relevant parameter in the likelihood function for the CEνNS analysis of the data is the s parameter, which scales the expected signal spectrum. The best fit value of this parameter is directly used to calculate the number of CEνNS counts in the spectra and their uncertainties and it is the only parameter which is shared between all detectors in the combined detector fit.

In a first step, the spectra of three detectors of run 1 (not including C4) were fitted separately in single detector fits. For each detector, strong hints for a CEνNS signal were found: (117 $\pm$ 57) counts for the C5 detector, (69 $\pm$ 47) counts for the C2 detector, and (186 $\pm$ 66) counts for the C5 detector. All values are consistent with SM predictions. Lastly, the combined likelihood fit was performed, in which reactor on and off spectra of all detectors were fitted simultaneously. With this the final result for the CEνNS analysis of run 1 of the CONUS+ experiment was found to be (395 $\pm$ 106) counts, which is equivalent to a flux-averaged cross section of $(0.215 \pm 0.071) \cdot 10^{-40}$ cm^{-2}. As mentioned, this result marks the first successful measurement of the CEνNS interaction for reactor neutrinos, and therefore the first measurement of the interaction in the fully coherent regime.

In late 2024, after the conclusion of run 1 of the experiment, three of the four detectors in CONUS+ were replaced with new generation 2.4 kg detectors. Like their predecessors, these detectors feature excellent energy resolutions below 50 eV FWHM and trigger efficiencies at close to 100% down to 150 eV. The aim of this replacement and the subsequent data taking in run 2 of the experiment, which started in February 2025, is a high-precision CEνNS measurement with large statistics. As explained previously, such a measurement is a powerful tool to probe the standard model of particle physics, as well as look into possible influences from BSM physics, like light mediators or electromagnetic properties of neutrinos. The data taking of run 2 is currently running and already featured one reactor outage period in May 2025. The first-order sensitivity study presented in this work shows the potential of the new setup in terms of statistical significance, where it was shown that 5σ significance can already be reached with an exposure of 290 kg days. A full analysis of the run 2 data is planned for the near future.

At the same time, the run 1 data set is currently being analysed for several possible BSM channels, including the aforementioned light mediators, and electromagnetic properties, but also including neutrino non-standard interactions. A full publication on the result of these analyses including new limits for key parameters is expected in the near future.

This work, as well as previous publications by the CONUS/CONUS+ experiments and all other mentioned collaborations, show the keen interest in coherent neutrino scattering in the broader world of neutrino and particle physics. Due to its large cross section in relation to all other neutrino channels, the interaction offers a unique opportunity for the study of neutrinos with detectors of moderate size. The result of run 1 of the CONUS+ experiment was able to validate the use of the germanium semiconductor technology to probe this channel in the context of a nuclear reactor and run 2 shows the possibility for the upscaling of the experiment to larger active masses. The future of the CONUS+ experiment, as well as the CEνNS field in general, is promising. With its help, the ”ghost particle” of the standard model, the neutrino, can hopefully be made a little less ghost-like.

Appendices

Appendix A

Supplementary figures for background model

Here, additional plots referenced in Chapter 3 of the main text are provided.

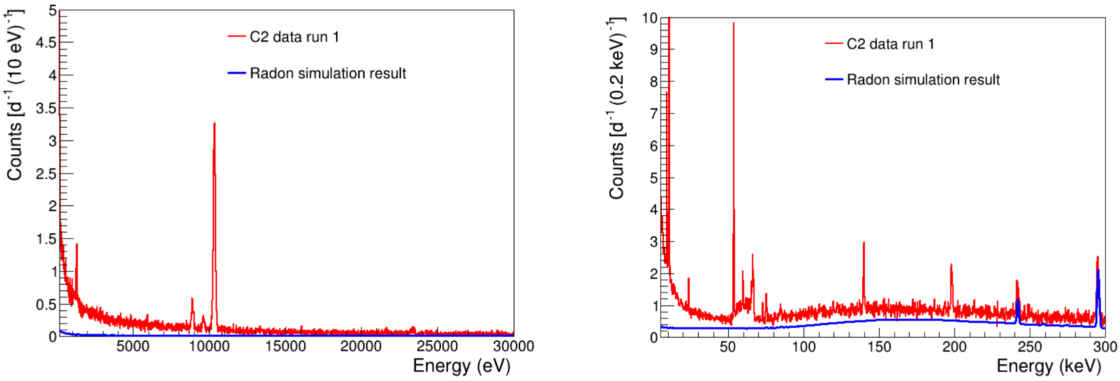

Figure A.1. Simulation of the radon component in the C2 detector.

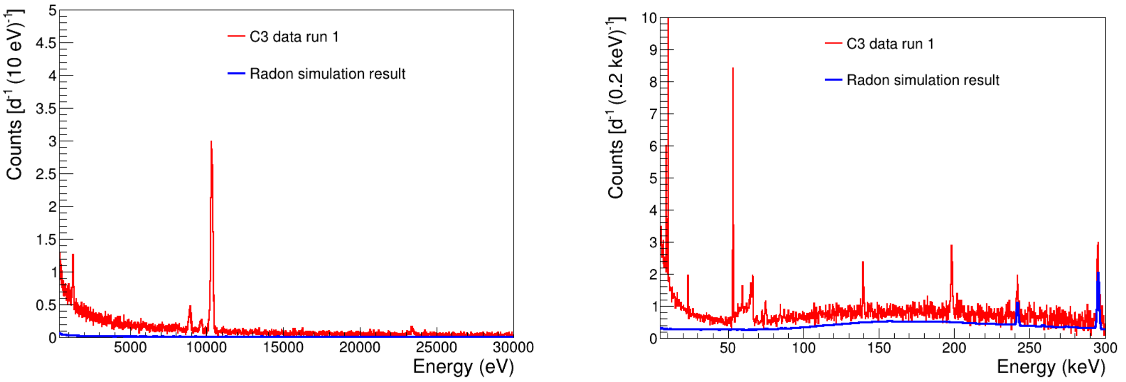

Figure A.2. Simulation of the radon component in the C3 detector.

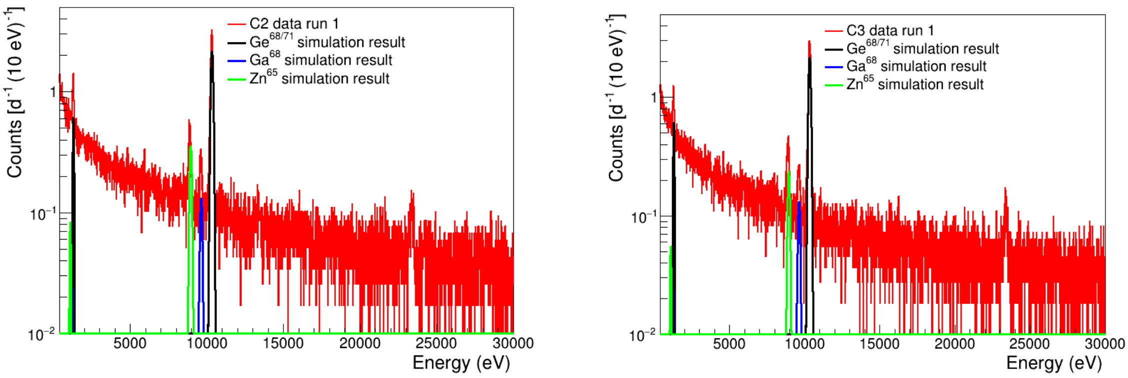

Figure A.3. Simulation of cosmogenically activated isotopes in the germanium crystals of C2 (left) and C3 (right).

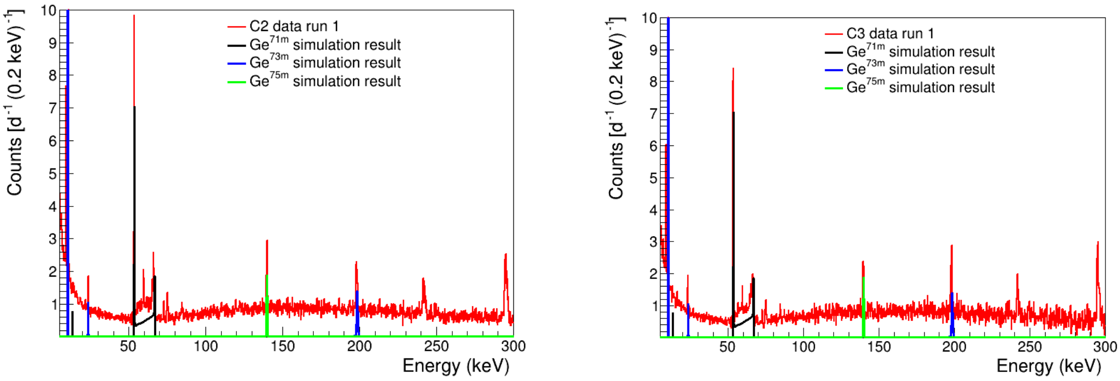

Figure A.4. Simulation of metastable germanium isotopes in the crystals of C2 (left) and C3 (right).

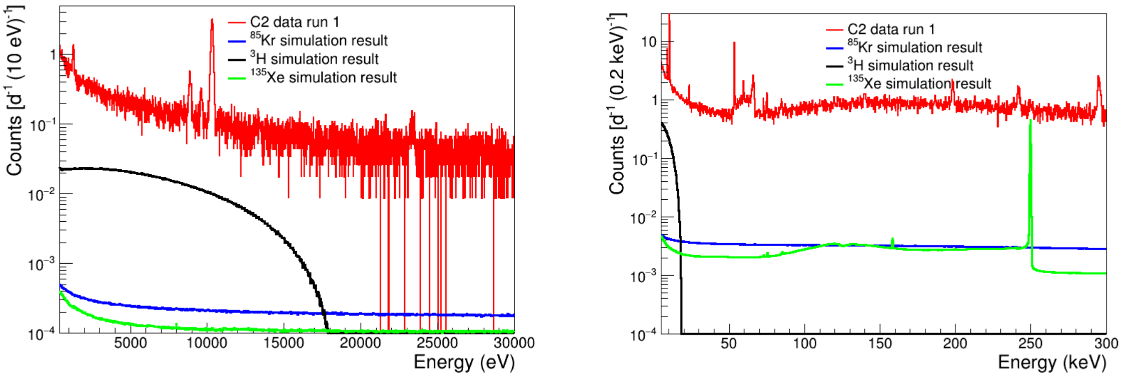

Figure A.5. Simulation of inert gases in the detector chamber for the C2 detector in reactor on

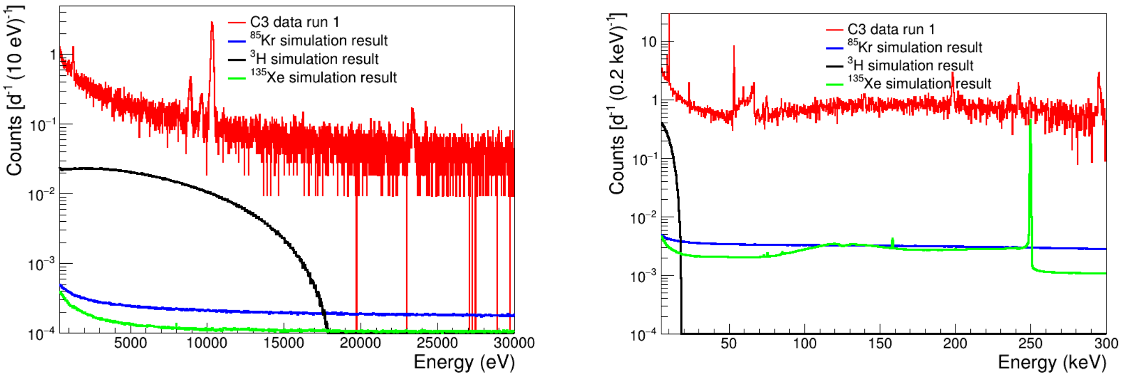

Figure A.6. Simulation of inert gases in the detector chamber for the C3 detector in reactor on

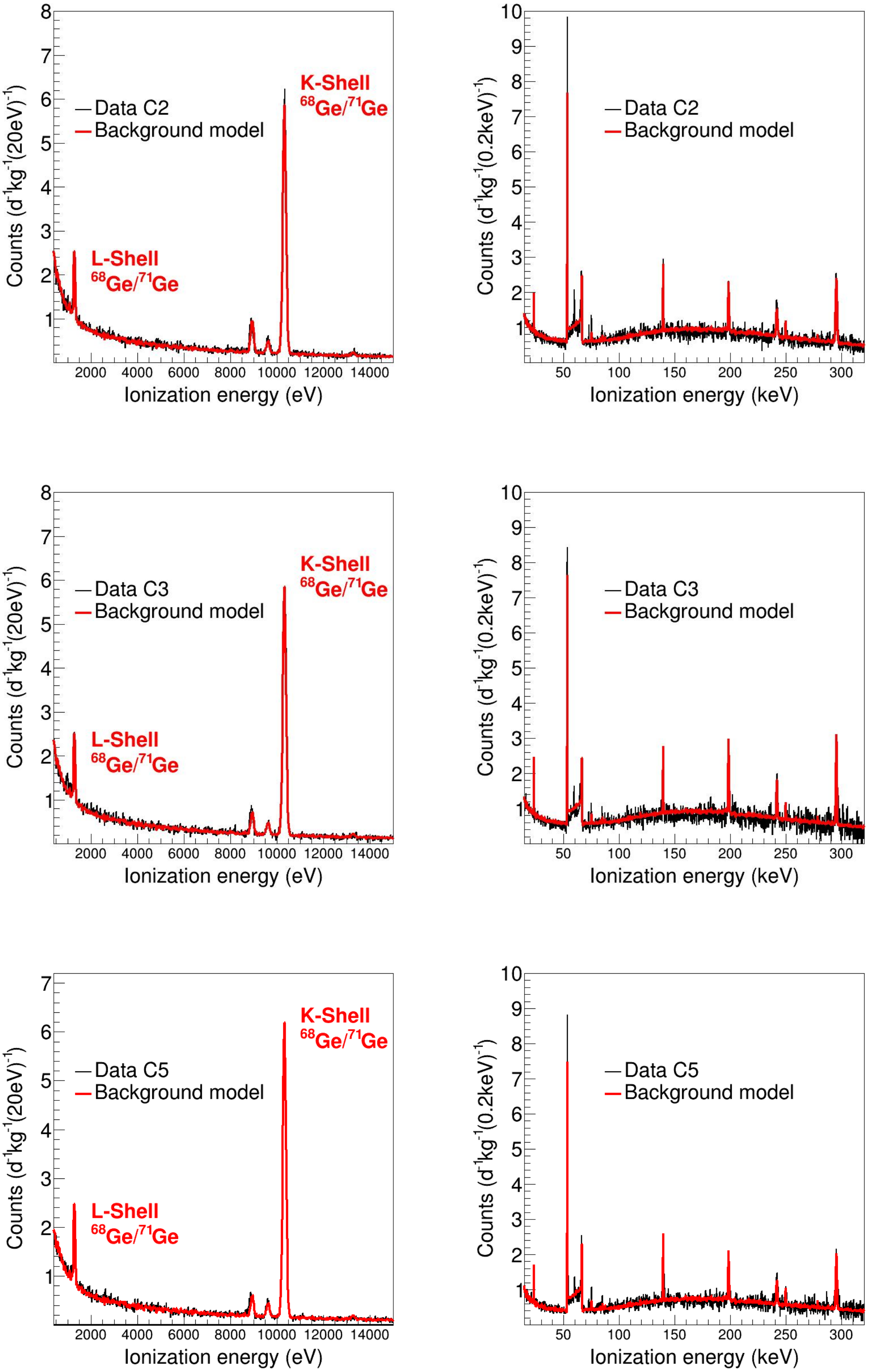

Figure A.7. Complete background model for the C2 (top), C3 (middle), and C5 (bottom) detectors during reactor on measurement. Excellent agreement is found for both detectors in all energy regions.

Appendix B

Supplementary figures for CEνNS result

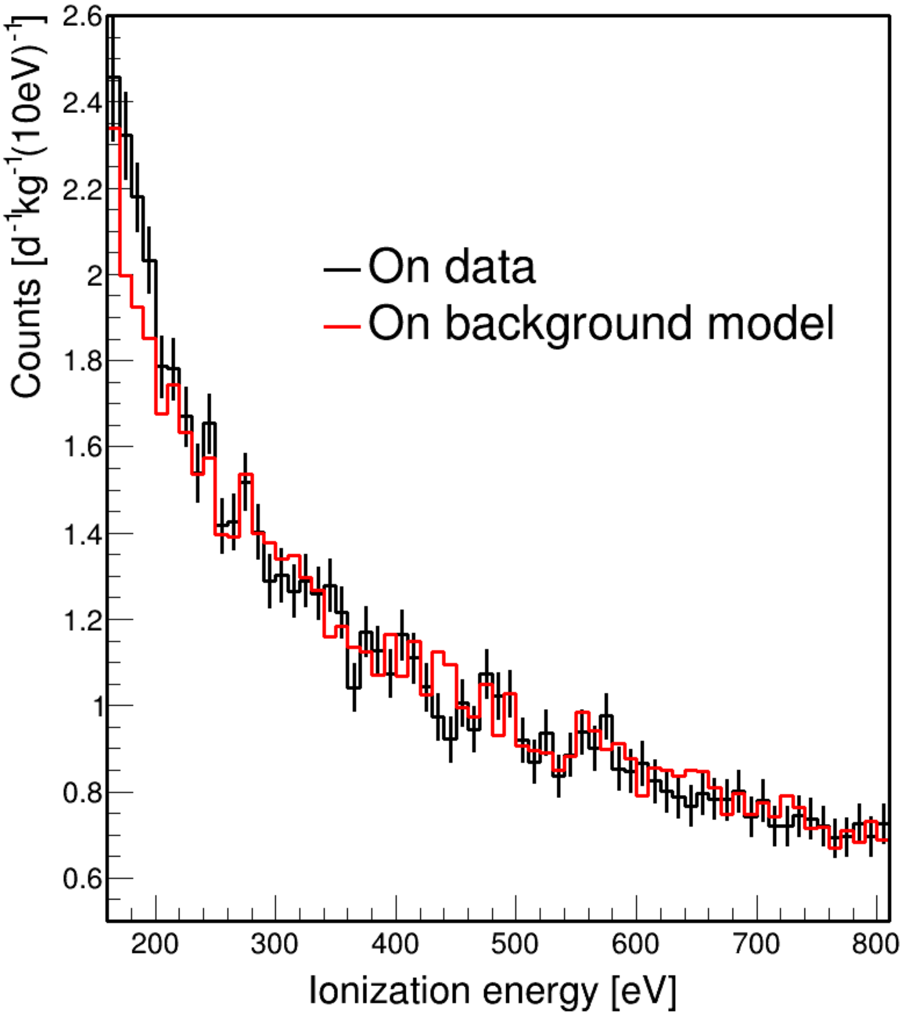

Figure B.1. Combined fit result for the sum of all detector background models to the full reactor on run 1 data set, with all relevant fit parameters included. The fit clearly shows an excess at energies below 400 eV, which is the CEνNS signal.

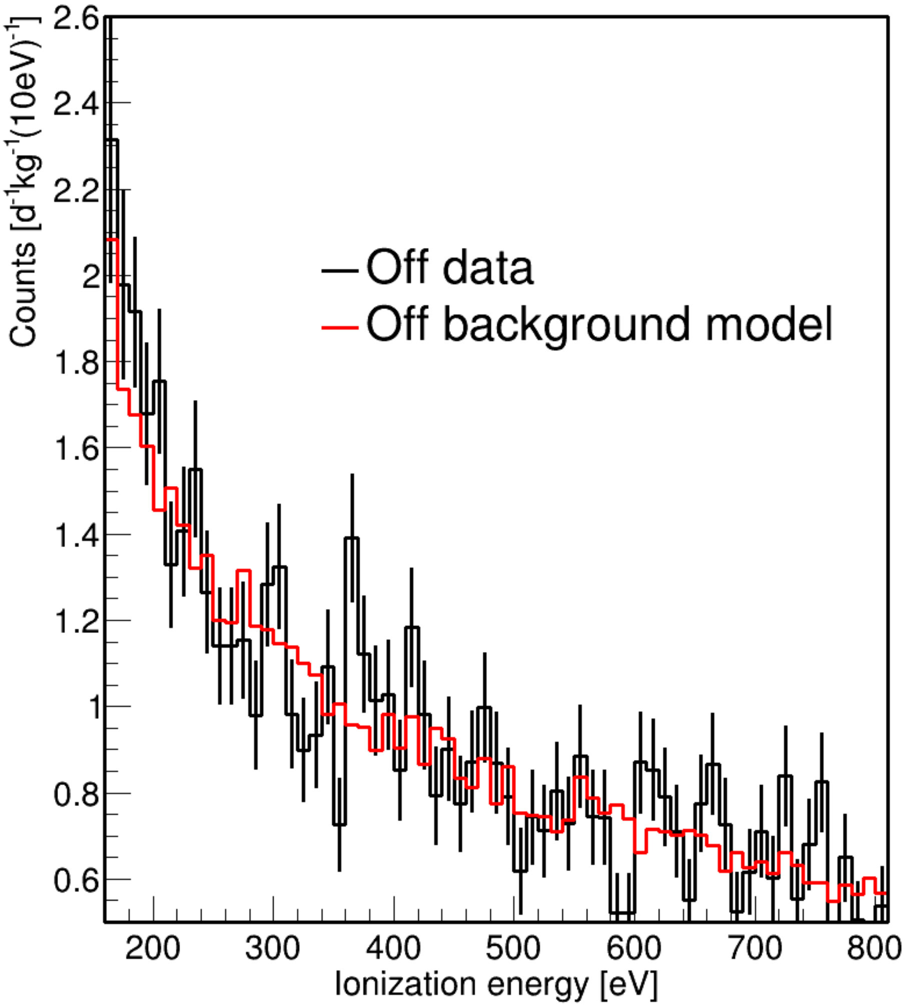

Figure B.2. Combined fit result for the sum of all detector background models to the full reactor off run 1 data set, with all relevant fit parameters included.

List of Publications

The results of this thesis are based on work done by the author in collaboration with others in the context of the CONUS and CONUS+ experiments. The following list contains all peer-reviewed articles published by the CONUS and CONUS+ collaborations with the participation of the author. A dedicated publication on the findings of Chapter 3 is in preparation.

1. N. Ackermann *et al.*
   Final CONUS Results on Coherent Elastic Neutrino-Nucleus Scattering at the Brokdorf Reactor.
   Physical Review Letters **133**(25), 251802 (2024).
   DOI: `https://doi.org/10.1103/PhysRevLett.133.251802`

2. N. Ackermann *et al.* (CONUS+ Collaboration)
   CONUS+ Experiment.
   European Physical Journal C **84**(12), 1265 (2024).
   DOI: `https://doi.org/10.1140/epjc/s10052-024-13551-6`

3. E. Sánchez García *et al.*
   Background characterization of the CONUS+ experimental location.
   European Physical Journal C **85**, 465 (2025).
   DOI: `https://doi.org/10.1140/epjc/s10052-025-14160-7`

4. CONUS+ Collaboration
   Direct observation of coherent elastic antineutrino–nucleus scattering.
   Nature **643**(8074), 1229–1233 (2025).
   DOI: `https://doi.org/10.1038/s41586-025-09322-2`

Bibliography

[1] D. K. Papoulias and T. S. Kosmas. Standard and nonstandard neutrino-nucleus reactions cross sections and event rates to neutrino detection experiments. *Advances in High Energy Physics*, 2015:1–17, 2015.

[2] J. Hakenmüller. Looking for coherent elastic neutrino nucleus scattering with the conus experiment, 2020.

[3] Leszek Roszkowski, Enrico Maria Sessolo, and Sebastian Trojanowski. Wimp dark matter candidates and searches—current status and future prospects. *Reports on Progress in Physics*, 81(6):066201, May 2018.

[4] N. Ackermann et al. The CONUS+ Experiment. *Eur. Phys. J. C*, 84(12):1265, 2024. [Erratum: Eur.Phys.J.C 85, 19 (2025)].

[5] E. Sánchez García et al. Background characterization of the conus+ experimental location. *The European Physical Journal C*, 85:465, 2025. Published online: April 26, 2025.

[6] J. I. Collar, A. R. L. Kavner, and C. M. Lewis. Germanium response to sub-kev nuclear recoils: A multipronged experimental characterization. *Phys. Rev. D*, 103:122003, Jun 2021.

[7] A. Bonhomme et al. Direct measurement of the ionization quenching factor of nuclear recoils in germanium in the keV energy range. *Eur. Phys. J. C*, 82(9):815, 2022.

[8] Janine Hempfling. *Optimization of CONUS+ Detectors and the Search for Neutrino Electromagnetic Properties*. PhD thesis, Ruprecht-Karls-Universität, Heidelberg, 2024.

[9] R.L. Workman et al. (Particle Data Group). Review of particle physics – cosmic rays. *Prog. Theor. Exp. Phys.*, 2024:083C01, 2024.

[10] M. Tanabashi et al. (Particle Data Group). Review of particle physics – cosmic rays. *Phys. Rev. D*, 98:030001, 2019.

[11] M.S. Gordon, P. Goldhagen, K.P. Rodbell, T.H. Zabel, H.H.K. Tang, J.M. Clem, and P. Bailey. Measurement of the flux and energy spectrum of cosmic-ray induced neutrons on the ground. *IEEE Transactions on Nuclear Science*, 51(6):3427–3434, 2004.

[12] H. Bonet, A. Bonhomme, C. Buck, K. Fülber, J. Hakenmüller, J. Hempfling, G. Heusser, T. Hugle, M. Lindner, W. Maneschg, T. Rink, H. Strecker, and R. Wink. Full background decomposition of the conus experiment. *The European Physical Journal C*, 83(3), March 2023.

[13] CONUS+ Collaboration. Direct observation of coherent elastic antineutrino–nucleus scattering. *Nature*, 643(8074):1229–1233, 2025.

[14] J. Colaresi, J. I. Collar, T. W. Hossbach, C. M. Lewis, and K. M. Yocum. Measurement of Coherent Elastic Neutrino-Nucleus Scattering from Reactor Antineutrinos. *Phys. Rev. Lett.*, 129(21):211802, 2022.

[15] National Nuclear Data Center. Nudat 3 database. `https://www.nndc.bnl.gov/nudat3/indx_dec.jsp`, 2025. Accessed: 2025-05-20.

[16] Charles Enz and Karl von Meyenn. *Wolfgang Pauli, A Biographical Introduction*. Springer-Verlag: 19., 1994.

[17] F. Reines and C. L. Cowan. Detection of the free neutrino. *Phys. Rev.*, 92:830–831, Nov 1953.

[18] Particle Data Group. Neutrino Masses, Mixing, and Oscillations. Review of Particle Physics 14, Lawrence Berkeley National Laboratory, Berkeley, CA, USA, December 2023. Section 14 of the 2023 Review of Particle Physics.

[19] W. N. Cottingham and D. A. Greenwood. *An Introduction to the Standard Model of Particle Physics*. Cambridge University Press, 2 edition, 2007.

[20] D. Akimov et al. Observation of Coherent Elastic Neutrino-Nucleus Scattering. *Science*, 357(6356):1123–1126, 2017.

[21] D. Akimov et al. First Measurement of Coherent Elastic Neutrino-Nucleus Scattering on Argon. *Phys. Rev. Lett.*, 126(1):012002, 2021.

[22] S. Adamski et al. First detection of coherent elastic neutrino-nucleus scattering on germanium. 6 2024.

[23] Daniel Z. Freedman. Coherent effects of a weak neutral current. *Phys. Rev. D*, 9:1389–1392, Mar 1974.

[24] R. Aaij, B. Adeva, et al. Measurement of the forward-backward asymmetry in z/γ□ → μ + μ − decays and determination of the effective weak mixing angle. *Journal of High Energy Physics*, 2015(11), November 2015.

[25] S. Fukuda, Y. Fukuda, et al. The super-kamiokande detector. *Nuclear Instruments and Methods in Physics Research Section A: Accelerators, Spectrometers, Detectors and Associated Equipment*, 501(2):418–462, 2003.

[26] M.G. Aartsen, M. Ackermann, et al. The icecube neutrino observatory: instrumentation and online systems. *Journal of Instrumentation*, 12(03):P03012–P03012, March 2017.

[27] Carlo Giunti and Alexander Studenikin. Neutrino electromagnetic interactions: a window to new physics, 2015.

[28] M. Atzori Corona, M. Cadeddu, N. Cargioli, F. Dordei, C. Giunti, and G. Masia. Nuclear neutron radius and weak mixing angle measurements from latest coherent csi and atomic parity violation cs data. *The European Physical Journal C*, 83(7), July 2023.

[29] G. Pagliaroli, F. Vissani, M.L. Costantini, and A. Ianni. Improved analysis of sn1987a antineutrino events. *Astroparticle Physics*, 31(3):163–176, April 2009.

[30] J. Billard, E. Figueroa-Feliciano, and L. Strigari. Implication of neutrino backgrounds on the reach of next generation dark matter direct detection experiments. *Phys. Rev. D*, 89:023524, Jan 2014.

[31] E. Aprile, K. Abe, et al. First dark matter search with nuclear recoils from the xenonnt experiment. *Physical Review Letters*, 131(4), July 2023.

[32] Shuaijie Li, Mengmeng Wu, et al. Search for light dark matter with ionization signals in the pandax-4t experiment. *Phys. Rev. Lett.*, 130:261001, Jun 2023.

[33] E. Aprile et al. First indication of solar <mml:math xmlns:mml=”http://www.w3.org/1998/math/mathml” display=”inline”><mml:mrow><mml:mmultiscripts><mml:mrow><mml:mi mathvariant=”normal”>b</mml:mi></mml:mrow><mml:mprescripts/><mml:none/><mml:mrow><mml:mn>8</mml:mn></mml:mrow></mml:mmultiscripts></mml:mrow></mml:math> neutrinos via coherent elastic neutrino-nucleus scattering with xenonnt. *Physical Review Letters*, 133(19), November 2024.

[34] PandaX Collaboration. First indication of solar ^{8}b neutrino flux through coherent elastic neutrino-nucleus scattering in pandax-4t, 2024.

[35] K.D. Irwin and G.C. Hilton. *Transition-Edge Sensors*, pages 63–150. Springer Berlin Heidelberg, Berlin, Heidelberg, 2005.

[36] Aaron Kraft, Christoph Rupprecht, and Yau-Chuen Yam. Superconducting quantum interference device (squid). `https://phas.ubc.ca/~berciu/TEACHING/PHYS502/PROJECTS/17SQUID.pdf`, 2017. UBC PHYS 502 Project, Fall 2017.

[37] C. Augier et al. Results from a prototype tes detector for the ricochet experiment. *Nuclear Instruments and Methods in Physics Research Section A: Accelerators, Spectrometers, Detectors and Associated Equipment*, 1057:168765, December 2023.

[38] R. Strauss et al. The ν-cleus experiment: A gram-scale fiducial-volume cryogenic detector for the first detection of coherent neutrino-nucleus scattering. *Eur. Phys. J. C*, 77:506, 2017.

[39] Mouli Chaudhuri. The Mitchell Institute Neutrino Experiment at Reactor (MINER). *Springer Proc. Phys.*, 277:589–593, 2022.

[40] D. Akimov et al. First measurement of coherent elastic neutrino-nucleus scattering on argon. *Physical Review Letters*, 126(1), January 2021.

[41] D.Yu. Akimov et al. The red-100 experiment. *Journal of Instrumentation*, 17(11):T11011, November 2022.

[42] M. Lesser. 3 - charge-coupled device (ccd) image sensors. In Daniel Durini, editor, *High Performance Silicon Imaging (Second Edition)*, Woodhead Publishing Series in Electronic and Optical Materials, pages 75–93. Woodhead Publishing, second edition edition, 2020.

[43] Irina Nasteva. New results on searches for CEνNS and Physics beyond the Standard Model using Skipper-CCDs at CONNIE. *PoS*, ICHEP2024:180, 2025.

[44] I. Alekseev et al. First results of the nugen experiment on coherent elastic neutrino-nucleus scattering. *Physical Review D*, 106(5), September 2022.

[45] N. Ackermann, H. Bonet, A. Bonhomme, C. Buck, K. Fülber, J. Hakenmüller, J. Hempfling, G. Heusser, M. Lindner, W. Maneschg, K. Ni, M. Rank, T. Rink, E. Sánchez Garcıa, I. Stalder, H. Strecker, R. Wink, and J. Woenckhaus. First observation of reactor antineutrinos by coherent scattering, 2025.

[46] G. Heusser. Low-radioactivity background techniques. *Ann. Rev. Nucl. Part. Sci.*, 45:543–590, 1995.

[47] H. Bonet, A. Bonhomme, C. Buck, K. Fülber, J. Hakenmüller, G. Heusser, T. Hugle, M. Lindner, W. Maneschg, T. Rink, H. Strecker, and R. Wink. Constraints on elastic neutrino nucleus scattering in the fully coherent regime from the conus experiment. *Physical Review Letters*, 126(4), January 2021.

[48] N. Ackermann, H. Bonet, A. Bonhomme, C. Buck, K. Fülber, J. Hakenmüller, J. Hempfling, J. Henrichs, G. Heusser, M. Lindner, W. Maneschg, T. Rink, E. Sánchez García, J. Stauber, H. Strecker, and R. Wink. Final conus results on coherent elastic neutrino-nucleus scattering at the brokdorf reactor. *Physical Review Letters*, 133(25), December 2024.

[49] G. Heusser, M. Weber, J. Hakenmüller, M. Laubenstein, M. Lindner, W. Maneschg, H. Simgen, D. Stolzenburg, and H. Strecker. Giove: a new detector setup for high sensitivity germanium spectroscopy at shallow depth. *The European Physical Journal C*, 75(11):531, 2015. Zugriff am 24. Mai 2025.

[50] J. Lindhard, M. Scharff, and H.E. Schiøtt. *Range concepts and heavy ion ranges*. Matematisk-fysiske meddelelser. Munksgaard, 1963.

[51] Zhong He. Review of the shockley–ramo theorem and its application in semiconductor gamma-ray detectors. *Nuclear Instruments and Methods in Physics Research Section A: Accelerators, Spectrometers, Detectors and Associated Equipment*, 463(1):250–267, 2001.

[52] H. Bonet, A. Bonhomme, C. Buck, K. Fülber, J. Hakenmüller, J. Hempfling, J. Henrichs, G. Heusser, M. Lindner, W. Maneschg, T. Rink, E. Sánchez García, J. Stauber, H. Strecker, and R. Wink. Pulse shape discrimination for the conus experiment in the kev and sub-kev regime. *The European Physical Journal C*, 84(2), February 2024.

[53] H. Bonet, A. Bonhomme, C. Buck, K. Fülber, J. Hakenmüller, J. Hempfling, J. Henrichs, G. Heusser, M. Lindner, W. Maneschg, T. Rink, E. Sánchez García, J. Stauber, H. Strecker, and R. Wink. Pulse shape discrimination for the conus experiment in the kev and sub-kev regime. *The European Physical Journal C*, 84(2), February 2024.

[54] J. B. Johnson. Thermal agitation of electricity in conductors. *Phys. Rev.*, 32:97–109, Jul 1928.

[55] Ugo Fano. Ionization yield of radiations. ii. the fluctuations of the number of ions. *Physical Review*, 72(1):26–29, 1947.

[56] P. Barbeau, J. Collar, and O. Tench. Large-mass ultralow noise germanium detectors: Performance and applications in neutrino and astroparticle physics. *Journal of Cosmology and Astroparticle Physics*, 2007(09):009, 2007.

[57] CAEN S.p.A. V1782 - 8 Channel 12-bit 2.5 GS/s Switched Capacitor ADC, 2025. Accessed: 2025-03-11.

[58] CAEN S.p.A. V1740d – 64 channel 12 bit 62.5 ms/s digitizer supporting dpp□qdc firmware. `https://www.caen.it/products/v1740d/`, 2025. Accessed: 2025-07-17.

[59] P. K. F. Grieder. *Cosmic Rays at Earth*. Elsevier Science, 2001.

[60] J. Hakenmueller. Master thesis, 2015.

[61] S. Navas et al. (Particle Data Group). Review of Particle Physics 2024 (2025 Update): Passage of Particles Through Matter. *Phys. Rev. D*, 110:030001, 2024. Update as of January 15, 2025; see PDG Atomic and Nuclear Properties, https://pdg.lbl.gov/2025/AtomicNuclearProperties/adndt.pdf.

[62] Eljen Technology. *EJ□200 Plastic Scintillator Data Sheet*, July 2010. PDF datasheet, accessed via Jefferson Lab wiki.

[63] Phillip M. Rinard. Neutron interactions with matter. In *Neutron Interactions with Matter*, 1997.

[64] P. Goldhagen, J. M. Clem, and J. W. Wilson. The energy spectrum of cosmic-ray induced neutrons measured on an airplane over a wide range of altitude and latitude. *Radiation Protection Dosimetry*, 110(1-4):387–392, 08 2004.

[65] W. F. McDonough and S.-S. Sun. The composition of the earth. *Chemical Geology*, 120(3-4):223–253, 1995.

[66] National Institute of Standards and Technology. X-ray mass attenuation coefficients for elements, 2025. Accessed: 2025-03-03.

[67] J. Hakenmüller, C. Buck, K. Fülber, G. Heusser, T. Klages, M. Lindner, A. Lücke, W. Maneschg, M. Reginatto, T. Rink, T. Schierhuber, D. Solasse, H. Strecker, R. Wink, M. Zbořil, and A. Zimbal. Neutron-induced background in the conus experiment. *The European Physical Journal C*, 79(8), August 2019.

[68] H. Bonet, A. Bonhomme, C. Buck, K. Fülber, J. Hakenmüller, G. Heusser, T. Hugle, M. Lindner, W. Maneschg, T. Rink, H. Strecker, and R. Wink. Novel constraints on

neutrino physics beyond the standard model from the conus experiment. *Journal of High Energy Physics*, 2022(5), May 2022.

[69] S. Armbruster. Master thesis, 2023.

[70] Janina Hakenmüller, Gerd Heusser, and CONUS collaboration. CONRAD-a low level germanium test detector for the CONUS experiment. *Applied Radiation and Isotopes*, 194:110669, 2023.

[71] D Budjás, M Heisel, W Maneschg, and H Simgen. Optimisation of the mc-model of a p-type ge-spectrometer for the purpose of efficiency determination. *Applied radiation and isotopes : including data, instrumentation and methods for use in agriculture, industry and medicine*, 67(5):706—710, May 2009.

[72] A. Bonhomme, C. Buck, B. Gramlich, and M. Raab. Safe liquid scintillators for large scale detectors. *Journal of Instrumentation*, 17(11):P11025, November 2022.

[73] B Wiegel and A.V Alevra. Nemus—the ptb neutron multisphere spectrometer: Bonner spheres and more. *Nuclear Instruments and Methods in Physics Research Section A: Accelerators, Spectrometers, Detectors and Associated Equipment*, 476(1):36–41, 2002. Int. Workshop on Neutron Field Spectrometry in Science, Technolog y and Radiation Protection.

[74] M. Reginatto. Bayesian approach for quantifying the uncertainty of neutron doses derived from spectrometric measurements. *Radiation Protection Dosimetry*, 121(1):64–69, 2006.

[75] Martyn Plummer. Jags: A program for analysis of bayesian graphical models using gibbs sampling. *3rd International Workshop on Distributed Statistical Computing (DSC 2003); Vienna, Austria*, 124, 04 2003.

[76] C. Augier et al. Fast neutron background characterization of the future ricochet experiment at the ill research nuclear reactor. *The European Physical Journal C*, 83(1), January 2023.

[77] Chloé Goupy, Stefanos Marnieros, Beatrice Mauri, Claudia Nones, and Matthieu Vivier. Prototyping a high purity germanium cryogenic veto system for a bolometric detection experiment, 2024.

[78] Yuen-Dat Chan, Jason A. Detwiler, Reyco Henning, Victor M. Gehman, Rob A. Johnson, David V. Jordan, Kareem Kazkaz, Markus Knapp, Kevin Kroninger, Daniel Lenz, Jing Liu, Xiang Liu, Michael G. Marino, Akbar Mokhtarani, Luciano Pandola,

Alexis G. Schubert, and Claudia Tomei. Mage - a geant4-based monte carlo framework for low-background experiments, 2008.

[79] S. Agostinelli, J. Allison, K. Amako, J. Apostolakis, H. Araujo, P. Arce, M. Asai, D. Axen, S. Banerjee, G. Barrand, et al. Geant4—a simulation toolkit. *Nuclear Instruments and Methods in Physics Research Section A: Accelerators, Spectrometers, Detectors and Associated Equipment*, 506(3):250–303, 2003.

[80] J. Allison, K. Amako, J. Apostolakis, H. Araujo, P. A. Dubois, M. Asai, G. Barrand, R. Capra, S. Chauvie, R. Chytracek, et al. Geant4 developments and applications. *IEEE Transactions on Nuclear Science*, 53(1):270–278, 2006.

[81] C. E. Aalseth et al. The Majorana neutrinoless double-beta decay experiment. *Physics of Atomic Nuclei*, 67:2002–2010, 2004. [Majorana Collaboration].

[82] S. Schönert et al. The GERmanium detector array (GERDA) for the search of neutrinoless $\beta\beta$ decays of ^{76}ge at LNGS. *Nuclear Physics B - Proceedings Supplements*, 145:242–245, 2005. [GERDA Collaboration].

[83] R. Brun and F. Rademakers. ROOT — an object oriented data analysis framework. *Nuclear Instruments and Methods in Physics Research Section A: Accelerators, Spectrometers, Detectors and Associated Equipment*, 389(1–2):81–86, 1997.

[84] D. Reyna. A simple parameterization of the cosmic-ray muon momentum spectra at the surface as a function of zenith angle, 2006.

[85] E. V. Bugaev, A. Misaki, V. A. Naumov, T. S. Sinegovskaya, S. I. Sinegovsky, and N. Takahashi. Atmospheric muon flux at sea level, underground, and underwater. *Physical Review D*, 58(5), July 1998.

[86] J. Hakenmüller, W. Maneschg, and G. Heusser. Neutron flux at the gran sasso underground laboratory revisited. In *Journal of Physics: Conference Series*, volume 718, page 042028. IOP Publishing, 2016.

[87] J. A. BEARDEN and A. F. BURR. Reevaluation of x-ray atomic energy levels. *Rev. Mod. Phys.*, 39:125–142, Jan 1967.

[88] R. Agnese et al. New results from the search for low-mass weakly interacting massive particles with the cdms low ionization threshold experiment. *Phys. Rev. Lett.*, 116:071301, Feb 2016.

[89] Ute Eberle. Auf teilchen-jagd. *mare*, (150), Februar/März 2022. Zugriff am 24. Mai 2025.

[90] H. Bonet, A. Bonhomme, C. Buck, K. Fülber, J. Hakenmüller, G. Heusser, T. Hugle, J. B. Legras, M. Lindner, W. Maneschg, V. Marian, T. Rink, T. Schröder, H. Strecker, and R. Wink. Large-size sub-kev sensitive germanium detectors for the conus experiment. *The European Physical Journal C*, 81(3), March 2021.

[91] F.P. An et al. Seasonal variation of the underground cosmic muon flux observed at daya bay. *Journal of Cosmology and Astroparticle Physics*, 2018(01):001–001, January 2018.

[92] Wikipedia contributors. Isotopes of californium. `https://en.wikipedia.org/wiki/Isotopes_of_californium`, 2025. Accessed 21 June 2025.

[93] Internetchemie ChemLin. Curium□248 – daten und eigenschaften des isotops cm□248. `https://www.internetchemie.info/isotop.php?Kern=Cm-248`, April 2023. Last updated April 15, 2023.

[94] J. Engel. Nuclear form-factors for the scattering of weakly interacting massive particles. *Phys. Lett. B*, 264:114–119, 1991.

[95] J. Silk et al. *Particle Dark Matter: Observations, Models and Searches*. Cambridge Univ. Press, Cambridge, 2010.

[96] M. Cadeddu, F. Dordei, C. Giunti, Y. F. Li, and Y. Y. Zhang. Neutrino, electroweak, and nuclear physics from COHERENT elastic neutrino-nucleus scattering with refined quenching factor. *Phys. Rev. D*, 101(3):033004, 2020.

[97] F. P. An et al. Antineutrino energy spectrum unfolding based on the Daya Bay measurement and its applications. *Chin. Phys. C*, 45(7):073001, 2021.

[98] Herbert Steiner. The Daya Bay Experiment to measure Theta(13). *Prog. Part. Nucl. Phys.*, 64:342–345, 2010.

[99] World Nuclear Association. Plutonium. `https://world-nuclear.org/information-library/nuclear-fuel-cycle/introduction/physics-of-nuclear-energy?utm_source=chatgpt.com`, 2025. Accessed: 2025-06-23.

[100] Markus Koehli, Klaus Reygers. *Statistical methods in experimental physics*. University of Heidelberg, Physikalisches Institut, Heidelberg, Germany, n.d. Accessed: 2025-06-24.

[101] F. James and M. Roos. MINUIT: Function Minimization and Error Analysis. Technical report, CERN, 1994.

[102] D. Akimov et al. Measurement of the Coherent Elastic Neutrino-Nucleus Scattering Cross Section on CsI by COHERENT. *Phys. Rev. Lett.*, 129(8):081801, 2022.

[103] Elena Aprile et al. First Indication of Solar B8 Neutrinos via Coherent Elastic Neutrino-Nucleus Scattering with XENONnT. *Phys. Rev. Lett.*, 133(19):191002, 2024.

[104] Zihao Bo et al. First Indication of Solar B8 Neutrinos through Coherent Elastic Neutrino-Nucleus Scattering in PandaX-4T. *Phys. Rev. Lett.*, 133(19):191001, 2024.

[105] Th. A. Mueller, D. Lhuillier, M. Fallot, A. Letourneau, S. Cormon, M. Fechner, L. Giot, T. Lasserre, J. Martino, G. Mention, A. Porta, and F. Yermia. Improved predictions of reactor antineutrino spectra. *Phys. Rev. C*, 83:054615, 2011.

[106] Patrick Huber. Determination of antineutrino spectra from nuclear reactors. *Phys. Rev. C*, 84:024617, 2011.

[107] Kroon-Oil coolant sp 12 evo - 1l bottle. `https://www.kroon-oil.com/de/coolant-sp-12-evo-12-x-1-l-flasche-39642/`, 2025. Ready-to-use Long Life antifreeze, patented LOBRID Si-OAT additive technology, freeze protection down to –37 °C; compatible with BMW HT-12 and VW G12 EVO specs.

Acknowledgements

On a last note, I would like to thank everyone who supported me over the course of this PhD and in the last few years in general.
First of all, I would like to thank Prof. Dr. Dr. hc. Manfred Lindner who was my primary supervisor and gave me the chance to study and work in his division at the MPIK and in the CONUS and CONUS+ experiment. Your mentorship and belief in me enabled me to perform at my highest capability and allowed me to learn so much, not only about physics, but also about myself.
Next, I would like to thank JProf. Dr. Loredana Gastaldo for agreeing to be the second reviewer of my thesis and one of my co-supervisors and for her friendly encouragement and enthusiastic support.
Special thanks and gratitude goes to my colleagues of the CONUS+ experiment: Dr. Christian Buck, Dr. Edgar Sanchez, Dr. Janine Hempfling, Dr. Werner Maneschg, Dr. Thomas Rink, Dr. Kaixiang Ni, Hannes Bonet, Herbert Strecker. I could not have wished for better colleagues or a better environment to start my career in science. I would also like to give special thanks to Dr. Janina Hakenmüller for her helpfulness and support throughout not only my PhD but also my Master thesis before that. Most of the things in this thesis would not have been possible without her work.
Additionally, I would like to thank Edgar Sanchez and Christian Buck again for proof reading and reviewing this work and giving me valuable feedback.
Furthermore, I would also like to thank Prof. Dr. Susanne Mertens for giving me the opportunity to continue my work at the MPIK after my PhD.
Many thanks also to Prof. Dr. Kate Scholberg for providing me with the input data for the cross section plot in Section 4.7.5.
I am also grateful for the support of countless people at MPIK working in the IT department, the mechanics workshop, and all other departments from which I needed help at some point in the last four years. The same goes for the employees of the KKL nuclear power plant, specifically Michael Rank, whose help made this experiment and thereby this thesis possible.
Zuguterletzt möchte ich mich bei meinen Freunden und meiner Familie bedanken. Danke an

meine Eltern, Gerd und Sabine, ohne die ich niemals soweit gekommen wäre und die mich immer unterstüzt haben. Vielen Dank auch an alle meine Freunde, die diesen Weg durch das Physikstudium mit mir von Anfang an gegangen sind: Lukas, Sofía, Tobi, Jules, Jänni, Lea, Annalena, Simon, Joey, Dome, Kathrin, Charly, Paula und viele andere. Ohne die zahlreichen gemeinsamen Abende, Konzerte und Festivals wäre ich vermutlich jetzt nicht hier. Genau das selbe gilt für alle meine Freunde aus meinem Chor. Mit euch Musik zu machen hat mir einige der schönsten Erinnerungen der letzten jahre gegeben. Und zuletzt an meine wundervolle Partnerin Kathi: Danke, dass du immer für mich da bist, egal wie nervig und aufreibend die Physik auch ist. Ich liebe dich.